A Structural Sizing Methodology for the Wing-Fuselage of the Flying-V

T.P. Dotman

Delft University of Technology

TU Delft

This page is intentionally left blank

A Structural Sizing Methodology for the Wing-Fuselage of the Flying-V

by

T.P. Dotman

For obtaining the degree of Master of Science in Aerospace Engineering
at Delft University of Technology

TU Delft

DELFT UNIVERSITY OF TECHNOLOGY
FACULTY OF AEROSPACE ENGINEERING
DEPARTMENT OF AEROSPACE STRUCTURES AND MATERIALS

GRADUATION COMMITTEE

Dated: 16 December 2021

Chair holder:

Dr.ir. R.C. Alderliesten

Committee members:

Dr.ing. S.G.P. Castro

Dr.ir. R. Vos

Dr.ir. X. Wang

Abstract

The demand for sustainability in aviation is at a historical peak. Efforts from industry and institutions have made the conventional tube-and-wing aircraft greatly efficient, to the degree that a performance ceiling is being approached. Unconventional aircraft configurations promise to reduce fuel burn further, at the cost of design complexity and risk. One aircraft configuration which has the potential to allow for this increase in performance is the Flying-V concept. This research aims to contribute to a better understanding of the structural design methods of the Flying-V.

Several studies into the viability and performance of the Flying-V have been performed, showing promising results. However, these results mainly pertain to the aerodynamic and flight performance fields. Preliminary structural analyses have shown a significant reduction in structural mass. However, these structural analyses have not regarded the wing-fuselage enough as a novel structure, applying analyses which work well conventional wings or fuselages, but not on the oval fuselage structure. More specifically, the hoop stresses in the skins and frames were not assessed beyond the membrane response. Furthermore, a clear opportunity was identified in the inclusion of a fatigue analysis, beyond using the material fatigue limit.

The wing-fuselage structure was identified to be dominant in terms of weight. Furthermore, there is a knowledge gap in the understanding of the behaviour of the unconventional wing-fuselage structure. Therefore, the research goal was to determine an improved structural analysis and sizing methodology for the wing-fuselage. For the sizing procedure, failure modes in three categories were selected: static material failure, fatigue and stability. With the selected failure modes, the stresses were determined.

An extensive load case study was performed, resulting in a weight and load distribution over the aircraft for a large number of different load cases and different weights. Due to the favourable weight distribution and open cabin structure, the cross-section stresses were considered to be equally important as the longitudinal stresses in terms of failure. Megson's[1] boom method was applied to determine the stresses in longitudinal direction, while an enriched 2-dimensional FEM model was used to determine the stresses in the cross-sectional plane. The first important insights were obtained in the stress analysis stage: the hoop stresses vary greatly over the constant arc sections, due to significant bending. The stress analysis was validated using a 3-dimensional *ABAQUS* model of a fuselage section.

With the obtained stress calculation approach, the failure modes were determined for each category. Static material failure was calculated in limit and ultimate load conditions for the yield and ultimate static material strength, respectively. The fatigue performance was assessed by calculating the crack initiation life and crack propagation life (including residual strength). A fatigue load spectrum was determined from the standardised load spectrum by Jonge et al.[2]. Finally, multiple stability-related failure phenomena were assessed. The well-known column and plate buckling phenomena were evaluated. Global buckling and panel buckling were assessed by using a smeared property plate buckling method. The buckling behaviour under combined loading was approximated with an interaction relation.

With the obtained failure index distributions, a sizing methodology was determined. The sizing methodology was based on the identification of the driving variable(s) for each failure mode using stress and failure distributions from a generic geometry. As the sizing and analysis loop proved to require a substantial runtime, the sizing procedure was reduced in scope. The critical load cases were selected, and an early material selection was performed, based on the failure index distributions of a solution using mean material properties.

The wing-fuselage structure was sized for two selected concepts, leading to two similarly performing designs. The designs showed large frames and cross-beams compared to conventional fuselage frames. This was the case as high stiffness was necessary in the components, due to high bending and compressive loads, primarily induced by pressurisation. The frames show a large potential for reusing the same frame design along the constant cabin, potentially leading to significant economical gains. Secondly, the floor and ceiling needed a far higher amount of stringers than the pressure shells, as the high compressive loads lead to an instability-prone structure. A structural mass estimation was performed, for the two concepts. The mass of the original and NLES concept were obtained to be 65.4e3 kg and 67.2e3 kg, respectively. Additionally, a mesh convergence analysis and input sensitivity analysis was performed.

Preface

Delft University of Technology

16 December 2021

Dear reader,

thank you for showing an interest in my research on the Flying-V. Over the past year, I have received many different questions on the Flying-V, but mostly: *"When will it fly?"*. While it is a bit early to answer this, the aim of this thesis is to answer some of the structure-related questions. The structural design and weight are key factors in determining the viability of the aircraft in an early stage. The largest contributor to these categories was identified to be the unconventional wing-fuselage structure. The goal of this research is therefore to contribute to the understanding of the structural response and design of the wing-fuselage. As its name suggests, this structure fulfils both the wing and fuselage functions and therefore faces some unforeseen challenges. While this research results in an improved view on the behaviour, design and mass of the wing-fuselage structure, it is clear that there is still much to be done.

I am very grateful for contributing to the extraordinary project that is the Flying-V. While this venture is not without risks, it has the chance of achieving genuine innovation, changing the course of aviation.

I would like to acknowledge the people that have made this thesis possible. Firstly, I would like to express my sincere gratitude to my supervisors, Saullo Castro and René Alderliesten, for being such dedicated guides and advisors over the past year. Secondly, I would like to thank the graduation committee, Roelof Vos and Xuerui Wang, for their invested time. Also, I would like to thank Yaïr for providing me with the needed aerodynamic data. Furthermore, I would like to thank Martijn, Tijmen, Declan and Robert for proofreading. Finally, I would like to thank my friends, my parents and my sister for showing their complete support over the past 7 years.

Thom Dotman

List of Figures

List of Tables

List of Acronyms

BC	Boundary Condition
BWB	Blended Wing Body
CA	Constant Amplitude
CCC	Constant Cross-section Cabin
CORSIA	Carbon Offset and Reduction Scheme for International Aviation
CS	Certification Specifications
DSG	Design Service Goal
ELG	Engine and Landing Gear
FC	Flight Cycles
FE	Finite Element
FEM	Finite Element Method
FH	Flight Hours
FM	Fuel Mass
FV	Flying V
GAG	Ground-Air-Ground
IATA	International Air Transport Association
ICAO	International Civil Aviation Organisation
KBE	Knowledge-Based Engineering
L/D	Lift-over-drag ratio
LE	Leading Edge
LoV	Limit of Validity
MLG	main landing gear
MOI	Moment of Inertia
MoS	Margin of Safety
MPL	Maximum Payload Mass
MPLW	Maximum Payload Weight
MS	Structure Mass
MTOM	Maximum Take-Off Mass
MTOW	Maximum Take-Off Weight
NEF	No Edge Free
OEF	One Edge Free
OEM	Operating Empty Mass
PL	Payload Mass
SCF	Stress Concentration Factor
SIF	Stress Intensity Factor
SMF	Static Material Failure
TE	Trailing Edge
TAW	Tube-and-wing
VA	Variable Amplitude
WFD	Widespread Fatigue Damage

Contents

1
Background

1.1. Introduction

Since the dawn of aviation, the possibilities of different aircraft configurations have been an intriguing topic. In the first half of the previous century, many radical designs were made to explore the boundaries of aircraft performance and practicality. However, in commercial aviation, a clear standard arose: the well-known TAW (tube and wing) configuration. This configuration has more or less been the only commercial aircraft configuration on the civilian transport market.

Developed knowledge in the fields of aerodynamics, propulsion, structures and materials has led to significant improvements in aircraft performance. While these advancements led to increased performance, they also led to a high attachment to the TAW configuration. Pursuing other (radical) configurations and designs is a large technical and financial risk which is not desirable in the competitive aerospace industry. However, in the last decade or two, it has been theorised that a performance ceiling is being approached by the TAW configuration (Martinéz-Val [22]). Aircraft configurations such as the BWB (blended wing-body) have been proposed (Martinéz-Val [22]) (Marino and Sabatini [23]), whose (aerodynamic) performance and weight distribution are hypothesised to allow for a significantly lower fuel consumption. As may be expected, with new configurations, new problems arise. The Flying-V (FV) aircraft configuration, first synthesised by J. Benad [7], appears to be a promising alternative. While allowing for high aerodynamic efficiency and favourable weight distribution, it also appears less affected by some of the major problems plaguing the BWB configuration. Figure 1.1 shows a recent visualisation of the FV.

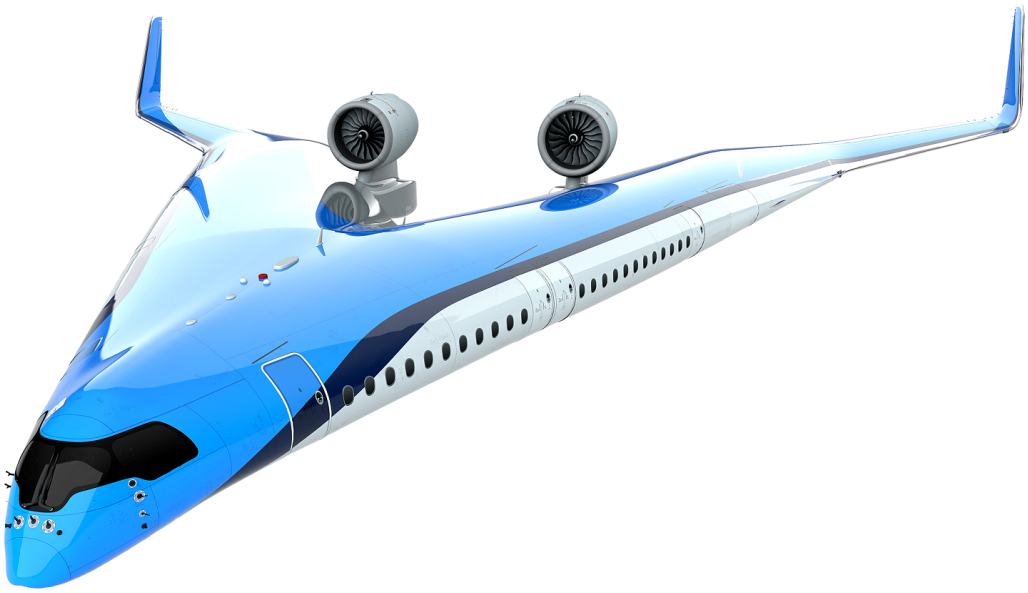

Figure 1.1: Flying-V concept visualisation by Edwin Wallet [3].

Preliminary aerodynamic and flight performance characteristics of the FV appear promising. However, there are multiple areas which have to be assessed to obtain a viable system, one of which is the structure. The oval fuselage, as introduced by Vos [24], was developed to prevent excessive deformations during

pressurisation. Previous research [10][11][13] has shown that this concept has high potential, but requires a more in-depth analysis.

1.2. The environmental impact of aviation

The goal of this research is to contribute to the ongoing efforts of making aviation sustainable. While sustainability is not an exact term, clear goals have been set by the higher organs in the aviation community. In collaboration with aviation industry stakeholders, the International Air Transport Association (IATA) [25] has set two objectives for the next 30 years. Firstly, net carbon neutral growth, from 2020 onward. This means that excess carbon emissions have to be balanced with carbon offsets, irrespective of passenger growth. The International Civil Aviation Organisation (ICAO) has set up the Carbon Offset and Reduction Scheme for International Aviation (CORSIA) to ensure this first goal may be met. Secondly, aviation industry carbon emissions in 2050 are reduced by 50% w.r.t. 2005. This formidable task demands commitment from all stakeholders in the aviation business, as this reduction cannot be realised in a single discipline. Initiatives such as the *Clean Sky Joint Undertaking* or *Continuous Lower Energy, Emission and Noise Program*, have been set up to coordinate research. These initiatives, as well as (inter)national policy changes are critical in order for this goal to be met. The prosperity of the aviation business has always been strongly susceptible to changes in economic or political policy. Additionally, COVID-19 has been a financial catastrophe, especially in the aviation sector. Support from governments is imperative in order to successfully continue research on sustainable aviation.

When performing a life cycle assessment of the greenhouse gas emissions of an aircraft, approximately 99% of emissions can be dedicated to fuel burn (Jakovljević et al. [26]). Therefore, it makes sense to focus on the minimisation of this fuel burn. Reducing carbon emissions by 50% is an ambitious goal and would certainly appear to have a large impact. However, climate change is not only dependent on the magnitude of carbon-based gas emission. Firstly, other greenhouse gases such as nitrogen oxides and particulates have a significant effect. Also, chemical reactions (e.g. formation of ozone) or physical reactions (freezing of water droplets, cloud formation) strongly depend on the deposition altitude (Penner et al. [27]). These phenomena also contribute significantly to the greenhouse effect. While this is considered out of the scope of this document, one should keep in mind that the focus on lowering carbon emissions is not the goal itself.

In aircraft structures, the goal of minimum fuel burn is achieved by creating a structure which is as light as possible. However, life cycle cost will always remain the primary design driver, and it is up to designers to find an optimum between manufacturing cost, operational cost and potential environmental costs. Additionally, practicality and comfort of the designed space are factors which should not be overlooked. For a modern conventional tube-and-wing aircraft, apart from cabin arrangement, there are no significant decisions which greatly affect practical space and comfort. In the design of the FV structure, in particular the oval fuselage, useful space and passenger comfort may differ greatly depending on the implemented solution. This should be taken into account moreso than in TAW aircraft structural design.

1.3. Unconventional configurations

In order to address the need for more sustainable and cheaper aviation, new configurations have been proposed. Most notably, the BWB has been considered a promising contender to decrease fuel burn. The lift generated by the body allows for a lower total wetted area, which decreases the drag. Also, the lift distribution is more similar to the weight distribution, which decreases the flight load induced stresses. This should result in a lighter structure.

Figure 1.2: Airbus ZEROe small BWB concept announced in September 2020[4].

Early BWB concepts showed the potential "supercarrier" capability, carrying over 1000 passengers (Denisov et al. [28]) (Liebeck [29]), due to its large internal volume. In the times of the "hub-and-spoke" philosophy, this was a promising outlook. Currently, the market has largely rejected this philosophy as there is a larger demand for point-to-point flights. Currently, smaller BWB concepts have been proposed, such as by *NASA* [25], or *Airbus*, as can be seen in figure 1.2. The mission specification of these smaller aircraft adheres well to market demand. They also reduce some of the disadvantages of "supercarrier" BWB aircraft with regards to evacuation, passenger acceptance and infrastructure.

The arrival of the FV concept calls for a comparison between these two configurations. In order to compare TAW, BWB and the FV aircraft concepts, a comparison has been made in table 1.1. This table highlights the advantages of the BWB over the TAW, which is then compared to the FV. Please note that the comparison is qualitative, unweighted and in no particular order. For reference, the current conceptual cabin and systems configuration of the FV may be found in Appendix H.

Table 1.1: Advantages of BWB over TAW compared to FV.

Advantages BWB over TAW	**Comparison with FV**
Body provides lift, wetted area is lowered, reducing drag and thus fuel consumption[7]	Should show similar performance
Less engine noise due to shielding [30]	Similar/Less: The engine is likely positioned further back, reducing shielding [31]
More favourable lift and weight distribution, inducing lower loads which reduces weight[7]	Similar
Boundary layer ingestion, potentially increasing thrust [23]	Depending on configuration, similar or less
Potential to carry many passengers [28][29]	Lower enclosed volume, less passengers
Higher Reynolds number, should decrease drag [5]	Similar

From the comparison it can be noted that the advantages over the TAW configuration are well-aligned with the future goals of aviation: more sustainable and quieter. The comparison between BWB and FV shows no great differences here, qualitatively speaking. Similarly, the disadvantages of the different configurations may be compared, as may be seen in table 1.2:

Table 1.2: Disadvantages of BWB over TAW compared to FV.

Disadvantages BWB over TAW	**Comparison with FV**
Evacuation is an issue for larger concepts, especially after ditching[22]	Easier to evacuate
Flat shape leads to large pressurisation loads, deformations may be an issue	Similar challenges, oval fuselage concept is better suited
Most of the passengers cannot see windows	Potentially more passengers can see windows
Existing freight containers may not work well	Similar
Uncomfortable for passengers far away from neutral axis during roll	Similar
Much harder to engineer family-type enlargements	Stretching is less of a challenge
Engines on top of AC pose maintenance challenges [23]	Similar
Stability may be more challenging [9]	Similar
Many unique parts due to complex shape	Less, especially concerning ribs and stringers
To accommodate enough fuel, tanks are in close proximity to passengers	Similar

From the comparison, it may be noted that there are some serious drawbacks to the BWB and FV configurations. For both configurations, challenges arise in a decrease in passenger comfort, by the limited amount of possible windows (and their weight penalty), as well as large roll accelerations far away from the neutral axis. Stability and engine maintenance may be more challenging. Also, space usage may not be optimal, due to the required tension walls and compression floors/ceilings as well as not being able to store fuel in close proximity to passengers.

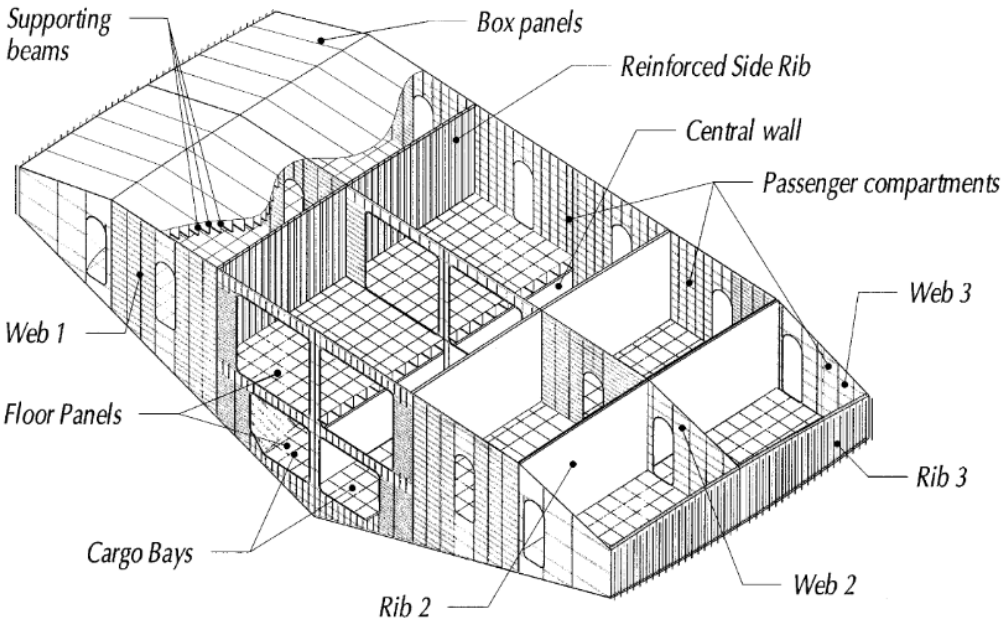

Figure 1.3: BWB interior structure as proposed by Bolsunovsky et al. [5]

However, for other points, the FV has some significant advantages over the BWB. Firstly, evacuation should be easier over large BWB configurations. This is less of a problem for small aircraft (Martinéz-Val [22]). A visualisation of a proposed BWB structure may be seen in figure 1.3, obtained from Bolsunovsky et al. [5]. It may be noted that the compartmentalisation of the passengers may create significant issues regarding

passenger acceptance and evacuation. Secondly, while the non-cylindrical pressure cabin problem is still a large challenge for the FV, its shape is a much more workable problem. It remains a tube-like structure, which should allow the determination of loads to be relatively straightforward. Also, the difference in pressure arc radii is smaller in the FV than BWB. The arc radius linearly increases the axial loads which must be carried by the internal force members.

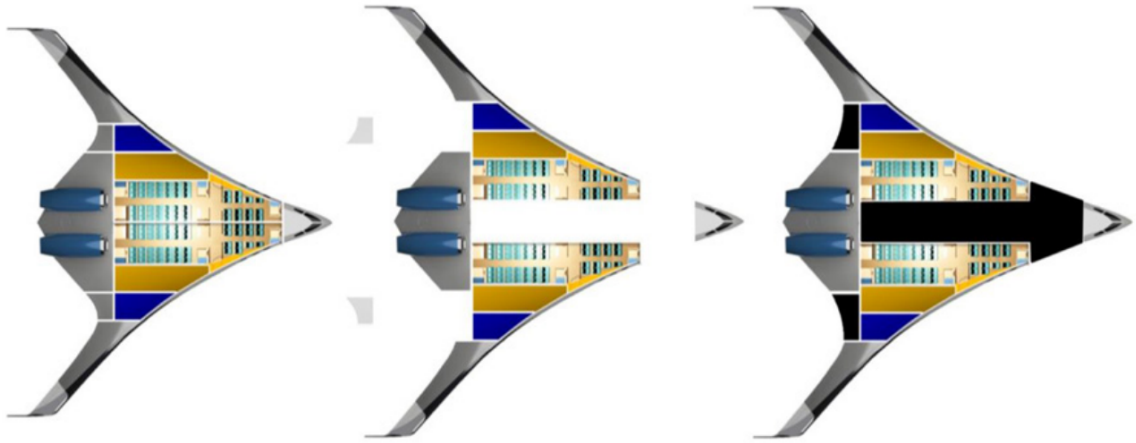

Figure 1.4: T-plug extension concept [6]

Another potential advantage of the FV is the difficulty of engineering family-type enlargements. The BWB concept has a complicated shape, and would require an extensive change to accomplish this. An example of a BWB enlargement may be seen in figure 1.4, as proposed by Page et al. [6]. Meanwhile, the enlargement of the FV is accomplished by stretching the tubes, similarly to TAW fuselage extensions. As the cross-section of the FV is constant until the first transition region, this is less complex. The last point is that the unique part count of the BWB configuration is much higher than that of the FV. Due to the complex shape of the BWB, elements such as ribs will each be unique. This is associated with a significant increase in cost. The FV has a much higher potential of bringing the number of unique parts down due to its tube-like shape.

Many of the advantages of the FV over the BWB configuration disappear when considering military (transport) or cargo aircraft. The pressurisation problem still is larger for the BWB configuration. However, for these types of aircraft, compartmentalising the interior becomes an option, possibly allowing for a lighter structure. For passenger transport, which is of main interest, the FV appears to be a better option.

1.4. Previous research on the Flying-V

1.4.1. Benad's concept

The Flying-V concept was synthesised in 2015 by J. Benad, in cooperation with *Airbus*, at the Berlin University of Technology ([7]). It was generated to fulfil the same mission as an *Airbus* A350-900, the most modern wide-body aircraft on the market. As the FV is a flying wing, an increase in aerodynamic performance is expected. Preliminary estimations by Benad show the estimated L/D is 10% higher w.r.t. the reference aircraft. Benad proposed two cylindrical fuselages in the flying wing, which should be structurally advantageous with regard to pressurisation. The favourable lift and weight distribution were estimated to lead to a 2% reduction in mass. Furthermore, preliminary analyses show longitudinal stability should be achievable without large problems. Furthermore, high-lift devices were shown to be unnecessary due to the large wing area. A visualisation Benad's concept may be found in figure 1.5.

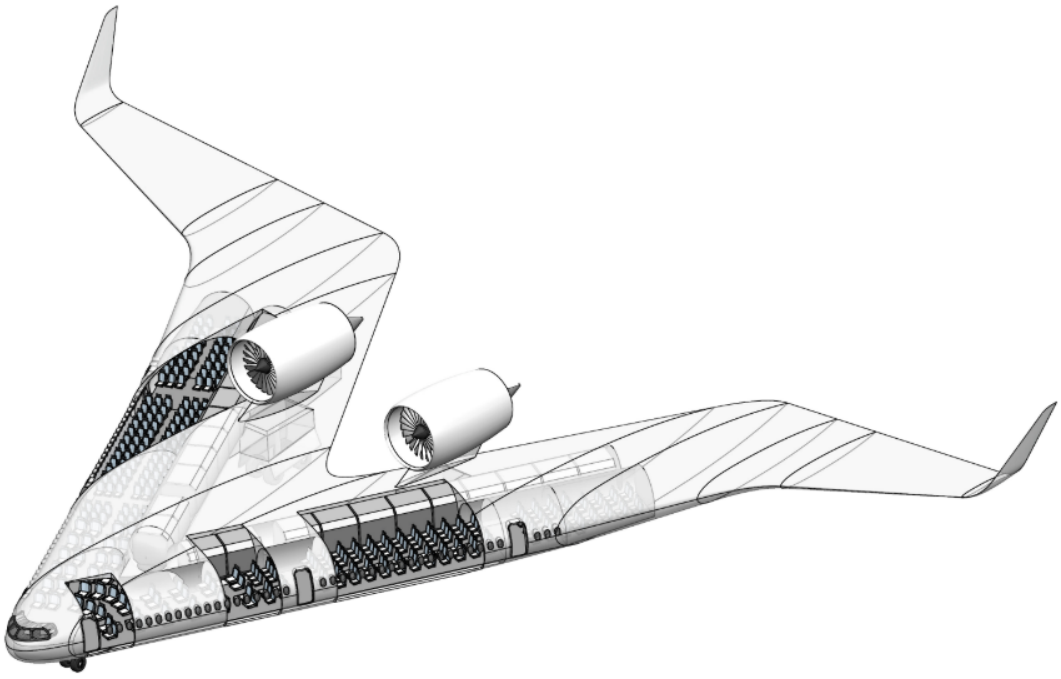

Figure 1.5: Benad's dual-tube Flying-V concept [7].

At this earliest stage of conceptual design, the values generated by Benad are prone to significant changes. However, the presented analyses appear conservative, which indicate an opportunity for more gains. Altogether, Benad synthesised a promising new aircraft configuration which kindled this research project.

Particularly relevant for this research is the construction of the wing-fuselage. Two tubes were used, for passenger and luggage/cargo storage, respectively. However, it was not clear how these structures would be connected to each other and the overall aerodynamic fairing.

1.4.2. Oval fuselage

Before the FV concept, efforts were made in the conceptual design of BWB aircraft in particular. One of the main structural challenges is the determination of a structurally efficient and practical fuselage structure. Several non-circular fuselage concepts were proposed over the years. Perhaps the most important next to the oval fuselage are the multi-bubble concept and the integrated skin-shell concept, as may be seen in figure 1.6. While they have their advantages, both are complex, and require the structure to be partitioned into separate "rooms".

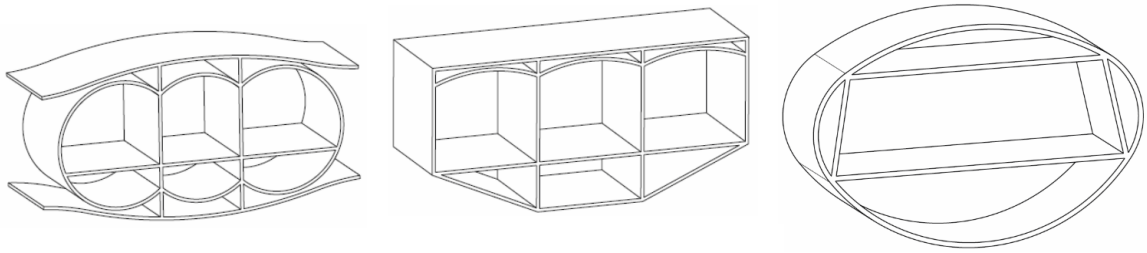

Figure 1.6: State of the art non-circular fuselage concepts, Schmidt [8].

First proposed by Vos et al.[24] in 2012, an "oval" fuselage could offer high structural performance while maintaining an open structure. The principle of the oval fuselage concept is the following. Four circular arcs of varying radius are joined together, while maintaining tangency at these joints. The parametrisation may be achieved in a straightforward manner, as described by Vos et al. [24] or Roelofs [32], depending on the desired freedom of variables. As the skins are circular arcs, their deformation was assumed to be like that of a membrane, and will therefore be purely in tension. This hoop load scales linearly with the arc radius,

and may easily be shown to be:

$$F = \frac{2dp \cdot r \cdot sin(\theta/2)}{2sin(\theta/2)} = pr \tag{1.1}$$

Here F is the force, dp the pressure differential, r the arc radius and θ is an infinitesimal angle. As this is a 2-dimensional representation, the force F is a distributed force ($[N/m]$). The resultant force at the joint will simply be equal to:

$$F_{res} = F_1 - F_2 \tag{1.2}$$

in the tangent direction. Were this oval unsupported, this resultant would cause the oval to obtain a circular shape. However, the skin joints may be connected through a floor, walls and a ceiling. The resultant force may be reduced to a tension force in the walls and a compression force in the floor and ceiling. As these structures will not be very thick, the axial stiffness is several orders of magnitude larger than the bending stiffness. Therefore, the implicit truss assumption of the floor, walls and ceiling was considered to be acceptable. The result is that this relatively simple structure only houses structural elements which undergo either tension or compression, while maintaining an open cabin. This is represented in figure 1.7.

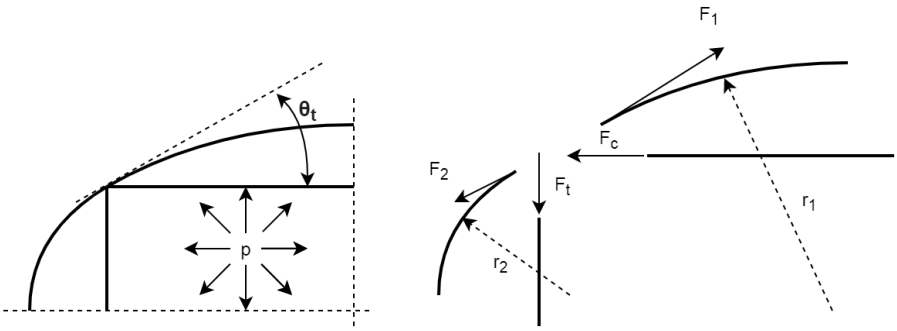

Figure 1.7: Forces in the skins, wall and ceiling in equilibrium.

This oval fuselage concept was carried forward in all ensuing Flying-V research based at the Delft University of Technology. The most relevant research is treated in the following sections.

1.4.3. Aerodynamic development

A year after Benad's publication, the FV was picked up by the Delft University of Technology for further analysis. To assess viability, an aerodynamic performance and payload capacity study was performed by Faggiano [9], optimising the planform for cruise.

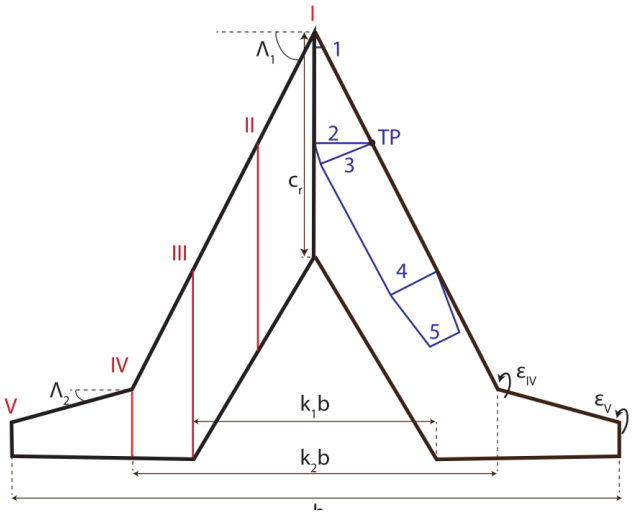

Figure 1.8: Streamwise profile sections as defined by Faggiano[9].

The work by Faggiano and Vos resulted in a planform parametrisation as may be seen in figures 1.8 and 1.9.

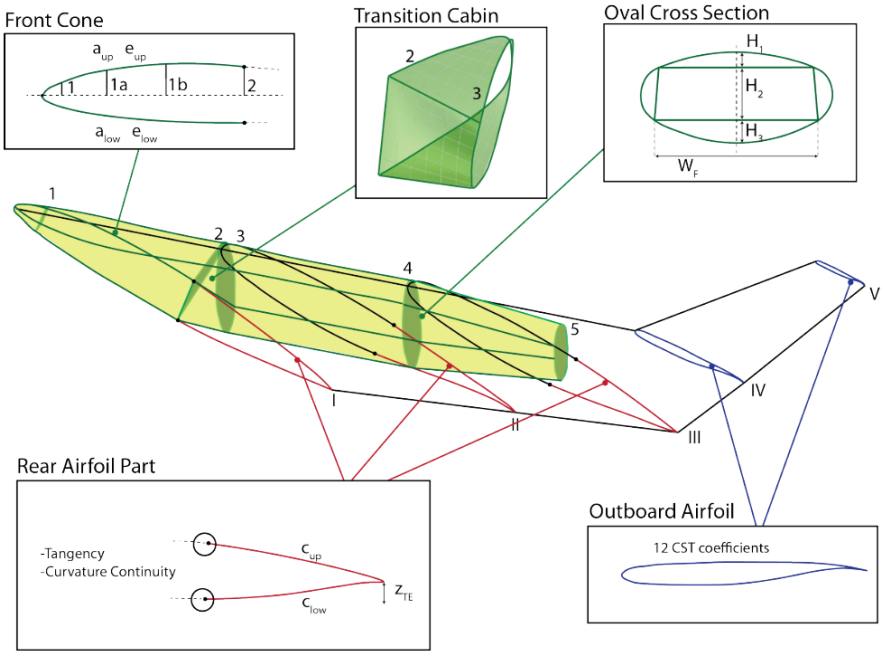

Figure 1.9: FV outer mould line parametrisation, Faggiano et al. [9]

To rapidly assess the aerodynamic design space, a vortex-lattice analysis was performed. Furthermore, an Euler solver was implemented to estimate the drag more accurately. Both wave drag and vortex-induced drag was taken into account. Empirical methods were used to estimate the profile drag. These analyses led to a higher-fidelity result than presented by Benad. The results were compared to the *NASA Common Research Model*, which possessed an estimated Lift-to-drag ratio of 18.9. Optimisation of the FV aerodynamics led to a maximum lift-to-drag ratio of 23.7 (Faggiano et al. [9]). The question arises how this translates into reduced fuel consumption. Using Breguet's range equation, one can determine the required fuel weight for a certain mission specification:

$$W_F = \left(W_{OE} + W_p\right)\frac{1-k}{k}, \qquad k = exp\left(\frac{-Rc_j}{Ma\,(L/D)}\right) \tag{1.3}$$

Where W_{OE} and W_p are the operating empty weight and payload weight, respectively. R is the range, c_j is the thrust-specific fuel consumption of jet engines, M is the cruise Mach number, a is the speed of sound at

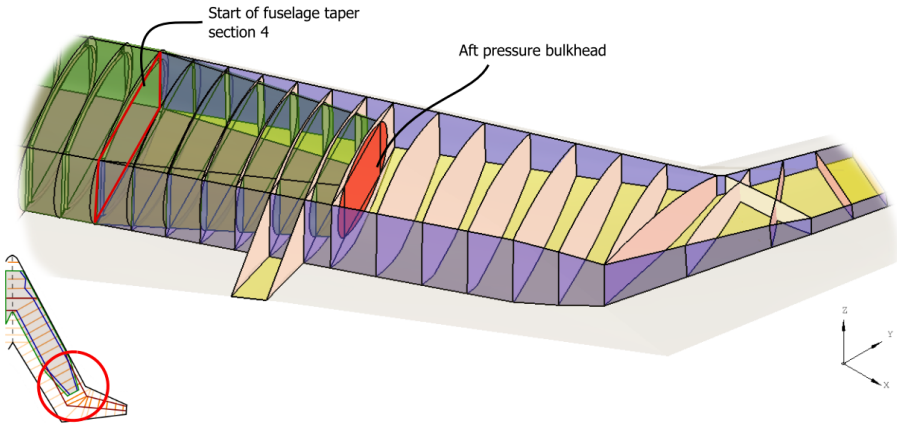

Figure 1.10: Graphical model of structure by van der Schaft [10].

cruise altitude and finally, L/D is the lift-to-drag ratio. It can be seen that in order to estimate the reduction in fuel consumption, not just the lift-to-drag ratio is of importance. Most notably, the weight should be prioritised as this parameter is the hardest to estimate, and it has a large effect on the required fuel weight. As the structure of the FV was unknown at this point, so was the weight w.r.t. a TAW aircraft.

Structural development

The first structural research was synthesised by van der Schaft[10] in 2017, in cooperation with *Airbus*. Again, the *ParaPy* Knowledge-Based Engineering (KBE) environment was implemented to perform a sizing optimisation procedure. A sizing procedure was set up, but only treats the spacing between structural elements and thicknesses, at predefined stringer and frames geometries. A structural lay-out model was assumed based on TAW wing box and fuselage structure element pitches, in consultation with Airbus. The underlying structural model relies on the oval fuselage concept, as well as the aerodynamic parametrisation of the outer mould line as determined by Faggiano and Vos.

While van der Schaft set up an impressive design procedure, the underlying structure was not well-substantiated. For example, as can be seen in figure 1.10, the rib placement near the wing kink is not sensible, nor manufacturable. The ribs intersect each other and ribs originate from the same point.

The Finite Element Method (FEM) solver *Patran / Nastran* was implemented to evaluate the structure. To assess for failure, the structure sizing tool ZORRO (developed by *Airbus*) was used. All structural elements are defined explicitly, except for the stringers. Modelling this was considered too complex for the first analysis. Instead, a stiffness alteration was proposed for the shell elements, implicitly including stringers. However, this yields invalid quantitative results for bending and buckling. The ZORRO tool can still qualitatively determine local buckling and bending loads. However, as stated by van der Schaft, the obtained quantitative results are not useful. Therefore, the results should only be interpreted qualitatively. Yield stress, local bucking and fatigue limit (500e8 cycles) criteria were implemented to assess failure. The thickness of elements is determined such that failure does not occur, and there is no large thickness difference w.r.t. neighbouring elements.

A qualitative interpretation of the results indicate several regions which require special attention. Firstly, the transition region from inboard to outboard wing clearly experiences stress concentrations. The fast decrease in cross-section geometry, as well as the change in angle call for extra attention. Secondly, the "first class" region required high thicknesses, as the underlying model is still lacking. This may be seen in figure 1.11. Secondly, the braking load case shows high local stresses at the nose and main landing gear strut locations.

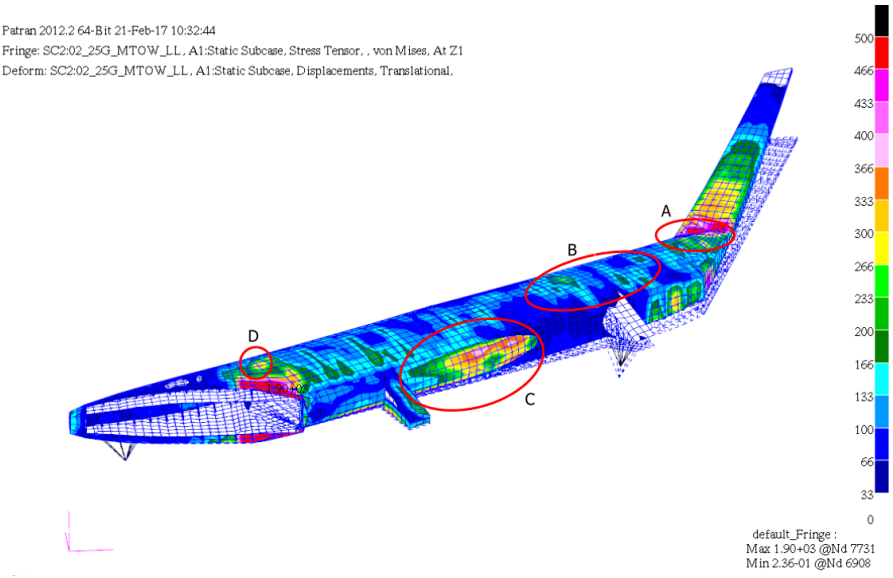

Figure 1.11: Stress [MPa] for a positive 2.5g load case, van der Schaft [10].

The mass estimation in its entirety is not very useful, as the set of load cases are incomplete, and the ZORRO results may not be interpreted quantitatively, and the underlying model is not substantiated adequately. While these results produced by van der Schaft are not particularly useful, the overall methodology appears promising for structural sizing. It should be noted that fatigue, one of the primary drivers in aircraft design, is only mentioned a few times in the report. The fatigue limit is applied as the material strength to determine the performance of a fatigue load case. This clearly indicates an opportunity improve the fatigue response of the aircraft.

1.4.4. Claeys

The work by van der Schaft was continued by Claeys in 2018. Again, *ParaPy* was used to determine a sizing routine, with the final goal of estimating the mass of the FV. The same underlying structural model was used in the sizing process. However, improvements were made by Claeys. Firstly, a weight estimation was performed on a reference aircraft, an *Airbus* A350-900. Secondly, the model was improved by including stringers explicitly. Similarly to van der Schaft, structural spacing values are not calculated but based on typical values as indicated by *Airbus*. The frame pitch, rib pitch and stringer pitch are 0.635 m, 1.0 m and 0.2 m, respectively. These pitches normally vary in different regions of the aircraft.

Aerodynamic loads were modelled using *Airbus*' ODILILA software. Claeys compiled a list of load cases. Unfortunately, Claeys does not specify any methods or results which allow for reproduction.

A weight analysis based on the FEM results of the FV and the reference model was performed. The FEM mass of the FV is approximately 17% lighter than the reference aircraft, at 49.5e3 kg versus 59.6e3 kg. While at a first glance this appears promising, it may be noted that some oddities are present. For example, the weight of the pressure bulkheads of the FV was calculated to be more than three times as light, while there are 3 bulkheads instead of 2. Secondly, FV has no empennage weight. Furthermore, for the reference aircraft, additional structural items are listed which are not modelled in the Flying-V. Therefore, the obtained 17% weight decrease is likely unconservative.

When doing a trial run Claeys noted that the deflections in the nose transition region where excessive, as may be seen in figure 1.12. Claeys proposed a structural modification which allows for proper local stiffness and stress redistribution.

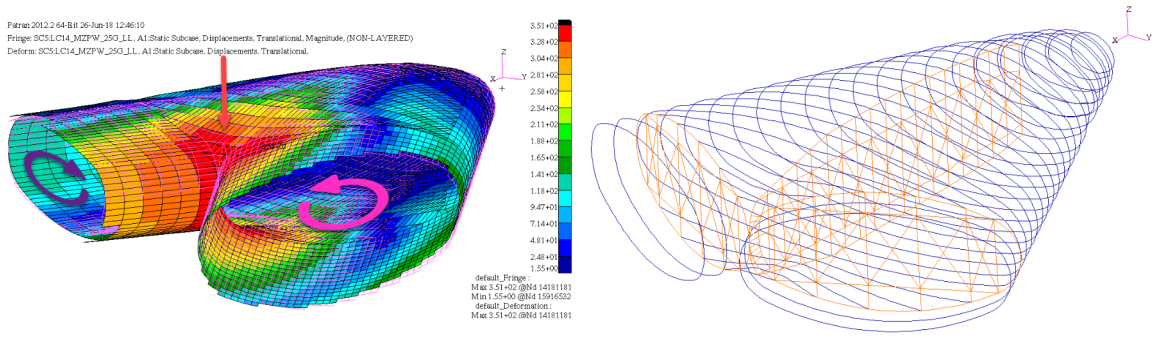

Figure 1.12: Proposed structure by Claeys [11] to counter excessive deformation.

Claeys generated a number of results showing the most critical load case for every element in the structure. The sized thickness of elements may be seen in figure 1.13. It may be seen that the thickness overall is thin, in the order of 4 mm. However, near the inboard-outboard wing transition, the sized thickness increases drastically. This is the case as high local stresses are generated by the change in cross-section and angles of the structure, introducing a stress concentration effect. It is expected that the generated thicknesses are a conservative estimate, as the local stresses may be alleviated by proper structural design.

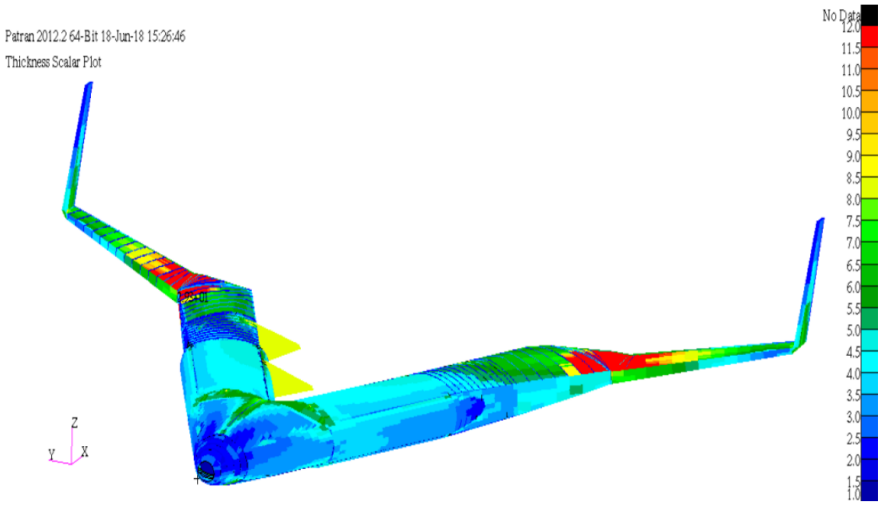

Figure 1.13: Thickness distribution as determined by Claeys [11].

Another result which may be of interest, is the deflection of the FV. From figure 1.14 it may be observed that the deflection of the inner wing is very small, which is a desirable property. Furthermore, the tip deflection is also significantly smaller compared to the wing of an *Airbus* A350. This may be assigned to the high stiffness provided by the FV structure, due to its large dimensions compared to the wing box of the A350.

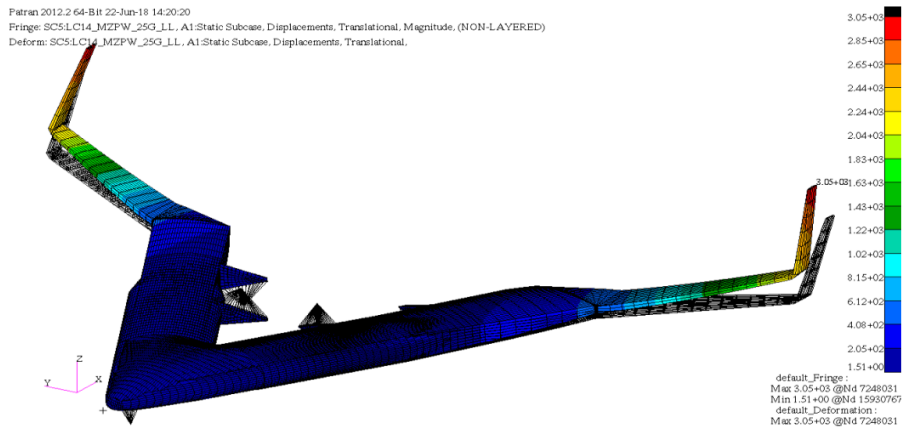

Figure 1.14: Deflection as determined by Claeys [11].

Remarkably, fatigue is not mentioned a single time in Claeys' research. Whereas Claeys' predecessor includes it (to a limited extent), fatigue is omitted from this piece of research. This indicates the unreliability regarding the weight estimation performed by Claeys. A large research opportunity is identified in fatigue research of the FV structure.

Hillen

Until recently, the geometry for the FV was primarily aerodynamics and performance driven. A manufacturability analysis of the concept was performed by Hillen in 2020 [12]. The main goal was to propose a new parametrisation which takes into account manufacturability and design flexibility. Manufacturability in the context of the thesis is primarily cost-related. Mainly, the manufacturability aspect is related to maximising a constant cross-section along the span, and minimising double curvature panels.

Hillen used the same *ParaPy* KBE environment in order to implement this manufacturability aspect. Unfortunately, as this research required compatibility with the previous work, the focus of the report is primarily the implementation of this parametrisation in *ParaPy*. Aerodynamic optimisations were not performed. This indicates the significant learning curve and compatibility concerns related to the use of the Flying-V *ParaPy* environment during a MSc thesis.

Hillen's parametrisation resulted in a significantly improved shape from a manufacturing and structures perspective. The shape can be defined in a more straightforward manner from the local wing axis. However, the resulting shape raises questions w.r.t. aerodynamic efficiency. The stream-wise continuity is severely hindered by this approach, as is presented in figure 1.15. The transition between the inboard wing-fuselage and the outboard wing are unviable. While not shown, the same is true for the transition between the constant and tapered cabin, albeit to a lesser degree. The sudden direction change which must be made by the airflow causes significant problems. Optimisation should reduce the severity of these transitions significantly, but there will always be sharp angles between these sections. It is therefore unlikely that a similar performance can be achieved compared to Faggiano's parametrisation.

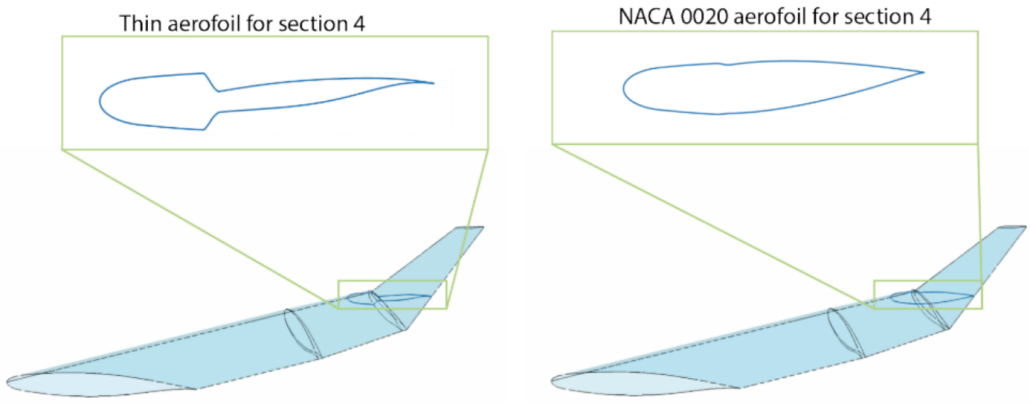

Figure 1.15: Streamwise transitions of Hillen's parametrisation. Obtained directly from Hillen [12].

It is remarkable that the design method did not result in a smoother inboard-outboard transition, or a thicker outboard wing. Without analysis, it can be seen that the obtained geometry is infeasible from both an aerodynamics and stress concentration perspective.

Oosterom

Oosterom's[13] research focused on the development feasibility of a family of Flying-V aircraft. As identified in 1.2, the Flying V has a large potential advantage over BWB aircraft in this respect. A multi-disciplinary analysis was performed in the *ParaPy* KBE environment, minimising for fuel burn. Oosterom performed a broad analysis, which included a significant amount of structural and weight analysis. These topics are discussed in more detail below. Oosterom performed impressive overall work, but for brevity, the following paragraphs focus on the potential improvements pertaining to the structural research of the Flying-V.

Structural analysis Oosterom analysed the structure with a limited set of 10 load cases. As the design loop contained many different analyses, and a high runtime had to be avoided, this choice was warranted. Nonetheless, the set of load cases is very limited for a structural analysis. Additionally, a number of concerns are listed below.

- Shear loads in local y-direction and x-direction were not considered in the analysis. The significant horizontal loads due to thrust, landing and aerodynamic drag were therefore not accounted for.
- Similarly, no moment about z was considered. Moments induced by thrust, landing and aerodynamic drag were therefore not accounted for.
- During a hard landing, the lift may exceed the weight: "... the landing gear has to withstand 125% of the takeoff weight, with the remaining 125% of the upward force provided by the aerodynamic forces." Oosterom [13], Ch. 4.3 p. 39. This is considered illegitimate, as during ground impact, the lift should not suddenly increase beyond its weight at touchdown. This reduces the stresses induced by landing, as the lift provides significant bending relief.
- Landing was only calculated at minimum fuel mass.

Oosterom produced running loads data, which could potentially be used for a longitudinal stress analysis (Appendix C p.96, figure C.4). However, there were a number of reasons why this data is not directly usable for further structural research. Next to the reasons as mentioned above, no associated weight distributions were provided. Furthermore, running loads data was provided for only 3 load cases: flight with maximum fuel, flight with minimum fuel and landing. This was identified as a research opportunity.

The remainder of the structural analysis was performed based on semi-analytical methods. For the longitudinal stresses, a boom method was used. For hoop stresses, only the pressure-induced stresses were determined with a membrane assumption, as shown in section 1.4.2. A sizing strategy was applied based on the selected failure modes, which is mostly clear. However, fatigue is not clearly included in the failure or sizing approach. While it is mentioned that the material strength is reduced for 1e5 cycles, it is not apparent how fatigue is implemented specifically.

Weight estimation Oosterom's weight estimation methods are quasi-empirical, resulting in structural and non-structural masses. The weight results can be found in table 1.3. The overall analysis has been performed thoroughly, but there are a number of caveats.

Table 1.3: Oosterom's[13] mass group results.

Group	**Mass** [10^3 kg]
Payload	30.9
Fuel	87.5
Landing gear	11.1
propulsion	19.6
operational items	5.8
furnishings	14.3
structure	52.4
systems	12.3
OEM	115
MTOM	234

Most importantly, the assumption was made that the use of composites leads to a 20% and 40% weight reduction to primary and secondary structures. This decision was based on work by Soutis [33]. Weight reduction is warranted in some cases, especially considering aged (empirical) weight estimation methods. However, 20% is a substantial decision based on a minimal amount of evidence. The Flying-V is a novel structure, which cannot be expected to perform as optimally as contemporary conventional structures, as more experience is needed. Additionally, the structure is under complex combined loading (especially in the wing-fuselage) as the structure has to perform more functions than a conventional wing or fuselage. Composite materials are not particularly suited to combined complex loads, giving them a far smaller weight advantage ('black aluminium').

A second important decision by Oosterom was to consider a factor between the model mass and the true mass. It was assumed that the modelled mass represents 60% of the true mass. Combining this with the above described weight reduction due to composites, the final factor between modelled and true mass was set at 1.2. The resulting weight is based on multiple large assumptions with limited substantiation. As the weight is one of the primary performance indicators, its analysis should be prioritised. Therefore, an improved structural weight estimation is warranted.

A remark on the empirical weight determination is the soundproofing weight W_{sp}, which makes up approx 5.0e3 kg of the furnishings mass. The empirical relation is based on the total enclosed fuselage volume, as shown below:

$$W_{sp} = 6.17\left(V_{cabin} + V_{cargo}\right)^{1.07} \tag{1.4}$$

Where V_{cabin} and V_{cargo} are the volume of the passenger cabin and cargo hold, respectively. This empirical method is based on the volume of a cylindrical fuselage. The oval shape of the Flying-V causes the perimeter of the cabin to be approximately 15% larger compared to the volume. Therefore, the soundproofing weight is likely underestimated. As this weight group is substantial, this should be reassessed in a more detailed design stage.

As mentioned above, the modelled structural mass estimate is hypothesised to be too low. On the other hand, Oosterom's family-optimised structure uses components which are viable for the whole family (e.g. oversized landing gear and structures), and therefore the conservativeness of the solution is somewhat increased. Overall, Oosterom produced useful results to use as input for structural analyses.

2
Overview of research methodology

The overview of the research project is clarified by stating the objective of the research, presenting research questions, stating hypotheses and describing the followed approach. The goal of this research is to obtain an improved structural sizing method of the wing-fuselage and to expand the understanding on the behaviour of the Flying-V structure. These results will advance the understanding of the viability of the Flying-V aircraft configuration.

2.1. Objectives and scope

As indicated in section 1.4, considerable research has been performed on the performance of the Flying-V. However, most of the research that has been carried out was related to the aerodynamic and operational performance. A number of multidisciplinary analyses have been performed which included structures as a significant factor (van der Schaft [10], Claeys [11], Oosterom [13].). However, the structural analyses were based on assumptions which are rather simplistic. Particularly, the treatment of the cross-sectional behaviour of the cabin structure may be considered lacking. The primary example is that the pressure-induced stresses have been determined by means of a membrane assumption, leading to a highly simplified stress state in the skins and frames, especially near joints. This research aims to improve the methods by which the stresses in the structure are obtained, and in turn, obtain an improved understanding of the associated failure modes and failure regions.

The oval cabin cross-section that has been used throughout the FV research in the past years was based on the above-mentioned membrane assumption (Hoogreef [34]). While the design presents many favourable properties, the choice for this design has been a constant in the past years, without its choice being properly examined or questioned. In the context of a membrane assumption, the choice for this layout is sensible. However, when a more realistic model is made, there is no guarantee that this layout is still favourable. With the same outer skin shape, many other concepts can be established and analysed, which should improve the understanding on the performance of the oval cross-section.

The inputs for all structural analyses are the load cases. While Oosterom in particular improved the visibility of the geometry and mass loads, There is much which remained unclear. Primarily, the mass distribution is an important uncertainty. In previous work, the mass groups were determined, but their location/distribution was not indicated directly. For regular aircraft, there are many different standardised or empirical procedures to distribute the weight over the aircraft structure in a straightforward manner. For the Flying-V, this is not the case. The weight distribution is not alike any wing or fuselage that has been previously made, and should not be treated as such. As was established by Benad [7] in the first research on the Flying-V, the weight distribution is one of the main envisioned benefits causing high performance. However, the balance associated with the fuel distribution throughout the aircraft has been one of the main challenges.

Previous research [10] [11] [13] has worked with an initial set of the expected critical load cases. However, a significant number of primary loads have not been included, such as the thrust. This research aims to determine weight distributions, and expand the set of load cases (and their respective distributions) applied to the Flying-V structure.

There are multiple areas in the FV structure which require more research. From previous recommendations, the inboard-outboard transition region and the engine pylon are some examples. However, as has been indicated above, the pressurised cabin structure has not been analysed to a degree that produced reliable results. Next to potential improvements in the analysis techniques/inputs, the novel structure demands

attention. The wing-fuselage concept, when analysed properly, is likely to show behaviour that is not seen in wings nor in regular quasi-cylindrical fuselages. The wing-fuselage dominates the structural weight of the aircraft. Therefore, the largest contribution to the viability estimate of the FV is identified to be an improved analysis and sizing of the pressure cabin.

The scope to this research is limited to the Flying-V-900. This was done as in previous research most information was presented for the -900.

As the name suggests, the wing-fuselage has to fulfil numerous wing and fuselage functions. Therefore, the stress state in the structure is expected to be complex. As a result, composites may not present such a large advantage over metallics. Taking this into consideration, as well as the large increase in modelling complexity associated with composites, the chosen materials for this research are limited to metallics. As the structure is comprised of highly loaded thin-walled structures, larger thicknesses offer significant advantages in terms of stability. Therefore, the metallics have been limited further to only aluminium alloys.

2.2. Research Questions

From the previously stated objectives, the main research question was formulated:

"What is the minimum weight design of the wing-fuselage structure of the Flying-V?"

The sub-questions which are to be answered:

1. What are representative load cases for structural design?
2. What is the structural response to pressurisation?
3. What is the distribution of stresses in the structure?
4. What is the distribution of critical failure modes in the structure?
5. What is a rapid preliminary sizing method?
6. What is the structural mass of the wing-fuselage structure of the Flying-V?
7. What is the difference in design and weight of the different cabin concepts?

2.3. Hypotheses

A number of hypotheses associated with the research questions were formulated, as indicated below.

A hypothesis for the main research question is not straightforward. Research by Oosterom [13] has shown a favourable weight reduction w.r.t. the latest generation of wide-body aircraft. However, the stress determination is (over)simplified. Moreover, it is unclear which mass distribution is being used, which is expected to have a large effect on the stress distribution. Overall, the hypothesis is that the obtained design is heavier than presented by Oosterom. This is indicated in more detail in the following paragraphs.

A hypothesis for the structural performance under pressurisation loads is as follows. In previous work, starting from Hoogreef [34], membrane elements were used to determine the hoop axial stress, without bending components. Meanwhile, tangency at the vertex joints is assumed. This combination is not possible. Firstly, the membrane assumption does not hold for a real structure, as the presence of frames will lead to appreciable bending stiffness, and thus bending-induced stresses. Secondly, tangency is required at the joints for aerodynamics. As a structural hinging joint is also not feasible, this is required for structures as well. While the skin arcs expand due to pressurisation, they are required to bend in the opposite direction near the joints to satisfy tangency. Large bending stresses are expected in these regions. Therefore, it is hypothesised that the structure performs worse than previously predicted under pressurisation loads. Additionally, as the arc radii are very large, the pressurisation load is hypothesised to be a major design driver.

A hypothesis on the performance of the different concepts is not straightforward. Each structural component in the oval fuselage concept has a clear function. Changing structural components leads to a shift in the functionality of each component, as different stresses and failure modes become critical. Therefore, specific hypotheses regarding the performance of different concepts have not been made.

Typically, an optimised design leads to a structure for which many failure modes become critical if the loads are increased beyond the design loads. Therefore, it is not straightforward to estimate which failure mode

is critical in each region. Based on the expected stresses in the structure, the critical failure modes are hypothesised as follows:

- Due to the hypothesised high hoop stresses, relative to the longitudinal stresses, fatigue will likely be a considerable design driver for both the crown and keel skin, as well as the attached frames. The critical regions will be where the pressure-induced bending increase the local tensile peak loads. As bending is expected to be high, the frames are hypothesised to be much larger compared to the results of previous research.
- The high compression loads in the floor and ceiling will likely cause stability-related failure modes to be critical in these structural members. As the panels are large and carry high loads, the amount of required stiffening is expected to be high in these components.
- As the lift and weight distribution have been shown to be favourable in previous research [7] [13], the longitudinal bending-induced compressive stresses are hypothesised to be relatively small. Therefore, the amount of stiffening assigned to the outer skins is hypothesised to be significantly lower than the stiffening to the floor and ceiling.

2.4. Analysis and sizing approach

This section aims to illustrate the global approach to meet the research objectives presented in the previous section. The main categories of the performed research are illustrated directly below, after which the specific considerations and dependencies are shown in more detail in the sections that follow.

The goal of the research is to design the wing-fuselage structure for a minimum weight. In order to perform this sizing, a number of activities were performed:

1. **Geometry and Layout:** The planform, cabin and system geometry was determined, which allowed the determination of load cases and primary structure geometry.
2. **Loads analysis:** A set of critical load cases was proposed, after which the respective weight and external load distributions were determined.
3. **Stress and failure analysis** The stresses were determined throughout the cabin structure. The stress analysis was divided into two categories: longitudinal and cross-sectional. The former was performed by using the well-known boom method, while the latter was performed using an enriched 2D FEM approach. The stresses were analysed throughout the structure for all concepts. The stresses were used to determine failure modes which correspond to three groups: Static Material Failure (SMF), fatigue and stability.
4. **Sizing:** A sizing procedure was proposed to minimise the structural weight, while denying the occurrence of failure in the structure.

Geometry To perform the structural analysis, geometric data of the structure, system dimensions and locations were required. This was primarily needed to determine the magnitudes, locations and orientations of loads, as well as the geometry of the structural elements. However, it became clear that much of the information regarding the geometry of the FV was scattered throughout previous theses, not compatible with the last iteration or simply not available. Chapter 3 aims to consolidate the available data. Additionally, some previous decisions, sizing results or other geometric parameters have been found to be incorrect or missing. These parameters are estimated where applicable. All other assumptions regarding the geometry are stated in this chapter. Also, next to the original oval fuselage cross-section concept by Hoogreef [34], one other concept is proposed.

Loads In order to produce stress and failure maps of the structure required for sizing, a representative set of load cases is required. The sets of load cases presented in previous research[10][11][13] were deemed incomplete. More importantly, no satisfactory weight distribution data was available for the Flying-V under different load conditions. Additionally, while aerodynamic analyses have been performed in *Parapy* by Faggiano [35], Hillen [12], Oosterom [13] and others, aerodynamic load data was not available. Therefore, a comprehensive study was performed on the weight distribution and load cases experienced by the Flying-V.

Stresses A typical first-order estimate of wing properties/design is to represent the wing as a beam element, and apply the respective loads (i.e. lift, weight, etc.). Due to the inherent slenderness of wings, combined with design lift loads that are far larger than the weight, bending is the dominant load for conventional wings. The bending induces high stresses in longitudinal direction of the wing axis, for which the wing box is primarily sized. In the case of regular wings, ribs provide high rigidity to the wing box cross-section. Ribs effectively retain the wings shape shape and provide support against buckling, while under a relatively low stress. Therefore, the effect of the loads on the stress state in the cross-section is typically postponed to a later stage. However, the above does not apply for the Flying-V. The open cabin leads to poor load distribution throughout the cross-section, and significant deformations of the cross-section. As is indicated in previous section, the cross-sectional (hoop) stresses are expected to be relatively high compared to the longitudinal stresses. Therefore, the stresses within the cross-section are much more likely to be critical over their longitudinal counterparts than for conventional wings or fuselages. The stresses in both the longitudinal direction and the cross-sectional plane were determined. The approach was to determine the stresses independently, after which a number of corrections were made to approximate a 3-dimensional stress state in the structure. The longitudinal and cross-sectional stresses could furthermore be combined, or used independently in the following failure mode analyses.

Failure modes To obtain a representative design, the most critical failure modes were identified, split in three categories:

1. Static material failure (SMF)
2. Fatigue
3. Stability

Static material failure was evaluated by determining the principal stresses for all elements in the structure. For the limit load cases, the stress values were compared to the yield strengths of the material, while a similar procedure was followed for the ultimate load cases and ultimate strength.

Fatigue failure was evaluated by determining the crack initiation life, crack growth life and residual strength of the structure. As the skins and frames were identified to be most prone to fatigue, these structures were analysed, while the stringers were omitted.

Stability failure was evaluated by determining the critical load for a number of stability phenomena. The stability of the global structure, stiffened panels and stiffeners was assessed at ultimate load, as their occurrence may lead to system loss. The stability of plates was assessed at limit load, as the load-carrying ability of the structure is still high after buckling has occurred.

Sizing From the above approach, every failure mode could be assessed throughout the whole structure. However, the above-mentioned analyses were associated with a significant runtime. To prevent looping over many input variables, a sizing strategy was proposed. A design algorithm was proposed to obtain a preliminary structural sizing design based on the critical variable for every failure mode. The sizing was performed initially for a number of cases to identify the optimal design space. After this, the minimum weight design was determined.

Approach visualisation The described research approach is illustrated globally in figure 2.1.

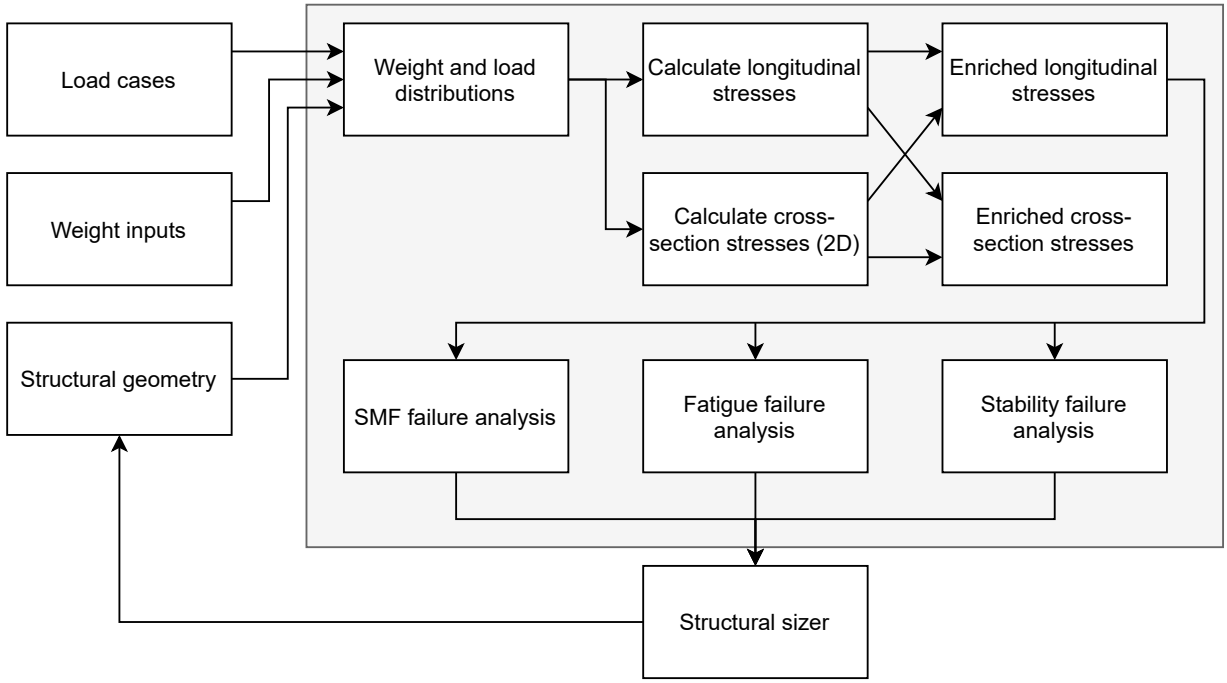

Figure 2.1: Global sizing approach

3
Geometric inputs

This chapter describes the geometry that has been carried forward in the loads and failure analyses. As this research focuses on the behaviour of the cabin structure, the inboard wing is described in more detail, while the outboard wing is represented in a simplified manner.

The first section discusses the geometry used in previous work, after which the planform and cross-section geometry is discussed. Additionally, the geometrical cabin simplifications are discussed, after which their effects are discussed. Finally, the different proposed cabin concepts are presented and their expected performance is discussed.

3.1. Planform geometry

The geometry and layout of the Flying-V have been continuously changing throughout the development process, as discussed in more detail in 1.4. For this research, the used geometry and layout were based on the results by Hillen [12] and Oosterom [13]. Hillen's parametrisation changed the outer mould line from a stream-wise concept to a more manufacturable concept. While this parametrisation raises some significant issues w.r.t the aerodynamic performance (as described in more detail in section 1.4.4), it allows for a more straightforward structural analysis approach. If Hillen's parametrisation cannot show high aerodynamic performance when optimised, the development may have to resort back to the stream-wise concept. This may have significant effects on the legitimacy of this research. However, assessing the consequences of this possibility is considered out of the scope of this research.

Below, the geometric parameters of the planform are described in the XY-plane. For reference, the used coordinate systems are defined first.

Coordinate systems Two coordinate systems have been defined for this research: global (X, Y) and local (x, y). The global system adheres to the standard global reference system of the aircraft. The local coordinate system is obtained by rotating the global coordinate system by the fuselage angle, such that the X-axis is coincident with the fuselage centreline. The origin is located on the aircraft symmetry plane, at the height of the cabin floor. Both coordinate systems are visualised in figure 3.1.

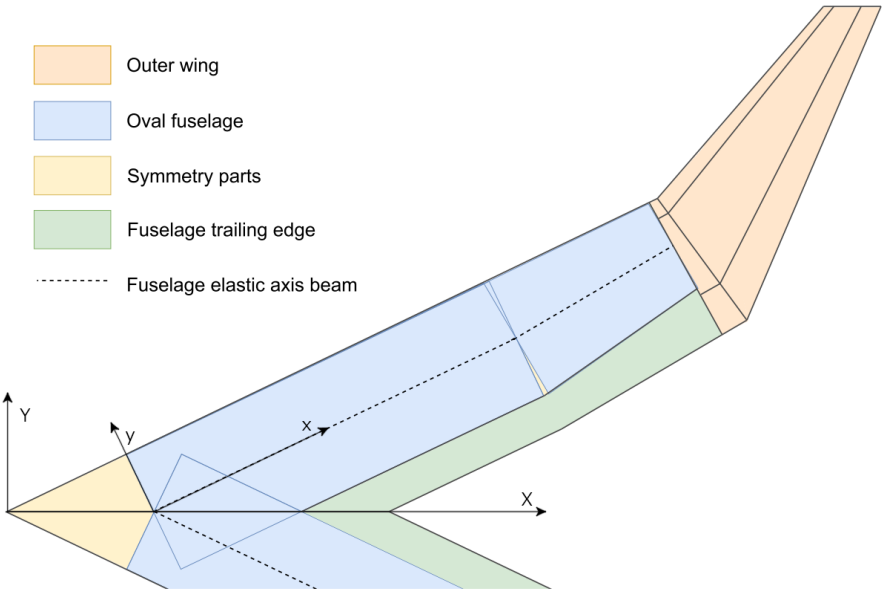

Figure 3.1: Cabin geometry simplification and coordinate systems, adapted from Oosterom [13], ch.4, p.38.

Geometric parameters The the majority of the planform geometry is taken directly from Oosterom's family optimised results of the Flying-V 900-series. These parameters may be found in table 3.1.

Table 3.1: Geometric input values.

Parameter	**Symbol**	**Length** [m]
Aircraft length	L_a	52.5
Span	b	60.7
Constant cabin length	L_1	24.0
Tapered cabin length	L_3	11.0
Inner-outer transition	L_4	1.5
Outboard LE length	b_{out}	14.75

Parameter	**Symbol**	**Angle** [deg]
Inboard LE sweep	λ_{in}	64.5
Outboard LE sweep	λ_{out}	40.7

While most information was readily available from previous work, some required geometric parameters were not readily available. These were estimated based on a CAD model of the outer mould line and cabin geometry as provided by Pieter-Jan Proesmans [12], as well as visualisations from Oosterom [13]. Table 3.2 shows the derived/estimated parameter values.

Table 3.2: Estimated planform parameters

Parameter	**Symbol**	**Value**	**Unit**	**Source**
Outboard TE sweep	lambda_out_TE	26.0	deg	Hillen's CAD
Outboard wing root chord	c_root_ow	6.0	m	Hillen's CAD
Outboard wing tip chord	c_tip_ow	3.2	m	Hillen's CAD
Passenger cabin length	L_cabin	25.8	m	Oosterom's visualisation
Business class length	L_bc	11.0	m	Oosterom's visualisation
Economy class length	L_ec	14.9	m	Oosterom's visualisation
Cargo bay length	L_cargo	9.2	m	Oosterom's visualisation
Fin length in global X	L_tip	5.8	m	Oosterom's visualisation

Engine and Landing Gear Pylon As may be seen in figure 3.2, the Engine and Landing Gear (ELG) pylon is attached to a certain length of the cabin. This length was estimated to be approx. 5.0 meters, based on Oosterom's moving structure section length.

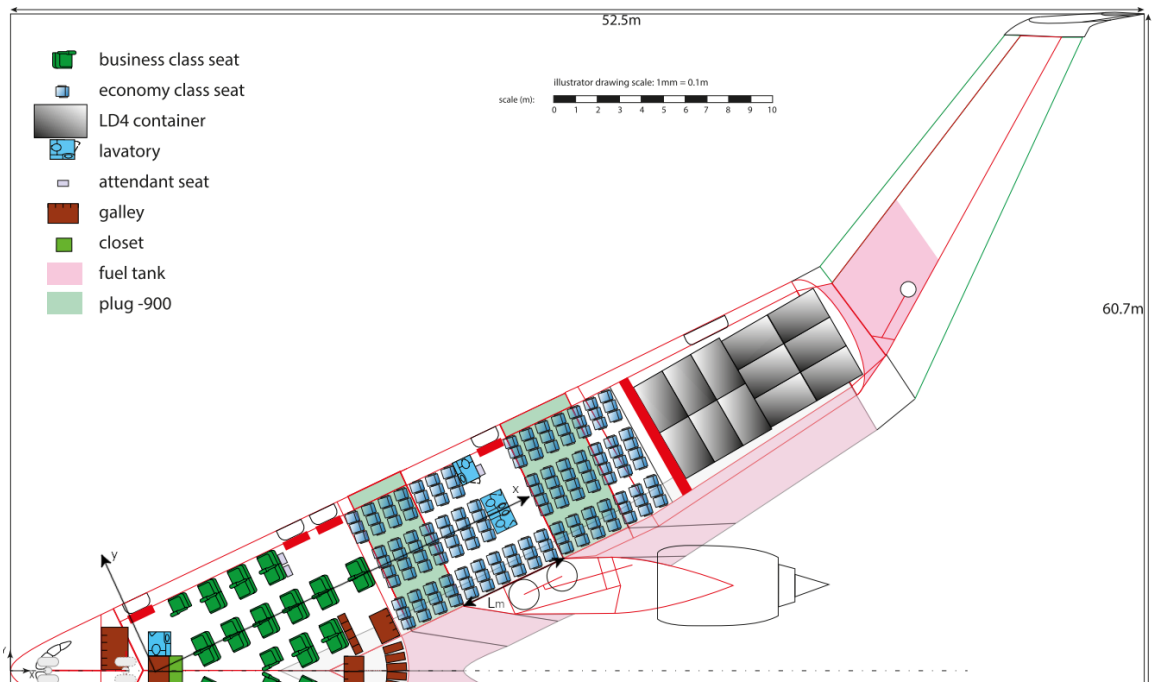

Figure 3.2: Flying-V-900 interior layout, adapted from R. Vos.

3.2. Cabin cross-section

More specific geometric parameters are described for the inboard wing cross-section. The wing-fuselage may be best described in the local xyz-coordinate system. The coordinate system and component names can be found in figure 3.3.

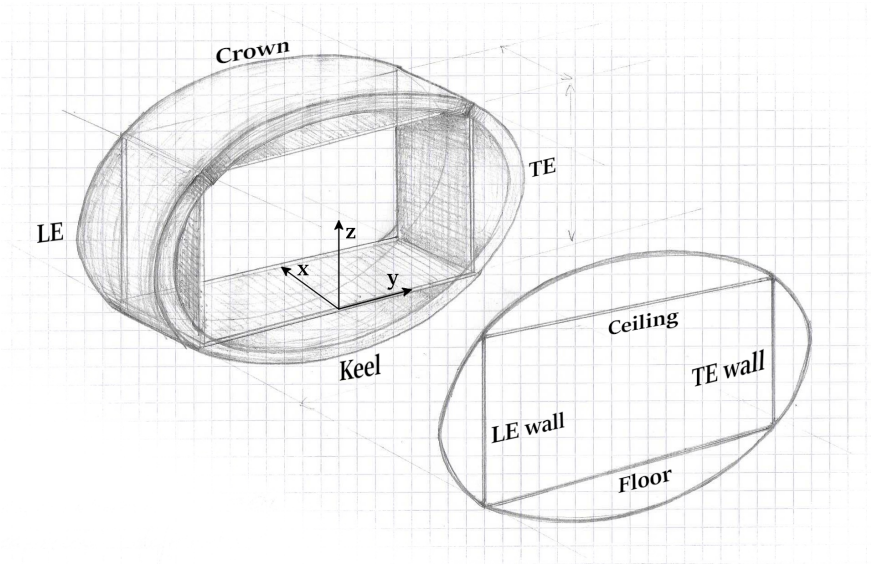

Figure 3.3: Names of the different panels of the oval cabin section.

The cabin input dimensions used throughout the analysis were obtained from Hillen[12] and Oosterom[13], and are repeated in table 3.3. While more cabin data was available, these geometric properties are coupled, and can therefore not be used as input values. This is discussed in the following section.

Table 3.3: Cabin geometric input data. Instead of cabin width, the cabin floor and ceiling width were used.

Parameter	Symbol	Value	Unit	Source
Untapered cabin height	h_{21}	2.25	m	Hillen[12]
Tapered end cabin height	h_{23}	1.22	m	Hillen[12]
Untapered keel height	h_{31}	0.68	m	Oosterom[13]
Tapered end keel height	h_{33}	0.45	m	Oosterom[13]
Untapered cabin width	w_1	6.20	m	Hillen[12]
Tapered end cabin width*	w_3	5.80	m	Hillen[12]
Trailing edge length	L_{TE}	2.885	m	Hillen[12]

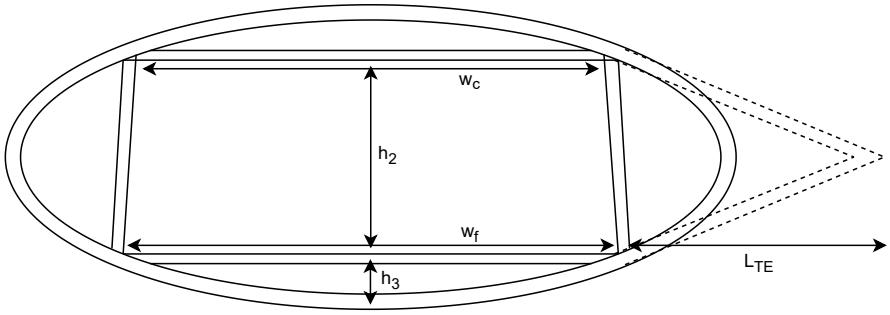

Figure 3.4: Oval cabin input parameters.

Cabin geometry parametrisation

The parametrisation from Roelofs [32] was first applied to define the geometry of the structure. The method is not repeated here, for reasons that will become clear as follows. From an aerodynamic and design perspective the requirements of the cross-section are:

- The pressure shells are circular arcs.
- The arcs must be tangential at the vertices.
- The floor and ceiling lengths may be varied, while the above conditions are maintained.
- The crown or keel height may be varied, while the above conditions are maintained.

Roelofs' method was tested, and found to be faulty when the crown arc height is not equal to the keel height. The result, while subtle, results in a cross-section which does not ensure tangentiality at the vertices. Instead, the Schmidt's[8] parametrisation was followed, which was verified to produce tangent geometries while varying the input parameters.

The manner in which input variables are provided must be clarified. In order to attain a cross-section which is tangent at the vertices, one must make a choice which variables to choose as inputs, as many variables are dependent and do not allow for a separate input. For example, the crown and keel arc height cannot both be treated as input variables if the floor and ceiling width have already been defined. For this research, the inputs as shown in table 3.3 have been used as input, i.e., the floor and ceiling width, as well as the cabin and keel height.

A note on cross-section reference system The obtained cabin cross-section can be discussed in terms of the local cross-section (figure 3.5), or in terms of the global (streamwise) cross-section (figure 3.6). In the entirety of this research, unless otherwise specified, the local cross-section is of interest.

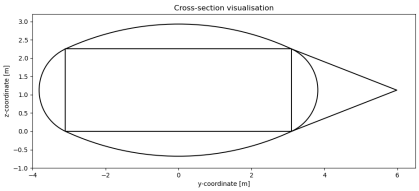

Figure 3.5: Cross-section, local yz-plane.

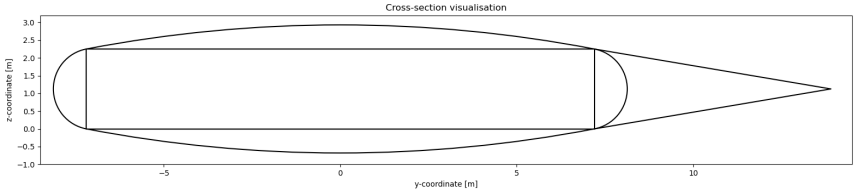

Figure 3.6: Cross-section, global XZ-plane.

3.3. Cabin structure simplification

One of the goals of this research is to obtain a better understanding of the optimal layout of the primary structure. In order to decrease the scope of the research, the novel inboard wing-fuselage structure has been selected as the structure of interest. The structure was chosen to be analysed in a simplified manner. This simplification excludes the inboard-outboard transition structure, the cockpit and symmetry structure. This decision was based on the simplification made by Oosterom [13]. This simplification allows for a more straightforward modelling procedure, and a better comparison to previous work. From figure 3.1, the argument can be made that the material of the cockpit is equal to the area that extends beyond the symmetry plane. This requires an assumption that the cockpit mass is approximately equal to the mass of this extra structure. This is not necessarily true, as the cockpit houses a large number of systems, which is likely to be dense. However, as the nose tapers to a point, the volume significantly decreases as well. Therefore, it is assumed that overall, the mass is approximately equal. This is a rough assumption, but the associated region is relatively small compared to the rest of the cabin, and the error is assumed to have a limited effect on the results. It may be noted that, while the masses may be assumed to be equal, their location is different, which has an effect on the weight distribution and balance of the aircraft.

Additionally, and perhaps more importantly, it is assumed that the behaviour of the whole structure in the symmetry section is comparable to that of the simplified structure. More specifically, the stress / failure index fields of the real and simplified structure should be similar enough such that the final sizing results are representative. This is a rather large assumption.

3.4. Effects of manufacturable geometry

The geometry as described in the previous subsections has effects on the analysis approach and the validity of the result. The current geometry is well-suited to analysis approach, as the local fuselage axis can be used to easily define the local cross-section of the cabin. The constant cross-section cabin and the tapering cabin are both straightforward to model. However, it does not make sense from an aerodynamic point of view. The tapering will cause undesirable aerodynamic effects to take place, flow separation being an obvious outcome. This is visualised in 1.15. As indicated in section 4.4.3, the aerodynamic loads that are associated with this geometry are not used specifically for this reason. The overall performance of the FV would degrade so significantly that the whole concept is not viable. Hillen indicated that no optimisation was performed. However, there is no indication that results comparable to the streamwise concept can be achieved. This is the case as all streamlines passing over the constant-tapered cabin border will still encounter a sudden change in surface angle, leading to flow separation. This could be addressed by gradually changing the cross-section. However, there would be a penalty to the commonality of the structure, leading to an increase in costs. Moreover, this would require double-curved panels, which would in turn require specific equipment to manufacture. To summarise, the continuation with this geometry should be critically regarded in the context of multidisciplinary design.

3.5. Cabin concepts

The discussion about efficient structural and practical designs for non-circular cabins is not a new one, as shown in 1.4.2. While a few options were considered, the oval fuselage concept was quickly adopted. The oval cabin concept was first coined by Vos and Hoogreef [34], and was the first solution which offered a large continuous cabin, while minimising bending, at the cost of higher pure axial stresses. While the solution

was aimed at BWB aircraft, it soon found application in the Flying-V.

While the qualitative arguments for this concept are considerable, they are based on a number of oversimplified assumptions. Firstly, all structural members are considered to be thin, and may therefore be regarded to act as membranes, which do not allow the introduction of bending stresses. This assumption is likely a poor one, as structures with a significant Moment of Inertia (MOI) are required to resist compressive loads (for stability), and frames are needed to transfer loads throughout the cross-section. Secondly, if there is no bending stiffness, an implicit assumption is that the joints must act as pins. By itself, this is not representative. Additionally, this implies that tangency is not satisfied at the joints as the structure deforms due to loads in the cross-section (e.g. pressurisation, aerodynamic loads). In order to obtain a structure which does not buckle, maintain an aerofoil shape, and transfer loads through the structure, frames and cross-beams are needed. Therefore, the resulting behaviour is unlike that of a membrane. This conclusion demands an examination of the previously regarded ideality of the oval concept.

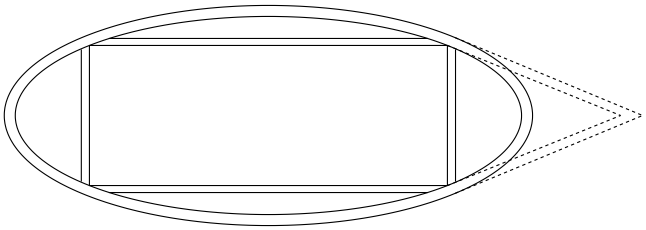

Figure 3.7: Original oval cabin concept

While a number of structurally favourable cross-sections may be proposed, practicality and passenger acceptance are of paramount importance. In order to synthesise a new concept for the structure, the drawbacks and challenges of the oval concept were analysed.

Concept 1: removing the LE wall In previous research regarding the structure and cabin design of the FV, one of the main issues has been the integration of the vertical tension structure. The vertical tension structure should be integrated such that it minimally hinders the practical internal space, and allows passengers to have an adequate view of the windows on the leading edge. One option is to apply trusses or a wall with holes, to take up these tensile loads. The space beyond the tensile structure would be partially useful for passengers, and allows a view of the windows. However, the useful space beyond the trusses or holes is limited. Furthermore, the distance from the wall to the window may be significant, depending on the LE arc radius. In turn, this leads to a tunnel-like window, which will decrease passenger acceptance. A proposed concept would be to circumnavigate these issues by not having a Leading Edge (LE) tension wall. This concept is visualised in figure 3.8.

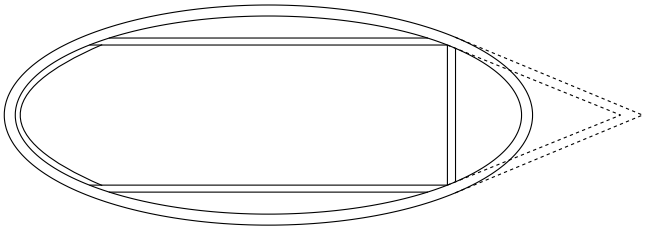

Figure 3.8: No leading edge spar (NLES) concept layout.

The function fulfilled by the tension structure is transferred to the LE structure. As the structure is arced, the transferred load induces pure axial stresses as well as bending stresses. These loads are significant, and the structure must be adequately reinforced to be able to withstand the increased stresses (bending in particular). While this may appear undesirable, a reinforced structure may in fact be advantageous. Firstly, the reinforced structure -i.e. an increased local strength and stiffness- reduces the criticality of stability-related failure in this region. This is the case as the MOI scales approximately cubically if material is added to a frame with the same geometric ratios. Secondly, and perhaps more importantly, this solution may show to

have a synergetic effect with the properties necessary to withstand bird strike. Bird strike has been identified by researchers in the Flying-V group as one of the main 'concept killers'. Independently of the structure required for pressurisation, the LE must be strong enough to withstand this (rather unconventional) failure mode. Furthermore, the joints at the corners of the cabin (vertices), have to connect 4 structures. The complicated structure and complex stress state in the joint can lead to a high joint weight. Removing 1 of the 4 components decreases the difficulty of joint design. Lastly, the space in the cabin is enlarged. While the space offers some more elbow and shoulder room, the removal of the wall increases the openness of the cabin significantly.

Due to the above reasoning, this concept is expected to outperform the original concept. The same reasoning is not applied to the TE tension structure, as there is certainly no bird strike, nor windows. Additionally, in order to put fuel in the trailing edge fairing, there will likely be a need for a considerable safety structure between the passengers and the fuel tank. The double structure between the passengers and the fuel tank (i.e., the trailing edge arc and the vertical tension structure) may provide adequate protection to the passengers from the fuel in case of a crash landing (and thus pass certification). Furthermore, large shear loads are introduced into the structure at the engine and landing gear pylon. Having the wall/spar structure at the trailing edge will improve the load transfer throughout the structure.

Other concepts Due to the lengthy sizing process, it was not viable to assess more concepts in this research. However, for future reference, two other concepts are stated in Appendix G.

4
Load calculation methods

In order to perform the stress and failure analyses, the loads throughout the structure were determined. As discussed in section 2.4, the stress analysis is divided into the longitudinal and cross-section analysis. Therefore, the running loads along the wing-fuselage must be known for each load case, and the load distribution must be known throughout the cross-section for every section, for each load case. Oosterom [13] has provided running load data in their research. Unfortunately, the data was not considered applicable for further analysis, as discussed in more detail in section 1.4.4. Therefore, the individual contributions to the running loads were determined. As there was no previous data on loads within the cross-section, calculation methods are shown as well.

Firstly, the load cases for design are presented. In the following sections, the corresponding calculation methods are shown. Finally, a comprehensive list of the load cases is shown in 4.6.

4.1. Load case selection

A number of considerations which affected the load cases selected for analysis are shown below.

Exclusion of asymmetric loads In order to reduce modelling complexity, only symmetric load cases were considered. The proposed set of symmetric load cases are hypothesised to still exert representative design-driving loads on the aircraft, which lead to a realistic design.

Inclusion of different weight distributions The weight distribution of the Flying-V is hypothesised to have a significant effect on the running loads. For example, full tanks could provide significant bending alleviation loads during positive manoeuvring. In some regions, this could lead to underestimation of the required structural geometry. The same argument could be made for different weight distributions and load cases. Therefore, for every load case, significantly different weight distributions should be evaluated. The different weight distributions are shown in section 4.2.

Load case categories The different load cases have been selected based on CS 25. For reference, the relevant certification specifications for structural design have been repeated in Appendix I. The load cases can be subdivided into 5 main categories:

- Weight loads. These loads are inertial loads due to gravity, other linear accelerations or angular accelerations. These loads are determined in section 4.2.
- Pressurisation loads, as discussed in section 4.3.
- Aerodynamic loads. Lift, drag and aerodynamic moment are considered, as shown in section 4.12.
- Landing gear loads occur due to landing, take-off or other ground loads, as presented in section 4.5.
- Engine loads, as presented in section 4.5.3.

Control surface loads have not been included explicitly. Implicitly, these are considered in the aerodynamic load calculations of the outboard wing, shown in 4.4. The full list of load cases is shown in section 4.6.

4.2. Weight loads

The loads caused by mass accelerations are treated in this section. The primary mass groups were determined, after which the weight loads were determined.

4.2.1. Mass groups

The identified mass (sub)groups can be found below.

1. Operating empty mass
   - 1.1 Structure mass
     - 1.1.1 Inboard wing structure
     - 1.1.2 Outboard wing structure
   - 1.2 Landing gear mass
   - 1.3 Propulsion system mass
   - 1.4 Operational items mass
   - 1.5 Furnishings mass
   - 1.6 Miscellaneous system mass
2. Payload mass
   - 2.1 Passenger mass
     - 2.1.1 Economy class passengers and luggage
     - 2.1.2 Business class passengers and luggage
   - 2.2 Cargo mass
3. Fuel mass
   - 3.1 Available fuel mass
   - 3.2 Residual fuel mass

Unless otherwise specified, the masses as described below were obtained from Oosterom [13](Ch.6.2.2, pp. 67-69). For the weight groups, Oosterom's family-optimised solution of the FV-900 was taken as a basis, which can be found in table 1.3. The mass groups which Oosterom obtained from empirical relations were verified by repeating the calculations (The used equations were obtained from Oosterom [13], Appendix A, pp.85-87). The weights of all empirical groups matched within at most a few percent. As mentioned in 1.4.4, the soundproofing weight was likely underestimated. To allow direct comparison to Oosterom's results, the value of 14.3e3 kg has been carried forward.

4.2.2. Mass distribution

The mass groups as defined in the previous subsection were distributed over the aircraft. This was not a trivial task, as the locations of many items were undefined at that stage. Additionally, the mass distribution of reference TAW aircraft is not comparable. The mass distribution was determined based on constant and variable mass items. The constant mass items include the structure, landing gear, propulsion system, miscellaneous systems, furnishings and operational items. The variable mass groups are the payload and fuel. The reasoning for the applied distributions are found in the paragraphs below.

Constant mass distribution

Structure The wing-fuselage structural mass distribution input was obtained from Oosterom[13] (Ch.6, p.72, figure 6.3). While issues as discussed in section 1.4.4 affected this data, it was considered the most reliable weight data. Oosterom provided the total structure mass, as well as the mass distribution of structural items. These distributions were provided in 1 dimension in the longitudinal direction. Therefore, the distribution over the cross-section needed to be determined for the cross section analysis. While this was straightforward for the original concept, the same mass was distributed over the cross-section of the other concepts.

For all concepts, stringers as defined by Oosterom were assumed to be attached to the skins only, as this was not explicitly mentioned. The stringer geometry and locations were not apparent from Oosterom's data. For simplicity, the stringer mass was uniformly distributed over the skin. While more stringers may be expected in some regions (e.g., the top skin), the effect of a more accurate stringer mass distribution was assumed to be small. For the other concepts, the weight of the missing wall(s) or ceiling were added to the corresponding LE/TE or crown, respectively. This was done as it is expected that these regions adopt the additional functions which were provided by these components, and therefore require increased reinforcements. This is schematically indicated in figure 4.1. The specific mass assignment to nodes is shown in section 4.2.5.

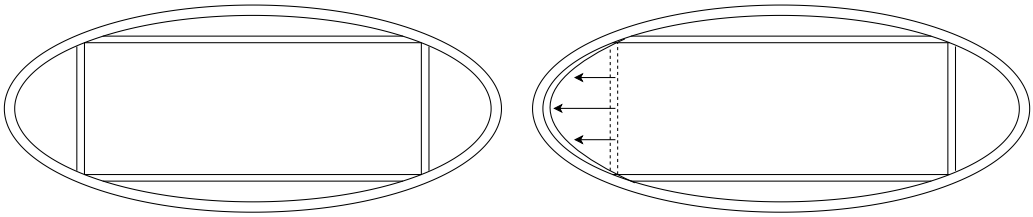

Figure 4.1: Example of mass transfer from LE wall to LE when removing wall.

The family-optimised outer wing mass determined by Oosterom[13] to be 6.6e3 kg. EMWET (a wing sizing algorithm) was used to design the outboard wing. This approach appears sensible as the outboard wing functions like conventional wing, moreso than the inboard wing. However, due to the large fins (shown in figure 4.2) and control surfaces, it also functions as an empennage. Oosterom estimated the fin mass, and placed this as a point mass at the wing tip. However, this may lead to an unconservative design. The fin mass causes bending relief, which is also mentioned by Oosterom. However, the control forces from the fin are not considered in the structural sizing of the outer wing. Additionally, Oosterom discounts the calculated mass by 20%, which is attributed to the use of composites. This is a significant reduction, based on a rather short substantiation. Therefore, the outer wing mass is likely on the low end of the scale. However, for this piece of research, a lighter outer wing reduces the bending relief on the inner wing, leading to a more conservative estimate.

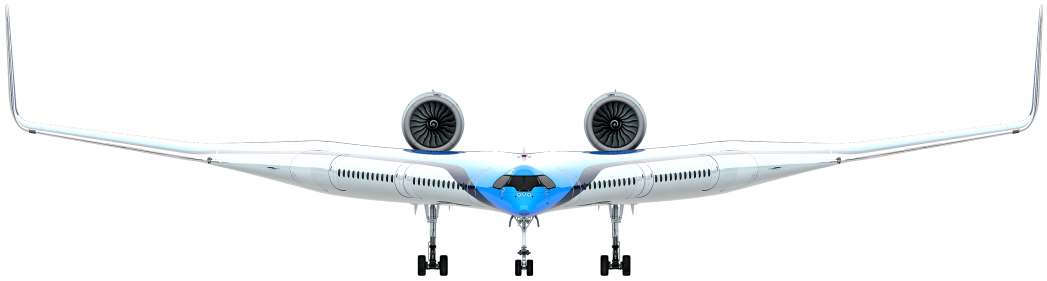

Figure 4.2: Front view impression of the Flying-V geometry, by Wallet[3].

Nose gear The total landing gear mass was distributed between the nose gear and main landing gear, with a ratio of 12% and 88%, respectively. This led to a nose gear mass of 1.3e3 kg. The nose gear position was obtained from Bourget [36], at 8.6 metres in global X-direction from the nose. The mass of the nose gear was distributed over the first 5 frame sections. It was assumed that a local reinforced structure would be implemented which would lead to a more effectively transferred load into the cross-section. Therefore, instead of a point load at the landing gear location, the loads from the nose gear are introduced to the bottom two vertices over the first 5 frames.

Main landing gear and propulsion system The main landing gear and propulsion system are both attached to the engine and landing gear (ELG) pylon, which introduces loads into frames over a 5 metre section of the cabin. This paragraph is limited to the mass of these systems, while other landing and engine related loads are discussed in 4.5. The landing gear and propulsion system are both assumed to have a c.g. that is on the pylon centreline in the XY-plane. The distance of these systems along the pylon has been approximated based on results by Bourget [36] and Oosterom [13]. The propulsion system mass can be divided into multiple components (e.g., engine, fuel system, thrust reverser). However, in this stage of the

design, it was deemed acceptable to bundle the total propulsion system mass as a point mass. The c.g. was assumed to be located at the geometric centroid of the engine, which was approximated using the geometry data from the Rolls-Royce Trent XWB-84 typce certificate data sheet [37]. The c.g. of the propulsion system was estimated to be at approx. 10.0 metres along the pylon length.

The c.g. location of the landing gear depends on its state. When retracted, it is located further forward than when extended. However, this was simplified to a static point mass at the centre of rotation of the main strut. The location of this centre of rotation was determined from Bourget[36] to be located 4.8 metres along the pylon.

Miscellaneous Systems The systems weight distribution was approached in a simple manner. The system mass was distributed over the wing-fuselage and outboard wing based on the projected area on the xy-plane, resulting in 72% inboard and 28% outboard system mass. The rationale is that a volume-based method would assign nearly all of the system mass in the inboard wing, as its volume eclipses that of the outboard wing. However, the outboard wing possesses some major systems, such as the control surfaces. In the inboard wing, the available space under the floor and above the ceiling were identified to be the the main locations for these system masses, as the volume in the LE and TE arcs was likely not available. The former is part of the cabin, while the latter is rather inaccessible, being in between the aft wall/spar and the fuel tank. Therefore, the mass was equally distributed over the ceiling and keel.

For the outboard wing, the centre of gravity of the system mass was assumed to be positioned halfway along the span, even though the wing tapers significantly. The reasoning is that the control surfaces and de-icing systems are located over the whole span of the outboard wing, as well as the fin.

The weight distribution approach of the miscellaneous system mass is a very simplified representation. The miscellaneous system mass is a significant portion of the OEM (10.6%), and thus has a large effect on the response of the structure. In order to improve the distribution, two specific improvements are listed below:

- **Cockpit systems:** The cockpit is not considered in this research, however, it contains are a large number of systems. Additionally, as the cockpit is at the front, this mass has a significant effect on the balance of the aircraft, and the cumulative load diagrams.
- **Control surfaces:** The weight of the control surfaces may be estimated individually, to obtain an improved estimation of the outer wing system weight.

However, due to time constraints, these improvements have not been implemented.

Operational items and furnishings The operational items and furnishings were grouped, as they are both only located in the cabin. While approximately half of the operational items weight depends on the number of passengers, this was simplified to be equal to the design weight under all circumstances. The total mass of the operational items and furnishings were distributed equally over the passenger cabin floor area.

Variable mass distribution

For the variable masses, two main mass groups were considered: payload and fuel. These are discussed in the following paragraphs.

Payload In Oosterom's[13] research, the design payload mass included solely passengers and luggage, with zero cargo. Additional cargo could be brought at a cost of fuel weight, greatly reducing the range of the aircraft.

The economy class passenger mass was determined to be 23.3e3 kg, with a luggage weight of 4.0e3 kg. Similarly, the business class passenger and luggage mass were determined to be 4.2e3 kg and 1.0e3 kg, respectively. While the passengers are all located in the cabin, the distribution of the luggage weight was not readily apparent. It was assumed that the majority of the luggage mass would be located in the cargo hold, while a smaller amount would be located in the cabin as hand luggage, at $\frac{2}{3}$ and $\frac{1}{3}$ of luggage mass, respectively. The total masses of the business class and economy class payload were divided over the assigned areas. It should be noted that these areas were approximated, as shown in section 3.1.

Additionally, a maximum additional cargo mass was calculated by Oosterom to be 22.9e3 kg, assigned to the

cargo hold. However, combining the design payload and fuel mass with the cargo mass would increase the weight beyond the MTOW. A number of weight combinations were determined which kept the total weight at or below MTOW at take-off, discussed in more detail in section 4.6.

Fuel The design fuel mass was determined by Oosterom[13] to be 87.5e3 kg. This fuel is located in fuel tanks in the trailing edge and outboard wing tanks. However, the geometry of the tanks was not apparent. According to Oosterom, the trailing edge fuel tanks needed to be enlarged to include the space between the trailing edge tension wall and the trailing edge arc, as indicated in figure 4.3. This was necessary to meet fuel volume requirements. However, this would place the fuel directly next to the passengers. This is highly undesirable, and would almost certainly fail in the certification process. Therefore, this proposition was not accepted in this research. In fact, the fuel being located in the trailing edge (excluding the aft arc), will still pose significant safety issues. Placing the fuel far away from the passenger, in the cargo hold and outboard wing would increase the safety. At its current state, the outboard wing does not offer enough volume to store all fuel, as it is very thin. Additionally, this problem is not simply solved by increasing the outer wing thickness, as the aircraft would experience significant balance issues.

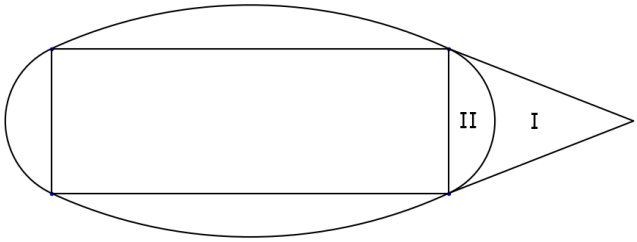

Figure 4.3: Cross-section visualisation of the tank enlargement (II) proposed by Oosterom, in local yz-plane.

In order to assess the availability of tank volume, and to determine the fuel mass distribution, a volume calculation was performed. The trailing edge length from the aft tension wall was determined to be 2.885 m by Hillen [12]. It was assumed that this trailing edge length was valid anywhere along the cabin, including the tapered fuselage. Together with the local cabin height, the volume of the trailing edge was straightforward to calculate. The local area enclosed by the aft vertical structure and the aft arc was subtracted from the triangular area. It should be noted that the tank volume is therefore also a function of the chosen skin radii.

The trailing edge tank is not continuous. The ELG pylon and the main landing gear (MLG) retraction mechanism require the available space, and therefore this 5 metre region contains no fuel. Furthermore, the tank geometry in the symmetry region was corrected. The maximum available fuel volume in the trailing edge tanks, for a single wing, was consequently calculated to be equal to 63.1 m^2. While the calculation is relatively simplistic, the obtained volume is larger than the required volume by some margin, which is Oosterom stated to be 54.5 m^2 [13]. Arriving at this result, it is unclear why the fuel tank expansion was proposed by Oosterom.

The fuel in the outboard wing was determined as well. The fuel tank was assumed to be equal to the wing box size. The wing box was assumed to run from 15%-60% of the chord. With the CAD model from Hillen's parametrisation [12], the tank shape was approximated. The tank shape was approximated as a frustum, with a base (at the root) of 0.6 m high and 2.70 m wide, and a tip (just before the fin) of 0.3 m high and 1.44 m long. The length of the tank was approximated at 18.0 m. The maximum internal volume of a single outboard tank was calculated to be equal to 17.3 m^2.

It was concluded that there was ample space to store the required fuel in the tanks. The following step was to consider the possible distribution of the fuel in the two tanks. For structural purposes (i.e. bending relief), it was hypothesised to be beneficial to store the maximum amount of fuel in the outboard tanks. However, this may pose problems in terms of stability. Therefore, a stability calculation was performed. The scope of this calculation was limited to on-ground stability, as the aerodynamic moment balance of the aircraft was deemed too complex to evaluate. According to Bourget [36], the centre of gravity must remain 17% in front of the axis of rotation of the MLG wheels. With the location of the landing gear, the wheel axis of rotation was determined in the global reference system. The limiting c.g. was determined to be 29.0 m in the global

reference system. This value is equal to the extreme c.g. value (29.0 m) calculated by Oosterom, which was provided after the calculation, verifying the outcome.

The last required input in the analysis was the centre of gravity of the fuel in the outboard wing tank. The local centre of gravity of the outboard fuel was determined as function of the outboard tank size. Expanding the tank farther outboard naturally extends the c.g. farther outboard. However, as the outer wing tapers to a thin wing near the fin a decreasing amount of volume is gained per unit of length. The maximum outboard fuel was calculated for each payload and cargo scenario (listed in section 4.6). The result was an outboard fuel tank which covers approx 70% of the span, corresponding to 82.4% of the available outboard volume. The maximum outboard fuel mass is 11.4e3 kg for a single wing, corresponding to 26% of the design fuel mass per wing.

During each load case, the fuel was assumed to deplete equally in all tanks. Therefore, any weight trimming actions have not been considered.

Remarks on fuel distribution The described fuel distribution method led to different fuel tank geometry than described in previous research. As data on the distribution in previous research was not presented, the difference could not directly be compared. However, it is clear that the fuel distributions could differ considerably. As the fuel mass is high compared to the other mass groups (inherent to the long-range design), the response of the structure is expected to be sensitive to the fuel weight distribution. More specifically, the outboard fuel mass will likely have a large effect on the longitudinal stresses, as it is positioned so far outboard. The sensitivity of the structural response to the outboard fuel mass is elaborated on in section 9.2.2.

Furthermore, in previous research, the emphasis on the fuel distribution has been on available volume and balance. While both are essential in designing a realistic concept, safety and favourable structural response has not been considered significantly. While a favourable structural response may affect the performance significantly, a far more important aspect is safety. The fuel is currently positioned close to the passengers. The fuel design requirements for certification should be included in an early stage to adequately design the layout of the fuel tanks, which is essential for the Flying-V to be successful.

4.2.3. Fuel mass per load case

During the different load cases, the aircraft has different weight distributions. These different weight distributions are caused by a change in the variable mass groups - payload, cargo and fuel. While the payload and cargo mass have been defined, the associated fuel mass requires some calculations. The different fuel cases are explained in section .

The fuel calculations are based on assumed operational fuel burn fractions, from Roskam[38]. The relevant fractions are shown in table 4.1. The composition(s) of these different masses are discussed in the paragraphs below.

Table 4.1: Used fuel fractions.

Name	Fraction [-]
Start and warm-up	0.99
Taxi	0.99
Take-off	0.995

Minimum fuel mass The minimum fuel mass was calculated to be an extreme minimum. Namely, is was assumed to correspond to residual fuel mass during cruise. The residual fuel mass was calculated as follows (from Torenbeek[39], Table 8-13):

$$m_{f,res} = 0.151 V_{f,t}^{\frac{2}{3}} = 2.76e3kg \tag{4.1}$$

Cruise fuel mass The maximum fuel mass in the cruise phase was taken as an extreme value to be the mass directly after take-off, omitting climb. This is the case as during climb, the air is often more turbulent, and manoeuvres are more likely to be carried out. Based on the fuel burn fractions for MTOM, the maximum cruise fuel for design payload mass and zero cargo was calculated to be:

$$m_{f,max,cruise,1} = DFM - (1 - 0.995)MTOM = 86.3e3kg \tag{4.2}$$

Where MRM is the maximum ramp mass. The maximum cruise fuel associated with maximum payload and maximum cargo was determined by subtracting the cargo mass from the design fuel mass, leading to a mass of 60.2e3 kg. As stated in the previous paragraph, the minimum cruise fuel was set to the residual fuel mass.

Take-off fuel mass The maximum take-off fuel mass was determined similarly as above, without the take-off fuel fraction, resulting in 82.7e3 kg. In the case of cargo, the cargo mass was subtracted from this number, leading to 61.1e3 kg. The minimum take-off fuel mass was calculated with the minimum fuel mass with the pre-take-off fuel fractions to be equal to 7.4e3 kg:

$$m_{f,min,TO} = m_{f,res} + MTOM(1 - 0.99 * 0.99) = 7.4e3 \tag{4.3}$$

Landing fuel Landing was calculated for two cases: maximum take-off weight and maximum landing weight. For the former, see the above paragraph. The total maximum landing mass was assumed to be 0.76MTOW, as is the case for the Airbus A350-900[40]. This results in a maximum landing mass of 177.8e3 kg. If no cargo is brought, at design payload mass, a maximum fuel mass of 32.4e3 kg is calculated. In the case of maximum cargo, a mass of 8.5e3 kg is obtained.

Ground fuel The ground loads are determined at maximum landing mass and maximum ramp mass. For the former, see the previous paragraph. For the maximum ramp mass fuel, the ramp mass was first determined as:

$$MRM = \frac{MTOM}{0.99 * 0.99} \tag{4.4}$$

The maximum ramp mass for design payload mass with zero cargo was then obtained to be 92.3e3 kg. Adding cargo reduces the fuel mass to 69.4e3 kg.

4.2.4. Inertial loads

With the obtained mass distributions, the specific inertial loads were determined. All external loads were balanced throughout the aircraft by the inertia of the mass items. Furthermore, the aircraft was represented as a rigid structure to determine the inertia loads.

Linear inertia For all mass items, the vertical force exerted on the structure scales vertically with the gravitational acceleration, multiplied by the vertical load factor n_z. Similarly, all mass elements may exert a horizontal load in the x-direction, which scales with the horizontal load factor n_x. As this research only treats symmetric loads, the lateral load factor n_y is zero at all times.

Angular inertia In the case of a resultant external moment (only about global Y, due to symmetry), the following approach was applied. As the aircraft is relatively large but slender, the mass items were idealised as point masses lying on a single plane, to simplify the calculation. The external resultant moment was assumed to induce an angular acceleration about the centre of gravity. This centre of gravity in global x was calculated for the corresponding mass distribution. With the centre of mass, the mass moment of inertia I of the aircraft was determined:

$$I_Y = \sum m_i r_i^2 \tag{4.5}$$

Where m is the mass and r is the distance from the centre of gravity. The angular acceleration is then determined to be:

$$\alpha_Y = \frac{M_Y}{I_Y} \tag{4.6}$$

The linear acceleration in z experienced by each mass element was determined simply by:

$$a_{Y,i} = \alpha_Y r_i \tag{4.7}$$

This linear acceleration was divided by the gravitational constant to obtain a linear distribution of the vertical load factors. Schematically, this distribution is illustrated in figure 4.4. The obtained vertical load factor distribution was then superimposed on the vertical load factors obtained from the vertical force resultant. The obtained load factor distribution was used to determine the forces that are locally exerted on the structure, which is treated in the next paragraph.

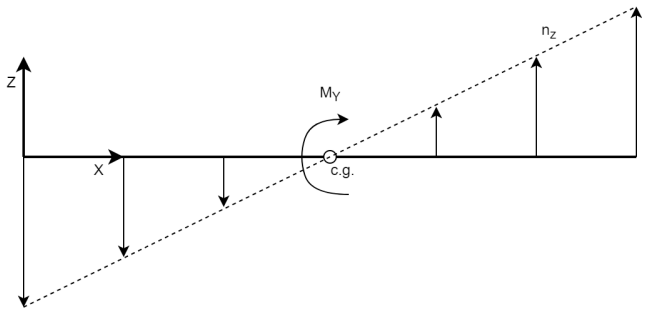

Figure 4.4: Simplified response to resultant moment.

4.2.5. Cabin weights locations in the cross-section

The node assignment of weight groups that are inside the wing cabin are treated in this subsection. For all the weights in the cabin, the loads originating from masses were directly assigned to certain nodes, without considering offsets. As the load cases are primarily in the z-direction, not including vertical offsets leads to a relatively small error in the nodal lode assignment. An example weight distribution is shown in figure 4.5. The assignment of the weight groups to nodes is described below.

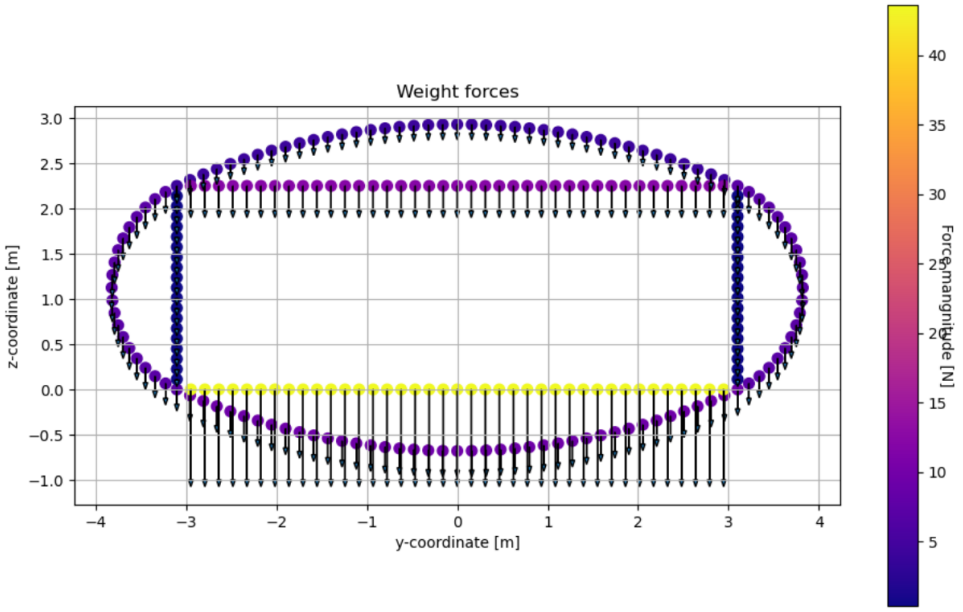

Figure 4.5: Example weight force distribution at the first frame (x=0), at $n_z = 1$.

The structural weight loads were assigned to the respective nodes of the structural components. Their distribution is identical to the mass distribution described in the previous section. All loads originating from the payload, furnishings, and operational items were uniformly applied to the floor nodes of the respective sections, without considering vertical offsets. As described in the previous section, the system weight loads were applied uniformly to the ceiling and keel nodes of the inboard wing, without considering offsets.

4.2.6. Fuel loads

The loads from the fuel mass require additional substantiation. The inboard fuel tanks are shaped like a pyramid, minus the TE arc, corresponding to region *I* in figure 4.3. The trailing edge / tank structure was considered separately from the cabin structure (this includes the trailing edge arc), and was treated as a separate, rigid structure. Effectively, the loads from the fuel mass are directly transferred to the vertices by means of rigid elements. This is schematically illustrated in figure 4.6. The force is equally distributed to the two vertex nodes, and the induced moment is transferred as a couple.

The above is a large simplification, and has significant consequences. In reality, the fuel would exert a distributed load on the tank structure. Especially the lower tank skin would exhibit considerable bending, which is then transferred to the rest of the structure. However, contrarily to the passenger cabin, the fuel tank is allowed to contain ribs (also acting as anti-slosh baffles), which may drastically increase the resistance to deformation. Therefore, the transferred moments on the adjacent structure may be relatively low.

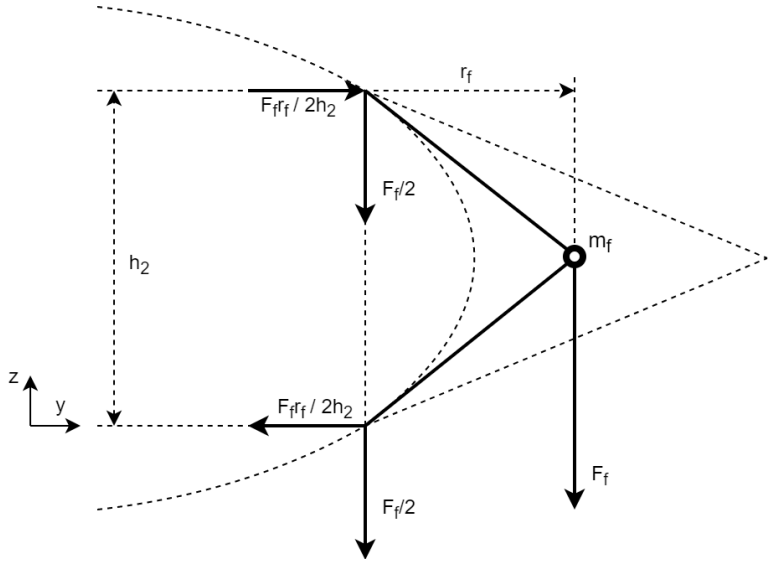

Figure 4.6: Assignment of the fuel weight to the vertex nodes.

The centre of gravity coordinate of the fuel in horizontal direction depends on the amount of fuel which it contains. To simplify the analysis, the centre of gravity of the fuel was calculated as a static location, at the geometric centroid of the tank.

4.3. Pressurisation

The pressure difference of the cabin with respect to the ambient air pressure requires defining the cruise altitude and the cabin pressure level. In previous research on the structure, starting at Claeys [11], the cruise altitude of the FV was set at a typical 11.5 km. In Claeys' research, one can derive the cabin pressurisation level be equal to approx 6900 ft. (approx. 2100 m) altitude. At the altitude of 11.5 km, this leads to a pressure difference of 57.5 kPa.

Research into the greenhouse effect of contrails at different deposition altitudes [27] shows significant gains are made at a higher altitude. Currently, studies are being performed for an increased cruise altitude of 13.5 km. This increased altitude is associated with a decreased ambient pressure. The increased altitude leads to an increased pressure difference of 63.2 kPa, an increase of approx. 10%. However, this decision should

not be made lightly, nor should it be solely based on a contrail effects study. The significant adverse effects of a heavier structure should be included in the decision-making process. The increased structural weight decreases efficiency and increases operational costs. As the majority of the Flying-V structure consists of the oval pressure cabin, it is expected that the overall structural weight is sensitive to pressurisation loads. The increased altitude is currently being pursued by researchers within the Flying-V research group. However, previous research has not used this value. To compare the results of this research more directly to previous results, the original cruise altitude of 11.5 km was maintained. Section 9.2.4 investigates the sensitivity of the pressurisation level on the solution.

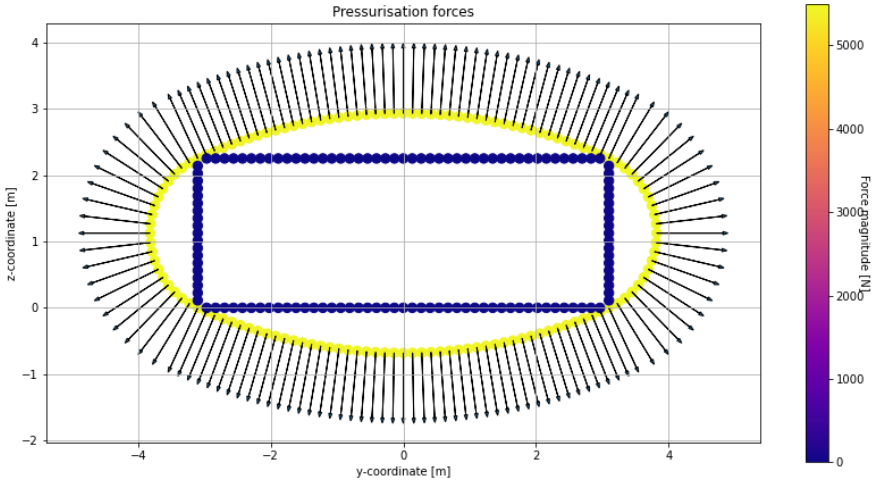

Figure 4.7: Pressurisation load on the cross-section.

The pressure load is applied perpendicular to all skins (as shown in figure 4.7), as well as to the front and aft pressure bulkheads. These pressure bulkheads are not explicitly modelled, but the pressure loads are directly transferred to the skins, in longitudinal direction. The pressure bulkheads are assumed to transfer the longitudinal pressurisation load such that the longitudinal stresses are equal in all adjacent panels. However, this is a simplification, as the different components deform in a particular way. As the crown and keel skin will be under higher hoop stresses when pressurised, they will contract more compared to the LE and TE. Therefore, the tensile loads transferred to the crown and keel are expected to be higher. However, locally adapting the structure could facilitate an improved load transfer. This is considered to be out of scope for this research.

4.4. Aerodynamic loads

The aerodynamic load distribution was determined in longitudinal (span-wise) direction and over the cross-section. The following paragraphs present the used approach to obtain these loads.

4.4.1. Representation as pressure field

The aerodynamic loads were treated as pressure forces, i.e. only load components which are normal to the local surface. This means that any aerodynamic force vector is in the local yz-plane of the wing-fuselage. The exception are drag loads on the outboard wing, as it is oriented at a different sweep angle than the wing-fuselage.

4.4.2. Aerodynamic loads for longitudinal analysis

The lift, drag and aerodynamic moment distributions over the length of the wing were determined based on lift coefficient distributions, L/D results and balanced flight, respectively.

Lift distribution

The longitudinal lift distribution was approximated from Oosterom's AVL trimmed spanwise design lift coefficient solution, as reprinted in figure 4.8[13]. It was compared to Faggiano's lift distribution [35], and a comparable solution was obtained. A comparable solution was also obtained with different analysis methods. Therefore, the data was deemed representative. This lift distribution was obtained during cruise, at the design lift coefficient, in the trimmed state. For the purpose of this research, it was assumed that this lift distribution was applicable for any state, and may be equally scaled by the required amount of lift.

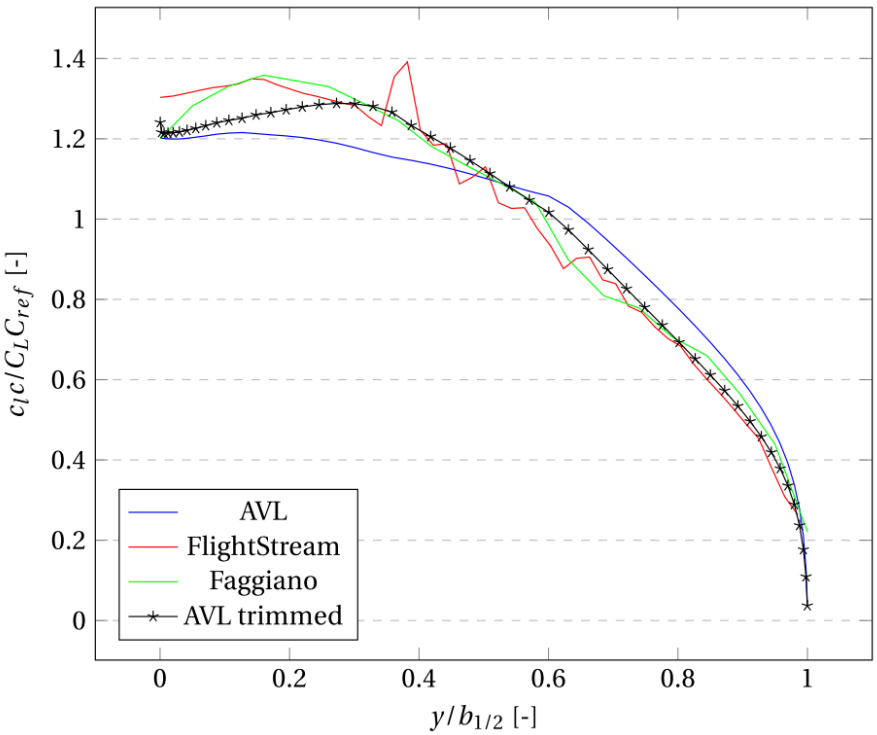

Figure 4.8: Spanwise lift distribution at the design lift coefficient, as reprinted from Oosterom [13], fig. 5.4, p. 55.

The lift distribution in figure 4.8 is represented in the global Y-coordinate, which has the following implication. As the inboard wing has such a high sweep angle, the inboard-outboard transition occurs already at $\frac{Y}{0.5b} = 0.51$. Integrating the lift before and after the transition, the total inboard and outboard lift were obtained. The inboard and outboard lift represents 62.5% and 37.5%, respectively. For reference, at MTOW with maximum fuel, the wing-fuselage contains 81.7% of the total weight, with 18.3% of the weight being assigned to the outboard wing.

The lift data was presented in the global spanwise coordinate, and was therefore transformed to the local coordinate system to obtain the local lift values at the wing-fuselage.

Outboard wing lift representation The outboard wing lift (L_{ow}) was represented as a resultant load, at the centre of lift (CoL). The CoL was placed at quarter-chord. This required the determination of the quarter chord line along the wing. This was achieved by representing the outboard wing as a trapezoid, which allowed for a straightforward determination of the quarter chord line. This is indicated schematically in figure 4.9. The distance along the outboard span was found by calculating the centroid of the outboard lift distribution. The local x and y distance was determined to the last wing-fuselage section, which allowed for the assignment of shear, moment and torque loads to the final section.

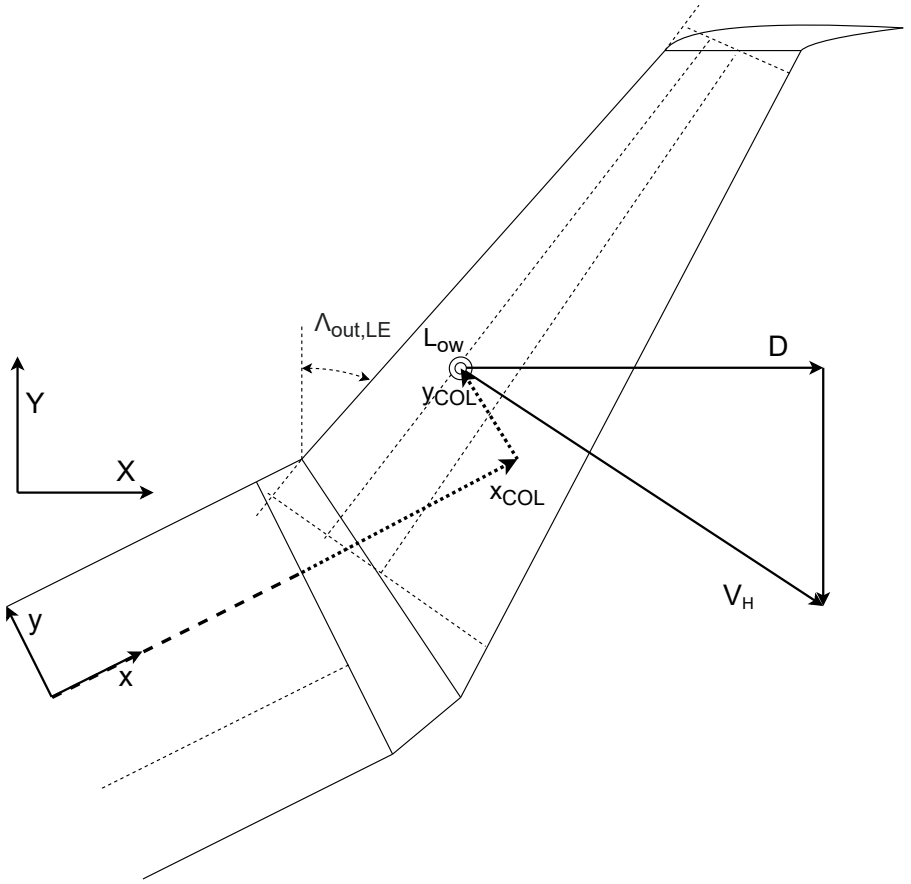

Figure 4.9: Centre of Lift (CoL) visualisation of outboard wing.

Drag distribution

It was assumed that the drag distribution possessed a similar distribution to the lift. The individual drag contribution of the fins were not considered. Therefore, the drag per section in global Y was obtained by scaling the lift distribution by the inverse of the Lift-over-drag ratio (L/D). A global L/D was obtained for the family-optimised from Oosterom [13] at 21.7. As this value is on the low end of the previously predicted range of lift-over-drag ratios[35], it is deemed to be somewhat conservative, but representative. The drag of the wing-fuselage and outboard wing differs significantly, which was accounted for. The pressure distributions of the inboard wing-fuselage and outboard wing were obtained for an unoptimised solution of Hillen [12], as shown in section 4.4.3. This allowed for the rough determination of a local L/D. As shown in section 4.4.3, the L/D of the wing-fuselage and outboard wing were calculated to be 8.8 and 10.5, respectively. It was assumed that, while they are much lower global (optimised) values, they are still proportional to each other. The inboard and outboard drag values were scaled proportionally to their L/D such that the global L/D remained 21.7. A scale factor was determined as follows:

$$(L/D)_{scale} = \frac{(L/D)_{target} + (1 - L_{frac,in})\frac{(L/D)_{in}}{(L/D)_{out}}}{(L/D)_{in}} \tag{4.8}$$

Here $L_{frac,in}$ represents the fraction of total lift on the inboard wing-fuselage (0.625). This was then multiplied by the inboard and outboard L/D to obtain their scaled values:

$$\begin{aligned} (L/D)_{in} &= 8.8\,(L/D)_{scale} = 20.4, \\ (L/D)_{out} &= 10.5\,(L/D)_{scale} = 24.3 \end{aligned} \tag{4.9}$$

The lift distribution was divided by the (L/D) to obtain the drag component in global Y. As all aerodynamic loads are perpendicular to the local surface, the drag is just the global Y-component of the total horizontal load. The horizontal pressure load in local y was obtained by dividing by the cosine of the sweep angle. For

the wing-fuselage, as the sweep angle is high, this resulted in a horizontal pressure load that is 2.4 times higher than the drag load in global Y-direction.

Outboard wing drag For the outboard wing, the drag was also represented as a resultant force. The centre of drag was assumed to be coincident with the centre of lift, at quarter-chord, as shown in figure 4.9. The total horizontal force V_H was determined by dividing the drag force by the cosine of the outboard sweep. This resulted in V_H being 32% higher than the drag.

Note on exclusion of other drag contributions In reality, the total horizontal load would likely be oriented more in global Y-direction, due to skin friction drag, wave drag and the orientation of the fin drag. The total horizontal load would consequently be lower. As the current representation has a higher total horizontal load, this is considered conservative.

Aerodynamic Moment

With the weight and aerodynamic forces of the aircraft, the loads over the aircraft were set up. At this stage, the aircraft was not yet longitudinally balanced in-air (i.e. the total moment about global Y was not zero). Therefore, aerodynamic moments were added as external loads, to impose this balance. The aerodynamic moments were assumed to act about the global Y axis. It was assumed that both the inboard wing, as well as the the outboard wing produce significant aerodynamic moment, proportional to their produced lift. The obtained global moment was transformed to local moment about y and torque about x.

While fin drag likely produces a significant moment about global Y, there was no straightforward way to quantify this. Therefore, it was not taken into account in this analysis.

4.4.3. Cross-section pressure distribution

The pressure distribution over the outer skin surface was obtained from Yaïr Brouwer [14], a fellow MSc student, researching the aerodynamic optimisation of the FV centre-body. The pressure distribution represents the pressure field over the surface of Hillen's[12] unoptimised parametrisation under cruise conditions. This pressure distribution may be found in figure 4.10.

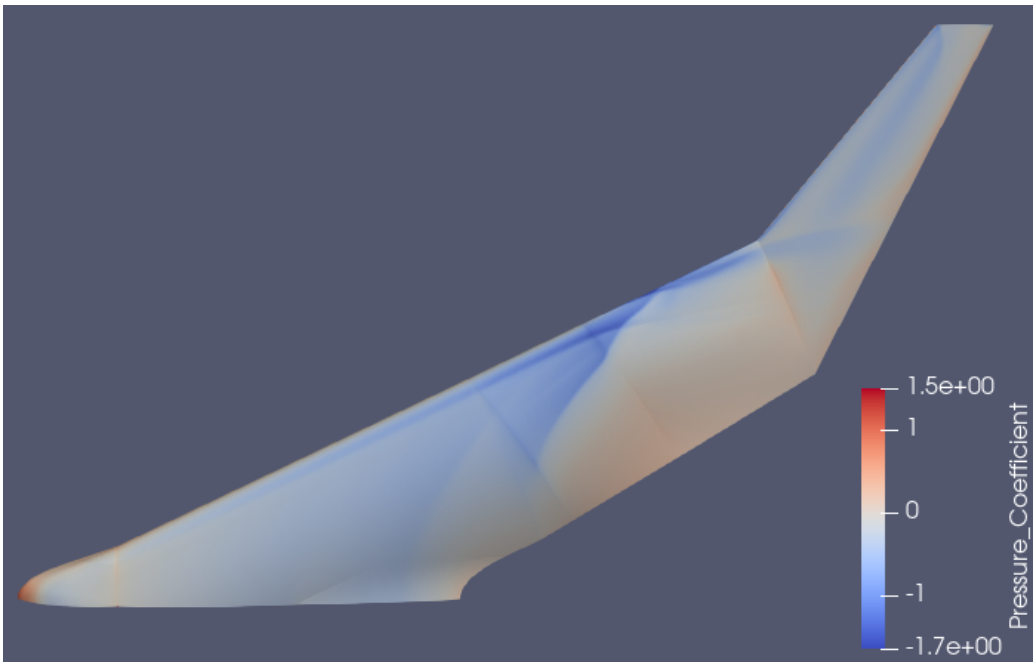

Figure 4.10: The pressure distribution over the surface of Hillen's parametrisation, obtained directly from Brouwer.

It should be noted that the parametrisation was not optimised. This led to unfavourable aerodynamic behaviour, such as shock waves, which are clearly visible in the figure 4.10. Moreover, undesirable effects are

present near the symmetry plane, as artefacts of the simulation locally lead to extreme pressures, as indicated by Brouwer. While this is not favourable, this was the only available data at the time. It was concluded that the undesirable behaviour in many areas would not yield representative forces on the structure. In order to obtain a reasonable pressure distribution over the surface, a single plane intersecting the surface in the global XZ-plane was chosen to be a representative pressure distribution for the whole cabin. Near the symmetry plane, effects from the cockpit and simulation artefacts were present, which should be avoided. Also, further along the wing, major shock waves invalidate the pressure distribution. An acceptable pressure distribution was found at a coordinate of 3.33 in global y-direction, as shown in figure 4.11.

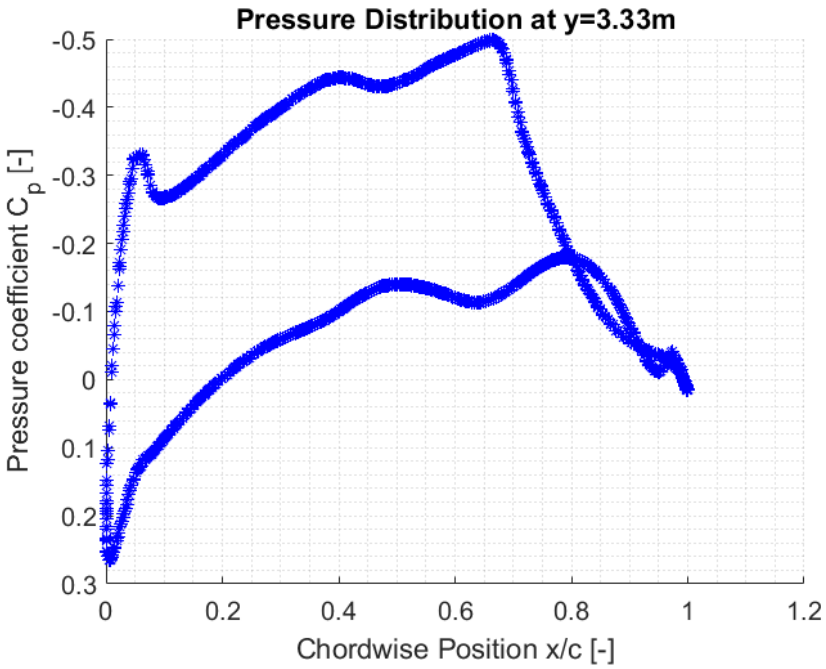

Figure 4.11: The pressure distribution at a streamwise cut at Y = 3.33, obtained from Brouwer [14].

While the pressure distribution is the most representative of the whole surface, it should be noted that there is still a shock wave. After an approximate chord-wise position of 0.68, the pressure on the top skin increases significantly. It is expected that the pressure increase would be more gradual for an optimised configuration. Therefore, a significant amount of lift is likely lost.

The pressure distribution was obtained in the global XZ-plane. As the pressure-induced aerodynamic force vectors are oriented normal to the surface, the pressure field was transformed to the local yz-plane of the wing-fuselage. The pressure data was consequently matched to points on the aerofoil surface, from which force vectors could be generated. The force vectors were normalised w.r.t. the total lift of the section, as determined from the spanwise lift distribution in section 4.4.2. As the force vectors remain normal to the surface, a total horizontal force was automatically obtained. Note that this is not the drag, as the horizontal force is oriented in local y-direction (approx. 65 degrees difference with global X). It became apparent that the lift over horizontal force ratio is very low: 3.8. The drag may be obtained by dividing by the cosine of the sweep, leading to a lift-over-drag ratio of only 8.8. With the same procedure, a L/D of the outboard wing of 10.5 was obtained. This is far below the values discussed in previous work. Similarly to section 4.4.2, the horizontal components of the force vectors were scaled such that a global L/D of 21.7 was obtained. The resulting distribution is shown in figure 4.12.

Trailing edge The trailing edge was modelled as an isosceles triangle, with the tip at 2.885 m from the TE vertices, as obtained from Hillen [12]. Like the rest of the section, the pressure loads were applied normal to the trailing edge, leading to force vectors. As the TE was not explicitly modelled, the resultant force and moment were transferred to the TE vertex nodes. The force and moment resultant were maintained by applying equivalent force couples. This is illustrated in figure 4.12. Note that due to the unfavourable pressure distribution at the aft of the airfoil, as can be seen in figure 4.11, there is an almost negligible

amount of lift, but a significant amount of drag.

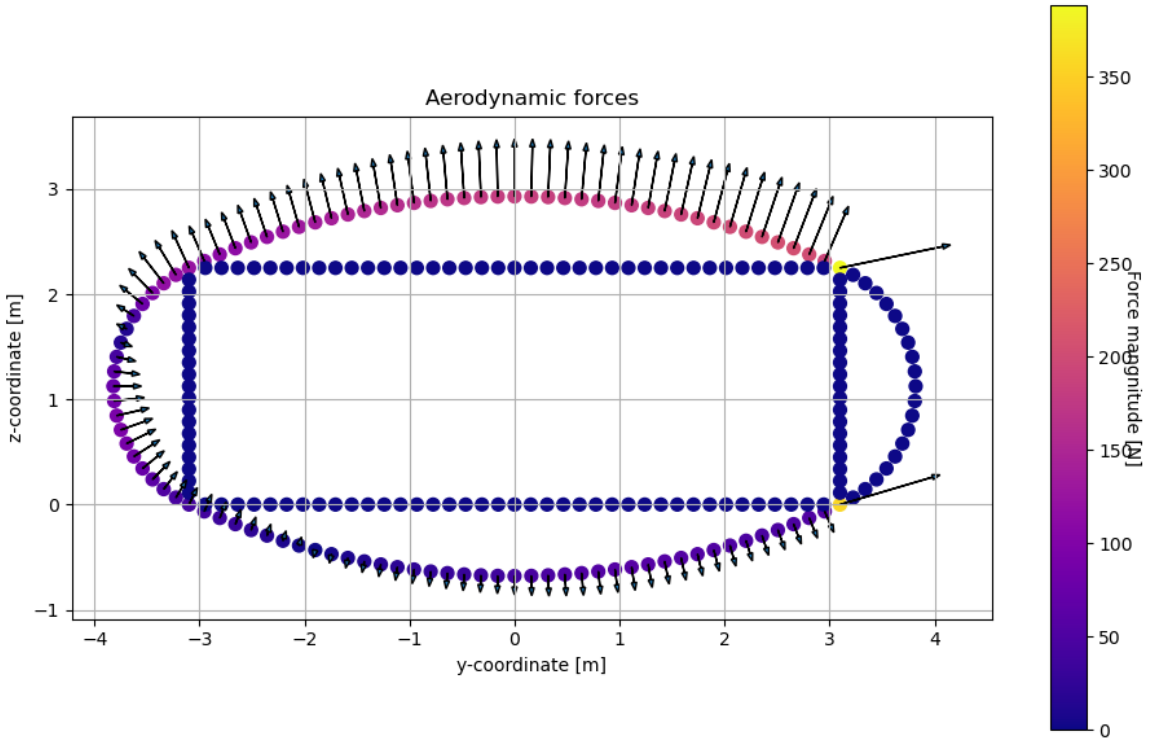

Figure 4.12: Example aerodynamic load distribution. Note the TE aerodynamic loads have been transferred to the TE vertices.

4.5. Landing gear and Engine loads

The landing gear and engine loads are grouped, as the loads of the MLG and engine are introduced into the main structure by means of the ELG pylon. The determination of these loads, as well as their introduction into the structure, as discussed in the following paragraphs.

4.5.1. Landing load cases

From from CS 25.471 - CS 25 493 [41], a set of landing load was determined. For reference, the most relevant items have been repeated in Appendix I. The scope has been limited to symmetric loads. Therefore, all lateral landing load cases have been omitted from analysis. As the vertical landing loads are greater than the lateral loads, this is considered acceptable.

For all landing load cases, the thrust was set equal to the aerodynamic drag. This was done as the aircraft was considered not to be accelerating or decelerating before touchdown. Secondly, as there is lift during landing, an upwards load is provided. It is assumed that the aircraft is in steady flight, the lift provides simply 1g upwards. The loads exerted by the landing gear on the structure are determined in the following paragraph.

Landing load factors

Maximum landing load factors at limit descent velocity (10 fps) were obtained from Lomax [15] (Ch.6.3.3, p.84 Table 6.3). The FV-900 is comparable to the heaviest shown aircraft (A, F), with 4 wheels per main gear. The associated mean was considered to be the representative limit load factor, at $n_{z,10fps} = 2.17$. This load factor corresponds to landing at the design landing weight.

For a landing at design take-off weight, the descent velocity corresponds to 6 fps. It was assumed that the deceleration was linearly related to this descent velocity. Taking into account that for steady flight $n_z = 1$, the deceleration landing factor at maximum landing weight was determined to be:

$$n_{z,6fps} = (2.17-1)((6/10)+1) = 1.87 \tag{4.10}$$

From CS 25.479d, the horizontal wheel reactions were taken to be 25% of maximum vertical reaction. Therefore:

$$n_x = 0.25(n_z - 1) \tag{4.11}$$

With this last piece of information, the loads on the gears were determined for two types of landing: two-point and three-point landing, discussed in the following paragraphs. The loads on the landing gear for both landing cases were determined using Lomax's [15] methods.

Three-point landing

Steady level flight is assumed, with the three gears touching the ground simultaneously. For the three-point landing case, the pitching moment is considered to be fully resisted by the nose gear. This is represented in figure 4.13. Missing from the figure is C, which represents the distance between the centre of gravity and the nose gear.

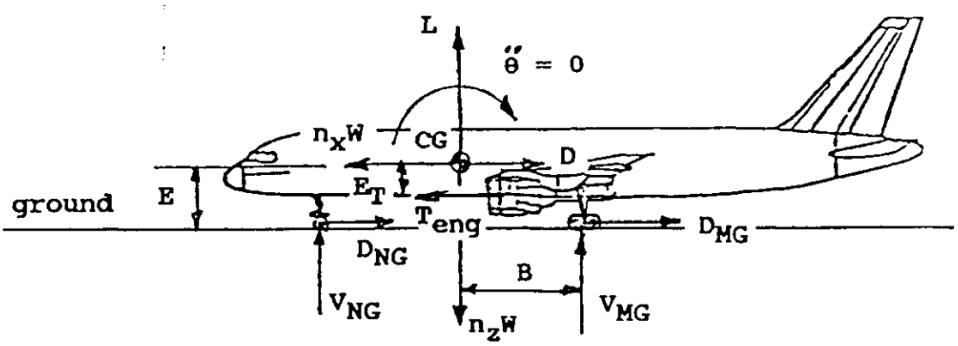

Figure 4.13: Three-point landing, reprinted from Lomax[15], fig. 6.4, p.86.

A system of force and moment equilibrium equations are formulated as shown in equation 4.12. The loads are obtained by solving the system:

$$\begin{bmatrix} 1 & 1 \\ -C+0.25E & B+0.25E \end{bmatrix} \begin{bmatrix} V_{NG} \\ V_{MLG} \end{bmatrix} = \begin{bmatrix} (n_z-1)W \\ 0 \end{bmatrix} \tag{4.12}$$

Two-point landing

Similarly to three-point landing, the two-point landing considered to be at steady level flight. However, the main landing gear impacts first, inducing an angular acceleration. This acceleration is considered to be fully resisted by the angular inertia of the aircraft. The loads on the main gears are easily determined to be:

$$V_{MG} = (n_z - 1)/W \tag{4.13}$$

Again, with the assumption that the drag load on the main gear is equal to 0.25 of maximum vertical reaction:

$$D_{MG} = 0.25 V_{MG} \tag{4.14}$$

The angular acceleration is determined simply by summing all moment contributions, and following the steps from section 4.2.4.

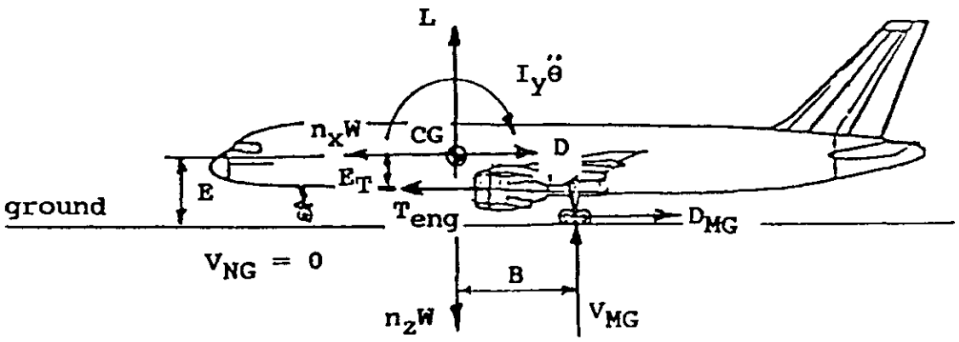

Figure 4.14: Two-point landing, reprinted from Lomax[15], fig. 6.1, p.82.

Centre of gravity in z

As shown in the previous paragraphs, the height of the centre of gravity is required to solve for the gear loads. For simplicity, it was assumed that the centre of gravity is located at half the wing-fuselage height.

4.5.2. Ground loads cases

For the ground load cases, only the braked roll and take-off were identified to be dissimilar enough to the landing cases in terms of applied loads, that they was added to the load case set. Both exert high horizontal loads on the structure, which was not particularly the case for the hard landings as described above.

Braked roll

For the braked roll load case, the aircraft experiences heavy braking, either prior to take-off, or after landing. The aerodynamic drag is considered to be equal to the thrust, and the lift is assumed to be zero. Pitching moment is considered to be fully resisted by the landing gears. The braking load was obtained from CS 25.473e, at a maximum value of 0.8 the vertical load. Both the main landing gear and the nose gear were assumed to possess brakes. A system of equilibrium force and moment equations was set up similarly as in section 4.5.1, which was solved to obtain the vertical and horizontal loads.

$$\begin{bmatrix} 1 & 1 \\ -C+0.8E & B+0.8E \end{bmatrix} \begin{bmatrix} V_{NG} \\ V_{MLG} \end{bmatrix} = \begin{bmatrix} W \\ 0 \end{bmatrix} \tag{4.15}$$

Associated weight This load case was performed at 1.2 the design landing weight, and at the design ramp weight, as per CS 25. Two weight distributions were considered for both weights: one with zero cargo and maximum associated fuel, and one case with maximum cargo and less associated fuel. For more information, see table D.1.

Take-off

For take-off, the aircraft was considered to be accelerated at peak thrust, at negligible aerodynamic lift and drag loads. The peak thrust value is determined in section 4.5.3. Pitching moment is considered to be fully resisted by the landing gears. Horizontal drag on the landing gear wheels was assumed to be negligible. Similarly as described above, a system of force and moment equilibrium equations were set up and solved to obtain the vertical gear forces. The prime difference is the addition of a high thrust force and moment.

$$\begin{bmatrix} 1 & 1 \\ -C+0.8E & B+0.8E \end{bmatrix} \begin{bmatrix} V_{NG} \\ V_{MLG} \end{bmatrix} = \begin{bmatrix} W \\ E_T T_{TO} \end{bmatrix} \tag{4.16}$$

4.5.3. Engine load cases

CS 25[41] lists a number of engine-related load cases, repeated for reference in Appendix I.

Thrust The thrust force was based on the use of Rolls-Royce Trent XWB-84 engines. These engines are flown by the Airbus A350, and are regarded to be representative engines, as shown by Faggiano [35]. The thrust exerted on the structure varies for the different load cases. At take-off, the highest thrust load occurs, at a peak value of 379 kN per engine, as per the EASA type certificate[37]. The height of the thrust vector was set at 0.8 m above the cabin centreline, obtained from Rubio Pascual[31].

Engine torque The engine spin-up and spin-down torques were assumed to be small compared to the landing gear induced torques on the ELG pylon. Therefore, the engine torque was omitted from the analysis.

4.5.4. ELG pylon load introduction

For every load case, the contributions of all engine and main landing gear loads were summed to obtain total shear and moment loads. To introduce the loads into the cross-section, the pylon was represented as a rigid structure. Similarly to the reasoning for the leading edge in 4.4.3, the pylon introduces the loads at the aft vertices of the cross-section.

4.6. List of load cases

The individual sources of loads were identified in previous sections. In order to evaluate the failure modes, a set of load cases was compiled. The load case set can be divided into two main categories: static loads and fatigue loads. The static cases comprise a large set of extreme load scenarios, while the fatigue load cases correspond to representative operating loads.

4.6.1. Static load cases

For the static load cases, a set of limit load cases and ultimate load cases were evaluated. The limit and ultimate load cases correspond to the same situation, but correspond to different load magnitudes. For both the limit and ultimate loads, the selected set of load cases is described below. The detailed information per load case may be found in table D.1.

- Pressurised positive manoeuvring, evaluated at:
  - **LC01:** Design payload mass, zero cargo, maximum cruise fuel mass.
  - **LC02:** Design payload mass, zero cargo, minimum cruise fuel mass.
  - **LC03:** Maximum payload mass, maximum cargo, maximum associated fuel mass.
  - **LC04:** Design payload mass, maximum cargo, minimum associated fuel mass.
  - **LC05:** Zero payload mass, zero cargo mass, maximum cruise fuel mass.
  - **LC06:** Zero payload mass, zero cargo , minimum cruise fuel mass.
- Unpressurised positive manoeuvring, evaluated at identical weights as above **(LC07-LC12)**.
- Pressurised negative manoeuvring, evaluated at identical weights as above **(LC13-LC18)**.
- Unpressurised negative manoeuvring, evaluated at identical weights as above **(LC19-LC24)**.
- Unpressurised landing cases:
  - **LC25:** 3-point landing landing at MTOW, 6 fps descent velocity. MTOW consisting of design payload mass and maximum fuel.
  - **LC26:** 2-point landing landing at MTOW, 6 fps descent velocity. MTOW consisting of design payload mass and maximum fuel.
  - **LC27:** 3-point landing landing at MLW, 10 fps descent velocity. MLW consisting of design payload mass and associated fuel.
  - **LC28:** 2-point landing landing at MLW, 10 fps descent velocity. MLW consisting of design payload mass and associated fuel.
  - **LC29:** 3-point landing landing at MTOW, 6 fps descent velocity. MTOW consisting of design payload mass, maximum cargo mass and associated fuel mass.
  - **LC30:** 2-point landing landing at MTOW, 6 fps descent velocity. MTOW consisting of design payload mass, maximum cargo mass and associated fuel mass.
  - **LC31:** 3-point landing landing at MLW, 10 fps descent velocity. MLW consisting of design payload mass, maximum cargo mass and associated fuel mass.

LC32: 2-point landing landing at MLW, 10 fps descent velocity. MLW consisting of design payload mass, maximum cargo mass and associated fuel mass.

- Unpressurised ground braking:

  LC33: Braking at maximum braking coefficient at MRW. MRW consisting of design payload mass, zero cargo and maximum ramp fuel.

  LC34: Braking at maximum braking coefficient at MRW. MRW consisting of design payload mass, maximum cargo and associated ramp weight fuel.

  LC35: Braking at 1.2*maximum braking coefficient at MLW. MLW consisting of design payload mass, zero cargo and maximum landing fuel.

  LC36: Braking at 1.2*maximum braking coefficient at MRW. MRW consisting of design payload mass, maximum cargo and associated ramp weight fuel.

- Take-off

  LC37: Take-off at MTOW. Maximum thrust. MTOW consisting of design payload mass, zero cargo and maximum fuel.

  LC38: Take-off at MTOW. Maximum thrust. MTOW consisting of design payload mass, zero cargo and maximum fuel.

  LC39: Take-off at MTOW. Maximum thrust. MTOW consisting of design payload mass, maximum cargo and maximum associated fuel.

  LC40: Take-off at MTOW. Maximum thrust. MTOW consisting of design payload mass, maximum cargo and minimum associated fuel.

  LC41: Take-off at low mass. Maximum thrust. Mass consisting of zero payload mass, zero cargo mass and maximum fuel mass.

  LC42: Take-off at low mass. Maximum thrust. Mass consisting of zero payload mass, zero cargo mass and minimum fuel mass.

- Overpressure:

  LC01: Over-pressure load. Pressurisation of cruise level, multiplied by a factor 1.33 and safety factor, excluding other loads, as per CS 25.365d.

Table 4.2: Load case set. For ultimate load cases: SF_p=1.33, SF=1.5.

Code	**Payload**	**Cargo**	**Fuel**	**delta p [kPa]**	n_z [-]	**Note**
LC01	DPLM	0	Max Cruise	57.5*SF_p	2.5*SF	Manoeuvres
LC02	DPLM	0	Min Cruise	57.5*SF_p	2.5*SF	
LC03	DPLM	Max	Max Cruise	57.5*SF_p	2.5*SF	
LC04	DPLM	Max	Min Cruise	57.5*SF_p	2.5*SF	
LC05	0	0	Max Cruise	57.5*SF_p	2.5*SF	
LC06	0	0	Min Cruise	57.5*SF_p	2.5*SF	
LC07	DPLM	0	Max Cruise	0	2.5*SF	
LC08	DPLM	0	Min Cruise	0	2.5*SF	
LC09	DPLM	Max	Max Cruise	0	2.5*SF	
LC10	DPLM	Max	Min Cruise	0	2.5*SF	
LC11	0	0	Max Cruise	0	2.5*SF	
LC12	0	0	Min Cruise	0	2.5*SF	
LC13	DPLM	0	Max Cruise	57.5*SF_p	-1.0*SF	
LC14	DPLM	0	Min Cruise	57.5*SF_p	-1.0*SF	
LC15	DPLM	Max	Max Cruise	57.5*SF_p	-1.0*SF	
LC16	DPLM	Max	Min Cruise	57.5*SF_p	-1.0*SF	
LC17	0	0	Max Cruise	57.5*SF_p	-1.0*SF	
LC18	0	0	Min Cruise	57.5*SF_p	-1.0*SF	
LC19	DPLM	0	Max Cruise	0	-1.0*SF	
LC20	DPLM	0	Min Cruise	0	-1.0*SF	
LC21	DPLM	Max	Max Cruise	0	-1.0*SF	
LC22	DPLM	Max	Min Cruise	0	-1.0*SF	
LC23	0	0	Max Cruise	0	-1.0*SF	
LC24	0	0	Min Cruise	0	-1.0*SF	
LC25	DPLM	0	Max TO	0	$(1+\delta n_{6fps})$*SF	3-point landing
LC26	DPLM	0	Max TO	0	$(1+\delta n_{6fps})$*SF	2-point landing
LC27	DPLM	0	Max Land	0	$(1+\delta n_{10fps})$*SF	3-point landing
LC28	DPLM	0	Max Land	0	$(1+\delta n_{10fps})$*SF	2-point landing
LC29	DPLM	Max	Max TO	0	$(1+\delta n_{6fps})$*SF	3-point landing
LC30	DPLM	Max	Max TO	0	$(1+\delta n_{6fps})$*SF	2-point landing
LC31	DPLM	Max	Max Land	0	$(1+\delta n_{10fps})$*SF	3-point landing
LC32	DPLM	Max	Max Land	0	$(1+\delta n_{10fps})$*SF	2-point landing
LC33	DPLM	0	Max Ramp	0	1.0*SF	Braking
LC34	DPLM	Max	Max Ramp	0	1.0*SF	
LC35	DPLM	0	Max Land	0	1.2*SF	
LC36	DPLM	Max	Max Land	0	1.2*SF	
LC37	DPLM	0	Max Take-off	0	1.0	TO Thrust
LC38	DPLM	0	Min Take-off	0	1.0	TO Thrust
LC39	DPLM	Max	Max Take-off	0	1.0	TO Thrust
LC40	DPLM	Max	Min Take-off	0	1.0	TO Thrust
LC41	0	0	Max Take-off	0	1.0	TO Thrust
LC42	0	0	Min Take-off	0	1.0	TO Thrust
LC61	N/A	N/A	N/A	57.5*1.33*SF_p	0	Overpressure

4.6.2. Fatigue load cases

In order to determine the fatigue loads on the structure, a base unpressurised cruise state was calculated, as well as a pressurised cruise state. The pressurisation level of the cabin was set at the fatigue safety factor of 1.15, as per CS.25. More information on the specific determination of a the fatigue load spectrum is treated in detail in section 6.2.3.

4.7. Load diagrams

Section 4.7.1 and 4.7.2 give a brief explanation of the distributed and running loads, respectively. A number of examples arre presented, but for a full set of running loads, see Appendix D.1.

4.7.1. Load distributions

Having defined all load distributions over the length of the cabin, load diagrams were constructed. An example diagram of the weight distribution diagram is shown in figure 4.15. The load diagrams were used to determine the loads in the local cross-section, as well as the local resultant, to determine the running loads.

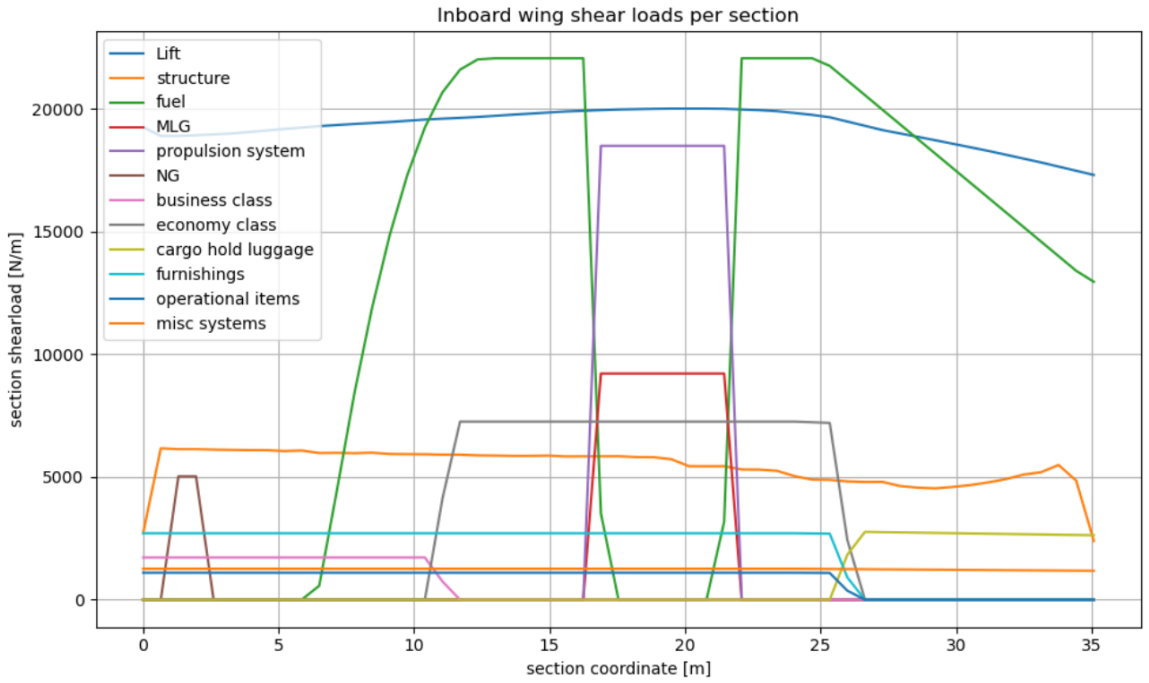

Figure 4.15: Individual S_z contributions along the wing-fuselage during cruise for design payload mass, zero cargo, at maximum cruise fuel.

4.7.2. Running loads

From the load distributions, cumulative shear, bending and torque diagrams (running loads) were calculated. For all three cases, an identical approach was followed. The cumulative shear, bending and torque is zero at the outboard wing tip. Moving to the aftmost cabin section, the contributions from the outboard wing are added. This is repeated for the contribution of each section, from which the cumulative diagrams may be constructed.

Check The procedure was followed correctly if the cumulative shear load in Z, and the moment about global Y are zero at the tip. As the Flying-V cabin is oriented at the sweep angle, moments about local x and y are not necessarily zero in the local reference frame.

Examples The cumulative diagrams for the limit load LC01 (positive manoeuvring at design payload mass, zero cargo and maximum cruise fuel) are shown below in figures 4.16-4.21. Note that transforming the local

moment about y and torque about x to the global reference frame, a tip moment of approx. zero is obtained.

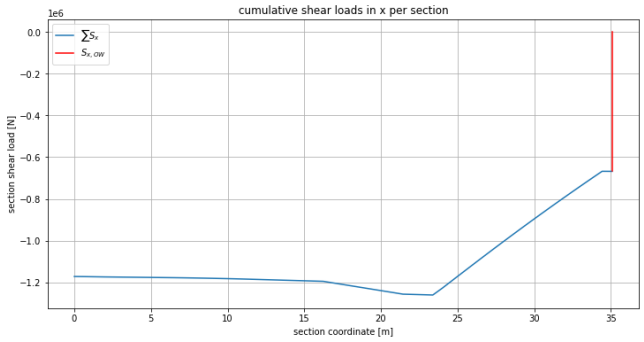

Figure 4.16: Cumulative S_x diagram for load case LC01. Note that the graph does not return to zero at the tip due to pressurisation.

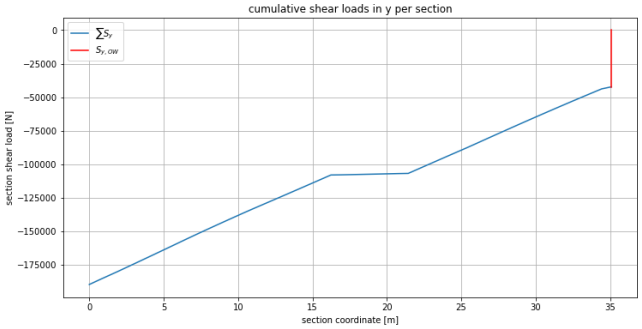

Figure 4.17: Cumulative S_y diagram for load case LC01.

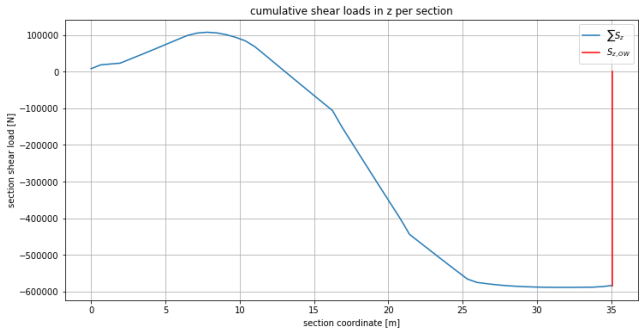

Figure 4.18: Cumulative S_z diagram for load case LC01.

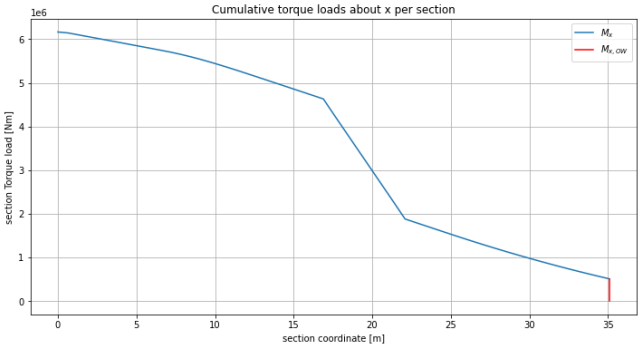

Figure 4.19: Cumulative T_x diagram for load case LC01.

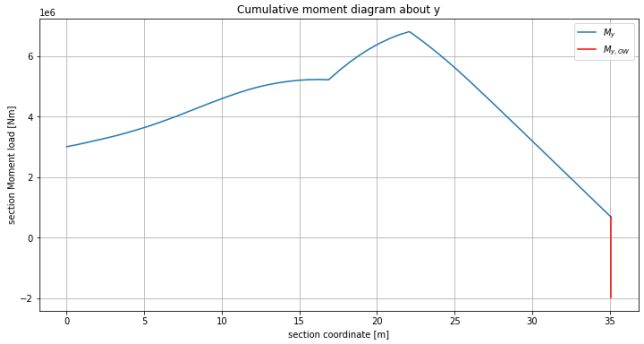

Figure 4.20: Cumulative M_y diagram for load case LC01.

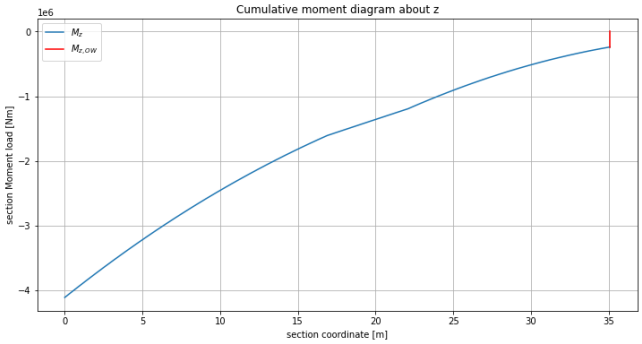

Figure 4.21: Cumulative M_z diagram for load case LC01.

Effect of mass distributions

To show an example of the impact of the mass distribution in the aircraft assigned to a load case, the cumulative shear, bending and torque loads may be found below in figures 4.22 - 4.24 for the 5 different mass distributions association with pressurised positive manoeuvring. Clearly, the mass distribution greatly influences load distribution within the structure. The running loads for all load cases and mass distributions are shown in Appendix D.

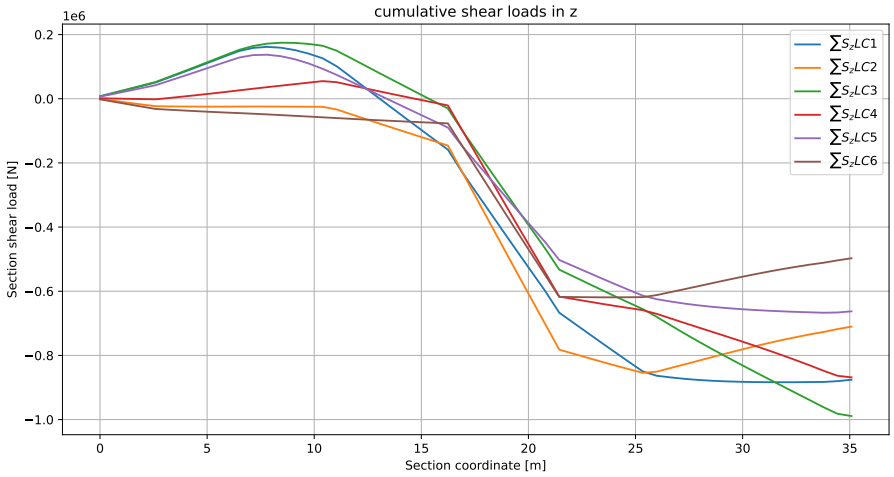

Figure 4.22: Cumulative S_z distribution for the 5 different mass distribution of the positive manoeuvring limit load case.

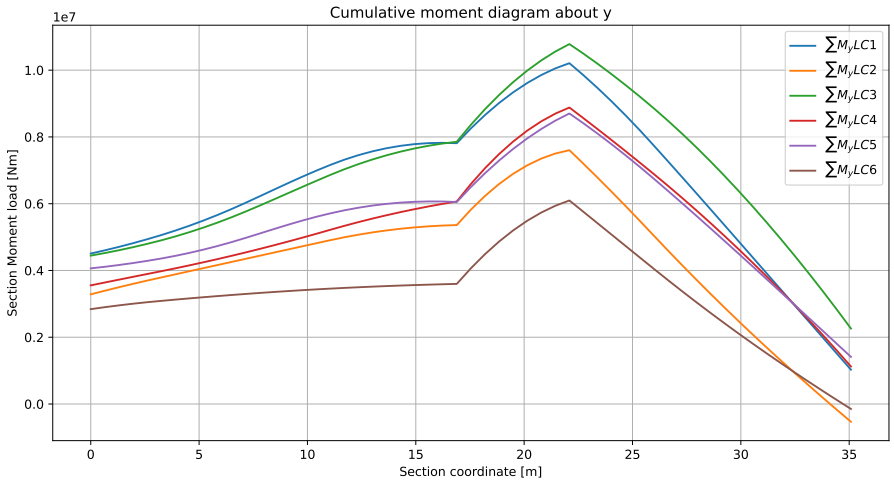

Figure 4.23: Cumulative M_y distribution for the 5 different mass distribution of the positive manoeuvring limit load case.

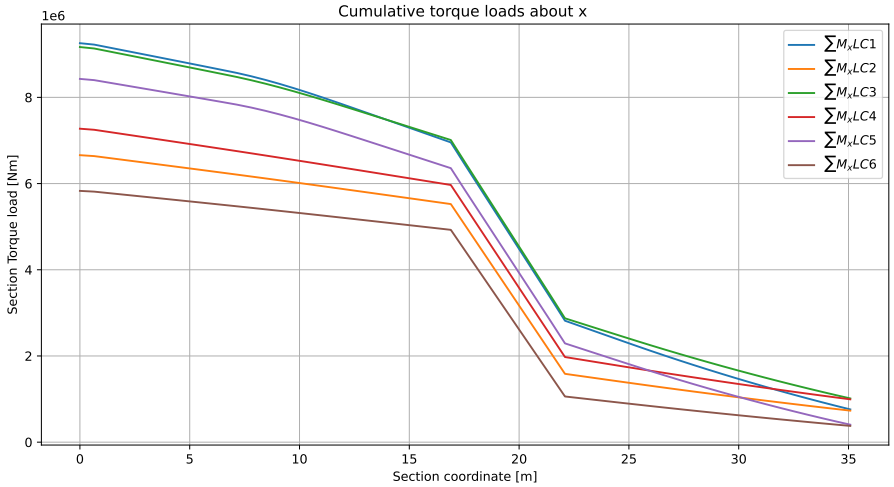

Figure 4.24: Cumulative M_x distribution for the 5 different mass distribution of the positive manoeuvring limit load case.

5
Stress analyses

This chapter elaborates on the stress analysis approach. The following sections illustrate the specific analyses used to obtain the longitudinal stresses (section 5.1) and cross-section stresses (section 5.2). Furthermore, section 5.3 discusses a method used to enrich the longitudinal and cross-section stresses by incorporating interactions. Additionally, stress distributions in a generic structure are investigated and compared to previous results in section 5.3.3.

5.1. Longitudinal stresses

In order to evaluate the stresses in the longitudinal direction of the cabin, structural idealisation was applied. This approach consisted of idealising the geometry, and lumping mass in so-called "booms", as described by Megson [1]. This approach is particularly useful for quickly evaluating bending, torsion and shear loads along the wing. Next to the relatively simple implementation, the straightforward calculations led to a short evaluation time, which was an important objective. Normally, the main drawback of this method is that loads are applied to the whole cross-section equivalently; no load transfer within the cross-section is evaluated. However, the cross-sectional stress analysis covers this shortcoming, described in the next section. Overall, the boom method was considered to give a good first estimation of stresses in the structure, at a high speed.

5.1.1. Idealising procedure

In a stiffened cross-section, stringers and spar flanges are relatively small compared to the cross-section size. When bending the cross-section, it may be assumed that the stress varies very little over the cross-section of the stringers and spar flanges. Therefore, the stress is assumed to be constant over a stiffener cross-section. As the exact size and shape of the stiffener is unknown at this stage, it makes sense to simply represent the cross-sectional area as a concentrated lump of area, a boom. The boom is placed on the skin, as this allows for an easy description of its location. Moreover, the stiffener centroid and the skin location are relatively close compared to the rest of the cross-section. This is slightly unconservative, as the centroid distance of the stiffening elements from the neutral line is increased. On the other hand, to evaluate bending, only Steiner terms are taken into account, which is a slightly conservative approach. Overall, this should give a very good approximation of the structural properties.

Depending on the ability of the skin to carry direct stresses, the structure may be simplified even further. If the skin is considered fully effective in resisting axial stresses, it may be assumed that skin area may be added to the boom areas. However, this area distribution depends on the stress distribution in the cross-section. Consider a plate under axial load, and an idealised panel under the same load, in figure 5.1.

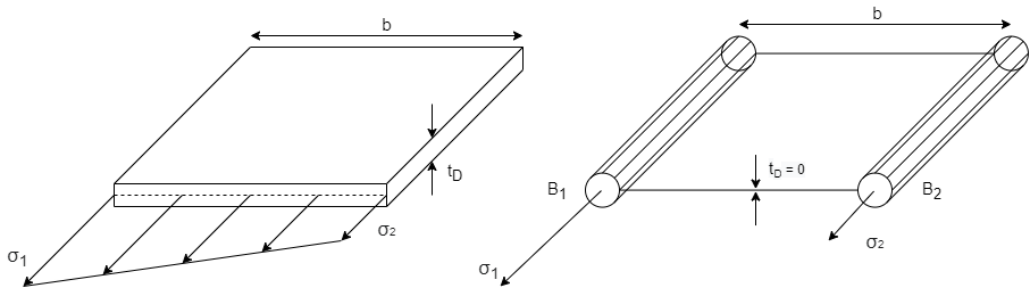

Figure 5.1: Panel idealisation.

Naturally, force equivalence must be maintained. However, moment equivalence should also be maintained. Taking the sum of moments yields equation 5.1 for the boom areas:

$$\begin{aligned} B_1 &= \frac{t_D b}{6}\left(2+\frac{\sigma_2}{\sigma_1}\right) \\ B_2 &= \frac{t_D b}{6}\left(2+\frac{\sigma_1}{\sigma_2}\right) \end{aligned} \tag{5.1}$$

It is important to note from the above equations that the distribution of area depends on the stresses and thus, the applied loads. Therefore, the idealisation changes for a different load case. However, this is only relevant for highly idealised cross-sections (i.e. with a few booms to represent the whole cross-section), as the stress ratios differ significantly. In this research, a high number of booms was used, which greatly reduced the effect the load has on the area distribution to a negligible amount. Therefore, in order to simplify the analysis, the boom area distribution as based on the geometry alone, effectively setting $\sigma_1 = \sigma_2$. The penalty to stress accuracy is very small.

Once the skin area has been divided over the booms, the effective skin thickness reduces to zero. Therefore, the analyses presented below present a stress or shear flow value which is constant for every boom and skin.

5.1.2. Bending

The axial stresses in booms induced by bending can be determined identically to a non-idealised section:

$$\sigma_x = \left(\frac{M_x I_{yy} - M_y I_{xy}}{I_{xx} I_{yy} - I_{xy}^2}\right) y + \left(\frac{M_y I_{xx} - M_x I_{xy}}{I_{xx} I_{yy} - I_{xy}^2}\right) z \tag{5.2}$$

5.1.3. Shear and Torsion

The determination of shear in an idealised closed cross-section is a well-known relation, whose derivation is omitted in this document, but can be found in Megson [1]. The shear flow along the cross-section can be described by 5.3. It should be noted that if the cross-section is fully idealised (i.e. $t = 0$) the shear flow is constant between booms, and represent the average shear flow.

$$q_s - \left(\frac{S_x I_{xx} - S_y I_{xy}}{I_{xx} I_{yy} - I_{xy}^2}\right) \int_0^s \left(txds + \sum_{r=1}^{n} B_r x_r\right) - \left(\frac{S_y I_{yy} - S_x I_{xy}}{I_{xx} I_{yy} - I_{xy}^2}\right) \int_0^s \left(tyds + \sum_{r=1}^{n} B_r y_r\right) + q_{s,0} \tag{5.3}$$

For the closed cell cross-sections, cuts need to be made to be able to start the summation. Once cut, the cross-section may be evaluated as an open cell, with zero shear flow at the cut. Once evaluated, the cell may be closed, and the constant shear flow $q_{s,0}$ may be added such that the torque is balanced in the section, as for a closed thin-walled cell, the torque is easily determined:

$$T = 2Aq \tag{5.4}$$

To evaluate stresses induced by torsion, the section can simply be evaluated with the equation above. However, in the case of the oval fuselage, it should be regarded as a multi-cell section. The total torque is simply determined by:

$$T = T_1 + T_2 + T_3 = 2A_1q_1 + 2A_2q_2 + 2A_3q_3 \tag{5.5}$$

The shear flow in webs which connect cells can simply be subtracted, e.g. $q = q_1 - q_2$, depending on the defined positive direction. If the thickness along each cell is different, equivalence in rate of twist needs to be introduced to solve the problem. The rate of twist in a closed cross-section (with the same material) is defined as:

$$\left(\frac{d\theta}{dz}\right) = \frac{1}{2A}\oint \frac{qds}{tG} \tag{5.6}$$

In a two-cell problem, the rate of twist of the first cell may be described as:

$$\left(\frac{d\theta}{dz}\right)_I = \left(\int \frac{q_1 ds}{t_1} + \int \frac{(q_1 - q_2)ds}{t_2}\right) \tag{5.7}$$

The same relation may be set up for a second cell. Then using equation 5.4 and the two relations obtained by equations 5.7, one can solve for q_1 and q_2. However, when evaluating the shear flows in the members, it may be found that the shear flow in the web connecting the two cells is zero. Therefore, in the case of pure torsion, the cross-section may simply be regarded as a single cell section, cutting away the connecting elements. For pure torsion, adding an extra web thus only adds weight.

For multi-cell shear, the story is different, as the webs connecting cells in fact do carry shear. Firstly, all cells are cut on the skins. The cells may be evaluated according to equation 5.3. If the skins are idealised, t is zero. Then, similar to the multi-cell torsion problem, rate of twist equivalence is applied. However, another relation is required to solve this problem; moment equivalence. The moment induced by the shear loads about any point must be equal to the moment induced by shear flows in the shells about that point:

$$S_x\tilde{y} - S_y\tilde{x} = \oint pq_b ds + 2Aq_{s,0} = \sum_{R=1}^{n}\oint pq_{bR}ds + \sum_{R=1}^{n} 2A_R q_{s,0R} \tag{5.8}$$

Which is the last required relation to solve for the shear flows. The shear flows obtained by torsion and shear can be directly summed to obtain the final shear flow state of the cross-section.

In order to check that the described method was performed correctly, shear and torque equivalence between the shear flows and external shear and torque loads were evaluated. Shear and torque equivalence holds if:

$$\begin{aligned}
\sum S_y &= \sum_{i}^{m} q_{s,i}L_i cos(\theta_i) \\
\sum S_z &= \sum_{i}^{m} q_{s,i}L_i sin(\theta_i) \\
\sum T_X &= \sum_{i}^{m} q_{s,i}L_i cos(\theta_i)(z_i - \overline{z}) - q_{s,i}L_i sin(\theta_i)(y_i - \overline{y})
\end{aligned} \tag{5.9}$$

5.1.4. Taper in Cross-section

Tapering the cross-section has a number of effects on the distribution of forces and moments in the cross-section. The structural idealisation method by Megson [1] is also particularly applicable to analyse a tapered section.

A generalised idealised tapered beam problem may be approached in the following manner. As seen in figure 5.2, for some cross-section undergoing taper in two dimensions, the boom forces can be decomposed into Cartesian components.

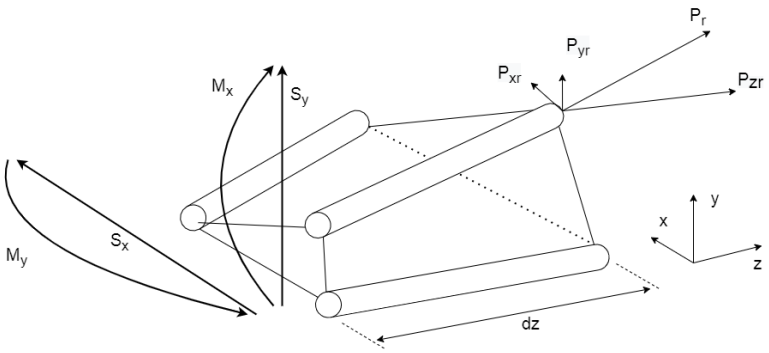

Figure 5.2: Generalised taper problem.

The applied moments yield the force components in z. The other components can be found using basic trigonometry. It should be noted that the shear forces taken up by the skins are affected by the angled force vectors in the booms:

$$\begin{aligned} S_x &= S_{x,web} + \sum_{r=1} P_{x,r} \\ S_y &= S_{y,web} + \sum_{r=1} P_{y,r} \end{aligned} \tag{5.10}$$

The closed-cell shear approach may be applied to obtain the shear flows in the skins. The shear centre may be found by a modification which takes into account the angled boom forces (Megson [1]):

$$S_x \tilde{y} - S_y \tilde{x} = \oint p q_b ds + 2Aq_{s,0} - \sum_{r=1} P_{x,r}(y_r - \tilde{y}) + \sum_{r=1} P_{y,r}(x_r - \tilde{x}) \tag{5.11}$$

The outputs provided by the analysis are the longitudinal axial stress in the skins and stringers, as well as the shear stresses in the skins.

5.2. Cross-section stresses

In previous work, the cross-section of the FV was analysed analytically / empirically, based on the structure at hand. Direct stresses were only determined for the pressurisation case. Clearly, a need arose for the improved estimation of the stresses in the cross-section. The second main goal of this analysis was to compare the structural response to pressurisation with previous solutions. A comparison between the membrane approach and the FEM solution is given in section 5.3.3 .

5.2.1. Approach

In order to determine the stresses in the cross-section plane, a number of methods were considered. In this stage of development, the goal was to obtain a better representation of the stresses in the cross-section compared to previous research, but a high accuracy was not the only consideration. Being able to quickly evaluate the large structure was considered to be equally important. Therefore, a number of methods were assessed. Firstly, analytical methods for over-determined structures were trialled. However, in the FV cross-section, axial and bending displacement are highly coupled. Some degree of decoupling was required to solve for the stresses, but no satisfactory solution could be obtained as the decoupling led to an unrepresentative stress distribution.

In order to obtain a satisfactory solution, it was decided to determine the behaviour of the cross-section with FEM. However, depending on the complexity and the refinement of the model, FEM analysis could be

much slower than desired. In order to speed up the FEM evaluation, the structure was simplified, which is elaborated on in the next subsection.

5.2.2. Structural simplification

The structural simplification was based on condensing the behaviour of a whole (frame-to-frame) cabin section into one 2-dimensional cross-section. This is illustrated in figure 5.3. The section contains the following main structural elements:

- **Skins:** This includes the aerodynamic outer skins, as well as the aft pressure arc, floor skin, ceiling skin and the skin of the vertical support structure.
- **Frames:** Two frame halves are present on each end of the section. The frames are connected to the pressure skins, while cross-beams are attached to the floor, ceiling and wall skins.
- **Stringers:** longitudinal stiffeners are present on each element.

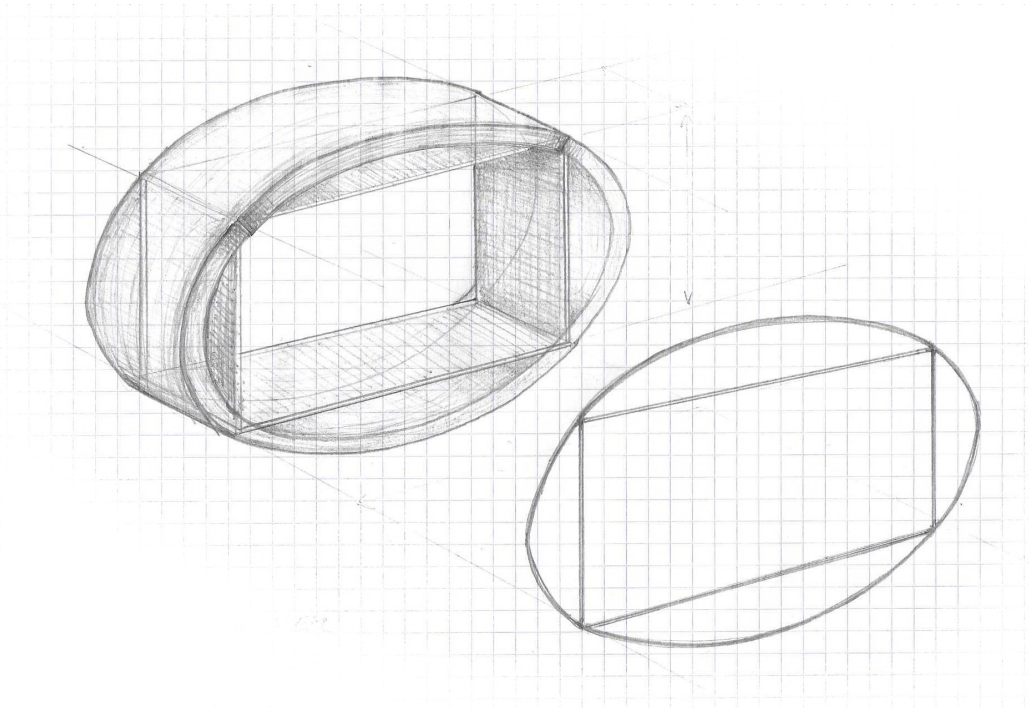

Figure 5.3: Frame-to-frame section 2-dimensional representation.

The properties of the cross-section changes from frame to frame, and so does the behaviour. The frames acts like beams, and the skin near the frame conforms to the shape of the frame. Moving away from a frame towards the centre of the section, the skin may deform in a different manner to the frames (in the local yz-plane). Therefore, it may be expected that the stresses in the skin are very different near and far from frames. However, with adequate longitudinal stiffening (i.e., by using enough stringers), the difference in deformation of the whole section is highly limited. It was hypothesised that the stringers enforce this equal behaviour enough such that the deformation of the whole section can be condensed into a 2-dimensional problem. In other words, the out-of-plane deformation of the skin near the frames and in the centre of the section is almost identical. The more uniform the section is, the better this assumption holds.

A second hypothesis is that all components may be adequately represented by 1-dimensional frame elements. This is the case as all components are slender, and the out-of-plane deformation is dominated by bending, and thus the effects of shear are limited. The properties of the section were determined, and assigned to equivalent 1-dimensional FEM frame elements (resisting axial and bending deformations). The local cross-section of each frame element is indicated schematically in 5.4. The relevant parameters to note are displayed in the figure, namely: the frame pitch b_f, the skin and frame thicknesses t_s and t_f, the frame height and flange width h_f and w_f. Also, it is important to note that the local coordinate system of the element was determined as zero from the outer skin edge, and being positive in the direction of the frame.

With the defined geometry and the coordinate system, the local neutral line s_n was determined. Note that the stringers were not taken into consideration as they contribute a negligible amount to the hoop properties, other than retaining its shape. The stringers are considered in the 3D corrections, which are discussed in section 5.3.

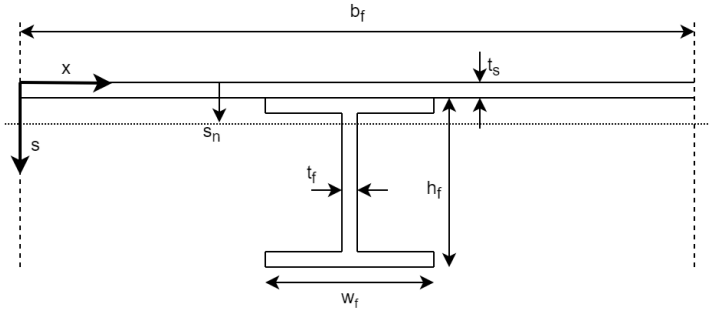

Figure 5.4: Cross-section of each component perpendicular to x-axis.

By applying the above rationale, each cabin section is effectively reduced to a 2D problem. Additionally, it should be noted that this representation does not include interaction with neighbouring sections. The fact that there is no interaction is considered a legitimate approach. This is the case as the cross-section of the cabin does not change rapidly over the cabin length. However, this is not necessarily true for all loads. For the pressurisation, aerodynamic and weight loads, the load of consecutive sections are mostly identical. However, the landing gear and engine loads are introduced in a predefined number of sections. The sections respond to this load, and consequentially deform significantly. However, the neighbouring sections are unaffected. Including out-of-plane interaction of consecutive sections was deemed beyond the scope of this thesis. If the deformations remain relatively small, and the frames are stiff enough to effectively transfer the loads to the rest of the cross-section, the error in the exclusion of interaction is expected to be small.

5.2.3. FEM

In order to obtain the stresses in the cross-section, the standard FEM approach was followed, described globally in the following paragraphs.

The first step in the FEM process was to define the type of elements that were used. As all elements were slender and the effect of shear was assumed to be small, frame elements were deemed appropriate. The properties of the frame elements were straightforward to determine, combining axial stiffness with bending stiffness. To adequately describe the bending shape, a third-order polynomial was used for the out-of-plane displacement function. From the displacement function, the following four shape functions were derived:

$$N_1 = \frac{l^3 - 3lx^2 + 2x^3}{l^3}, \quad N_2 = \frac{l^2x - 2x^2l + x^3}{l^2}, \quad N_3 = \frac{3x^2l - 2x^3}{l^3}, \quad N_4 = \frac{x^3 - x^2l}{l^2} \tag{5.12}$$

Minimising the total potential energy allows for the derivation of the elemental frame stiffness matrix, shown below.

$$\begin{bmatrix} \frac{EA}{L} & 0 & 0 & \frac{-EA}{l} & 0 & 0 \\ 0 & \frac{12EI}{l^3} & \frac{6EI}{l^2} & 0 & \frac{-12EI}{l^3} & \frac{6EI}{l^2} \\ 0 & \frac{6EI}{k^2} & \frac{4EI}{L} & 0 & \frac{-6EI}{l^2} & \frac{2EI}{L} \\ \frac{-EA}{l} & 0 & 0 & \frac{EA}{l} & 0 & 0 \\ 0 & \frac{-12EI}{l^3} & \frac{-6EI}{l^2} & 0, & \frac{12EI}{l^3} & \frac{-6EI}{l^2} \\ 0 & \frac{6EI}{l^2} & \frac{2EI}{l} & 0 & \frac{-6EI}{l^2} & \frac{4EI}{l} \end{bmatrix} \tag{5.13}$$

For each concept, the connectivity matrix was established, after which the global stiffness matrix $[K]$ was assembled. The obtained matrix was tested for symmetry and positive definite, which are the required prop-

erties of a valid global stiffness matrix. For each load case, the force vector $[f]$ was constructed, consisting of the sum of pressurisation, weight/inertia, aerodynamic, thrust and landing forces/moments.

With the stiffness matrix and force vector present, the boundary conditions were enforced. It was considered that each section does not show global rotation or translation, but is allowed to deform in an unconstrained manner. However, no single node may be constrained in rotation, as the nodes should be free to locally rotate. As the component properties are not necessarily symmetric, not symmetric rotation distribution is present. In order to achieve the required level of constraint, two translation conditions were imposed. The first, located at one floor vertex, was constrained translational motion in y and z. A second node, located at the other floor vertex, was only constrained in z. With the selected constraints, the stiffness matrix and force vector were reduced, after which the Eigenvalue problem was solved.

$$a_r = [K_r]^{-1}[f_r] \tag{5.14}$$

Where a denotes the displacement solution, and the subscript r denotes the reduced state. The adequate zeros were added at the constrained nodes, after which the full displacement solution was obtained. With the displacement solution, the strains and stresses were determined per element. For each element, the global displacements were transformed to the local element reference system, after which the following operations were performed. Firstly, the pure axial stresses could be trivially obtained by determining the strain from the axial displacement, and multiplying this by the Young's modulus. The bending stresses were determined as follows. Firstly, the B-matrix was determined, which is defined as:

$$B = [N_1 \quad N_2 \quad N_3 \quad N_4] \tag{5.15}$$

where N_i are the shape functions as shown in equation 5.13. However, the B-matrix requires an input along the element length. As inputs, the node coordinates were supplied (i.e. $x = 0$ and $x = l$), as it was assumed that the maximum bending stress would be present at one of the extremes of the element. With the two B-matrices, the bending stress at a point in the cross-section was calculated as follows:

$$\sigma_i = -E(h_i - h_n)[B][a] \tag{5.16}$$

where h_i and h_n denote the coordinate of the point along the cross-section and the coordinate of the neutral line, respectively. The stress was evaluated at the following points of interest: The inner and outer skin surface, the edges of the inner and outer flange of the frame, to determine the extreme stresses in both components. This is illustrated in figure 5.5. Note that the extreme outer flange stress of the frame is equal to the inner skin stress.

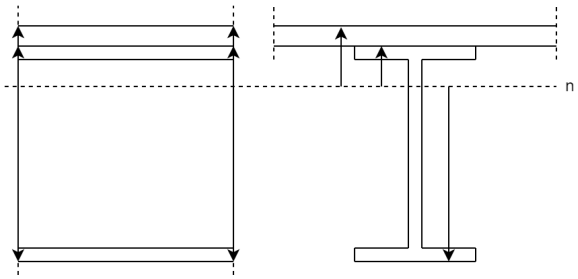

Figure 5.5: stress evaluation locations

10 stress values were obtained, namely: 1 pure axial stress value and 4 component values at each node. The maximum and minimum combinations of the stresses were determined for each component extreme, after which these values were saved. It should be noted that evaluating the stresses at the nodes allows for limiting the number of elements in the cross-section, and obtaining accurate maximum stress values at the joints. This concluded the pure 2-dimensional representation of the stresses in the cross-section.

5.3. 3D interaction

Having obtained the stresses in the longitudinal direction and the lateral direction, the stress fields over the whole structure was investigated from a 3-dimensional perspective.

5.3.1. Coupling

A significant coupling was expected between the longitudinal stresses and the cross-section stresses. This was the case as the stresses in the different adjacent structures differ wildly (e.g.,the crown and ceiling are under high tensile and compressive load, as seen in figure 5.13), causing large differences in lateral expansion. However, these components are directly connected to each other at the vertex joints. Therefore, their interaction was investigated, which is discussed in this section. This effect is primarily caused by pressurisation. Therefore, the discussion in the following paragraphs is limited to the context of the pressurisation load.

5.3.2. Lateral expansion

While the cross-section analysis aims to decouple itself from the longitudinal stresses, there are interactions which were modelled by implementing straightforward corrections to the 2D representation. Firstly, contraction and expansion in the global x-direction should be considered. For the continuation of this section, please note the used reference system in figure 5.6. The 1-direction runs on the YZ-plane along the structure, while the 2-direction is aligned with the wing-fuselage x-axis.

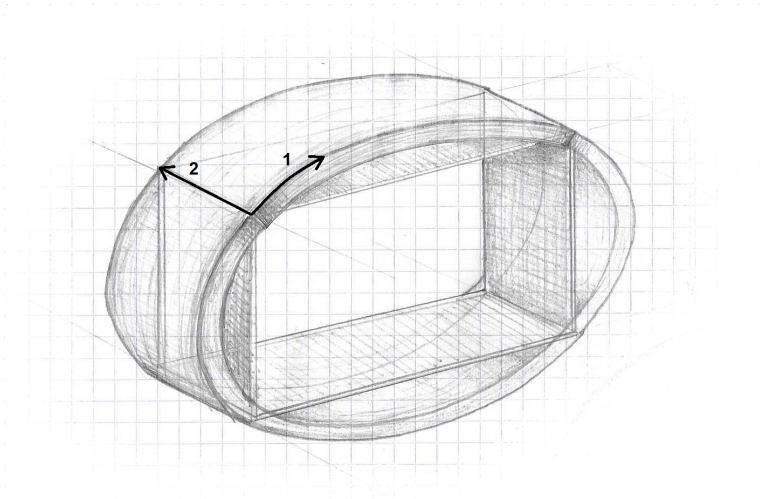

Figure 5.6: Local reference system

As the loads are applied to the cross-section, deformations can be determined by solving the FEM Eigenvalue problem. From this, S_{11} may be determined over the length and through the thickness of all components. As expected, tensile stresses are high in the outer skins and walls, while compressive stresses are high in the floor and ceiling. The Poisson's effect causes the components to significantly contract (skins, walls) or expand (floor, ceiling). This is schematically indicated in figure 5.7

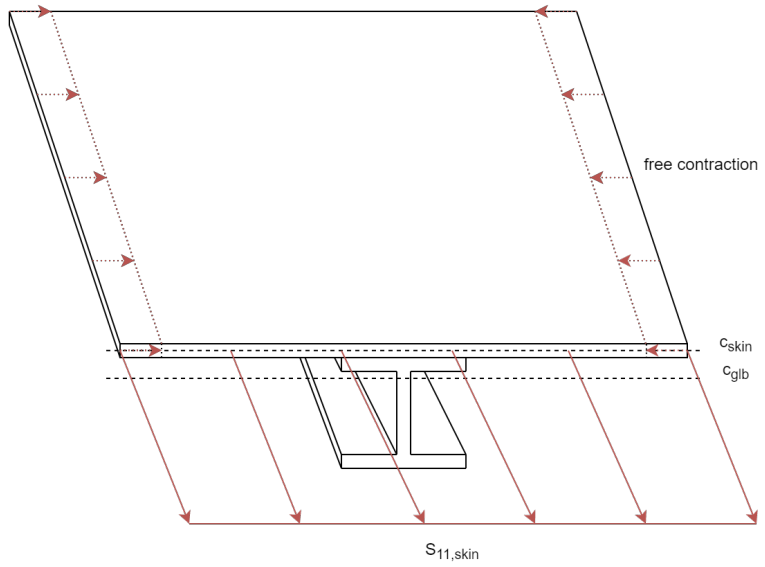

Figure 5.7: Free contraction under hoop stress.

If not addressed, the model would be equivalent to allowing this expansion and contraction freely, leading to a shape as illustrated in figure 5.8.

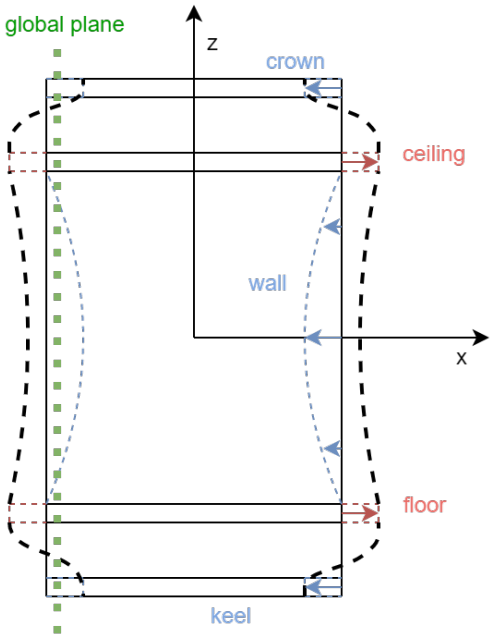

Figure 5.8: Hourglassing effect by unrestricted expansion and contraction.

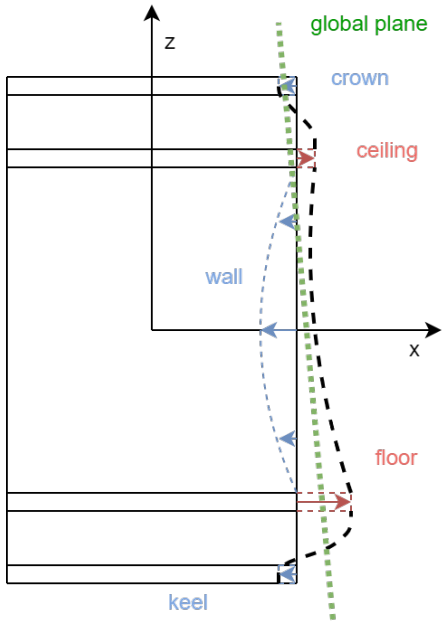

Figure 5.9: Asymmetric hourglassing due to different lateral expansions, causing a change in angle about y.

This 'hourglassing' should be resisted effectively by the adjacent structure, and therefore the edges should all lie on a single contraction plane. Additionally, the stringers resist the expansion and contraction, and were taken into account. Consequently, all edges must lie on one global plane. For symmetric loads (pressurisation) and a symmetric cross-section, bending about Y or Z should be zero, and thus this symmetry plane should be plane with the global YZ-plane. An angled plane may be determined by summing the moment contributions of all lateral expansions. For a resultant moment about y, the angle can be determined as shown in equation 5.17

$$UR_3 = \frac{M}{EI} pitch \tag{5.17}$$

$$M = \sum E\epsilon_{i,22} A_{i,yz} (r_i - r_n) \tag{5.18}$$

where UR_3 is the rotation about the local 3 direction, which in this case is equivalent to rotation about the y-axis. $\epsilon_{i,22}$ is the lateral strain due to the expansion/contraction, and $(r_i - r_n)$ represents the distance from the element to the neutral axis. The same calculation must be performed consecutively with the moment about z, to solve for a neutral plane orientation satisfying both equalities. The above implies that pressurisation causes the cabin to bend if the structure is asymmetrical in terms of lateral expansion. It is assumed that the design will not be very asymmetrical, and therefore, this bending is small. An assumption is made that the designed structure will not be very asymmetric, which prevents the calculation of an angled plane in 3d space.

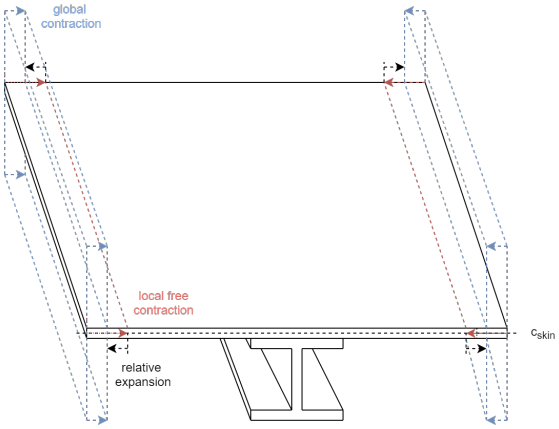

Figure 5.10: free, global and imposed relative lateral expansion.

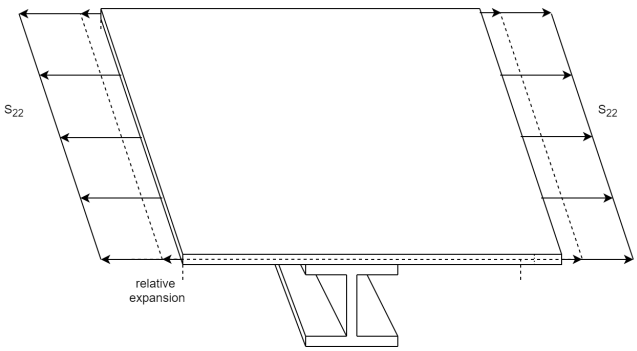

Figure 5.11: Resultant required S_{22} to impose relative expansion.

defining a global expansion/contraction plane (indicated at section level in figure 5.8, indicated at component level in figure 5.10), allows for the calculation of S_{22}. The difference between the local free contraction and global contraction must be overcome by this imparted stress, as shown in figure 5.11. The obtained values for S_{22} are added to the results from the longitudinal stress calculation.

Having obtained S_{22}, it must be considered that this imposed lateral stress again causes contraction/expansion of the skin in the 1-direction. While the skin contracts, as S_{22} is imparted on it, the frame resists this contraction. It is assumed that the frame acts as a 1-dimensional member, and therefore it experiences no lateral contraction. An equilibrium state of longitudinal expansion of the skin and frame was determined which is proportional to the relative areas of the skin and frame.

This obtained expansion/contraction in the 1-direction was imposed in the FEM calculation by applying artificial forces to the elements. As the skin contracts due to the lateral stress (and not due to these artificial forces), an incorrect stress in the 1-direction would be obtained. Therefore, a stress correction was performed, equal to the artificial force divided by the area. These artificial forces are visualised in figure 5.12 However, this correction was only applied to the skin. The frame, on the other hand, has attained a correct stress state, as the skin imparts these contraction forces on the frame. Note that the pure axial stresses in the skin and frame (not considering bending) have now obtained a different value, where they were first equal.

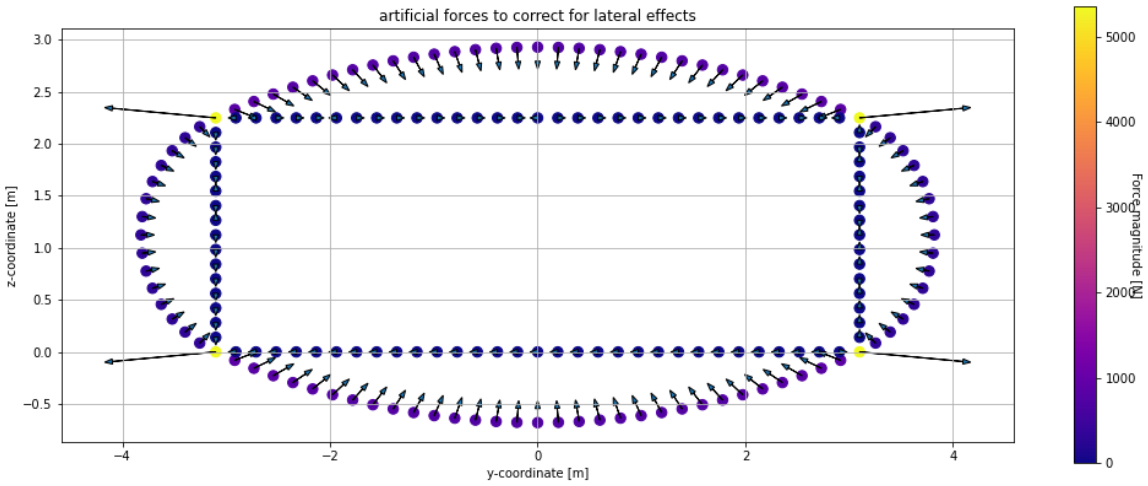

Figure 5.12: Artificial forces to account for lateral interaction.

With the updated force vector, the Eigenvalue problem was solved once more, which delivers a new solution, which was then corrected as described above. The change in results scales approximately with the square of the Poisson's ratio, as it is multiplied twice in the above calculation. Theoretically, one could loop the above operations multiple times to approach the true solution. However, the next loop is expected to only change the results by less than 1% (ν^4). Additionally, there are likely other effects which are not treated, which have a larger effect on the solution than this 1%. Also, another loop requires solving the Eigenvalue problem another time, which costs a significant amount of runtime. Therefore, a single loop was determined to be the most favourable.

The described approach was validated with *ABAQUS*, as shown in detail in Appendix A. Clearly, enriching the solution with lateral corrections shows an improvement in prediction accuracy.

5.3.3. Pressurisation induced stress distributions

Understanding the response of the structure under the pressurisation load is one of the main research goals. Mainly, the response of the cross-section is of interest. To correctly proceed with the following steps of the research (i.e. failure modes and sizing), a better understanding of the behaviour of the deformation and stress distribution was desired. However, as the structure was not sized at this stage, a generic, but representative, baseline structure was needed. Based on Oosterom's[13] results, a geometry was determined, discussed in more detail in Appendix F.

Membrane approach

For thin cylindrical pressure shells, the hoop stress is related to the pressure difference dp by:

$$\sigma_{hoop} = \frac{dpr}{t} \tag{5.19}$$

where r is the radius of the shell, and t represents the shell thickness. The stresses in the skins can be easily determined to be:

$$\begin{aligned} \sigma_{crown} = \sigma_{keel} = 85.2MPa \\ \sigma_{LE} = \sigma_{TE} = 14.2MPa \end{aligned} \tag{5.20}$$

Correcting for the frame area:

$$\begin{aligned} \sigma_{crown} = \sigma_{keel} = 65.9MPa \\ \sigma_{LE} = \sigma_{TE} = 11.0MPa \end{aligned} \tag{5.21}$$

The residual load at each vertex is then simply:

$$F_{res} = dp(r_{large} - r_{small}) \tag{5.22}$$

The load components in the ceiling/floor and walls is then determined to be equal to -49.8 MPa and 23.0 MPa, respectively.

FEM solution

For the FEM solution, a number of figures are shown below which describe the pure axial stress and bending stress in the extremes of the different components (i.e. skins and frames). From the pure axial stress plot, it may be found that the average stress values are: $\sigma_{crown} = \sigma_{keel} = 63.8MPa$, $\sigma_{LE} = \sigma_{TE} = 11.1MPa$. For the ceiling, floor and walls, the stresses are $\sigma_{ceiling} = \sigma_{floor} = -47.7MPa$ and$\sigma_{walls} = 22.8MPa$ These stresses are very comparable, as would be expected.

The second part of this comparison is about the stresses which are not captured by using the membrane analysis: the bending stresses. As may be seen, the peak bending stresses induced in the skin are relatively small, but significant. On the skin outer surface, at the centre of the arc, a bending stress of 8.5 MPa is recorded (13% increase of the pure axial stress). Near the vertex joints, a bending stress of -16.8 MPa is recorded. The peak stress in the frame inner flange (pointing towards the inside of the cabin), is far higher than the pure axial stress. At the joint, a peak stress of 106 MPa is attained by the inner flange. The minimum and maximum bending in the LE and TE frames is -6.3, 4.1 MPa, respectively. The bending stresses in the cabin structure is negligible, as it is all lower than 1 MPa.

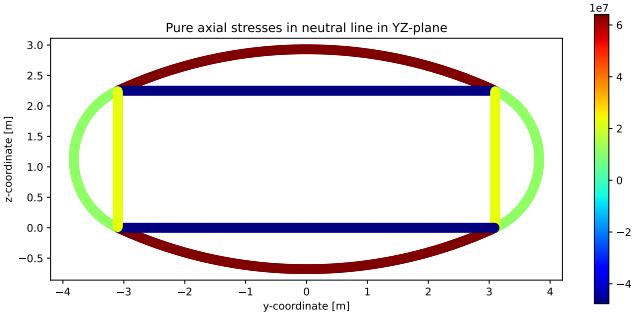

Figure 5.13: Original concept pressure induced axial stress through the neutral line.

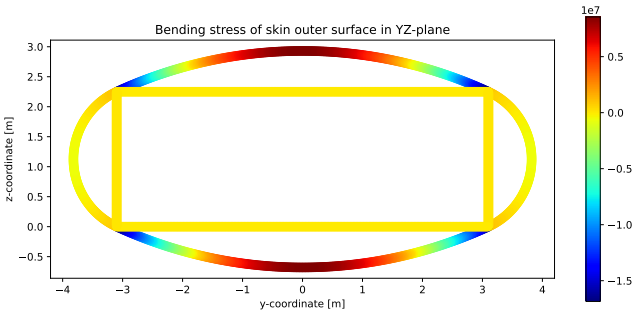

Figure 5.14: Original concept pressure induced bending stress in the skin outer surface.

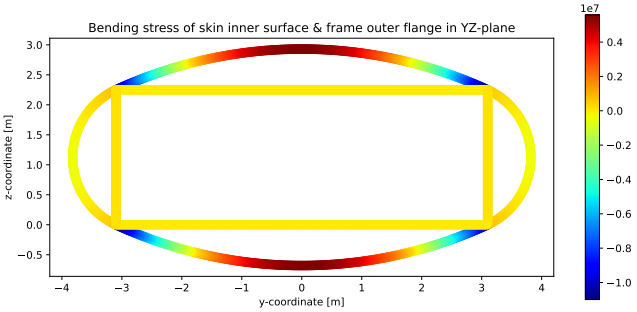

Figure 5.15: Original concept pressure induced bending stress in the skin inner surface, equal to the frame outer flange.

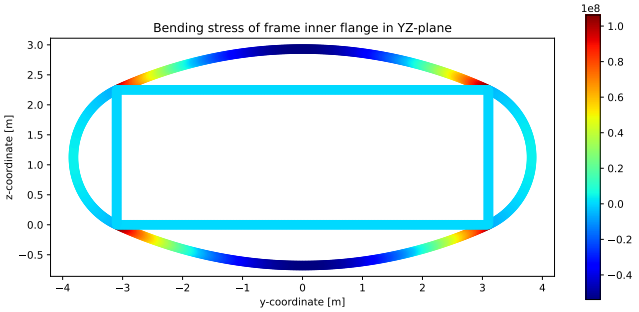

Figure 5.16: Original concept pressure induced bending stress in the frame inner flange.

The stresses in the inner flange of the frame are high as the inner flange is relatively far away from the neutral line. Therefore, the bending-induced stress in the skin is relatively low. If the neutral line would be farther away from the skin (thinner skin relative to the frame area), the bending-induced stresses would be higher. Summarising, the above FEM analysis shows that the bending stresses must be taken into consideration for structural design.

NLES concept

While the membrane analysis is not applicable to the "no leading edge spar" concept, the pressure-induced stress behaviour must still be understood. Therefore, for the same generic design (without the wall), the cross-section stresses are shown below.

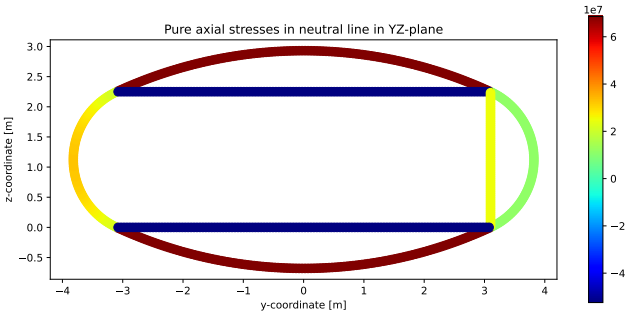

Figure 5.17: NLES concept pressure induced axial stress through the neutral line.

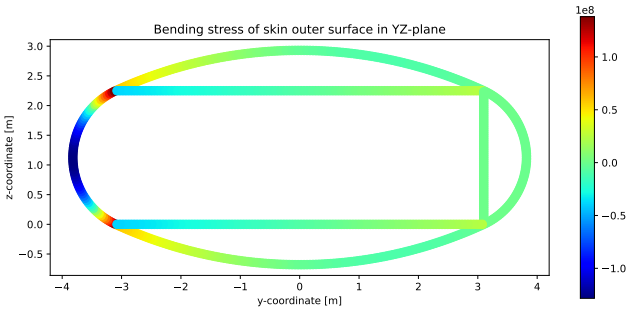

Figure 5.18: NLES concept pressure induced bending stress in the skin outer surface

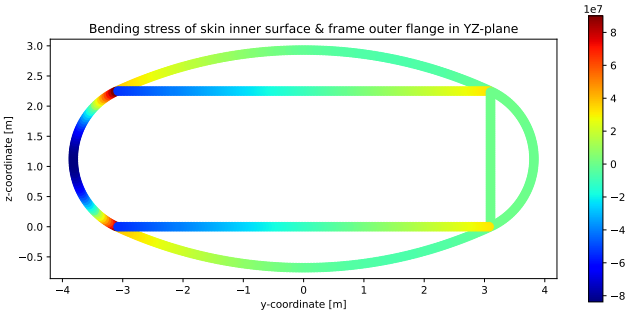

Figure 5.19: NLES concept pressure induced bending stress in the skin inner surface, equal to the frame outer flange.

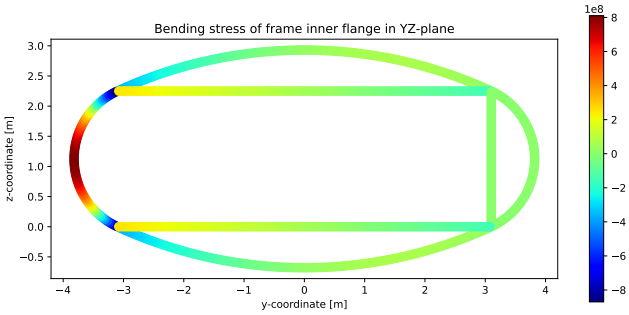

Figure 5.20: NLES concept pressure induced bending stress in the frame inner flange.

From figure 5.21, it may be seen that the obtained axial stresses in the neutral line are practically the same as earlier, except for the leading edge. The axial stress is significantly higher there, and varies over the arc. Figures 5.18, 5.19 and 5.20 each tell the same story: the leading edge is significantly bent. This leads to two peak locations. Firstly, as the LE arc is 'opened up' due to the pressure, the LE skin and frame outer flange are under significant compression. conversely, the frame inner flange is under very high tension. Compared to the original concept, the peak bending stress value is about 8 times higher. Secondly, the LE bends in opposite directions when approaching the vertex joints. Additionally, significant bending stresses are imposed on the floor and ceiling, which were practically unaffected in the original concept.

However, this comparison is not completely fair as the wall is removed, without a reinforcement to the LE. The material of the previously removed wall is approximately added, to obtain an impression of the stresses for a reinforced leading edge at a similar structural mass. Specifically, the thickness is doubled, and the frame area is doubled as well, for the same ratios between frame height, width and thickness. The results can be found in figures 5.21 to 5.24.

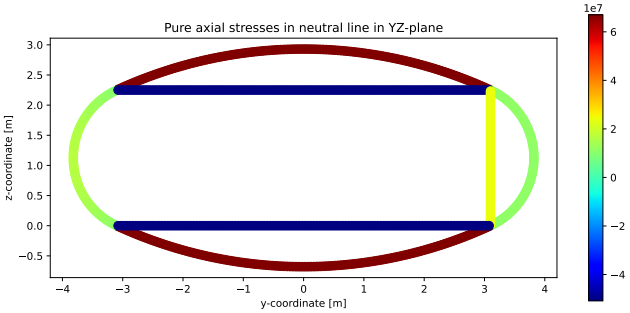

Figure 5.21: NLES concept pressure induced axial stress through the neutral line. Reinforced LE.

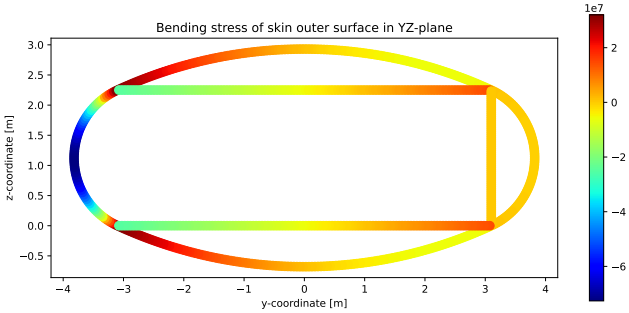

Figure 5.22: NLES concept pressure induced bending stress in the skin outer surface. Reinforced LE.

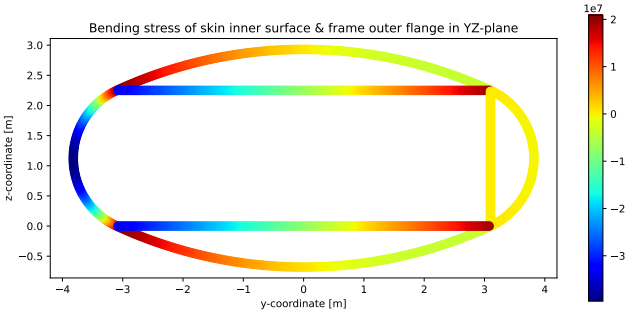

Figure 5.23: NLES concept pressure induced bending stress in the skin inner surface, equal to the frame outer flange. Reinforced LE.

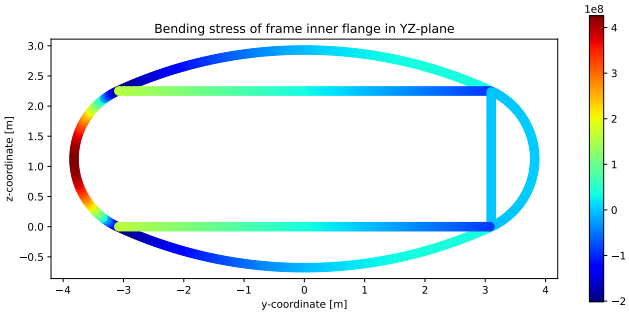

Figure 5.24: NLES concept pressure induced bending stress in the frame inner flange. Reinforced LE.

A few things are clear from this leading edge reinforcement. Firstly, the axial stress through the LE neutral line is approximately equal to that of the TE. Secondly, the peak bending stresses have decreased significantly. The bending distribution throughout the adjacent components is clearly affected significantly by the deformation of the LE. For the crown and keel, the peaks which were in the centre of the arcs move to LE joint region. Secondly, the floor and ceiling are bent significantly. This is an undesirable effect, as these components are under high compression loads, leading to potential stability-related issues. It should be noted that the above stress distributions are highly dependent on the component properties. Therefore, the above examples should not be interpreted to generally describe the behaviour of the sections.

6
Failure analyses

A plethora of failure modes may occur in the aircraft. These failure modes are dependent on the material, the applied loads and geometry. In the preliminary design stage of aircraft development, a limited number of failure modes may be selected as critical. These selected failure modes should be the main design drivers, which should result in a design which is comparable with the design in later stages. The selected critical failure modes consist of three categories: static material failure (SMF), fatigue-related failure and stability-related failure. These failure modes are selected as each category is likely to be critical for different load cases, and in different parts of the structure. This is expected to lead to a structure which is able to cope with many more load cases and failure modes which are not considered in this research.

6.1. Static material failure

Material failure may occur under static loads which may occur some time during the life of the aircraft. Typically, an allowable is selected for limit load and ultimate load, as described below. The most limiting case drives the design.

6.1.1. Yielding

According to the CS 25.305[41], no detrimental permanent deformation is allowed in the structure up to and including limit load. The boundary of permanent (plastic) deformation is typically indicated by yielding. The yielding stress is defined as 0.2% of permanent strain upon unloading. it is assumed that the yield stress constitutes this non-detrimental deformation limit.

The *Handbuch Struktur Berechnung*[19] was used to obtain allowable yield strength values for the structure in an expected thickness range.

6.1.2. Plasticity

At loads beyond limit load, plasticity is allowed to some degree. However, it is difficult to assess exactly to what degree this is allowed. One could define a margin of safety, to remain below the ultimate strength. However, safe operation of the aircraft must be guaranteed after the ultimate load. Strain, and thus deformation, increases rapidly by increasing the stress beyond the yield stress. Large deformations may significantly alter the distribution of loads within the structure. This may cause some structural elements to fail, which may in turn trigger total failure.

For simplicity, it was assumed that the ultimate strength is selected as the strength value under ultimate load. Similarly to the yield strength data, the *Handbuch Struktur Berechnung*[19] was used to obtain allowable ultimate strength values for the structure in an expected thickness range. This was done for the selected materials, whose properties are discussed in B.

6.1.3. Principal stresses

Material may yield under axial stresses, shear, or a combination of the two. In order to determine if failure occurs under a combination of stresses, the principal stresses were determined. Under applied loads, the stress state of an element is unique. However, the measured stresses depend on the assumed coordinate system. Therefore, axial and shear stresses may be transformed, if the coordinate system is rotated by some

angle:

$$\begin{aligned}\sigma_X &= \sigma_x cos^2\theta + \sigma_y sin^2\theta + 2\tau_{xy} sin\theta cos\theta \\ \sigma_Y &= \sigma_x sin^2\theta + \sigma_y cos^2\theta - 2\tau_{xy} sin\theta cos\theta \\ \tau_{XY} &= -\sigma_x sin\theta cos\theta + \sigma_y sin\theta cos\theta + \tau_{xy}\left(cos^2\theta - sin^2\theta\right)\end{aligned} \tag{6.1}$$

The principal axial stresses act along two planes, separated 90 degrees from each other. The orientation of these planes depends on the presence of axial and shear stresses. Differentiating the transformation equations w.r.t. θ and setting to zero, the orientation of the principal stresses may be found:

$$tan(2\theta) = \frac{2\tau_{xy}}{\sigma_y - \sigma_x} \tag{6.2}$$

Similarly, maximum shear stresses occur in planes separated 90 degrees from each other, and 45 degrees from the principal axial stresses, given by:

$$tan(2\theta) = \frac{\sigma_y - \sigma_x}{2\tau_{xy}} \tag{6.3}$$

The values of the principal stresses can readily be determined, as can be seen below.

$$\begin{aligned}\sigma_{max} &= \frac{\sigma_x + \sigma_y}{2} + \frac{1}{2}\sqrt{\left(\sigma_x - \sigma_y\right)^2 + 4\tau_{xy}^2} \\ \sigma_{min} &= \frac{\sigma_x + \sigma_y}{2} - \frac{1}{2}\sqrt{\left(\sigma_x - \sigma_y\right)^2 + 4\tau_{xy}^2} \\ \tau_{max} &= \pm\frac{1}{2}\sqrt{\left(\sigma_x - \sigma_y\right)^2 + 4\tau_{xy}^2}\end{aligned} \tag{6.4}$$

The principal axial and shear stresses were evaluated for static material failure. This procedure was only followed for the stresses in the skin. It was assumed that the frames and stringers can be adequately represented by 1-dimensional elements, and therefore, a stress transformation was not necessary.

6.2. Fatigue analysis

Introduction fatigue failure analysis has been one of the main pillars of structural analysis in aerospace industry since the 1950's. Fatigue failure has developed into a mature discipline in aircraft analysis, due to the development of many theories and analysis methods. However, fatigue is still considered a precarious phenomenon, especially when problems evolve beyond Constant Amplitude (CA) loading. Estimating the fatigue response of a single stiffened panel is already complex, not to mention the fatigue characteristics of a full aircraft. Many methods require the aircraft construction to be known in detail in order to apply them. Thankfully, straightforward methods exist to obtain a first-order estimation of the fatigue performance of the structure. The relevant, albeit basic, theory and methods are described below which were used to evaluate the aircraft for fatigue failure in a preliminary fashion.

Firstly, the input for the fatigue analysis, the structural representation and load spectrum, are presented. Secondly, the approaches to model crack initiation and crack propagation failure in the structure are discussed.

6.2.1. Selected fatigue phenomena for design

Two main fatigue phenomena have been selected for the preliminary fatigue analysis of the wing-fuselage structure, described below.

Fatigue failure in an aircraft typically consists of a crack which grows until the structure can no longer perform its intended functions. Aircraft inspections are carried out to timely identify cracks and repair them before they reach a critical length. Therefore, the crack may not grow to a critical size before being successfully identified in an inspection. The crack propagation life is modelled to ensure failure is unlikely to occur in the selected amount of flight cycles. The crack propagation approach is presented in section 6.2.5.

While cracks are allowed after some time in some structures (typically repairable, fail-safe structures), other structures may not develop cracks during any part of the intended life. The effects of a crack to cause either safety or economical damage that would be too substantial to allow. The initiation of cracks must then be prevented to ensure the aircraft can complete its operational life. For the primary structure of the aircraft, this consideration is especially relevant, as the repair of primary structures is particularly undesirable. Furthermore, in high-cycle fatigue applications, crack initiation typically covers the majority of the total fatigue life. Therefore, the crack initiation period should be well-matched with the number of goal flight cycles. The crack initiation modelling approach is presented in section 6.2.4.

6.2.2. Selection and representation of structures

Structures selected for fatigue analysis

The first structures that have been selected are all skin structures, both outer skins and cabin structure skins. These structures are typically prone to fatigue failure, and there are large consequences if they fail. Secondly, due to the high bending stresses in the frames, the frame flanges have also been included in the fatigue analysis. Stringers were excluded from the fatigue analysis. This is the case as the stringers are under lower tensile stresses than the skin, and their failure has a lower impact on the full system safety.

Representation of structural components

To apply the fatigue modelling methods, the different structural components have been treated individually. In other words, interactions between the different types of structural components have not been modelled. The structural representation is schematically shown in figure 6.1. The structures are naturally attached to each other, by means of fasteners. For the skin, there are rows of holes in longitudinal and hoop direction, as they are attached to other skin panels, frames and stringers. Logically, the skin is under combined loading: under biaxial stresses and shear. The frames are assumed to only possess one row of fasteners along its length. Therefore, the frames are considered to be in a uniaxial stress state. The frame outer flange (pointing outwards from the cabin centre) is attached to the skin, and therefore it contains fastener holes. The inner flange is assumed to not possess any holes.

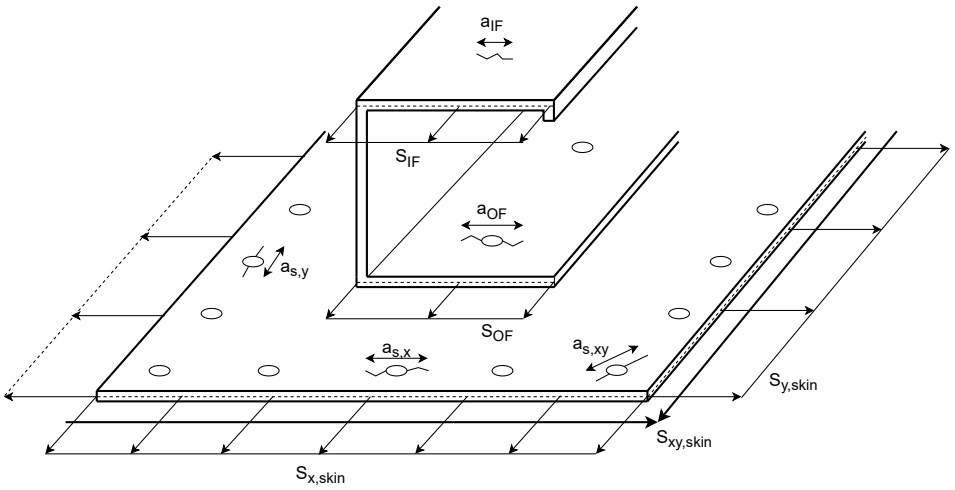

Figure 6.1: The evaluated crack cases in the skin due to axial and shear stresses, the frame outer flange (OF) and the frame inner flange (IF).

The skin, the frame outer flange and the frame inner flange are all represented as plates. This is visualised in figure 6.2. The skin panel is assumed to be very large, such that the crack size remains small compared to the size of the panel during the crack growth life. For the frame flanges, this is not the case, as the crack is of comparable size as the flange width.

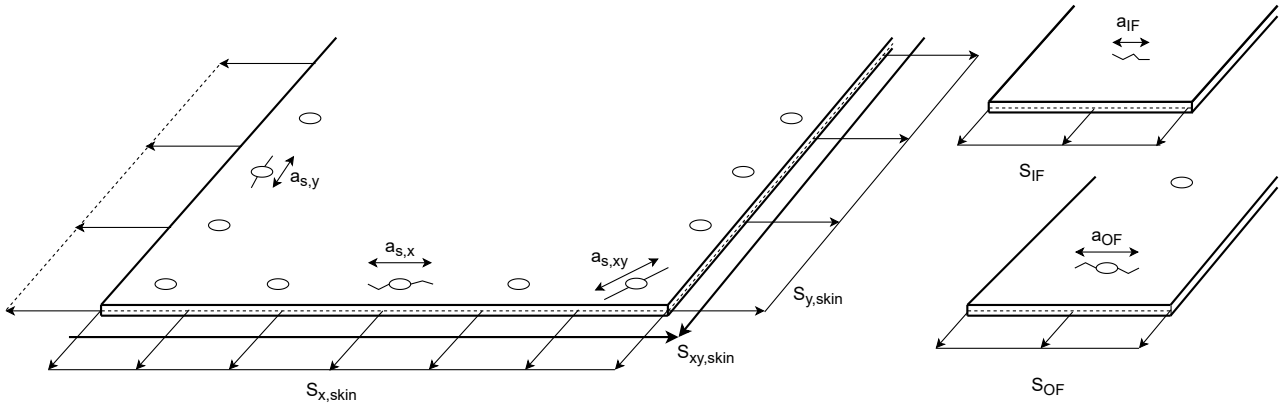

Figure 6.2: Representation of the evaluated fatigue structures as independent plates.

2-dimensional cracks It is assumed that only 2-dimensional "through" crack problems may be considered. Therefore, we are only concerned with the crack propagation in the 2-D plane.

Hole size In aerospace structures, many different fastener sizes are used for different applications. However, one of the most widely used fasteners is the AN4 airframe bolt. It possesses a quarter inch diameter (6.35 mm). It is assumed that this diameter is representative for all joint holes in the structure.

Representation of combined stresses

The skin panels are under combined loading, i.e., in hoop direction, longitudinal direction and shear. This has significant consequences for both the crack initiation and crack propagation approach.

Combined loading in crack initiation For crack initiation, combined loading has a significant effect on the value of the stress concentration factor, especially when the stresses are of comparable magnitude.

Ideally, the stress concentration factors should be superimposed all around the holes. This is straightforward for biaxial stresses are their minima/maxima are at the same locations. The stress concentrations induced by shear also impose a stress state which may be superimposed onto the biaxial case. However, the tangential stress distribution due to shear has peaks rotated 45 degrees from biaxial peaks. The maximum

may be determined for this stress state, which requires the magnitudes of the applied stresses. As the degree of stress reversal differs per load, upon unloading, the distribution of tangential stresses is completely different. Due to the different combination of biaxial and shear stresses, the location of maximum stress is also in a different location. Furthermore, bearing stresses are not even considered. It quickly became clear that the determining a superimposed stress concentration under combined loading in joints was a precarious task.

A second option was to work with the principal stresses. However, similar problems are encountered, in that the maximum stress location around the hole moves depending on the flight or ground stress state. Again, bearing stresses could also not be implemented. Therefore, a simplified approach was followed:

The combination of different stresses has beneficial and detrimental effects in terms of the stress concentration, depending on the magnitudes. It was hypothesised that the biaxial stresses are of primary concern, and the shear stresses would have a relatively minor effect on the superposition of stress concentrations: Firstly, the shear stresses were expected to be smaller than the axial stresses. Secondly, due to the 45-degree offset, the axial-shear interaction was considered to be small. Then, assuming the biaxial stresses and the shear stresses can be considered separately, one further decoupling step was made. If biaxial stresses have the same sign, the result is a reduced SCF, while the inverse is true for stresses with different signs. So, for the keel skin panel, which experiences biaxial tension, the SCF is reduced. The inverse is true for the crown skin panel. Overall, the whole structure experiences as much beneficial as detrimental biaxial stresses. Therefore, not considering the interaction on a global level is assumed to result in a representative weight estimation. The result is that regions which have biaxial stresses of the same sign will be over-designed, while regions with opposite signs will be under-designed.

For the bearing stresses, the following rationale was considered: The stress state of two neighbouring panels is very similar, due to similar (pressure-induced) hoop stresses, and similar longitudinal stresses at the joint. Therefore, joints along the hoop direction practically only transfer longitudinal stresses, as the neighbouring plate will have a similar stress state in the hoop direction. Conversely, this is true for joints along the longitudinal axis, which mainly transfer hoop stresses. The assumption is that only evaluating these longitudinal or hoop stresses at their respective joints will still result in a representative first-order approximation of the fatigue behaviour.

However, this reasoning is flawed for the FV structure, as the joints at the vertices possess a complex stress state with significant stresses in both directions. However, maintaining this assumption does not necessarily lead to an unconservative estimate. The bottom skin will experience high tensile loads in both hoop and longitudinal direction. Due to the biaxiality effect, the SCF will be lower than if these cases were considered separately. Therefore, making this assumption will lead to conservative estimates for the bottom skin panels. For the top skin panels, the inverse is true. During flight, high tensile stresses are expected in hoop direction, while large compressive stresses are expected in the longitudinal direction. A larger SCF is the result, which will make this estimate unconservative for the top panels. While locally the estimate may thus be (un)conservative, the overall design against fatigue is considered to still be representative.

The above reasoning and consequent assumption for omitting the biaxiality effect in the determination of the SCF should be viewed as simplistic. In particular, the stress state at the vertex joints requires a much more thorough analysis. However, this is considered out of the scope of this research and is therefore not pursued. A significantly more detailed design of the structure is required to do this, which is currently far from available. However, this is clearly identified as a research need.

Combined loading for crack propagation Similarly to crack initiation, biaxiality plays a significant role when a crack is very small. For small cracks originating at a stress concentration, the stress intensity factor depends on the stress concentration factor, as shown in equation 6.15. For biaxial loading where both loads are tensile, a reduction factor can be determined in a straightforward manner. However, this reduction factor becomes much less applicable when the crack is large relative to the hole or notch, as the stress field differs more from a normal hole. It follows that the reduction factor reduces as the crack grows. Once the crack is of similar magnitude to the hole (or notch) radius, the reduction factor is negligible. For the performed analysis, the reduction factor was not considered. This was considered to be slightly conservative. In the case of the analysis, a reduction factor could be calculated at the bottom skin, which experiences

biaxial tension. On the other hand, the top skin experiences tension and compression, which would cause K to increase. However, as the peak tensile loads are higher on the bottom skin, this is more critical. By not taking it into account, the effect would be a slightly conservative overall estimate.

Fatigue-prone regions in the structure In regular aircraft, the lower wing skin panels and the fuselage top panels experience the greatest amount of fatigue-related issues. High tensile stresses during flight are combined with significant compressive stresses during landing and ground operations, leading to a high stress amplitude with high tensile peak and mean stress. In principle, the same reasoning may be applied to the Flying-V. However, there are a number of additional considerations.

The outboard wing generates a relatively high amount of lift, while the inboard wing possesses a relatively high weight. Therefore, the outboard wing induces a high bending load, while the inboard wing reduces this load during flight. Therefore, for the longitudinal stresses, the fatigue-prone area is expected to be on the lower skin, towards the aft of the cabin. For the cross-section stresses, the pressurisation induces high tensile stresses in the crown, keel and walls. These are the regions where fatigue is expected to be critical.

6.2.3. Variable amplitude load spectrum representation

The selected fatigue analysis methods apply exclusively to CA loading. However, structural components undergo very different stresses during operations, which alters the fatigue behaviour significantly. Many theories and methods exist which describe and estimate the effects of variable amplitude loading. However, in this research, it is not feasible to approach variable amplitude loading in a detailed manner. This would require a more detailed understanding of the FV construction, which is currently unavailable. In order to ensure feasibility, the Variable Amplitude (VA) spectrum was condensed into a representative number of discrete CA cycles.

This set of discrete CA load cycles was determined with the following approach. The number of flight cycles was estimated by collecting design flight cycle data of reference aircraft, illustrated in the next paragraph. Following this, a method was proposed to describe the loads experienced by the aircraft in a flight by a single cycle. Following this, an estimation method is presented for the stress amplitudes experienced by the structures during the operational life.

Number of flight cycles estimation

In order to establish the number of loads which are experienced by the aircraft, the expected number of flight cycles were determined. In order to estimate the number of flight cycles, reference data was collected, mainly from *Airbus* and *Boeing*. Design data from *Airbus* aircraft may be found table 6.1. It should be noted that the presented flight cycles and flight hours in the first two data columns are specified as the Design Service Goal (DSG). The DSG is an operating limit up to which the maintenance programme has been validated. According to *Airbus*, the DSG is defined as:

"The reference figure used for design and justification for Type Certification. It reflects the utilisation of the aircraft model for about 20-25 years of the expected aircraft service." (Turrel and Auriche [42])

As stated by Airbus, this term should not be confused with the Limit of Validity (LoV), which is unrelated. According to the FAA, the LoV is:

"The LoV is the period of time (in flight cycles, flight hours, or both), up to which it has been demonstrated that Widespread Fatigue Damage (WFD) is unlikely to occur in an airplane's structure by virtue of its inherent design characteristics and any required maintenance actions." (FAA [43])

Unfortunately, the design flight cycles of the most applicable reference aircraft, the A350, is unavailable. The A330 and A340 models show some relevant data which should be comparable to the desired amount of cycles for the FV. As the A330neo is the most modern model, with a very comparable mission to an A350, its LoV of 33,000 is deemed most appropriate. While the range of the A380 is comparable, it was designed per the hub-to-hub philosphy. Therefore, the number of DSG cycles is lower than the A330 or A340 models.

Table 6.1: Airbus aircraft flight cycle data.

Aircraft Type	DSG [cycles]	DSG [hrs]	LoV [cycles]	MTOW [tonne]	Range [km]	Year
A300 B2	48,000[44]	52,000	60,000[45]	142[46]	3,400[46]	1974
A300 B4-100/200	40,000[44]	53,000	57,000[45]	157.5/165[46]	5,400[46]	1979
A300-600	30,000[44]	67,500	30,000[45]	172[47]	7,500[47]	1974
A310-200/300	35,000[44]	60,000	40,000[45]	144/164[48]	6,500/9,500[48]	1983
A320 family	48,000[44]	60,000	48,000[45]	68-93.5[49]	5,740-6,940[49]	'87-'05
A330-200/300	40,000[44]	60,000	40,000[45]	242[50]	13,450/11,750[50]	1992
A330neo	33,000[44]	100,000	33,000[45]	251[50]	13,300-15,100[50]	2018
A340-200	20,000[44]	80,000	30,000[45]	275[51]	12,400[51]	1993
A340-300	20,000[44]	100,000	20,000[45]	276[51]	13,500[51]	1993
A340-500/600	16,600[44]	100,000	16,600[45]	380[52]	16,670/14,450[52]	2002
A350-900	N/A	N/A	N/A	210-280[40]	15,500[40]	2013
A380-800	19,000[53]	N/A	N/A	575[54]	14,800[54]	2007

Design data from *Boeing* aircraft may be found in table 6.2. DSG data was not available for reference. As the LoV is required for certification by the *FAA*/*EASA*, and it is equal or higher than the DSG FC set for *Airbus* models, the LoV is used as reference parameter.

Unfortunately, similar to *Airbus*, the most comparable *Boeing* model, the 787, was not available. It may be noted that *Boeing* aircraft possess a higher LoV than their *Airbus* counterparts. The *Boeing* aircraft (for which data was available) most similar to the FV are the 777 family models and the newest 747 models. The 747-400/8 has comparable range, but is heavier than the envisioned FV. Its LoV is equal to 30,000 cycles. The 777 variants possess an LoV of 40,000 cycles. As the range of the 777 is lower than envisioned for the FV, one could argue that the 777 will experience more cycles during its life than the FV. Therefore, the 40,000 cycles is likely more than should be expected of the FV.

Table 6.2: Boeing aircraft flight cycle data.

Aircraft Type	LoV [cycles]	MTOW [tonne]	Range [km]	Year
737 NG/MAX	75,000[45]	65.5-88.3[55]	5,440-7,130[55]	1997-2017
747-400/8	30,000[45]	413-485[56]	14,200[56]	1989-2012
757-300	50,000[45]	124[57]	6,295[57]	1999
767-400ER	50,000[45]	104[58]	10,415[58]	2000
777-200(ER)/-300	40,000[45]	247-299[59]	9,700-13,100[59]	1995-1997
777-300ER/-200LR	40,000[45]	348-351[60]	13,650-15,850[60]	2004-2006

A reference LoV was selected based on the reference data. Clearly, short-range narrow-body aircraft should be able to withstand more flight cycles for a certain amount of flight hours, as the flights are much shorter. The presented data of *Airbus* and *Boeing* describes trends based on mission specification quite well, even though data from the most comparable aircraft is unfortunately missing. From the available data, the LoV was assumed to be 40e3 flight cycles, excluding safety factors. The most representative aircraft from the table average at approx. 35e3 cycles. However, due to the lack of data for the most representative aircraft, an increase to 40e3 cycles was made, which was also chosen to simplify VA calculations, as will become apparent in following paragraphs.

Load phases Variable amplitude loading is experienced in the different operational phases of the aircraft. However, these variations are not easily implemented. To simplify the loads experienced by the FV, the different load phases were investigated. The different phases of a single flight are shown in figure 6.3. This figure qualitatively represents the stresses experiences by the wing or pressurised fuselage.

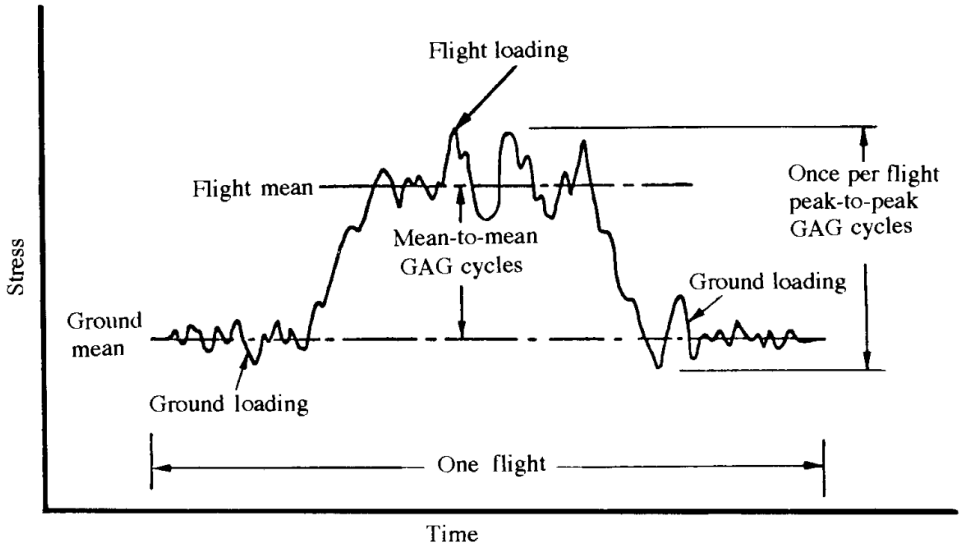

Figure 6.3: Ground-Air-Ground loading, Niu [16].

On the ground, loads occur due to taxiing, gusts and braking. There is no pressure difference inside the pressure cabin, so the pressure loads are zero. During take-off, the aircraft is still very heavy, and positive load factors are experienced by the rotation and ascent. As the air is typically more turbulent at lower altitudes, significant oscillations may occur in the loads. During cruise, an obvious constant load of +1 g is experienced by the aircraft. Manoeuvring and gusts increase this load. During landing, the aircraft experiences loads due to runway impact and braking. During landing it is assumed that the pressure difference of the cabin w.r.t. the ambient air is zero.

The scope of this thesis does not allow for the evaluation of a VA spectrum in different flight phases. Depending on the value of a load, it may contribute greatly to the initiation of cracks in the structure, or not at all. Both crack initiation and crack propagation scale very nonlinear in terms of introducing/progressing damage (i.e., the damage induced by larger amplitudes eclipses the damage induced by much smaller amplitudes). However, this statement may only be made if the large amplitudes are in the context of high-cycle fatigue. In the case of high-cycle fatigue, smaller amplitudes require a tremendous amount of cycles before fatigue failure occurs, or may never occur at all, if below the fatigue limit. While there is no definitive boundary for low-cycle or high-cycle fatigue, is is generally considered when more than $10^4 - 10^5$ cycles occur, according to Schijve [17]. There are some caveats to the preceding statements, which are indicated in their respective reasoning steps in the following sections.

In the context of fatigue analysis, the stress amplitude is far more important in driving failure than the mean stress. The largest stress amplitude is experienced once by the structure during a single flight, also known as the Ground-Air-Ground (GAG) cycle. Therefore, the loads experienced in a single flight will be condensed in a representative CA spectrum, based on the GAG cycle. According to Niu [16] (Ch.15.0, p. 660), this is a good assumption in this stage of design:

"The use of GAG load cycles provides a relatively rapid means for establishing the permissible design ultimate tension stress for preliminary sizing of structures subjected to complex spectra of loading. The GAG load cycle is a measure of the severity of the anticipated loading spectra and it produces the same fatigue damage to the structure as would be produced if the complete spectra of loading were considered."

The ground-air-ground (GAG) cycle typically causes low stresses during ground operations, while it causes very high tensile stresses during flight (in the wing bottom panel and pressure cabin). The highest and lowest stress do not need to occur in consecutive cycles to act as a single amplitude [17]. Therefore, applying the maximum/minimum stress experienced during the GAG cycle as one cycle is considered acceptable.

Both crack initiation and crack propagation scale very nonlinearly in terms of introducing/progressing damage (i.e., the damage induced by larger amplitudes eclipses the damage induced by small amplitudes). However, this statement may only be made if the large amplitudes are in the context of high-cycle fatigue.

In the case of high-cycle fatigue, smaller amplitudes require a tremendous amount of cycles before fatigue failure occurs, or may never occur at all, if below the fatigue limit. There are some caveats to this statement, which are indicated at their corresponding reasoning steps in the following sections. However, the ample substantiation to treat the fatigue load spectrum as the extremes from the GAG cycle led to a high confidence in the applicability of this method.

The GAG cycle of the FV was assumed to be comparable to the standardised load spectrum of TAW aircraft, with a number of corrections. Research performed by Jonge et al. at NLR [2], led to the creation of a standardised load spectrum for the lower skin panel at the root of the wing. Stress data was collected for high amount of flights for a set of 9 aircraft, during normal operations. For simplicity, the data was discretised into a small amount of load levels, as may be found in figure 6.4. Note that the loads are expressed as stresses normalised with the mean flight stress. This mean flight stress is the case when the aircraft is in steady flight, without any load amplitudes caused by gusts or sudden control inputs. This case may be represented by $n_z = 1$ during cruise. An important assumption was made by the researchers in this piece of research. Namely, that the flight stress distribution is similar to the ground stress distribution in the wing. This is not the case for the FV. During flight, the wing is stressed significantly different than on the ground. This is the case as the landing gear is attached far along the wing-fuselage, while for the reference aircraft, the landing gear is attached to the fuselage / wing root. This poses a difficulty in continuing with the data. However, The stress distribution of the FV on ground is more favourable than for regular wings, as it is supported more by the landing gear. The area between the nose and main landing gear is very well supported, and experiences low bending loads. The outboard wing experiences a negative bending load on ground, like a regular wing. While the stress distribution on ground is different from the reference data, there was no apparent other manner to construct a load spectrum. Therefore, it was decided that the standardised load spectrum could be applied to the FV. As the stresses on ground are in reality more favourable, applying this approach would yield a conservative approach. In the hoop direction, the stresses are virtually unaffected. Due to the large arc radii, the hoop stresses are expected to be relatively high. As these stresses will consequently be driving the fatigue analysis, the approach is considered acceptable.

Exceedance frequency per 400000 flights	Loads in airborne condition $\frac{S_m}{S_{m_{flight}}} \pm \frac{S_{a_{flight}}}{S_{m_{flight}}}$	Loads in ground condition $\frac{S_{m_{ground}}}{S_{m_{flight}}} \pm \frac{S_{a_{ground}}}{S_{m_{flight}}}$
10^1	1.0 ± 1.600	- 0.3 ± 0.244
10^2	1.0 ± 1.215	- 0.3 ± 0.207
10^3	1.0 ± 0.916	- 0.3 ± 0.165
10^4	1.0 ± 0.628	- 0.3 ± 0.133
10^5	1.0 ± 0.419	- 0.3 ± 0.096
10^6	1.0 ± 0.247	- 0.3 ± 0.071

Figure 6.4: Standardised load spectrum [2].

Aircraft weight of airborne condition In order to determine the stresses in the structure, a weight needed to be assigned to the aircraft. In the context of fatigue analysis, the nominal operating weights should be applied, instead of extremes. In the case of payload, a nominal payload would consist of passengers + luggage, without additional cargo. This assumption has been made as the FV is envisioned as a passenger transport rather than cargo transport. However, the weight and its distribution vary significantly over the

course of the flight due to fuel burn. As the data is expressed in terms of mean stress, it is assumed that this is associated with the mean weight. While the weight does not vary linearly over the course of the flight, for simplicity, it is assumed that half the design fuel weight is burned. While the aircraft would burn more fuel at the first stages of the flight, due to its heaviness, take-off and climb, there also needs to be a considerable amount of reserve fuel. Therefore, taking half of the design fuel weight is considered to be an acceptable assumption.

Pressurisation A second consideration is pressurisation. For all reference aircraft, the wing is not pressurised for obvious reasons. However, for the wing-fuselage, the pressurisation plays a large role. As linear stress analyses are performed, the pressurisation stress can be linearly superimposed to a stress solution with an unpressurised cabin. An unpressurised FV is considered analogous to a TAW wing. Therefore, to determine the stresses in the structure, the unpressurised stresses are multiplied by the factors as indicated in the standardised load spectrum, to obtain the unpressurised stress values. the pressurisation stress is consequently added to the flight case to obtain the maximum flight stresses. Pressurisation is considered to be zero during ground operations throughout the entirety of this research. Therefore, no stress superposition is necessary on ground. This approach is visualised in figure 6.5.

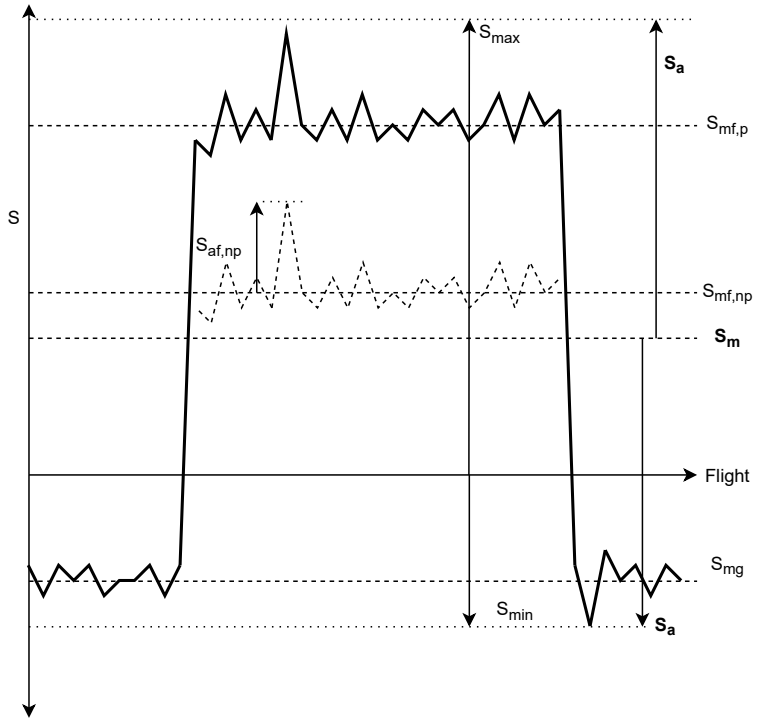

Figure 6.5: Determination of the mean stress S_m and stress amplitude S_a.

The pressurisation level for fatigue analysis was the nominal cruise pressure, multiplied by the fatigue analysis safety factor of 1.15, as per CS.25.571b(i)(ii) [41], which may be found in Appendix E. According to CS25, a separate analysis needs to be performed on the fuselage pressurisation, omitting other loads and multiplying the pressurisation level by 1.15. In this research, these analyses were performed simultaneously. This is a harsher treatment, but similar results are expected.

Constructing load cycles

All the required information was obtained to construct the representative CA load cycles for the crack initiation and crack propagation period. However, both methods require a different approach. Therefore, the specific load cycles that were used for the crack initiation analysis and crack propagation analysis are presented below.

Load cycles for crack initiation analysis To assess the fatigue life of the VA loaded Flying-V structure, the linear cumulative damage accumulation hypothesis was applied, also known as the Miner rule, shown in equation 6.5.

$$\sum_{i=1}^{n} \frac{n_i}{N_i} = 1 \tag{6.5}$$

At the core, applying the Miner rule allows to assign a damage fraction from all different type of load cycles, and decoupling any sequence effects. This greatly simplifies the analysis, and allows for straightforward application of the stresses obtained from the standardised load spectrum. However, this approach has its shortcomings.

Firstly, with this rule, amplitudes below the fatigue limit do not contribute to damage accumulation. However, if a crack has already nucleated, these small cycles may lead to failure. Therefore, the error associated with a steep spectrum (i.e. many cycles below fatigue limit) is higher than for a flat spectrum. In the case of this research, the low amplitudes have already effectively been removed by using the standardised load spectrum. Additionally, for aluminium alloys the SN-curve, as discussed in the next paragraph, may be extended past the fatigue strength. In this research, this was done to obtain a cautious estimate of the fatigue performance.

Secondly, sequence effects are not included. Low cycles are retarded successfully by plasticity induced by overloads. In aircraft operations, this typically leads to a favourable effect. In the case of the standardised load spectrum, there are a number of significant overloads, which are likely to cause significant crack growth retardation. However, in this research, sequence effects, or mean sequence effects are not considered. This affects the calculated fatigue life unfavourably, and therefore, the estimations are prudent.

Applying the standardised load spectrum The standardised load spectrum was based on 400e3 cycles, as seen in figure 6.4. The shown cycles indicate the frequency and the magnitude of the air and ground phase of the different cycles. As the operational life of the FV was estimated at 40e3 cycles, the 40e3 most severe cycles in the spectrum were used for calculations. This means that the load cycle in the top row is applied once, the second row applied 10 times, down to row 5, which is then applied 28.9e3 times.

Using the Miner rule, the failure index for crack initiation was determined for every element as follows:

$$FI_{CI} = \frac{1}{N_1} + \frac{1e1}{N_2} + \frac{1e2}{N_3} + \frac{1e3}{N_4} + \frac{1e4}{N_5} + \frac{2.9e4}{N_6} \tag{6.6}$$

To determine mean stress and stress amplitude, the approach shown in figure 6.5 was followed. The unpressurised and pressurised flight stresses were computed at n=1. From the unpressurised stresses, the airborne load ratio was used to determined the maximum unpressurised stress, after which the pressurisation stresses were superimposed. The ground stress state was approximated by multiplying the unpressurised airborne stress by ground load ratio. These two stresses represented the maximum and minimum stress in the element, not necessarily in that order. From the maximum and minimum, the mean and amplitude were easily determined. With the obtained input stresses, the performed calculations to obtain N_1 to N_6 are shown in the following paragraphs.

Load cycles for crack propagation The load spectrum used for crack initiation was not compatible for the crack propagation analysis, as the procedure only works for constant amplitude cycles. In order to obtain a representative CA cycle, the weighted mean flight factor and ground factor were determined:

$$FF_{mean} = \frac{[(1.0 + 1.600) * 1e0 + (1.0 + 1.1215) * 1e1 + ... + (1.0 + 0.247) * 2.89e4]}{40e3} = 1.301 \tag{6.7}$$

$$FG_{mean} = \frac{[(-0.3 + -0.244) * 1e0 + (-0.3 - 0.207) * 1e1 + ... + (-0.3 - 0.071) * 2.89e4]}{40e3} = -0.379 \tag{6.8}$$

The amplitude and mean stress were calculated identically as shown in the crack initiation section. It was

assumed that a weighted mean would lead to a representative result. While the crack growth scales with the exponent n_f, including this was deemed over-conservative. High loads cause significant crack growth retardation due to their induced plasticity, which is not considered in this research. Applying a mean value scaling with the exponent n_f would only lead to an overcautious design.

6.2.4. Crack initiation life

The modelling approach of crack initiation is illustrated in the following subsections. In order to show a streamlined approach, the fundamentals of crack initiation mechanics have been omitted.

SN-curves To estimate the crack initiation life of the selected structures, SN-curves were applied. The upper knee value was assumed to be located at $N = 10^2$ cycles for the applied aluminium alloys, and is assumed equal to the static ultimate tensile strength of the material.

In to order to construct a lower knee, high cycle fatigue strength data was obtained from *Handbuch Struktur Berechnung* [19], this data can be found in B. To construct the equation describing the fatigue strength as a function of cycles, Basquin's relation was used. The obtained material data applied to fully reversed loading of an unnotched structures. Therefore, the effects of the stress ratio and stress raisers were determined.

Stress ratio For the Flying-V structure, the stresses are not fully reversed, and thus a correction to the fatigue curve was applied. The Goodman relation describes a linear relation between the decrease in S_f for an increase in mean stress, as seen in equation 6.9. The relation between S_m and the strength can be observed in figure 6.6.

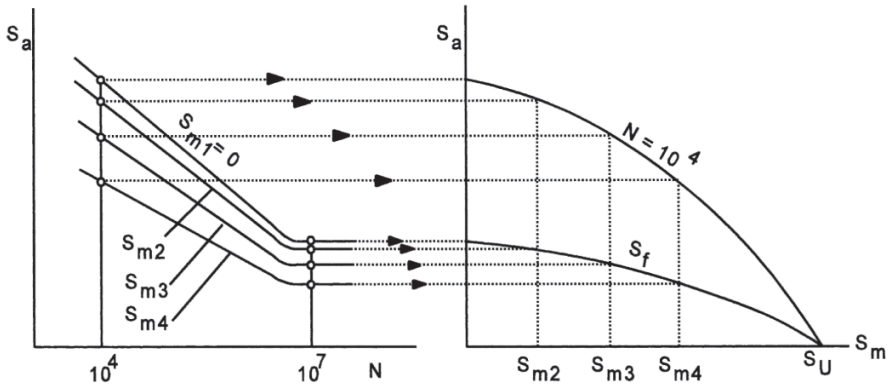

Figure 6.6: Fatigue strength for varying S_m Schijve [17].

$$\frac{S_f}{(S_f)_{S_m=0}} = 1 - \frac{S_m}{S_U} \tag{6.9}$$

The Goodman curve represents a conservative correction and is typically applied to brittle materials. As high-strength alloys often show limited ductility, these adhere better to the Goodman relation. It was considered that the chosen alloys belong to this group, and are thus best represented by the Goodman relation.

Stress concentrations

In practical design against fatigue failure, and crack initiation in particular, one of the main challenges is to address stress concentrations. As a first approximation, analytical methods are used, which can be very useful in the conceptual design stage. Estimates of many types of SCFs for holes and notches, as well as SCFs due to interaction of stress concentrations, can be found in literature. However, to obtain an accurate estimate, detailed knowledge of the design is required. As the goal is to obtain a first order estimation of the fatigue, a more generalised approach for the SCF was applied, namely the fatigue severity factor (FSF). Before discussing the workings of the FSF, a number of SCF-related topics are discussed which are important to consider to obtain an understanding of their potential effect to the solution.

Fatigue Severity Factor In order to determine a stress concentration for all structures, a relatively detailed amount of knowledge on the size and construction is required. As this was not available, a blanket solution has been applied in the form of the Fatigue Severity Factor, a method by Niu [16]. Effectively, the fatigue severity factor includes a larger number of variables to obtain the performance of the structure beyond the sole application of the SCF. The FSF is defined as follows:

$$FSF = \frac{\alpha\beta}{\sigma_{ref}}\left(\sigma_{bearing} + \sigma_{bypass}\right) = \frac{\alpha\beta}{\sigma_{ref}}\left(K_{tb}\theta\frac{P}{dt} + K_{tg}\frac{P}{wt}\right) \tag{6.10}$$

Where the shown terms represent the following:

- α is the hole/surface condition factor, which is an empirical factor increasing or decreasing the stress severity based on the production method. For holes, a standard drilled hole has the value 1.0. Reamed holes reduce this to 0.9, due to the improve surface quality. Cold worked holes greatly reduce this factor (0.7-0.8 [21]), as favourable residual stresses are imposed on the structure. The plasticity induced by cold hole expansion imposes a residual compressive stress region around the hole which effectively resists the growth of cracks.
- β is the hole filling factor, another empirical method which describes the effect of the type of fastener on the local stress state. Without a fastener, this factor is 1, but with fasteners, this factor ranges from 0.9-0.5.
- σ_{ref} is the infinite reference stress. The two terms in the brackets represent the bearing and bypass load contributions, respectively. K_{th} is the bearing SCF, K_{tg} is the bypass SCF, P is the applied load, d is the hole diameter, t t is the plate thickness and w the panel width. As mentioned before, obtaining these SCFs is not straightforward, as the design has not advanced enough.

Fortunately, Niu has recommended that including all above parameters lead to a minimum FSF of 4.0 for real structures, with a practical design factor of 4.5. Therefore, it is assumed that the application of an FSF of 4.5 will lead to a representative fatigue behaviour. Niu's recommendation of a factor of 4.5 is not a very thorough substantiation. To assess this assumption, the sensitivity of the solution to this factor is analysed in section 9.2.5. It may be noted that Niu's recommended method is presented in 1988-dating book. In the 30+ years since, manufacturing and detail design methods have improved significantly, primarily due to the availability of advanced FEM software. Therefore, the FSF of 4.5 is considered to be a realistically attainable value. The FSF of the evaluated shear stresses was multiplied by a factor 4/3, to account for the higher shear-induced SCF at holes. These factors were applied to the skin and the frame outer flange for crack initiation analysis.

For the frame inner flange, it was assumed that no holes are present. However, stress raisers were not excluded. A FSF of 2.0 was assumed for the inner flange. This is substantially less than the FSF for holes, but this accounts for imperfections or limited damage. While this has no physical substantiation, it is assumed that this is an acceptable first-order approximation.

Fatigue strength The notched fatigue limit, may then be determined as follows:

$$S_{fk} = \gamma\frac{S_f}{K_t} \tag{6.11}$$

Where $K_t = FSF$ It should be noted that the obtained value is an approximation. The notched fatigue limit may differ significantly from the value obtained above, as it this method is simply based on reducing the unnotched fatigue limit. According to Schijve [17], the approximation improves greatly if data is used with a K_t close to the K_t of the structure. Now that the fatigue limit has been found, the upper and lower knees may be connected by Basquin's relation. The strength at a number of cycles may then be determined as follows:

$$\frac{S_{up}}{S_x} = \left(\frac{N_x}{N_{up}}\right)^m \tag{6.12}$$

where the subscript $_{up}$ indicates the value at the upper knee, subscript $_x$ indicates the value of interest. The exponent m is determined by the following relation:

$$m = \frac{log\left(\frac{S_{up}}{S_f}\right)}{log\left(\frac{N_f}{N_{up}}\right)} \tag{6.13}$$

For the load cycle set, the fatigue life was determined. Using the Miner rule, the failure index was consequently determined.

6.2.5. Crack propagation life

While cracks are preferably avoided in any structure, cracks may be allowed to some degree to relax the measures taken to prevent crack initiation. The resulting lighter structure offers advantages in terms of weight and thus cost. The second reason to consider crack propagation is that even when properly designed against crack initiation, cracks may still form in a structure. Cracks may occur due to manufacturing defects, damage during manufacturing and operations, improper maintenance, corrosion, etc. Therefore, the behaviour of the crack must be such that failure may not occur during service for a reasonable amount of time, and that the crack may be adequately identified during maintenance to be repaired. The applied approach treated in the following subsections.

Stress intensity factor

In order to describe crack growth after initiation has taken place, the stress concentration factor can no longer be applied to describe the stress field. As the radius of a crack tip is essentially zero, the stress concentration factor would go to infinity, and therefore it loses its physical meaning. The Stress Intensity Factor (SIF) was introduced by George R. Irwin to address this problem [61]. The derived relation of the stress intensity factor K is shown in equation 6.14.

$$K = \beta S\sqrt{\pi a} \tag{6.14}$$

Where S is the applied stress, a is the crack length and β is a geometry factor. This geometry factor varies significantly in value, depending on the context of the crack. The geometry correction factor β addresses the finite dimensions of the structural component containing the crack. For an infinite sheet, $\beta = 1$. As the skin is considered to be much larger than the crack during any time in the crack propagation life, $\beta = 1$ for the skin cracks.

A useful relation was determined for an edge crack originating at a notch. When the crack is very small compared to the notch, the crack can be assumed to be in the highly stressed region caused by the notch. The peak stress here is σ_{peak}, which is equal to $K_t S$. Equation 6.15 then logically follows. It must be stressed that this is only valid for a crack which is very small compared to the notch root radius. As cracks typically initiate at stress raisers, it is a very important relation to consider.

$$K = 1.1215 K_t S\sqrt{\pi a} \tag{6.15}$$

For a centrally cracked specimen, no exact solution could be determined. However, Feddersen [62] derived the equation below. According to Schijve [17], it agrees very well with FEM solutions, and is widely used.

$$\beta = \sqrt{sec\frac{\pi a}{W}} \tag{6.16}$$

Another relevant case is the SIF for a finite plate with a circular hole which contains two symmetric edge cracks. Using FEM, Newman [18] identified some interesting behaviour. For cracks which are very small compared to the hole radius, a good agreement was found with equation 6.15. However, when the crack length exceeds 10% of the hole diameter, the value of K is approximately equal to a single crack as long

as the sum of the crack length and the hole diameter. This is visualised in figure 6.7. In order to include the length of the hole, the effective crack length a_{eff} is introduced. Using the effective crack length with Feddersen's equation yields a practical approximation for crack originating at holes or cut-outs.

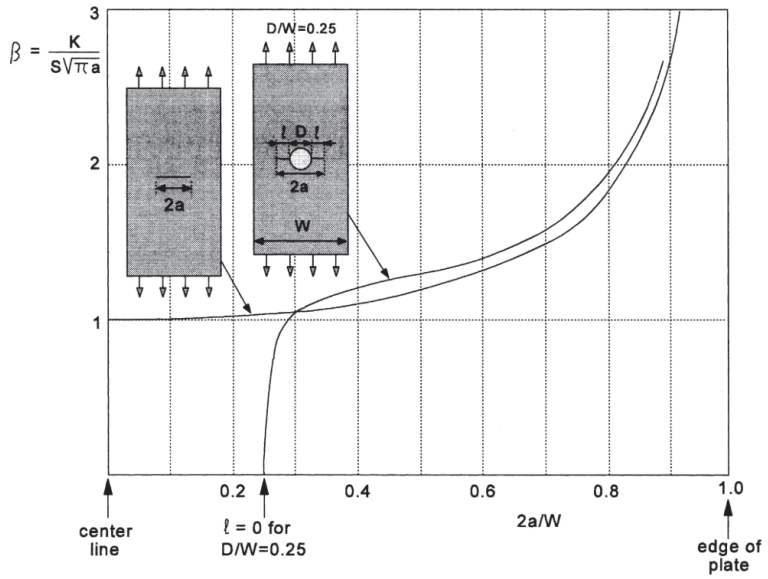

Figure 6.7: Geometry factor of a hole with two edge cracks and a central crack with the same length. Obtained from Schijve [17], visualised from data by Newman [18].

Newman's method was considered to be applicable for the skin and outer flange. For the geometry factor of the flange cracks, Feddersen's method for determining β was applied. However, as mentioned above, the initial crack size must be at least 10% of the hole diameter to obtain representative results. This condition is shown to be fulfilled in the following paragraphs.

Calculating the crack propagation life

For the crack growth calculation, the relation proposed by Forman et al. [63] was applied, as shown in equation 6.17. This relation includes the Paris region and the stable tearing crack growth region. Schematically, this is indicated in figure 6.8

$$\frac{da}{dN} = \frac{C\delta K^{n_f}}{(1-R)K_F - \delta K} \tag{6.17}$$

Where C and m are material constants, as may be found in B for the chosen alloys. Additionally, the stress ratio R is included in this relation.

$$\text{Region I} \quad \Delta K \leq \Delta K_{th}: \qquad da/dn = 0$$

$$\text{Region II} \quad \Delta K > \Delta K_{th}: \qquad da/dn = \frac{C_f \cdot (\Delta K)^{n_f}}{(1-R)\cdot K_f - \Delta K}$$

$$\text{Region III} \quad \Delta K \geq (1-R)\cdot K_f: \quad da/dn = \infty$$

$$\Delta K_{th} = A \cdot (1 - B \cdot R)^k$$

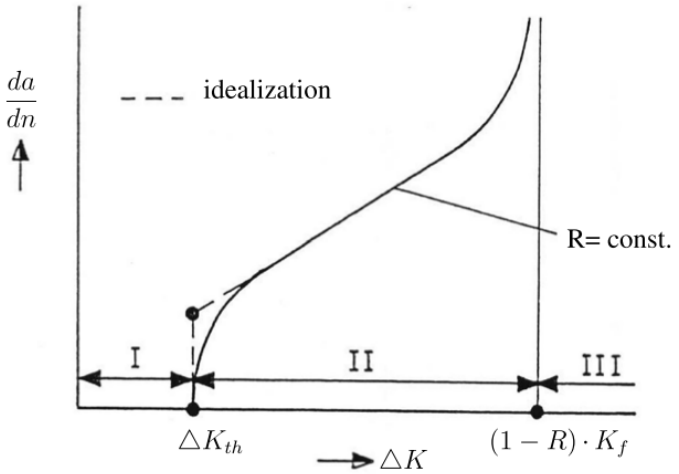

Figure 6.8: The Forman theory includes the stable tearing crack growth behaviour. Reprinted from *Handbuch Struktur Berechnung* [19], Ch. 63205-01, p.3.

Here the crack growth rate will tend to infinity as K approaches K_f. This effectively includes the threshold region. K_f is the Forman value, representing the fracture toughness, which was obtained from HSB [19] for both aluminium alloys. δK is the stress intensity range which may occur during flight. During flight, larger loads than nominal may occur, during which the structure may not fail. As the structure is significantly damaged at this state, it was deemed too conservative to consider the ultimate load to determine K_{max}. Instead, it is associated to the limit load, which must be withstood to prevent tearing to occur. Therefore, after every cycle, the limit load must be applied to check for residual strength.

As indicated above, δK is an important driver for crack growth. However, it makes sense to consider that no growth is possible when the crack is closed. This is the case when the crack tip is under compression. This can be either because the external applied stress is compression, or there are residual compressive stresses preventing the crack to open. The residual compressive stresses, from plasticity or manufacturing, were not considered in the analysis. However, applied compressive stresses were easily implemented into the analysis. The only alteration in the analysis is to replace the minimum stress S_{min} with zero if it becomes negative.

In order to approximate the number of load cycles for a crack to grow from barely visible (a_0) until failure (a_f), the following equation is applied:

$$N = \int_{a_0}^{a_f} \frac{da}{\left(\frac{da}{dN}\right)} \tag{6.18}$$

Substituting the Forman relation and the definition of K, this becomes:

$$N = \int_{a_0}^{a_f} \frac{(1-R)\,K_f - \delta K}{C \delta K^{n_f}} \qquad = \qquad \frac{1}{C \delta S^{n_f}} \int_{a_0}^{a_f} \frac{(1-R)\,K_c - \left[\beta \delta S \sqrt{\pi a}\right]}{\left(\beta \sqrt{\pi a}\right)^{n_f}} da \tag{6.19}$$

Initial crack size Important parameters to consider are the selection of a_0 and a_f. For small cracks, the majority of the crack growth life is spent remaining very small, as the crack growth rate heavily depends on the crack size itself. Therefore, changing a_f has a small effect on crack growth life, as the number of cycles for this growth is limited. On the other hand, changing a_0 has a large effect on the crack growth life. It is therefore important that this parameter is not chosen rashly. According to Schijve [17], the minimum crack size to apply the above calculations, depending on the material, is in the range of 1 - 3 mm. In the context of a crack propagation analysis, the crack is considered to be in the macro crack domain. While this is not explicitly defined, cracks which can be spotted without aids during inspection may be considered to be in the macro domain.

As described earlier, Newman's method is used to describe the crack behaviour originating at the holes in the skin and frame outer flange. A macro crack originating at a hole such that l/d > 10%, the hole size is included to obtain an effective crack size. As the hole is included in the effective crack size, the initial conditions change marginally if the minimum visible crack size were changed from 2 mm to 1 mm. Therefore, the solution is not very sensitive to the initial choice. A 1 mm initial crack size was assumed for the skin and the frame outer flange.

The insensitivity to the initial crack size does not apply to the inner frame flange. The difference in crack growth life is substantial by choosing a 1 mm over a 2 mm initial crack. However, changing the 1 mm to a 2 mm initial crack was deemed to be too strict for the inner flange. This is the case as the inner flange is straightforward to inspect during C/D-checks, as it is fully exposed on the inside of the cabin. Cracks originating at holes connecting the skin and frame inner flange are much harder to spot, as these cracks typically originate at the context surface, due to a bearing stress peak (as visualised in figure **??**. As this type of crack is not exposed, it could be missed much more easily during an inspection.

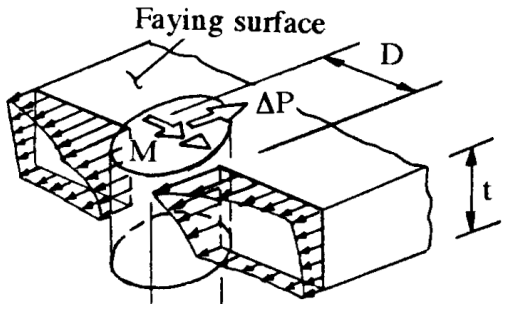

Figure 6.9: Local stress caused by fastener load transfer, with a peak at the faying (contact) surface. Reprinted from Niu[16], figure 9.12.11.

Maximum crack size To perform the cycles calculation, a minimum and maximum crack size needed to be set. Twice the initial effective crack size corresponds the length of the AN4 bolt hole and edge crack of 1 mm, so a_0 3.675 mm. The final crack size was determined to be the minimum of 2 options: a maximum preset length, or the length corresponding to the critical residual strength crack size.

For the skin, a crack of 100 mm was set as the maximum, which should be viewable from a pre-flight walkaround. While this size is relatively small compared to the large skin panel, a crack in a pressurised container is much more undesirable than in an unpressurised, but equally-stressed structure. out-of-plane load on the crack, rapid decompression, and ensuing effects are all not modelled, but may be catastrophic. Therefore, this was one critical length set for the skin. For the frames, the critical length was set at the width of the flange.

The second value for the critical crack size corresponds to the residual strength ($K_{lim} = K_f$):

$$a_f = \frac{1}{\pi}\left(\frac{K_f}{\beta S_{lim}}\right)^2 \tag{6.20}$$

Approximating the Integral The integral obtained in 6.19 is not solvable, as β is described by Feddersen's relation (equation 6.16). Therefore, the integral could not be evaluated. This normally means that the crack

growth calculation must be evaluated numerically. However, for this research, this would lead to an extreme runtime during sizing. Instead, it was opted to describe the behaviour by approximating the integral in equation 6.19. The assumption was that a reasonable estimation could be obtained by setting β to a constant value, which does not depend on the crack length.

Determining β As the crack remained very small compared to the skin panel, the geometry factor for the skin was set at 1.0.

For the frame inner and outer flange cracks, stresses were trialled to obtain an estimation of constant β. With the obtained bounds, a stress range set was determined at different values of dS. However, the factor R needed an assigned value. As the pressure-induced hoop stresses were expected to be dominant in providing frame stresses, R was set to 0. Furthermore, in order to apply Feddersen's relation (equation 6.16), a flange size needed to be set. It was hypothesised that the frame dimensions from Oosterom[13] would be far surpassed in the sizing approach, as explained in 1.4.4. From Oosterom's results, the frame weight was calculated to correspond to a flange width of approx 36 mm. It was deemed overly conservative to set the flange width at this value, as the frames are hypothesised to increase in size significantly. However, in order to remain somewhat cautious, a relatively small increase was used, with a flange width of 50 mm. This was a relatively unsubstantiated assumption. To ensure that

A numerical solution was determined for the set of dS using equation 6.17, and equation 6.23, while setting beta equal to a constant value ($1 \leq \beta$). A constant β showed different behaviour than the numeric solution; generally underestimating the life for high dS, and overestimating for low dS. A β was selected for both cases such that the same value of dS reached the goal number of cycles (40e3*SF). This resulted in a β of 1.680 for the inner flange, and 1.235 for the outer flange. The difference may be explained by the initial crack sizes of the two flanges.

Derivation of direct solution Having obtained the integral limits and β, this allowed for the following derivation:

$$N = \frac{1}{C}\int_{a_0}^{a_f} \frac{(1-R)\,K_f}{\beta^{n_f}\delta S^{n_f}\pi^{n_f/2}a^{n_f/2}} - \frac{1}{\beta^{n_f-1}\delta S^{n_f-1}\pi^{(n_f-1)/2}a^{(n_f-1)/2}} \tag{6.21}$$

introducing constants K_A and K_B:

$$N = \frac{1}{C}\int_{a_0}^{a_f} K_A\frac{1}{a^{n_f/2}} - K_B\frac{1}{a^{(n_f-1)/2}}\,da \tag{6.22}$$

which is equal to:

$$N = 2a^{-\frac{n_f}{2}}\left[\frac{K_B a^{\frac{3}{2}}}{n_f-3} - \frac{K_A a}{n-2}\right]|_{a_0}^{a_f} + C.O.I. \tag{6.23}$$

where:

$$K_A = \frac{(1-R)K_f}{C\beta^{n_f}\delta S^{n_f}\pi^{n_f/2}} \tag{6.24}$$

$$K_B = \frac{1}{C\beta^{n_f-1}\delta S^{n_f-1}\pi^{(n_f-1)/2}} \tag{6.25}$$

The constant of integration is zero as there should not be any crack growth at zero crack size. This allowed for the direct calculation of the number of cycles.

Inspection for fatigue cracks

In the context of fatigue crack propagation, the inspection threshold is an important parameter. For several parts of the structure, an inspection threshold may be established which describes the time from first flight

until no large inspections have to be performed. The reasoning is that fatigue is not as relevant when the aircraft is new. Inspections are therefore pushed back, which saves a lot of costs. According to the *Handbuch Struktur Berechnung* [19], the inspection threshold should be no larger than half the design life, which defines an upper boundary. As the whole fatigue approach has steered towards a cautious approach, for the inspection threshold, it is considered acceptable to select this value as the inspection threshold.

During the second part of its life, multiple inspections should be performed. It is assumed that one more D-check is performed in the second part of its life, setting the design amount of crack growth cycles to 10e3. To account for human error, it is assumed that during this check, the crack is missed, doubling the amount of cycles to its end of life. Due to the large uncertainties in the presented approach, a safety factor of 2 is applied. This value was chosen as the current tendency with safety factors for crack growth has shrunk from 3 to 2, according to Schijve [17]. Therefore, the design amount of cycles for crack propagation is equal to 40e3.

6.2.6. Safety Factors

Due to material scatter, uncertainties in the standardised load spectrum, the transformation from VA to CA, and simplicity of the method, a safety factor was applied to the number of design cycles. Determining a good safety factor in this stage is not exact science, and requires an assessment of the applied techniques and consequences, based on experience.

For crack initiation, a safety factor of 4.0 was applied to the number of cycles which were to be withstood by the structure. As the crack initiation life was set at 40e3, this puts the design number of cycles at 160e3.

For crack propagation, the reasoning was discussed in section 6.2.5. A total safety factor of 4.0 was applied on the number of cycles which were to be withstood. This leads to a design number of cycles of 40e3 cycles.

6.3. Stability

As the Flying-V is made of highly loaded thin-walled structures, stability is one of the main design drivers. The stability analysis was divided into 5 main categories, namely:

- Stiffened panel buckling
- Plate buckling
- Global buckling
- Column buckling
- Crippling

These types of instability were selected as they they represent the instability phenomena at three different size levels. Locally, the skins between stringers and frames can buckle. Plate buckling typically has no large consequences and may be considered benign. However, during normal operations is is not desired. Another local instability phenomenon which was selected is crippling, as it affects the ability of the stringer to carry load. Combining the skin and stringers, the buckling of stiffened panels requires a more extensive method to evaluate the critical load. Lastly, including the frames and cross-beams into the stability analysis, general instability was evaluated, which is the global buckling of whole fuselage sections.

These five failure modes are discussed in the following subsections. Additionally, the strategy to implement biaxiality and shear stresses jointly in the stability approach is discussed. Also, the independence of buckling phenomena and simplifications are discussed.

6.3.1. Instability classification

While some modes of structural instability are catastrophic, others are benign and are allowed to occur in certain circumstances to obtain a lower structural weight. The instability modes which are considered to be catastrophic are: column buckling, global buckling, stiffened panel buckling and crippling, in order of severity. While the post-buckling load-carrying capabilities differ for the above phenomena, this loading region is not considered in this research. Overall, these phenomena cause the structure to lose its load-carrying ability, likely leading to full system failure. Therefore, these instability phenomena are evaluated at the ultimate load cases.

For plate buckling of stiffened panels, the post-buckling load-carrying capability is high. Therefore, this mode is evaluated at limit load cases, as it otherwise would lead to an over-conservative design.

6.3.2. Structural representation

The structure of the Flying-V contains straight and curved components. The stability methods as described in the following paragraphs apply principally to straight members. However, these methods were also applied to the curved members. This decision was made as there were no suitable methods for curved panels which applied the biaxial and axial-shear interaction, as described below. However, the choice to treat these panels as straight should lead to a prudent design:

- For the plate buckling method, practically the same critical loads are obtained, as the curvature of the skin between two stringers is very small.
- As the crown and keel panel are only lightly curved, the obtained critical loads should reflect the true critical load well.
- The LE and TE are heavily curved, and lead to the most over-designed structures. However, these panels are relatively small, and are not expected to be under large compression loads.

It is worth mentioning that the curved panels are more stable against shear loads as well, which is not as apparent as for pure compression. From Gerard and Becker[64] (p. 67):

"... rectangular plate with transverse curvature will buckle under shear loading at a stress greater than the flat plate of the same developed width as a result of the restraint of radial deflection due to the curvature." (Gerard and Becker [64])

A second point is that all panels are considered to be rectangular. This is not strictly true for the panels in the tapered cabin section. However, the taper is very gradual, at only 0.4 and 1.0 metre decrease in width

over 11 metres for the floor/ceiling and walls, respectively.

Thirdly, the boundary conditions of the structures are simplified. In (analytical) calculations there is a limited choice of boundary conditions (i.e. free, simply-supported, clamped). However, in real aircraft structures, there is no such thing as simply-supported or clamped. Often, the value of lies somewhere in between the analytical boundary conditions, which depends on the adjacent structure acting as the boundary. The used boundary conditions are specified per failure mode in the following sections.

6.3.3. Biaxial-shear interaction

The following subsections illustrate the methods for biaxial buckling, as well as an applied relation for shear buckling, based on an interaction between axial and shear buckling. However, no semi-analytical solution exists which adequately describes the interaction of biaxial loading with shear. However, there is a straightforward interaction relation available for uniaxial and shear loading, obtained from Bruhn[20]. This relation is shown in equation 6.26, and visualised in figure 6.10.

$$\frac{R_c}{R_{c,crit}} + \left(\frac{R_s}{R_{s,crit}}\right)^2 = 1 \tag{6.26}$$

The assumption is made that this relation is also applicable to biaxial buckling and shear. While perhaps not an accurate assumption, this rule effectively restricts design space that would otherwise allow a high biaxial load and shear load consecutively. For the purpose of this research, this is deemed satisfactory.

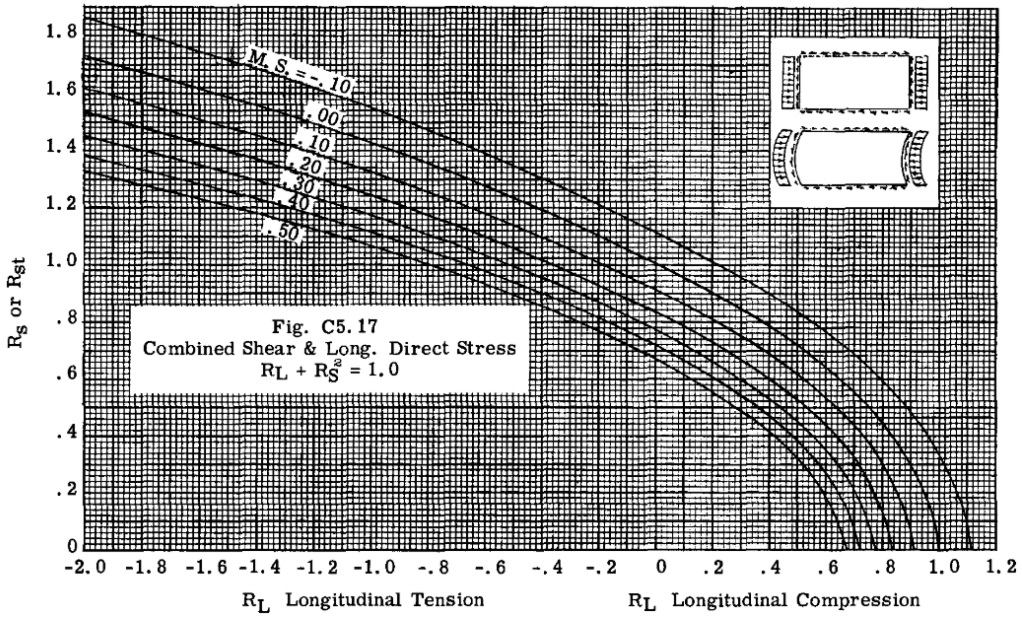

Figure 6.10: Axial-shear interaction curve, reprinted from Bruhn[20], C5.9, figure C5.17.

6.3.4. Stiffened panel buckling

The structure is made up of panels which are stiffened in multiple directions. In longitudinal directions, stringers provide stiffness, while the frames and cross-beams perform the same task in the lateral direction. Straightforward solutions for the critical buckling load may be obtained for simple structures such as plates. However, this is not the case for stiffened panels. The relatively complex geometry does not allow for a direct analytical solution. The skin and the stiffeners possess different qualities which are not easily generalised. Instead, the panel was analysed used classical laminate theory (CLT), which is used to analyse laminated composites. This allows the separation of properties into a stiffness matrix, which may in turn be used to apply composite plate buckling theory.

The following subsections illustrate the applied methods to assess the buckling loads of the stiffened panels under biaxial and shear loads. Both methods were obtained from Kassapoglou [65]. The approach for biaxial

panels is indicated in the following subsection, after which the shear approach and interaction is shown.

Panel properties

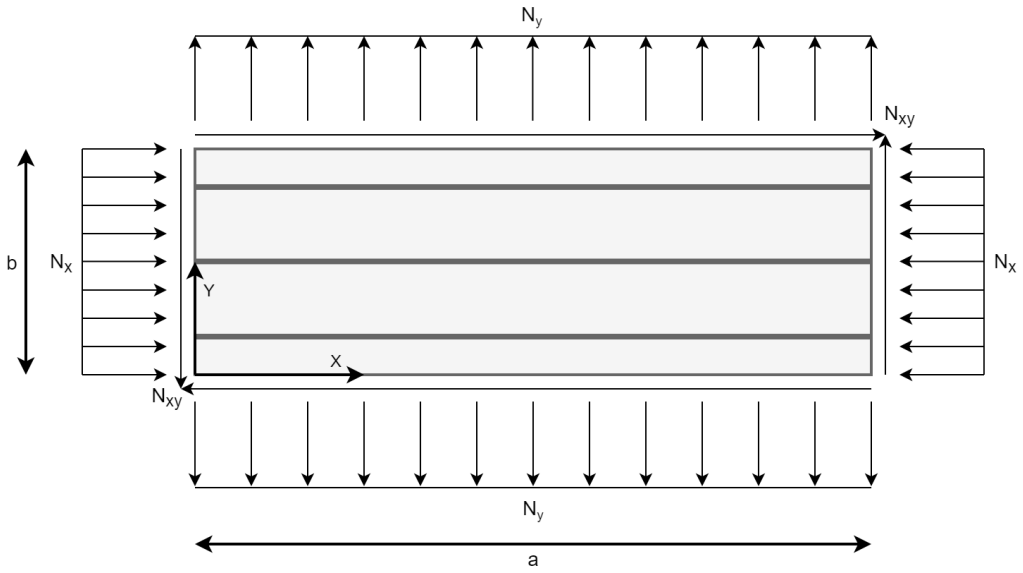

Figure 6.11: Stiffened panel under combined loading.

A stiffened composite panel under combined loading, as shown in figure 6.11. In this example, the stiffening is limited to the x-direction. These stiffeners possess bending stiffness EI and torsional stiffness GJ. To determine the equivalent properties of the panel, the skin properties are summed with the relevant stiffener properties.

$$\begin{aligned}(D_{11})_{eq} &= (D_{11})_{skin} + n_s \frac{EI}{b} \\ (D_{12})_{eq} &= (D_{12})_{skin} \\ (D_{22})_{eq} &= (D_{22})_{skin} \\ (D_{66})_{eq} &= (D_{66})_{skin} + n_s \frac{GJ}{2b}\end{aligned} \tag{6.27}$$

As the panel cross-section is not symmetric through the thickness, a B-matrix would be found when determining the equivalent properties. However, to simplify, this B-matrix is considered zero. For more accurate analysis, it is recommended to determine the effect of this assumption, as the coupling would decrease the critical bucking load. However, as the stringers resist out-of-plane motion rather than shear itself, the coupling matrix should be small. Therefore, this assumption is deemed reasonable.

As the stiffener properties are smeared over the panel, plate equations may be applied to obtain the approximate behaviour of the panel. It should be noted that thee methods which are described below are based on simply-supported boundary conditions.

Biaxial loading

The evaluation method presented by Kassapoglou [65], which is followed in this paragraph, was based on the approach as described by Whitney [66]. The derivation of the critical load is shown in Appendix C.

$$N_0 = \frac{\pi^2 \left(D_{11} m^4 + 2 \left(D_{12} + 2 D_{66} \right) m^2 n^2 \left(\frac{a}{b} \right)^2 + D_2 n^4 \left(\frac{a}{b} \right)^4 \right)}{a^2 \left(m^2 + k n^2 \left(\frac{a}{b} \right)^2 \right)} \tag{6.28}$$

where k equals N_y / N_x, and $N_0 = -N_x$. This value is to be minimised by trialling pairs of m and n.

Shear loading

Similarly, a solution for shear buckling may be found. However, multiple options were available, which led to a trade-off between accuracy and evaluation speed. These methods are discussed below.

Available shear buckling methods Firstly, the exact solution may be found by using a semi-analytical approach. However, finding an accurate solution for the shear buckling problem requires evaluating a high number of m, n terms. As the code of the Flying-V consists of a very large analysis and design loop (due to the large structure and the large amount of analyses), this was deemed undesirable. Secondly, relatively accurate solutions may be found for panels with common aspect ratios (close to 1). However, as the floor panel width (which is of most interest) is an order of magnitude larger than the length, the aspect ratio is approximately 10. Therefore, this method was not an option. A third option, which was selected for this case, was to apply a semi-analytical method, based on the combined loading of composite panels. This method is described below.

Combined loading method The method described in this subsection is based fully on section 6.5 (pp. 132-138) of *Design and analysis of composite structures* by Kassapoglou [65]. The method is based on an approximate relation for axial-shear interaction buckling. However, by setting the ratio of shear to axial load to infinity, a very straightforward answer is obtained, which does not require the evaluation of a high number of terms, which is the case for the exact solution. The derivation is shown in detail in C.

The method assumes simply-supported boundary conditions on all edges. In reality, the panel boundary stiffness is in between simply-supported and clamped conditions. This may be considered especially true for panels which are constrained by the vertex joints, as these joints are hypothesised to be very stiff. The simply-supported solutions may initially appear to lead to an over-conservative design. However, there are a number of factors which reduce the conservativity of the method.

Firstly, and most importantly, bending is not considered during the buckling analysis. Introducing a moment significantly reduces the critical buckling load. While this is not necessarily a large issue for all structures, such as for the outer skin of the aircraft, this is a significant problem for the floor and ceiling panels. These panels are expected to bend due to the significant weight which they carry.

Secondly, the properties of the stiffening elements are smeared uniformly over the panel, which allows the use of plate buckling methods. Local instabilities may trigger the failure of the panel earlier.

Thirdly, axial and out-of-plane coupling is considered zero. Depending on the construction, load is introduced non-uniformly into the panel. As there is load transfer between the skin and the stiffening elements, axial-bending coupling occurs.

Due to these significant uncertainties, the simply-supported boundary conditions are applied. It should be noted that the choice of boundary conditions for a stiffened panel does not increase the critical buckling load as much as is the case for the well-known Euler beam buckling. Where the latter corresponds to a factor of 4, for plates the ratio is approximately 2.2 [65]. As the true conditions are in between clamped and simply-supported, this overestimation is reduced. However, due to the aforementioned reasons, this factor is likely reduced much further. Therefore, simply-supported boundary conditions are deemed suitable.

The critical shear load was obtained to be:

$$N_{xycrit} = \pm \frac{9\pi^4 b}{32a^3}\left(D_{11} + 2\left(D_{12} + 2D_{66}\right)\frac{a^2}{b^2} + D_{22}\frac{a^4}{b^4}\right) \tag{6.29}$$

Note that the $\pm$ sign makes sense, as for shear in either direction, buckling may occur. As stated by Kassapogou [**?**], this solution is typically 27-30% higher than the exact solution. As a higher buckling load is unconservative, this load is therefore divided by 1.3.

$$N_{xycrit} = \pm \frac{9\pi^4 b}{1.3 * 32a^3}\left(D_{11} + 2\left(D_{12} + 2D_{66}\right)\frac{a^2}{b^2} + D_{22}\frac{a^4}{b^4}\right) \tag{6.30}$$

The obtained solution may be directly applied to obtain an estimate of the critical buckling load under

pure shear. Notably, this approach does not require the evaluation of a number of m, n terms to obtain the minimum buckling load. This trait lends itself very well to the design problem at hand.

6.3.5. Plate buckling

The stability of uniform metal plates may be described in a more straightforward manner than was presented in the previous section on panel buckling. However, plates could also evaluated with this method, albeit that there were no additional stiffeners whose properties were smeared over the plate.

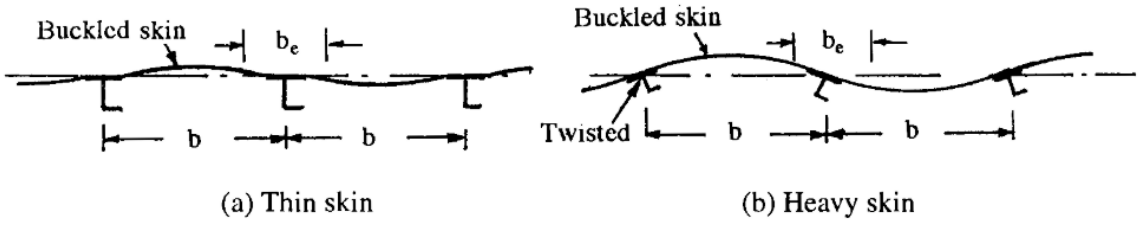

Figure 6.12: Panel behaviour depending on thickness of skin and stiffener torsional stiffnessNiu [21].

The boundary conditions imposed on the skins depends on the torsional stiffness of the boundaries (i.e. stringers and frames). This is indicated in figure 6.12. As the stringers were chosen to be z-profile open-section stringers, the torsional rigidity is negligible. While the frames offer much more support, for conservativity, the boundaries were taken to be simply-supported on all edges.

6.3.6. Global buckling

Global buckling (also called general instability) of a fuselage is the buckling of the whole fuselage structure, including frames. This is indicated schematically in figure 6.13. This is normally approached by treating the fuselage as a stiffened cylinder. Cylinder bending buckling relations may be applied, or spring-like methods, as shown in the figure. However, treating the Flying-V wing-fuselage as a cylinder is not sensible, as the cross-sections are obviously more complicated than a cylinder. However, the fact that the cross-section has multiple components also has a significant advantage. Namely, the vertex joints may be regarded as boundary conditions, which effectively split up the fuselage into the different panels. Therefore, while frames are included, the buckling load is still only evaluated per panel, i.e. crown, LE, floor, etc.

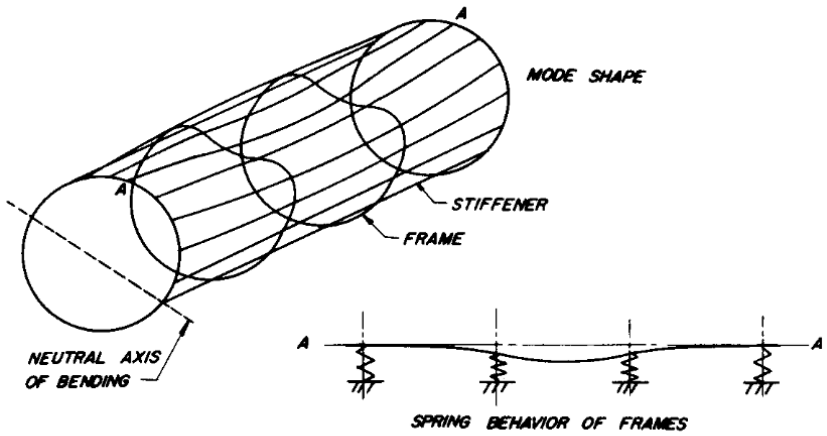

Figure 6.13: General instability of a fuselage top skin, as obtained from Bruhn [20].

Therefore, the global buckling approach was practically identical to the stiffened panel. The only difference is that the properties of the frames were also smeared over the skin panels. There are a number of caveats to the approach, described below.

The frames are quite stiff and spaced far apart compared to the stringers. This reduces the applicability of the method. However, the structure is very large, containing 55 frames. From a global perspective, this is not considered to be a big issue.

The panels must be stiffened adequately in longitudinal direction to impose the buckled shape. While not clear how to assess this, it is considered a large potential shortcoming. If the frames are not too stiff, the behaviour will be plate-like, and the global buckling approach is legitimate. However, if the frames are very stiff, it makes more sense to simply assess column buckling of only the frames. Therefore, this is pursued in the next section.

While more accurate methods are available in the form of numerical methods, the focus was on evaluation speed. For the purpose of this preliminary sizing approach, this was deemed acceptable.

6.3.7. Column buckling

The most simple and well-known stability phenomenon is column buckling. Column buckling comprises the rapid and catastrophic failure of a structural member by kinking and consequentially collapsing. Euler determined the well-known relation for the buckling of a perfect column, as shown in equation 6.31 This failure mode was only assessed for frames and cross-beams. As the adjacent stiffened panels possess a significant post-buckling load-carrying capability, the panels were allowed to carry load. Therefore, the load was still considered to be carried by the frame-panel combination, but only the out-of-plane moment of inertia of the frame was considered for the following relation:

$$P_{cr} = \frac{n^2 \pi^2 EI}{L^2} \tag{6.31}$$

Where P_{cr} is the critical load, n is a factor dictated by boundary conditions, EI are the section bending stiffness properties and L is the column length. As the frames are the stiffest components in the structure, the resistance from the vertex joints is relatively small. Therefore, simply-supported boundary conditions were assumed, at $n = 1$.

6.3.8. Crippling

For stiffening elements, crippling is an important local type of instability. Crippling is the final failure of a stiffener beyond local buckling of its flanges and webs. The onset of buckling in flanges and webs may be considered a type of plate buckling, but is not treated individually in this research. Due to the small cross-sectional dimensions of stiffeners, boundary conditions have a large effect due to their proximity. As sections of the cross-section distort at a certain load, more load can be carried by stable material supported by the stiffener geometry (i.e. corners). The stress in the buckled sections remains approximately equal, while the stress of material near corners rises. This is portrayed in figure 6.14, obtained from Niu [21].

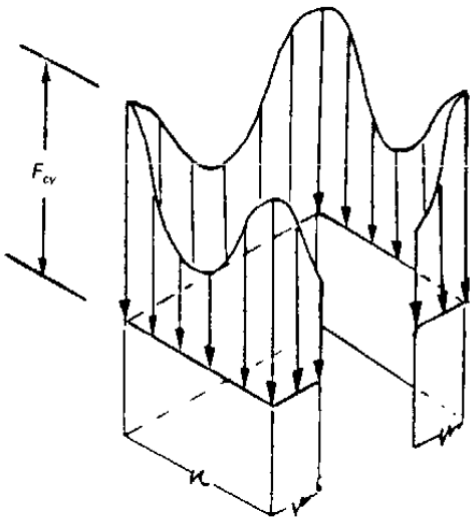

Figure 6.14: Stiffener crippling stress distribution, Niu [21].

At some point, the full stiffener collapses catastrophically as the stress in the corner material approaches yield stress. This collapse may not occur in a structure, but is still preferred to column buckling as the failure may be confined locally. However, the relation between average stress in the stringer and the stress in the corner, which triggers the final failure, is not exact. Based on test results, several different methods have been set up to estimate the crippling load. Here the concept of one-edge-free flanges and no-edge-free flanges is important. As may be imagined from plate buckling, a one-edge-free flange cripples substantially sooner than no-edge-free.

Niu's method

For preliminary design, empirical approaches exist to quickly estimate stringer properties under compression. Gerard [67] and Niu [16] proposed very similar methods to evaluate crippling in stiffeners in a preliminary fashion. As Niu's data was much more recent than Gerard's (1957 vs. 1988), Niu's method was preferred. For generic sections, the relation between the critical crippling stress is [21]:

$$F_{cc} = B\left[\left(\frac{1}{A/gt^2}\right)^m\right]\left[E^m F_{cy}^{3-m}\right]^{1/3} \tag{6.32}$$

where B is a constant which is 0.58, m is 0.8, A is the cross-sectional area, g is the number of flanges and cuts to open No Edge Free (NEF) webs, t is the thickness and m is the slope of the crippling curve.

A second consideration is the cut-off stress. This occurs if the mean stress in the section reaches yield stress, after which it also collapses. According to Niu[21], the use of this yield cut-off stress is an effective boundary.

The results obtained with the above method give satisfactory agreement with test results [**?**]. Accuracy is not necessarily the primary concern in this research, as the general structural performance of the Flying-V is pursued. However, this method allowed for the fast evaluation of stiffener crippling. Therefore, it was deemed suitable.

Stringer stresses

The stringer stresses were assumed to be constant over the cross-section. As the stringers were modelled as booms, only a single stress value was available per stringer. In reality, bending will occur of the stiffened panels between frames. Depending on the stress distribution over the stringer, and the flanges which are more heavily loaded, the stringer can collapse at a lower compressive load. As this is not considered in the stringer analysis, it makes the results somewhat unconservative.

Extension to frame crippling

Crippling was also determined in the frames. However, the frames must not be regarded equally to the stringers. The stresses in the frames vary significantly from flange to flange surface, due to the large bending loads which are simultaneously resisted.

An applicable stress value was found by considering the workings of the crippling phenomenon. Under even compressive stresses, the OEF flanges buckle first, while the stresses in the NEF flanges/webs continue to rise. The NEF flanges buckle, after which the stress only increases at the material close to the corners. The final failure load is thus decided by the stress in these corners. It is assumed that, as soon as a single corner fails, the entire section collapses. Therefore, the highest stress in a single corner is selected to trigger crippling. Under bending, this means that the highest compressive stress in a corner is applied. It is assumed that this stress can then be applied to equation 6.32 to obtain the critical crippling stress.

6.3.9. Independence

The buckling phenomena as described in the previous sections may occur under different conditions, depending on load and geometry. However, all buckling conditions have been treated independently from each other. Especially the panel behaviour as shown in figure 6.12, indicates the triggering action of buckling modes. For this research it is assumed satisfactory to consider the presented buckling cases and interaction curves, and to disregard the triggering of buckling modes of different structures.

7
Sizing methodology

The applied sizing methodology is discussed in the following sections. The goal of the sizing is to obtain the geometric parameters associated with the minimum mass, while meeting all failure requirements. For this design, the selected materials are discussed, after which the used component geometries are discussed. Thirdly, the sizing strategy is discussed.

7.1. Material selection

As discussed in section 2.1, aluminium alloys were selected for the preliminary design of the Flying-V.

The materials which were selected for analysis were two aluminium alloys: AL2024-T3 and AL7075-T6. The reason for this choice was twofold. Firstly, these alloys have proven to be high-performance structural materials in aerospace applications, and are the go-to aerospace alloys in their respective families. AL-2024-T3 exhibits moderate to high strength, but possess exceptional fatigue properties. AL-7075-T6 has exceptional strength, but conversely has less favourable fatigue properties. Detailed material data can be found in Appendix B.

Ideally, a modern aluminium-lithium alloy would be included, as this class of aluminium alloys exhibits high stiffness, at a significantly lower density. These alloys are ideal for stiffness-driven applications, which is something not explicitly shown by AL2024-T3 and AL7075-T6. However, due to the unavailability of fatigue-related data, these type of alloys were not included. However, due to the prolific use of aluminium-lithium alloys in modern aerospace applications [68], it is clear that these alloys offer significant improvements. Therefore, their exclusion in this research will unfavourably affect the final result.

7.2. Reductions in sizing complexity

During the development of the analysis framework in this research, emphasis was put on the ability to tailor the analysis to allow research into the effects of many variables. Controlling/varying many different variables leads to a high analysis time to find an optimum solution. Therefore, the analysis speed was also considered to be of great importance while selecting the analysis methods. However, during the sizing stage it became apparent that due to the large structure, in combination with many load cases, stress analyses and failure analyses, obtaining a solution by looping many variables took an excessive amount of time. Looping over all desired design variables was considered infeasible in terms of runtime, and therefore, a simplified sizing is presented.

The simplifications which were applied in order to size the structure more quickly are shown in the next subsections. Firstly the materials are discussed, after which the structural component approach is presented.

7.2.1. Reduction in the number of load cases

To allow for much quicker evaluation of representative load cases, the critical load cases were identified. Based on the maximum running loads and cross-section resultant load distributions, a critical set was selected. This included at least one load case from each category (manoeuvering, landing, etc.). The distributions and selection are shown in detail in Appendix D. Load cases LC02, LC03, LC09, LC15, LC21, LC26, LC28, LC30, LC32, LC34, LC39 and LC61 were evaluated. These load cases correspond to pressurised/un-

pressurised positive/negative manoeuvring, multiple 2-point and 3-point landing scenarios, braked roll, take-off and over-pressure. For reference, please see table D.1.

7.2.2. Assigning material properties to the structure

In order to reduce the evaluation time associated with looping over the possible materials, the material evaluation was simplified. Having to loop over the possible materials for each structure increases the amount of runtime by a factor n^m, where n is the number of different structures, and m is the number of materials. Instead, the materials were to be assigned based on the critical failure modes, obtained from a design using mean material properties. Specifically, this was done in the following two steps.

Step 1: averaging material values The first step consisted of performing the sizing with mean material values. These material values and calculation methods are shown in Appendix B. It was assumed that the structure would present globally representative results with mean material properties. With these mean material properties, the goal was twofold. Firstly, is allows for the assignment of materials to structures. Secondly, it allows for a quick identification of a favourable region in the design space. The sizing steps which followed for the assigned materials could then be limited to a more constrained design space.

Step 2: assigning specific materials The second step consisted of assigning specific materials to the components based on critical failure indices. As may be found in Appendix B, the two materials are favourable for different applications:

- AL2024-T3:
  - Favourable for stability-related failure modes due to the higher Young's modulus.
  - Favourable for crack propagation failure due to the lower crack growth rate and higher fracture toughness.
- AL7075-T6:
  - Favourable for static material failure due to significantly higher strength values.
  - Favourable for crack initiation due to high ultimate/fatigue strength combination.

The critical failure modes for the mean material values are shown in Appendix E.2.1. Summarising, stability-related failure and crack propagation failure were found to be the driving failure modes. From the above discussion on materials, this resulted in the assignment of AL2024-T3 to all structures. This approach is a rather large simplification, but greatly reduces the sizing complexity.

7.2.3. Evaluating the component variables

Frames and cross beams

The frames and cross-beams were represented as channel sections, as shown in figure 7.1. The channel section was chosen because it offers high structural performance, full inspectibility and a single row of fasteners, such that the uniaxial stress assumption holds. The web height to flange width ratio of 2 was set constant throughout the sizing.

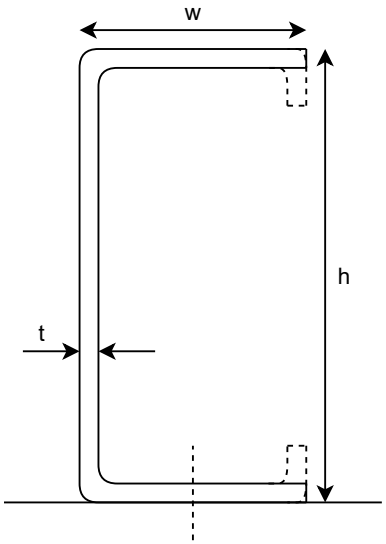

Figure 7.1: Frame representation, with constant h = 2w. The additional flange supports have not been included in the original sizing.

The frames and cross-beams were considered to be of primary importance in the sizing approach. This is the case as the out-of-plane loads are high, and a high degree of stability is required in the floor and ceiling. The frames and cross-beams are expected to be large and have a significant effect on total mass. With this in mind, a priority was to allow the variables associated with these structures to be tailored. The size of the frame cross-section was therefore variable along its length. However, the height-thickness ratio was set the same for all frames. This was done such that frame crippling could be easily controlled.

Keeping frame pitch constant The obtained number of frames, as well as their locations, were obtained from Claeys [11]. A variation in frame pitch was not included in the sizing approach. The frame pitch affect a large number of variables, which causes the sizing setup to be increasingly difficult. The frame spacing primarily affects the stability modes, in particular panel and global buckling. Not being able to vary the frame pitch is expected to adversely affect the performance of the structure for these failure modes. This is discussed in more detail in **??**. While not varying the frame pitch, the frame design is varied considerably, as shown below.

Frame sizing For the frames and cross-beams, failure index surfaces were present for each element along its length. Therefore, using the sizing methods as described in the following subsections, the properties of the frame along its length were adjusted. It was opted to calculate the optimal geometry for each individual frame, and not re-using frames. As the frame pitch could not be varied, making many equal frames would pose a too large weight penalty. Realistically, a large number of frames will have to be the same geometry for cost-effectiveness. However, the associated weight penalty was deemed too severe in with this sizing methodology.

Skin panel segments

In order to take into account manufacturability and decrease cost, fuselage panels with constant skin thickness were implemented, over a varying number of frames, depending on the location. These segments were selected based on stress field data from the generic structure as described in Appendix F, as may be found for a number of failure modes in Appendix E.1. For an indication, two figures are repeated below in figures 7.2 and 7.3.

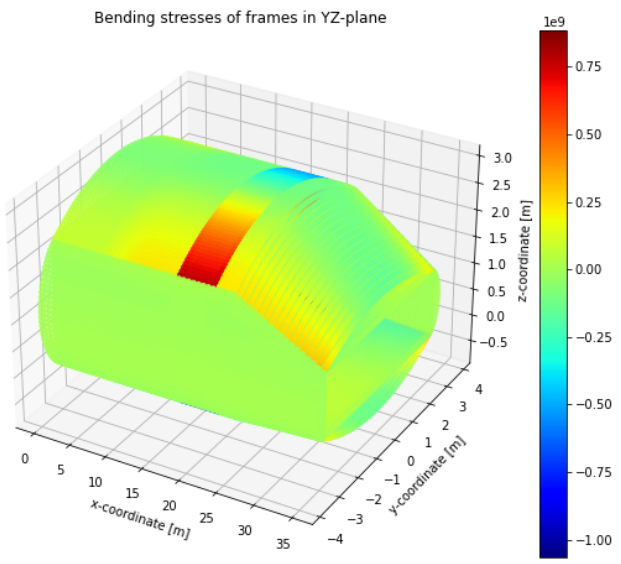

Figure 7.2: Maximum absolute bending induced axial stresses in the frames. Aft top view.

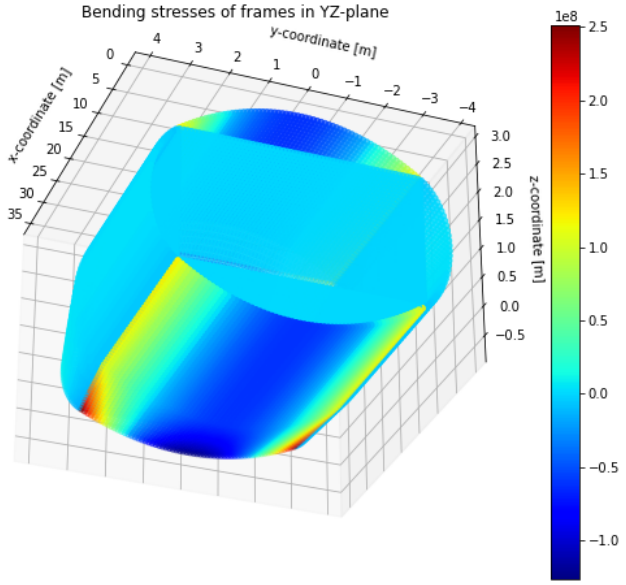

Figure 7.3: Maximum absolute bending induced axial stresses in the frames. Front bottom view.

A number of specific segments were identified which required an own panel (i.e. stresses are very different from neighbouring sections):

- The Engine/MLG structure possesses significantly higher stresses under nearly every load case. Therefore, this region (frames 27-34), was assigned its own fuselage segment.
- Similarly, a nose gear segment was established from sections 1-5.
- The transition between the constant and tapered cabin was considered to be a clear end/beginning of a panel, as panels with this geometry would be exceedingly complex to manufacture. Therefore, a segment was determined to go from the end of the Engine/MLG segment to this transition.

Finally, the leftover regions at the front and aft of the fuselage were divided into 4 and 3 segments, respectively. This was done to obtain segments with an approximately equal size. The result may be found in figure 7.4.

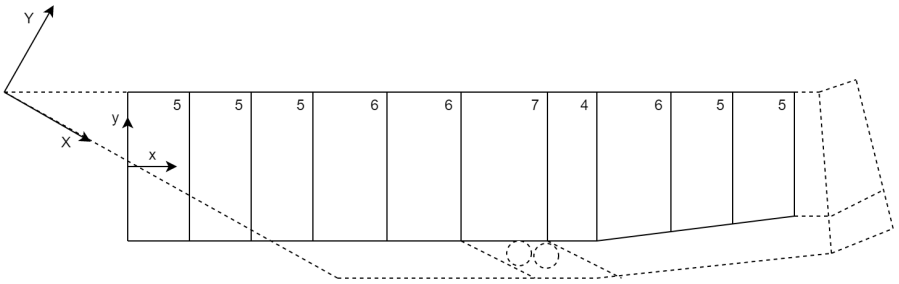

Figure 7.4: Schematic indication of the fuselage segments, and the number of frames they contain.

Stringers

The stringers were represented as z-profile stiffeners, schematically visualised in figure 7.5. This was done for a few reasons. Firstly, they possess high structural efficiency, but also allow complete inspection. Secondly, a single row of fasteners is applied such that the assumption of uniaxial stress state is justified. Thirdly, they are easy to manufacture. The stringers were initially applied as plain z-stringers, without an additional flange support. The effect of the increased flange support is discussed in section 9.2.3.

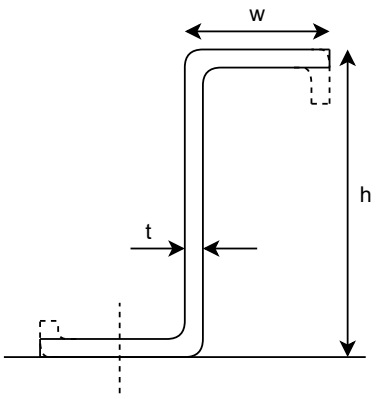

Figure 7.5: Z-stringer design, where h = 2w. The excluded flange support is indicated by dotted lines.

The dimensions of the stringer were described by ratios. A constant web-flange length ratio of 2 was assumed. The thickness was considered constant over the cross-section of the stringer, to allow construction from constant thickness plate material. Additionally, this reduced sizing complexity and evaluation cost. The thickness was set at a minimum of 1 mm, but could be varied. The variation of the thickness ensured proper control over the crippling failure mode.

Identical stringers were applied to all structures. Again, this was done to reduce modelling complexity. This decre

Stringer spacing The number of stringers per skin were assumed to remain constant over the whole cabin length. This was deemed a realistic assumption, while having the added effect of reducing the sizing complexity.

For a fixed number of stringers per skin, the sizing procedure (as described in the next sections) was able to converge to a solution. However, including the stringer pitch in the calculations did not lead to a convergent algorithm. The reason is that the number of stringers affects a large number of failure modes, while not being dominant for any (the stringer geometry and skin thickness are dominant over the pitch for related failure modes). Simplifications, such as relating the stringer pitch to the skin thickness, again led to divergent behaviour. Therefore, the number of stringers had to be set outside of the loop.

However, looping over a large amount of stringer combinations for each of the 8 component skins would have led to an extremely high runtime. Therefore, the number of stringers was based on the following reasoning.

The crown, keel, ceiling and floor were the main structures which were expected to experience buckling, albeit during different load cases. This is the case as they are under significant compressive loads. All were expected to require significant longitudinal stiffening to meet the stability failure criteria. To reduce the troubles with runtime, the aim was to express the stiffener numbers of all components to each other with a constant factor. In the context of longitudinal loads, the crown and keel were expected to experience larger loads, as they are positioned far away from the neutral line. In particular, the crown would be prone to buckling under high positive load factor. However, the floor and ceiling panels are under a disadvantageous high lateral compression load due to pressurisation.

Trialling component stringers for the mean material A general quantitative argument could not be made for the allocation of more or less stringers on any of the above structures. Therefore, for a low number of elements in each section (2 for the vertical, 4 for the horizontal components), trials were performed to assess the effects of the number of stringers.

The underlying assumption is that the optimal number of stringers found for a rough mesh is applicable to a fine mesh. While the sizing behaviour changes when refining the mesh, the optimal number of stringers should still be approximately the same. This approach does not yield an optimised result, but achieving a representative sizing result was a priority. The optimal number of stringers is expected to change somewhat when going from a rough to a fine mesh. Therefore, it is not very useful to evaluate the number of stringers

in small steps. This will greatly increase the runtime, and will present an incorrect perception of obtaining an optimised result for a fine mesh. The stringer trials for the original concept were set up as follows:

- For an equal number of crown, ceiling, floor and keel stringers, the number of LE, TE and wall stringers was varied, considering an equal number.
- For an equal number of LE, TE and wall stringers, the effect of altering the ceiling, floor and keel number of stringers was studied.

For the first trial, the ratio r_n between the number of crown stringers and stringers attached to the vertical components was assessed. The ratio was varied from 1.5 - 5.0. As the stringer geometry is constant everywhere, the procedure was repeated for 3 different number of crown stringers (24, 36 and 48 stringers). The results are shown in table **??**. The minimum stringer fraction varies based on the number of crown stringers, as shown in bold. The results indicate that the minimum mass is not associated with a fraction, but with the same number of stringers (i.e. 24/2.0 = 36/3 = 48/4 = 12 stringers). Therefore, the number of stringers attached to the LE, TE and walls was set to 12. Overall, the mass shows to be relatively insensitive to this number of stringers.

Table 7.1: Stringer trial results for $n_{crown} = n_{keel} = n_{ceil} = n_{floor} = r_n * n_{LE} = r_n * n_{TE} = r_n * n_{walls}$. Minima indicated in bold. maximum FI shown to indicate MoS associated with solution.

n_{crown}	24	36	48
n_{frac}	mass [kg]	mass [kg]	mass [kg]
1.5	25090	25515	26299
2.0	**25074**	24913	25372
2.5	25089	24780	25134
3.0	25143	**24722**	24940
3.5	25238	24723	24883
4.0	25356	24782	**24851**
4.5	25356	24840	24854
5.0	25523	24840	24873

A second study was performed to determine the ideal number of stringers on the floor and ceiling. Preliminary results were produced based on an equal amount of crown, keel, floor and ceiling stringers to obtain an impression of the required stiffening. Global and panel buckling were found to have much higher mean failure index in the floor and ceiling than the crown and keel (approx. an order 3-4).

Therefore, more stringers were assigned to the floor and ceiling than the crown and keel in these trials. As the failure index distribution of the floor and ceiling were very similar, the same number of stringers were applied. For a range of crown stringers (14-32), the solution was obtained for a range stringer of fractions (2-4). The number of floor and ceiling stringers are represented by the product of the crown/keel stringers and the stringer fraction. The behaviour is visualised in table 7.2. The minimum weight solution is associated with a high stringer fraction for a low number of crown/keel stiffeners, and vice versa. The minima for each trial of n are shown, which indicate a global minimum. This minimum was found at a number of stringers ranging from 16-24, at an approximate stringer fraction of 3.0. it should be noted that the stringer mass rises quickly outside this zone. While the lowest mass value was found at $n = 16$, the mass quickly increases when reducing the number of stringers further, as can be seen from $n = 14$. The final sizing results are generated at a much finer mesh, which can lead to different results than generated at this rough mesh. Therefore, is was instead opted to choose 18 stringers, at a fraction of 3.0, as this solution was deemed more stable. The increase in mass associated with this change is negligible.

Table 7.2: Wing-fuselage mass as a function of crown/keel stringers and floor/ceiling stringers. $n_{floor/ceil} = n_{frac} * n_{crown/keel}$

$n_{crown/keel}$	14	16	18	20	24	28	32
n_{frac}	mass [kg]	mass [kg]	mass [kg]	mass [kg]	mass [kg]	mass [kg]	mass [kg]
2	24301	23826	23695	23617	23749	23817	23936
2.5	23945	23555	23456	23401	**23416**	**23708**	**23784**
3	23690	23397	**23364**	**23368**	23497	23733	24280
3.5	**23657**	**23333**	23504	23547	23497	24055	24677
4	23702	23468	23679	23756	24019	24399	25088

Having found an optimum global solution region, the minimum mass solution was calculated with the stringers as described above for the mean mass properties. The obtained failure indices allowed for a choice of materials per component group (skins, frames, stringers). These failure indices are shown in E.2. It was found that AL2024-T3 was beneficial for all cases. This is the case as crack propagation and stability phenomena are more critical than static material failure or crack initiation in all structures. The stringer trials as described above were then performed once more, for the newly assigned materials.

Trialling stringers for the assigned materials With the optimal region for the mean material properties being identified in the previous section, more targeted trials were performed with the assigned materials. Again, a low number of elements were used per component (2 for the vertical components, 4 for horizontal components) and the same set of load cases as in the previous trials. As the mass was found to be very insensitive to the number of LE/TE/walls stringers, it was assumed that 12 stringers were applicable here as well.

The obtained results were similar, with an optimum at 20 crown stringers with a floor/ceiling stringer fraction of 3.0, (i.e. 60 stringers). The results may be found in table 7.3. Clearly, the minimum mass has decreased by approx 1100 kg, indicating that the choice for AL2024-T3 is beneficial. Having estimated the optimal number of stringers per component, the sizing could be performed for a refined structure.

Table 7.3: Floor/ceiling stringer trials for AL2024-T3.

$n_{crown/keel}$	16	18	20	22
n_{frac}	mass [kg]	mass [kg]	mass [kg]	mass [kg]
2.5	23497	23136	22511	22387
3	23311	22386	**22210**	22287
3.5	22848	22344	22343	22465

With the number of stringers selected for each component, the results were produced for a fine mesh. These results may be found in section 8.1.1.

NLES concept stringers

An identical approach was applied to the NLES concept, with the exception of the number of stringers on the leading edge. Firstly, the leading edge number of stringers was assessed, whose results can be found in table 7.4. As the solution was found to be very insensitive to the number of stringers, it was not assessed in detail. An optimal number of 14 stringers was obtained.

Table 7.4: NLES concept leading edge stringer trials for mean material.

ncrown	20
n_LE	mass [kg]
10	25723
12	25685
14	**25645**
16	25647
18	25663
20	25684

The same number of TE and wall stringers as found in the original concept were assumed to be optimal, at 12. For the crown and keel, 18 stringers were obtained to be optimal as well. For the floor and ceiling, 54 stringers were obtained. A solution was generated for this layout for the mean material properties, as shown in Appendix E.2.1. Again, AL2024-T3 was identified to be the best choice for all structures, as buckling and crack propagation were the design drivers.

A second set of stringer trials were then performed for the NLES concept, with the new material. The results of the number of floor/ceiling stringers are shown in table 7.5. Clearly, the assignment of the new material has a favourable effect on the mass, as the difference in optimal mass is approx. 1600 kg.

Table 7.5: NLES concept crown/keel stringer trials for AL2024-T3.

n_{crown}	16	18	20	22
n_{frac}	mass [kg]	mass [kg]	mass [kg]	mass [kg]
2.5	25474	24875	24513	24262
3	25375	24399	**24059**	24124
3.5	24725	24079	24088	24256

The leading edge number of stringers was found to be insensitive for the mean materials analysis. However, as the leading edge design is the key difference for this concept, it was assessed once more. An optimum was found at 17 stringers, as shown in table 7.6. Clearly, the sensitivity of the solution has not increased for the application of the new material.

Table 7.6: NLES concept leading edge stringer trials for AL2024-T3.

n_{crown}	20
n_{LE}	mass [kg]
12	24094
14	24059
16	24043
17	**24041**
18	24043
20	24054

With the number of stringers selected for each component, the results were produced for a fine mesh. These results may be found in section 8.1.2.

7.3. Variable updating method

Firstly, for each failure mode, the dominantly affecting structure and variable were identified. Insights into the stress fields of a generic structure as shown in section E.1 were key in determining the failure drivers. The main insights were:

- Hoop stresses are dominating fatigue and static failure for the skins and frames. The hoop stresses

are caused by pure axial stresses and bending about the x axis. The observed peak bending stresses were observed to be higher in most cases than the pure axial stresses. Increasing the area and MOI of the skin and frame are effective in reducing these stresses. The most effective approach is to increase the frame dimensions. This greatly increases the local MOI. For the same geometric ratio between the web height, flange width and thickness (uniform), the moment of inertia scales by h_{web}^4/k, where k is a constant based on the geometric ratios. Additionally, increasing the frame dimensions increases the cross-sectional area, reducing pure axial stresses. Adding the same amount of material to the skin would result in the same reduction of pure axial stress, but the change in bending stresses would almost be negligible.

- The frames / cross beams are dominant in the global instability failure mode, and naturally, in column buckling. The frames / cross beams are most effective as they have a larger expected total MOI than the stringers. Additionally, for global instability, the frames and cross-beams are in the short direction of the structure (simplified as a stiffened panel), which is more effective than the stiffening in the long direction (i.e. the stringers).
- The stringers are dominant in panel buckling. As the skin provides little stiffening, and the frame pitch is unchanged, the total stringer MOI is the parameter to vary. Similarly to the frames, the stringer geometry was described fully by the web height and the height-thickness ratio.

To summarise, the structural components and specific variables that are used to design against the failure modes are:

- **Frame dimensions:**
  - Global buckling
  - Crack initiation and crack propagation in the skin and frame.
  - Static material failure of the frame and skin in hoop direction.
- **Stringer dimensions:**
  - Panel buckling
  - Crippling
- **Skin thickness:**
  - Plate buckling
  - Static material failure skin in axial and shear.
  - Crack initiation and crack propagation in longitudinal direction.

7.3.1. Updating algorithm

The algorithm to update the values is illustrated below. Based on the dominant identified variables, as shown in previous section, new values were derived. The global approach is illustrated in figure 7.6. As described in the previous sections, the frames and the stringers were determined to be the most effective for the majority of the failure modes. Secondly, the effect of these two structures could be decoupled adequately, and so their values could be updated through a straightforward process. The skin, on the other hand, affects most failure modes, in both longitudinal and hoop direction. Therefore, the skin was updated after the frame and stringer properties.

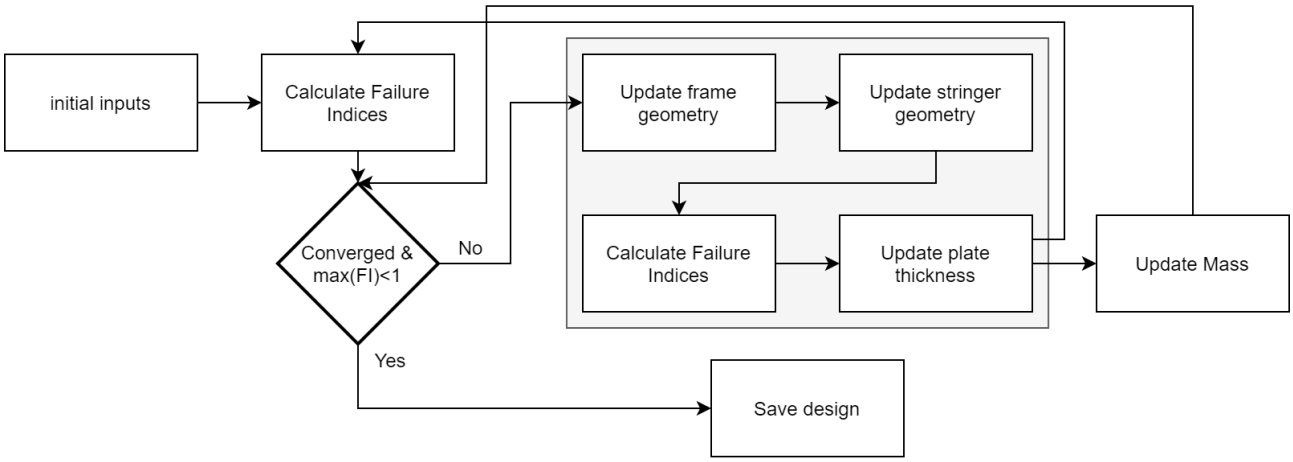

Figure 7.6: Global sizing approach.

For the initial geometrical inputs, the failure indices were calculated. A decision block tests that all failure indices are below 1, and if the mass has converged. If either fails, the geometrical properties are updated. The updating logic is shown in section 7.3.2. As the effects of updating the frame properties and the stringer properties are adequately decoupled, their values are calculated consecutively, without an intermediate recalculation of the FI's. This effectively reduces evaluation time by a third. After these updates, the FI's are recalculated, after which the plate thicknesses are updated. As all variables have been updated at this point, the mass is calculated, and the FI's are determined once more before returning to the decision block. This process is repeated until convergence has been achieved, after which the data is saved.

Initial values

For the initial values, plate thicknesses of 1 mm were used. A stringer height of 10 mm was used, with a constant ratio between the web height and flange width of 2. Additionally, an initial ratio between the web height and stringer thickness of 20 was applied. An initial frame height of 250 mm was chosen, with a constant ratio between the web and flange of 2, as well as an initial ratio between the web height and the thickness of 40.

Table 7.7: Variable initial values.

Parameter	**Value**	**Unit**
All plate thicknesses	0.001	m
Stringer web height	0.010	m
Stringer height-thickness ratio	20	-
Frame web height	0.250	m
Frame height-thickness ratio	40	-

Variable bounds

The sizing loop contained bounds which were not to be exceeded, as shown in table 7.8. The bounds aided in obtained realistic structures, and disallowing extreme values which could cause instability in the early stages of the sizing algorithm.

Table 7.8: Variable bounds.

Parameter	**Minimum [m]**	**Maximum [m]**
All thicknesses	0.001	0.05
Stringer web height	0.01	0.20
Frame web height	0.05	0.5
Frame height-thickness ratio	N/A	40

Convergence criteria first and foremost, all failure indices must be below 1. Secondly, convergence is attained when the consecutive mass solutions are within ±1.0%. The latter criterion is considered to be rather relaxed, but this was deemed necessary to obtain an acceptable runtime.

Margin of Safety The final structure should have a positive Margin of Safety (MoS) on all failure indices throughout the structure. Therefore, all failure indices should be lower than unity. Applying a target margin of safety lowers the failure index goals to a value lower then 1. When perfectly converged, this margin of safety is attained by the failure index. However, as the approach is based on evaluation speed above accuracy, the loop is allowed to stop once all FI's are below 1, even if the goal is $1 - MoS$. Due to the nature of the sizing approach, the failure indices do not show a single trend downwards or upwards towards this value, but may alternate about the final target. Additionally, this 'bouncing' around the target value may continue for a significant amount of iterations, depending on the interaction between different variables. Therefore, setting the MoS at a value which is significantly larger than zero, the term also functions as a stabilising factor, ensuring that all FI's quickly attain a value lower than 1. Monitoring the convergence progress, an effective target MoS was set at 0.05.

7.3.2. Variable Updating Derivations

The relations between the failure indices and dominant variables are shown with the following derivations / substantiations. From the obtained relations, updated values of the respective variables were determined. For brevity, only the most important relations are shown, which can be applied to the other components. The full updating list is shown in 7.3.3.

Frame / stringer MOI The following description uses the frame as an example, but an identical procedure is followed for the stringers, albeit for other failure modes.

The frame MOI is dominant in a number of failure modes, as described previously. Defining the example constant geometric ratios: $h_f = 2w_f = 40t_f$, the MOI of the I-section equals:

$$I_f = \frac{t_f h_f^3}{12} + 2t_f w_f \left(\frac{h_f}{2}\right)^2 = \frac{h_f^4}{90} \tag{7.1}$$

As the geometric ratios cause the denominator to remain constant when updated, it can be neglected. Therefore, MOI scales with the frame height to the power 4. For all failure modes where the MOI is dominant, the failure index is linearly related to the MOI. Then, the updated and current value may be related to the previous value and failure index as:

$$h_{f,i+1} = \left(h_{f,i}^4 * \frac{1}{1 - MoS} * FI\right)^{\frac{1}{4}} \tag{7.2}$$

Here MoS indicates the margin of safety. The failure modes for which the MOI scales linearly with the failure index, this relation is applied. These failure modes are:

- Static material failure
- Global buckling
- Column buckling

Similarly, for the stringers, the height was dominant for:

- Panel buckling

Failure modes which do not linearly rely on the MOI are discussed in the following paragraphs.

Crack propagation for crack propagation, the failure index scales by $1/N_{crit}$, where N_{crit} represents the critical number of cycles. The approximate integrated relation for this number of cycles, as derived in section 6.2.5, is shown below.

$$N_{crit} = \left(a_f^{-n_F+1} - a_0^{-n_F+1}\right)\left(\frac{K_1^{3/2}}{n_F-2} - \frac{K_2 a_f}{n_F-2}\right) \tag{7.3}$$

where a_0 is the initial crack size, a_f is the final crack size. n_F denotes the Forman exponent, and K_1 and K_2 are defined as:

$$K_1 = \left(C_F dS^{n_F-1}\beta^{n_F-1}\pi^{\frac{n_F-1}{2}}\right)^{-1} \tag{7.4}$$

$$K_2 = \frac{(1-R)K_F}{C_F dS^{n_F}\beta^{n_F}\pi^{\frac{n_F}{2}}} \tag{7.5}$$

where C_F is the Forman constant, β is the geometry factor, dS is the stress range. For the stress range, it is assumed that the hoop stresses are driving the design against crack propagation. The final crack size is the minimum of either a predefined length, or calculated by means of the fracture toughness under limit load:

$$a_f = \frac{1}{\pi}\left(\frac{K_F}{S_{lim}}\right)^2 \tag{7.6}$$

The limit load is defined as the limit load factor multiplied by the unpressurised stress, and then added to the pressurisation stress. In the hoop direction, pressurisation is by far the most stress-inducing cause. Therefore, it is assumed that the limit load is equal to this pressure-induced stress, i.e.:

$$\sigma_{lim} = F_{lim}\sigma_{0p} + \sigma_{dp} \approx \sigma_{dp} \tag{7.7}$$

The hoop stresses develop from approx. zero on ground to the maximum value during cruise. Therefore, σ_{dp} is approximately equal to the stress range dS in hoop direction. It is assumed that σ_{dp} may then be equalled to dS. Substituting the stress values back into equation 7.3, and assuming $a_f >> a_0$, this leads to:

$$\frac{1}{FI} \propto N_{crit} \propto \left(\frac{1}{dS}\right)^2\left(\frac{k_{II}}{dS^{n_F-1}} - \frac{k_{III}}{dS^{n_F}}\right) \tag{7.8}$$

where the k symbols represent constants. Unfortunately, the two terms in the set of brackets are of comparable magnitude, as they represent the structure quickly tearing for high stresses. Therefore, ignoring the constants and continuing with the highest power would lead to a too strong relation between the stress range and the failure index. However, knowing that n_F is approximately 3, the dependence on the stress range scales at least with a power 2, at most a power 5. Again, it is assumed that the bending stress is dominant. The relation between the bending stress and the MOI is linear. Then, finally obtaining a design variable, the relation between the moment of inertia and the frame height scales by the power 4. This leads to a range of possibilities:

$$h_{f,i+1} = \left(h_{f,i}^{4+i} * \frac{1}{1-MoS} * FI\right)^{\frac{1}{4+i}} \tag{7.9}$$

where possible i ranges from 2 to 5. Based on a number of test runs, evaluating the speed and stability of the iterations, i was set to 2.

Crack initiation for crack initiation, a derivation was inconclusive. However, the same reasoning for the relation between the frame MOI and the stress was applied. Therefore the FI scales by a base of power 4. The stability and speed of the power 4 was simply tested, which was found to function properly.

Crippling The crippling failure stress is repeated below in equation 7.10.

$$F_{cc} = B\left[\left(\frac{1}{A/t^2}\right)^m\right]\left[E^m F_{cy}^{3-m}\right]^{1/3} \tag{7.10}$$

The changeable variables are the area and thickness of the stiffener. As has been stated previously, the web height and flange width were coupled at a constant ratio of 2. As changing the web height affects other failure modes so strongly (as shown in previous paragraphs), it was chosen to vary the thickness. The area depends linearly on t, and m is 0.82 for aluminium alloys [21]. With the stress being related to the load linearly, this finally leads to a dependency of approx the power 1.82. The power 2 was applied and was found to function properly for stringers. For completeness:

$$t_{i+1} = \left(t_i^2 * \frac{1}{1-MoS} * FI_{crip}\right)^{\frac{1}{2}} \tag{7.11}$$

For the frames, the above led to oscillatory failure index behaviour. This frame MOI affects such a number of failure modes, the effect of which was harder to assess. More stable behaviour was obtained by raising the power from 2 to 3, and simultaneously adjusting the frame height such that the moment of inertia of the frame remained equal to the previous state.

7.3.3. List of variable updates

$$\begin{aligned} t_{skin,i+1} = max\Bigg[&\left(t_{skin,i}^4 * \frac{1}{1-MoS} * FI_{plate}\right)^{1/4} \\ &\left(t_{skin,i} * \frac{1}{1-MoS} * FI_{SMF,skin}\right) \\ &\left(t_{skin,i}^3 * \frac{1}{1-MoS} * FI_{CI,lon}\right)^{1/3} \\ &\left(t_{skin,i}^4 * \frac{1}{1-MoS} * FI_{CP,lon}\right)^{1/4}\Bigg] \quad , \quad (.001 < t_{skin,i+1} < .05) \end{aligned} \tag{7.12}$$

$$\begin{aligned} h_{frame,i+1} = max\Bigg[&\left(h_{frame,i}^4 * \frac{1}{1-MoS} * FI_{global}\right)^{1/4} \\ &\left(h_{frame,i}^4 * \frac{1}{1-MoS} * FI_{SMF,frame}\right)^{1/4} \\ &\left(h_{frame,i}^3 * \frac{1}{1-MoS} * FI_{CI,hoop}\right)^{1/3} \\ &\left(h_{frame,i}^6 * \frac{1}{1-MoS} * FI_{CP,hoop}\right)^{1/6}\Bigg] \quad , \quad (.05 < h_{frame,i+1} < .5) \end{aligned} \tag{7.13}$$

$$h_{str,i+1} = max\left[\left(h_{str,i}^4 * \frac{1}{1-MoS} * FI_{panel}\right)^{1/4} \quad , \quad (.01 < h_{str,i+1} < 0.2)\right] \tag{7.14}$$

$$\left(\frac{t}{h}\right)_{str,i+1} = \left(\left(\frac{t}{h}\right)_{str,i}^2 * \frac{1}{1-MoS} * FI_{crip}\right)^{1/2} \quad , \quad (.001 h_{str} < \left(\frac{t}{h}\right)_{str,i+1}) \tag{7.15}$$

7.4. Weight calculation method

While the sizing methodology has been determined, it is useful to estimate the total structural mass. The structural mass estimation has been approached in a relatively simplistic manner, and should therefore be viewed as a preliminary estimation.

All weights discussed in the results pertain to the modelled weights of the wing-fuselage. Naturally, this is not equivalent to the mass of the fully Flying-V structure. The following steps are performed to obtain an estimate of the total mass.

Firstly, the mass of unmodelled items is added. Significant unmodelled masses are the outboard wing and bulkhead. The outboard wing mass from Oosterom [13] is used at 6.6e3 kg per wing, and bulkhead mass from Claeys [11] (120 kg per bulkhead). The trailing edge weight is estimated using an empirical relation from Torenbeek[69]:

$$W_{TE} = S_{TE} * 60 \left(1 + 1.6 \sqrt{\frac{W_{TO}}{10^6}} + \delta \right) \tag{7.16}$$

Where S_{TE} is the surface area of the trailing edge, W_{TO} is the take-off weight and δ represents a term for control surfaces, which in this case can be set to zero. Using this relation, a mass of 4.3e3 kg was obtained per wing. However, this treats the trailing edge as the trailing edge of a conventional wing. The FV trailing edge is very large, thick, and has to carry significant fuel loads. However, the trailing edge wall and trailing edge pressure shell may assist in carrying these loads. Furthermore, the empirical relation is based on 1980's technology. Therefore, a significant weight reduction is warranted due to the use of advanced structures and materials. Lacking the means for quantification, the weight of 4.3e3 kg has been carried forward.

Another consideration is translating the modelled weight to real weight. This accounts for secondary structures, fastener weights, etc. Including the estimated weight reductions of composite materials, Oosterom[13] used a fraction of 1.2. Lacking an improved substantiation, this factor was carried forward. This has a very large effect on the resulting weight, without adequate substantiation. Therefore, the modelled to real weight should be determined in more detail in further research.

In the sizing results, a reduction factor is to be identified, which estimates the effects of improving the sizing methodology, and the use of significant optimisation. this factor is discussed in section 8.2.

8
Sizing results

The sizing results are split up into three parts. Firstly, the obtained design, failure index distribution and weight distribution is presented for the two concepts in section 8.1. This section discusses the characteristics of the individual results, but does not host a general discussion. Secondly, the mass results are presented in 8.2. Lastly, all results are discussed more generally in section 8.3.

8.1. Results

Results are presented for the original concept and the no-LE-spar (NLES) concept in sections 8.1.1 and 8.1.2 below. As the results of both concepts are very similar, section 8.1.1 discussed the obtained results in more detail, while section 8.1.2 discusses the key differences of the NLES concept w.r.t. the original concept.

8.1.1. Original concept

The sizing resulted in a modelled inboard wing mass of 21.7e3 kg for the finest mesh (32 and 16 elements per horizontal and vertical component, respectively). The obtained design, mass distribution and failure index distributions are discussed in the following paragraphs. The total structural mass is discussed in section 8.2.

Design of original concept wing-fuselage

The constant obtained design values are shown in table 8.3, and the design is visualised in figures 8.1 to 8.8. From the table alone, it can be seen that the floor and ceiling are stiffened to a much higher degree than the crown and keel. It is quite remarkable to see that the LE, TE and walls have 12 stringers compared to the 20 of the crown and keel. The crown and keel are approximately 3 times as large, and are prone to high longitudinal bending loads. The obtained stringer geometry is of a typical size, so no specific conclusions are drawn from it.

Table 8.1: Constant parameters sizing results.

Parameter	Value	Unit
Crown/keel stringers	20	-
Floor/ceiling stringers	60	-
LE/TE/wall stringers	12	-
Stringer web height	0.046	m
Stringer flange width	0.023	m
Stringer thickness	0.0021	m
Frame height-thickness ratio	33	-

The skin thickness distribution is visualised below in figures 8.1, 8.2, 8.3 and 8.4. The skin thickness distribution can be seen to vary over the length of the cabin. For the crown and keel, the variation is limited, as the skin is more or less 3 mm over the whole length, within about 10-15%. A maximum thickness is obtained at the pylon region, and just aft of this region. Significant pylon-induced cross-section loads and maximum cumulative moment (see figure D.5) are the likely cause of this local thickening.

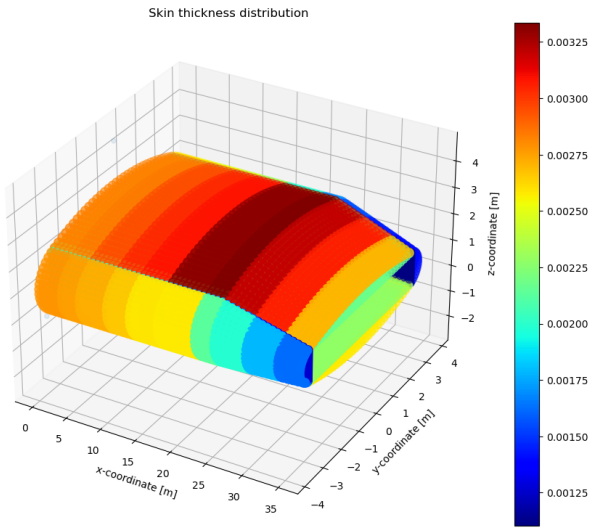

Figure 8.1: Original concept design skin thickness distribution. Aft top view.

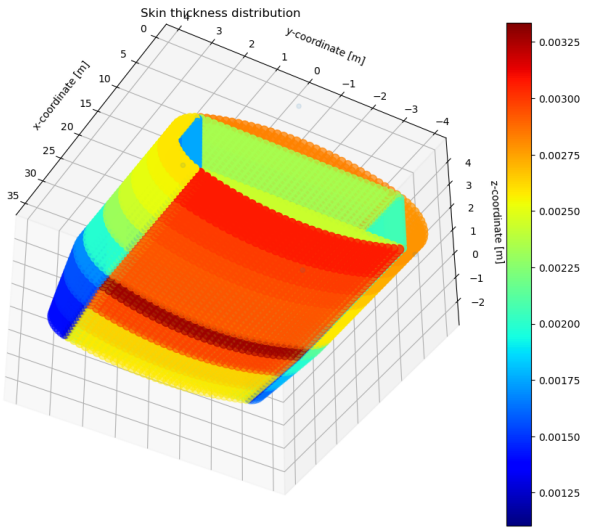

Figure 8.2: Original concept design skin thickness distribution. Front bottom view.

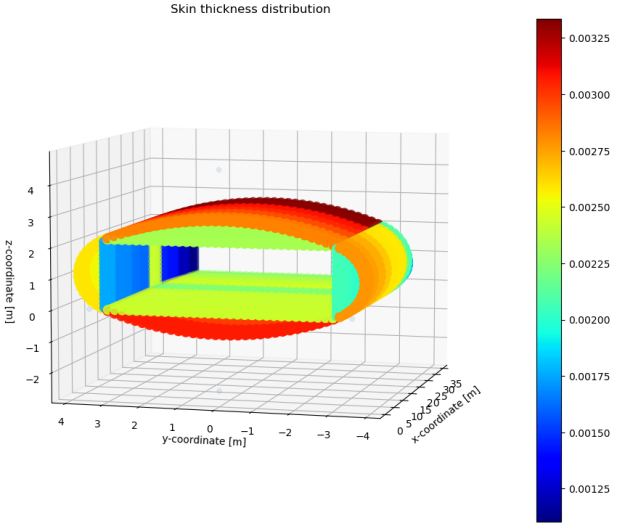

Figure 8.3: Original concept design skin thickness distribution. Cabin LE/floor view.

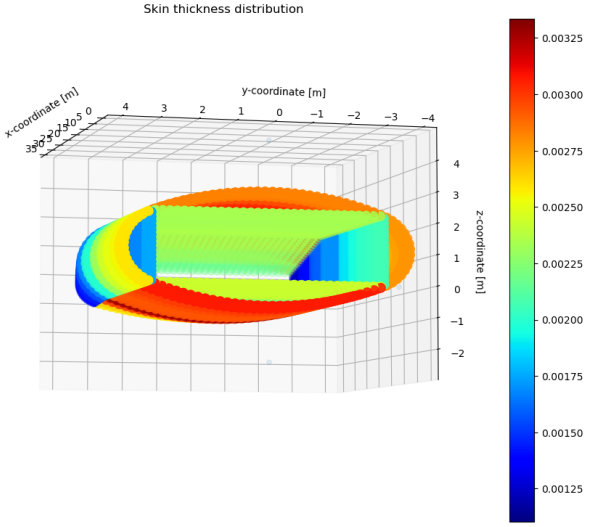

Figure 8.4: Original concept design skin thickness distribution. Cabin TE/ceiling view.

The LE and TE show a very similar thickness distribution. The TE is only consistently thicker by approx. 0.2 mm. The thickness decreases significantly from front to aft. This may be attributed to decreasing moment (about z) and torque (about x) towards the aft for practically all flight and ground load cases. A similar argument can be made for the LE and TE walls, whose thicknesses approach the lower limit of 1mm towards the aft of the cabin.

The cabin floor and ceiling thicknesses are almost completely constant over the length of the cabin. The same is true for the frames, as can be seen in figures 8.7 and 8.8. This can be attributed to the pressure-induced compression in these components. The pressure-induced compression in the floor and ceiling is constant over the length of the cabin, with a slight decrease as the cabin tapers. As shown in figures 8.32 and 8.26 further down, column buckling and plate buckling are the highest failure indices in these components. Column buckling is solely dependent on the lateral compression load, while plate buckling depends on combined loading.

The frame height distribution is shown in figures 8.5, 8.6, 8.7 and 8.8. A clear pattern is identified. For the crown and keel, the shape is very similar over the length of the cabin, with the following characteristics:

- The frame is large in the centre of the arc, due to a combination of high tensile loads and high bend-

ing loads, leading to high stresses in the skin and frame outer flange. These high tensile stresses are specifically important for fatigue-induced failure modes.
- The frame is large near the vertex joints, as the bending stresses spike, but in opposite sign as seen in the arc centre. The frame inner flange stress becomes critical. Again, fatigue is of primary importance.
- In between these regions, the bending is much lower, leading to a decreased frame size.

As the crown and keel arc radius increases significantly in tapered section, the above mentioned stresses increase, and thus the frame increases in size. So while the available space decreases for the tapered region, the frame size (and weight) increases.

The LE and TE possess frames which are near the minimum set boundary at a height of 50 mm, only slightly increasing in size near the vertex joints. This is the case as the LE/TE radius is small, inducing low pure axial stresses due to pressurisation. Furthermore, the walls support the arcs effectively, leading to low bending-induced stresses. As for the walls, the beams are also very small, near the lower boundary of 50 mm web height.

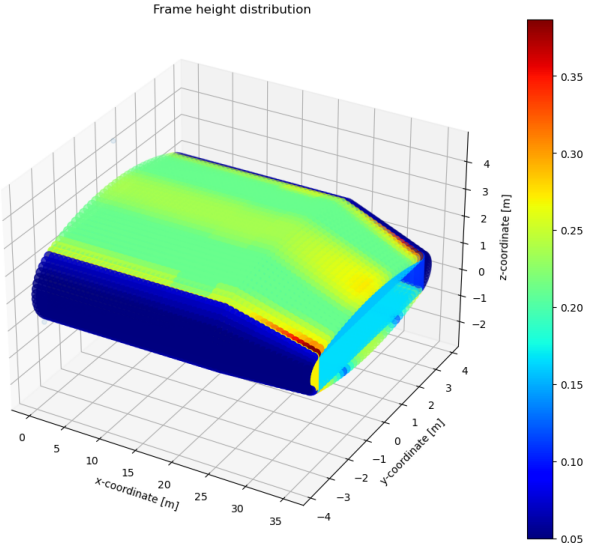

Figure 8.5: Original concept design frame height distribution. Aft top view.

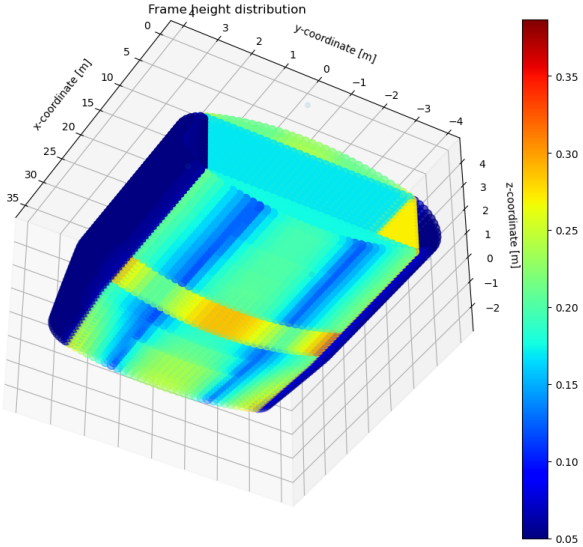

Figure 8.6: Original concept design frame height distribution. Front bottom view.

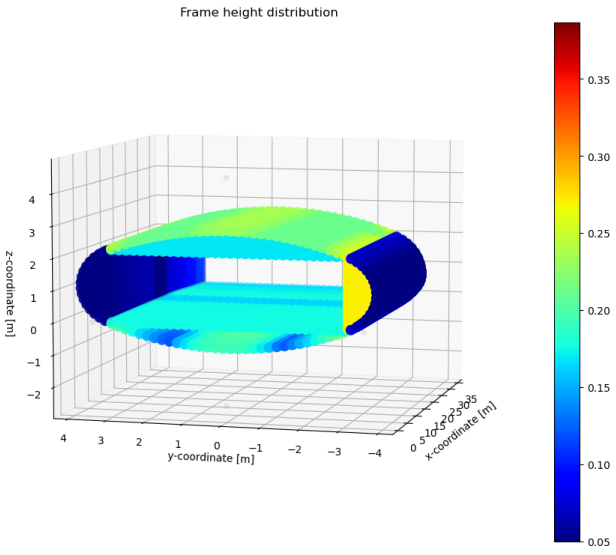

Figure 8.7: Original concept design frame height distribution. Cabin LE/floor view.

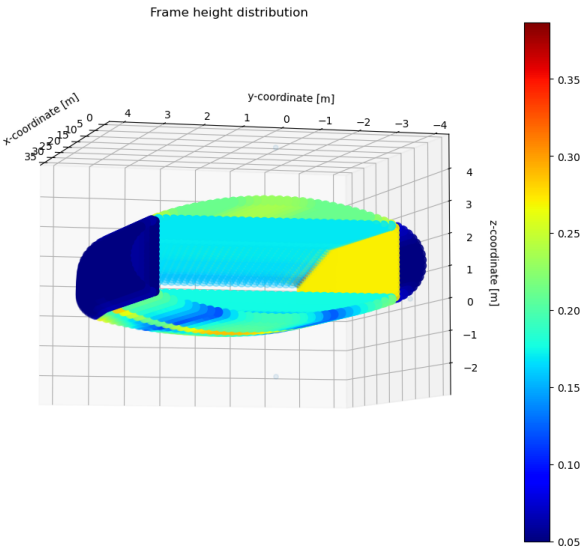

Figure 8.8: Original concept design frame height distribution. Cabin TE/ceiling view.

The obtained mass distribution can be found below in figures 8.9, 8.10 and 8.11, for the main groups, skin

and frame components. As the number of stringers are constant over the length of the cabin, a separate plot is omitted. Overall, the mass distribution is relatively constant, apart from the clear bump in frame weight at the pylon. Naturally, the stringer numbers have been set constant over the length of the cabin and therefore do not change. However, it is quite remarkable that the skin and frame weight remains so similar. The mass increase for the sections is rather limited. For the tapered region, inverse behaviour is observed for the skin and frame weight, as skin mass decreases significantly, while the frame mass increases.

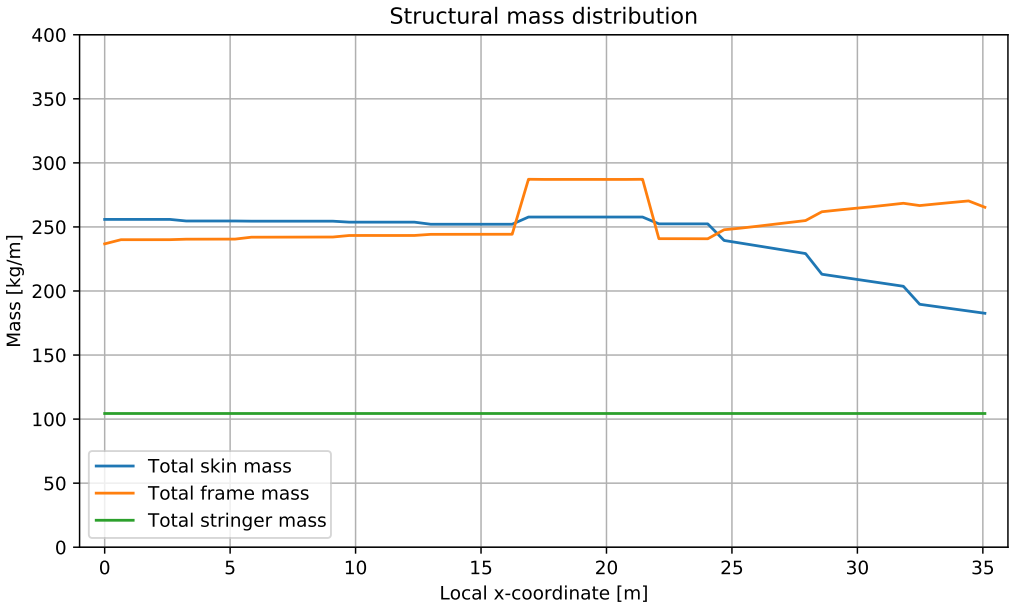

Figure 8.9: Mass distribution of the main structural mass groups.

From figure 8.10, the skin mass distribution shows a very gradual behaviour. Especially the floor and ceiling mass can be seen to be practically constant along the cabin, except for the pylon sections. All skin panels decrease in mass significantly in the tapered region. This is attributed to the decrease in thickness, but also as the components decrease in size.

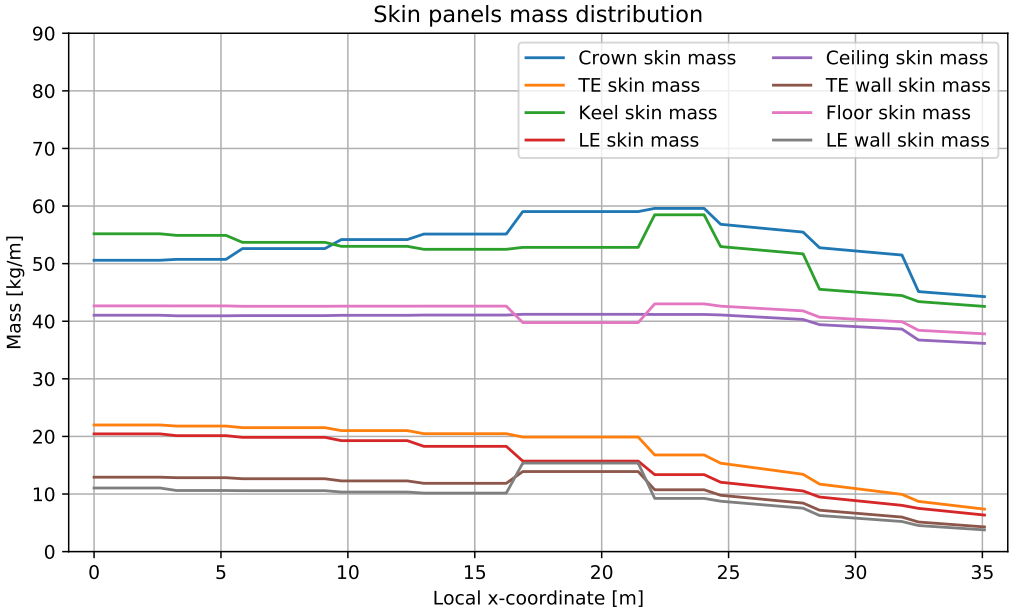

Figure 8.10: Mass distribution of the different skins.

From figure 8.11, the individual frame components can be seen to be almost completely constant until the pylon frames. Oddly, only the keel frames increase in size, while the other frame components are unaffected,

or even decrease (floor beam). Due to the flattening of the cross-section in the tapered cabin, the bending in the crown and keel increases, and so the weight increases greatly. The LE/TE frames and wall frames are very light.

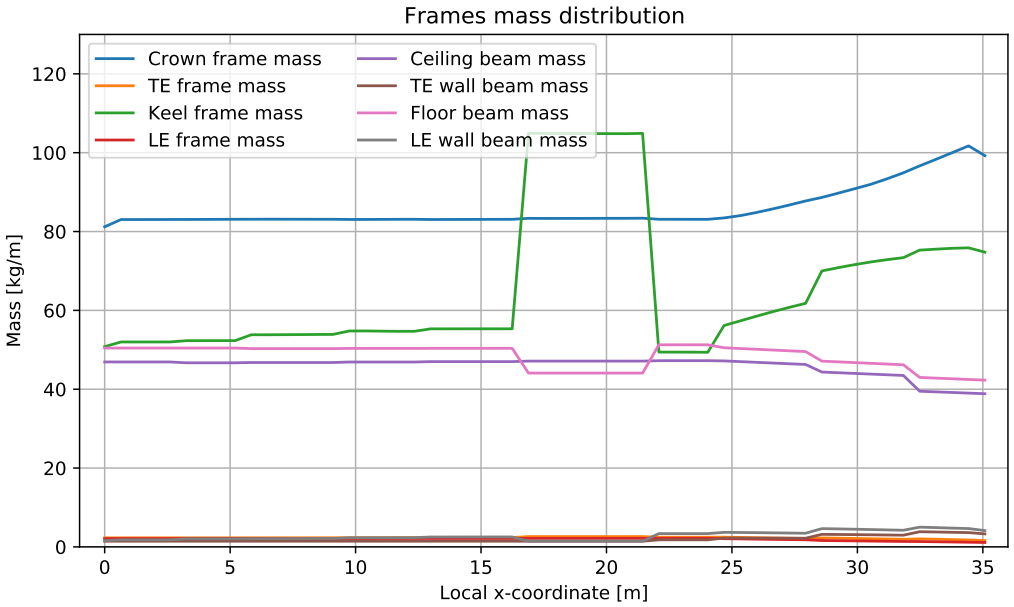

Figure 8.11: Mass distribution of the different frame/beam components. The TE frame mass is almost identical to the LE frame mass, which overlap.

Maximum failure indices

The maximum failure indices are presented in table 8.2. It can be seen that static material failure is not critical anywhere in the structure. On the contrary, many stability modes have critical maximum failure indices. For fatigue, clearly the longitudinal stresses are far less important than the stresses in the cross-section. The crack propagation failure of the frame inner flange is the highest, due to the high bending-induced tensile loads. Not far behind is the skin crack initiation. Overall, the design shows to be driven by stability and fatigue failure. A more detailed view of the individual failure index distributions is shown in the next paragraph.

Table 8.2: Original concept maximum failure indices. SMF = static material failure, CI = crack initiation, CP = crack propagation. Driving failure modes are shown in bold.

Code	Maximum FI	Value [-]
FI01	Skin axial SMF	0.50
FI02	Skin shear SMF	0.57
FI03	Stringers SMF	0.50
FI04	Frame inner flange SMF	0.65
FI05	Frame outer flange SMF	0.34
FI06	Biaxial global buckling	**0.95**
FI07	Shear global buckling	0.07
FI08	Combined global buckling	**0.95**
FI09	Biaxial panel buckling	**0.97**
FI10	Shear panel buckling	0.06
FI11	Combined panel buckling	**0.97**
FI12	Biaxial plate buckling	**0.96**
FI13	Shear plate buckling	**0.97**
FI14	Total plate buckling	**0.97**

Code	Maximum FI	Value [-]
FI15	Stringer crippling	**0.94**
FI16	Frame crippling	**0.98**
FI17	Crossbeam column buckling	**0.96**
FI18	Skin lon. axial CI	0.04
FI19	Skin shear CI	0.17
FI20	Skin hoop CI	**0.92**
FI21	Frame inner flange CI	0.27
FI22	Frame outer flange CI	0.59
FI23	Skin lon. axial CP	0.03
FI24	Skin shear CP	0.03
FI25	Skin hoop CP	0.36
FI26	Frame inner flange CP	**0.95**
FI27	Frame outer flange CP	0.47

Failure surfaces

Critical failure modes are indicated in figures 8.12 and 8.13. However, these figures should not be used directly to extract information on the most critical failure modes. Naturally, the shown failure modes correspond to the highest failure index at that location. However, as a high number of failure modes drive the design, for most locations in the structure there are many failure modes with a FI which is only a fraction lower than the critical one. The maximum failure mode at that location is simply the maximum one at the last state before the sizer stops, and is not necessarily the most important failure mode in that location.

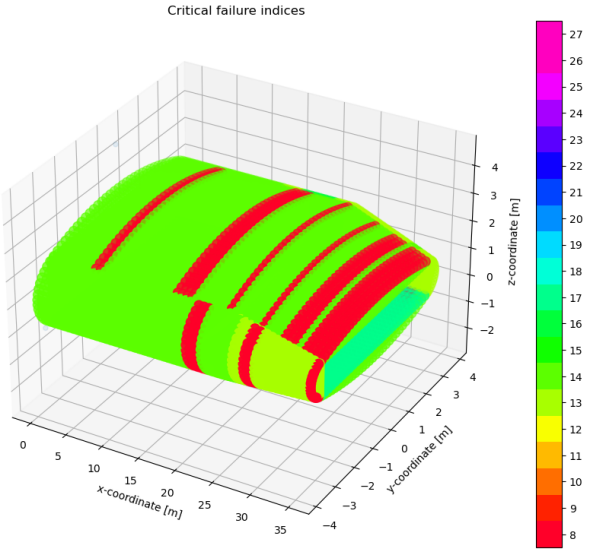

Figure 8.12: Original concept maximum failure modes.

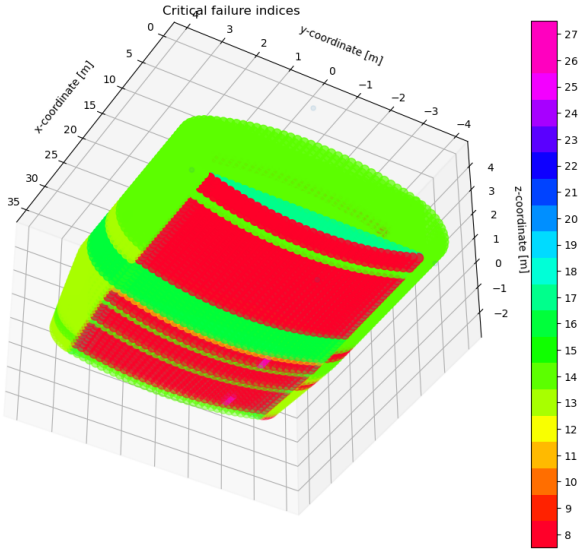

Figure 8.13: Original concept maximum failure modes.

The maximum failure index distribution is shown in figures 8.14 and 8.15. This distribution effectively shows the combined margin of safety of the structural components under all load cases, for the maximum load cases. However, one should not interpret this as a token of the efficiency, or the level of optimisation, of the structure, as the maximum failure indices are shown.

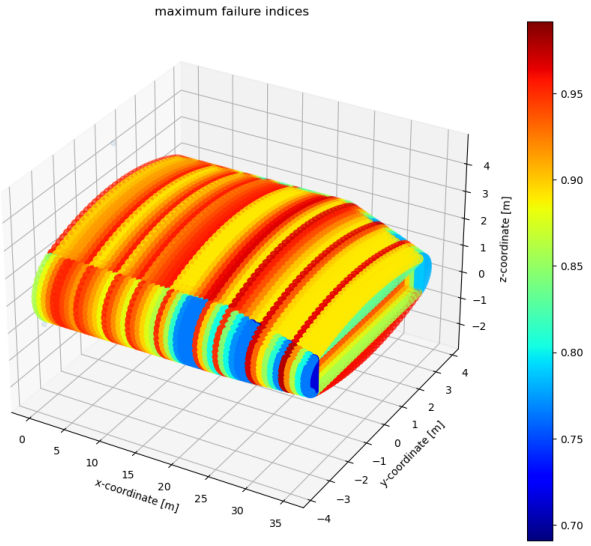

Figure 8.14: Maximum failure index distribution

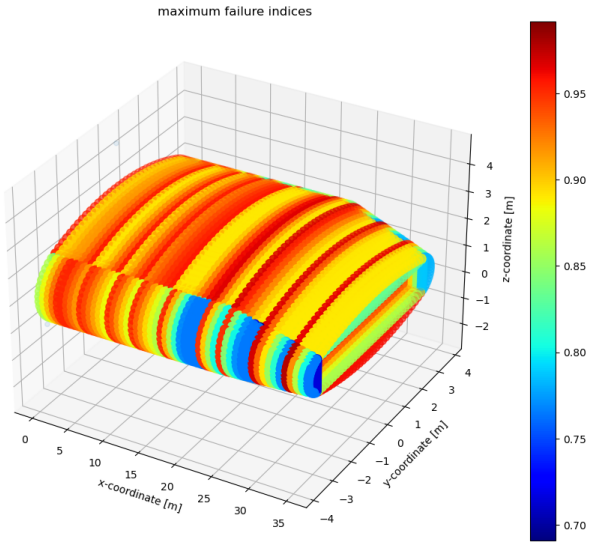

Figure 8.15: Maximum failure index distribution

In the figures below, the individual failure index distributions are presented, for the failure modes as shown in table 8.2. However, not all failure modes are shown, to reduce the number of plots. The reductions that have been made are listed below:

- For static material failure, only the surfaces of the skins and frame inner flange are shown. This is the case as the experienced stresses are always higher than the stresses in the stringers or frame outer flange, which are therefore omitted.
- Similarly, the static material failure distribution of the frame outer flange is not shown. This is the case as the failure index of the skin of frame inner flange will always be higher. Both the skin and the frame inner flange lie further away from the local neutral line.
- Buckling modes are only shown for the combined case, omitting the individual biaxial and shear distributions.
- While the maximum longitudinal and shear crack initiation failure indices are very low, the distributions are shown as the affected regions are of interest. The longitudinal and shear crack propagation failure index distributions are practically identical. As the maximum values are very low, these figures are omitted.

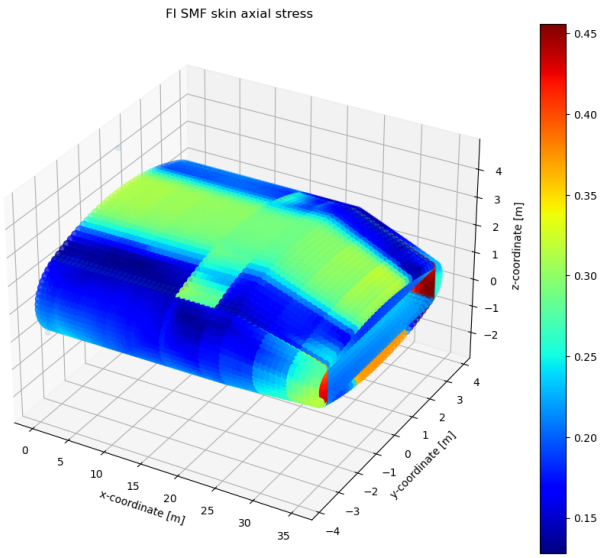

Figure 8.16: FI01 Skin principal axial stress static material failure

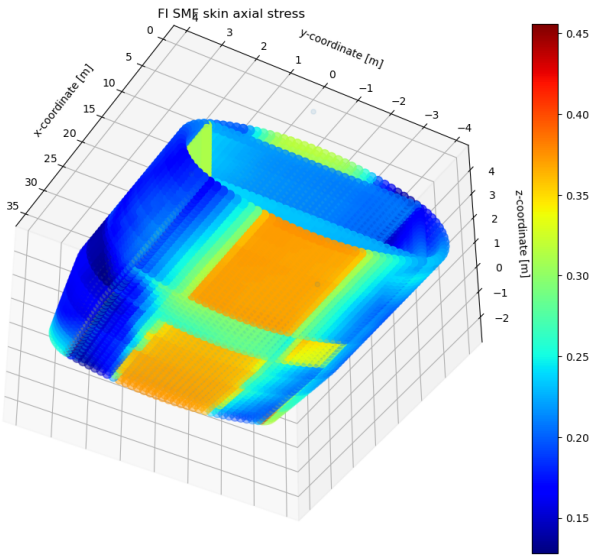

Figure 8.17: FI01 Skin principal axial stress static material failure

Figures 8.16 and 8.17 show the failure index distribution for the static material failure of the skin for the principal axial stresses. As it is the principal stress, both longitudinal and hoop stresses have been included. However, the observed distribution is very similar to that of only the hoop stresses. The bending contribution is clearly visible in the crown and keel arc centre. Furthermore, the pylon sections clearly show a different stress distribution due to the large difference in hoop stresses. The highest failure indices are obtained at the back of the tapered section, in the walls. This is the case as the wall plates are very thin, and the wall frames are very small. Overall, the principal axial stress FI remains relatively low throughout the whole structure. A very similar distribution was obtained for axial stresses in the outer flanges of the frames. However, as the flange is closer to the local neutral line, the cross-section stresses are lower. Furthermore, the frames do not carry longitudinal stresses. Therefore, its failure index distribution is lower over the whole structure compared to the skin. This led to the omission of this FI distribution.

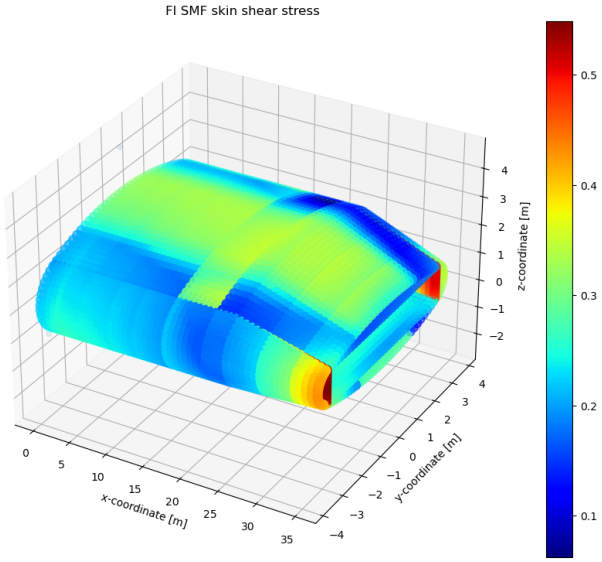

Figure 8.18: FI02 Skin principal shear stress static material failure

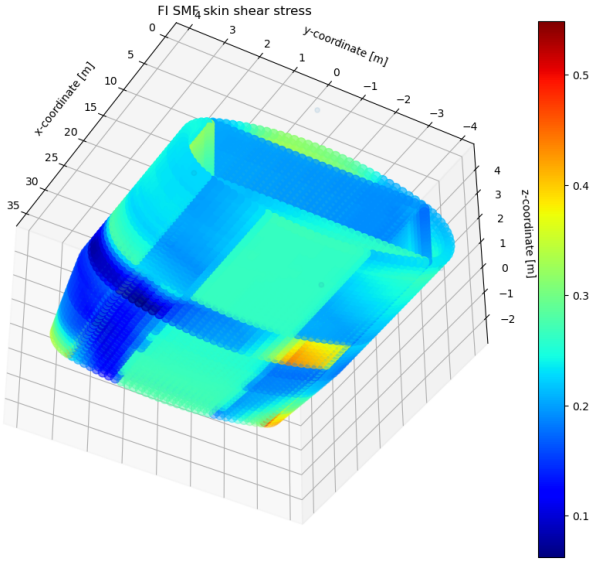

Figure 8.19: FI02 Skin principal shear stress static material failure

Figures 8.18 and 8.19 show the failure index distribution for the static material failure of the skin for the principal shear stress. A similar distribution is observed as for the principal axial stresses. Again, a maximum is found in the walls at the end of the tapered section.

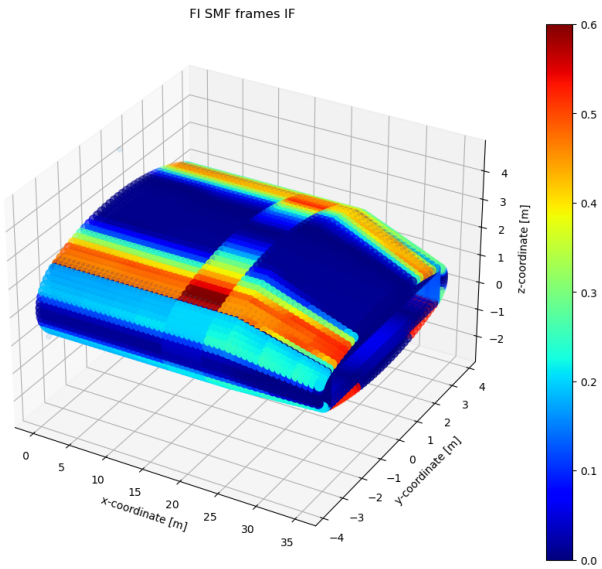

Figure 8.20: FI04 frame inner flange axial stress static material failure

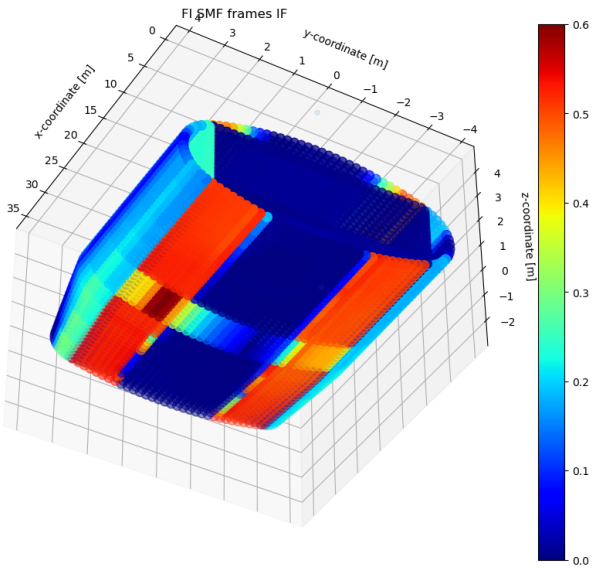

Figure 8.21: FI04 frame inner flange axial stress static material failure

Figures 8.20 and 8.21 show the failure index distribution for the static material failure of the frames inner flanges (pointing towards the inside of the structure) for the axial stresses. An opposite behaviour is observed than for the skins. This is the case as the inner flange is on the other side of the local neutral line. Maximum failure indices are observed in the crown and keel frames, near the vertex joints. CLearly, the pylon frames show a large shift in stresses due to loads on the landing gear and engine. Overall, the failure index is relatively low.

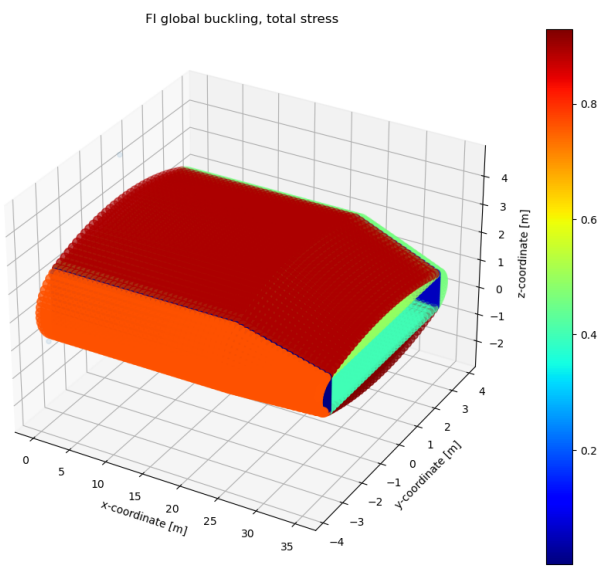

Figure 8.22: FI08 Global buckling FI distribution.

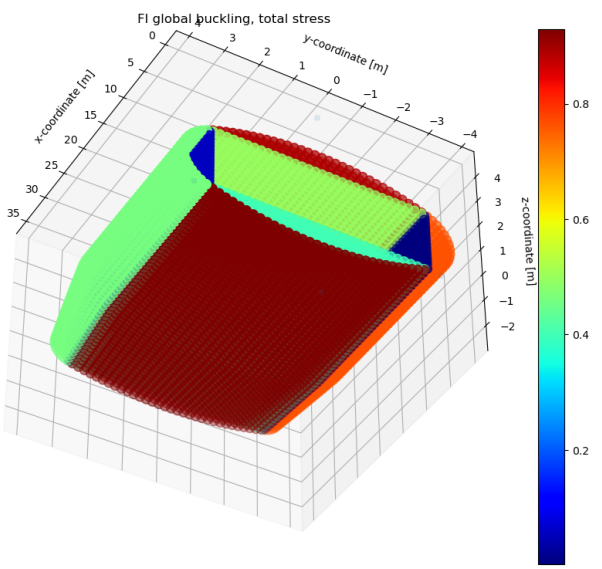

Figure 8.23: FI08 Global buckling FI distribution

Figures 8.22 and 8.23 show the failure index distribution for global buckling under combined loading. The failure mode was assessed using the mean properties of the whole crown, keel, etc. Therefore, a single value can be seen for each region. Clearly, the highest failure index can be found in the crown and keel. It is remarkable that the keel possesses a higher failure index than the crown, as typically this is critical for top panels. This failure mode is a clear design driver for the keel and crown structure. Specifically for global buckling, the frames were identified to be the main contributors, and are therefore sized to counteract this failure mode.

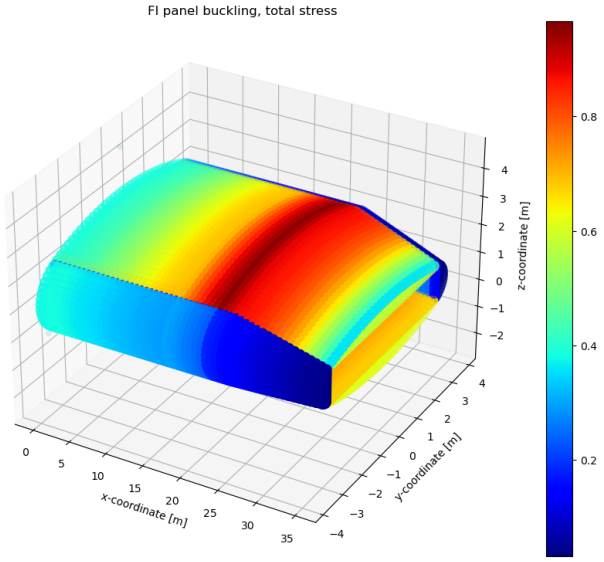

Figure 8.24: FI11 Panel buckling FI distribution.

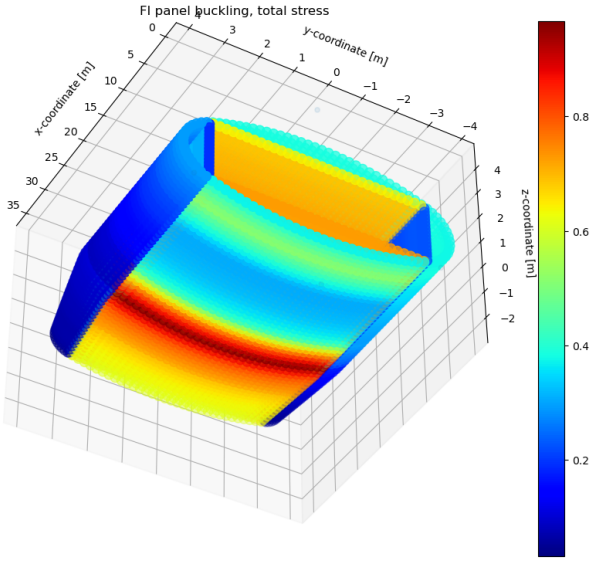

Figure 8.25: FI11 Panel buckling FI distribution.

Figures 8.24 and 8.25 show the failure index distribution for panel buckling failure under combined loading. Considering that the aspect ratio and number of stringers is equal for each panel along the cabin length, the observed FI distribution corresponds to the maximum compressive running load along the cabin. More specifically, it corresponds to the peak moment about y, as shown in figures D.5, D.11, D.17, etc. This failure mode is a clear design driver for the stringers.

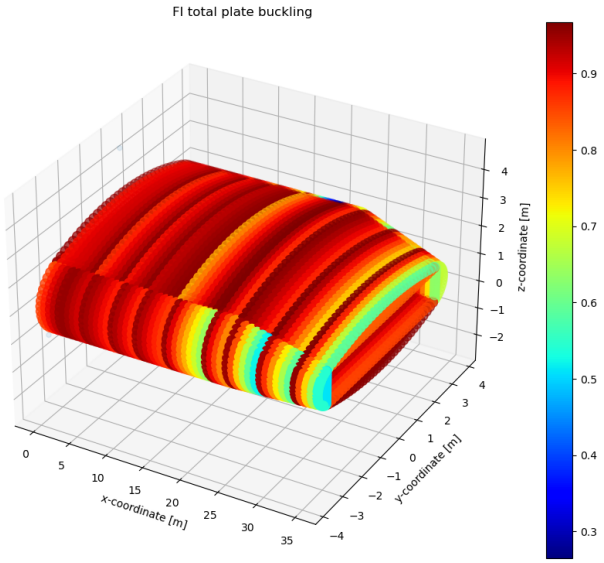

Figure 8.26: FI14 Plate buckling FI distribution.

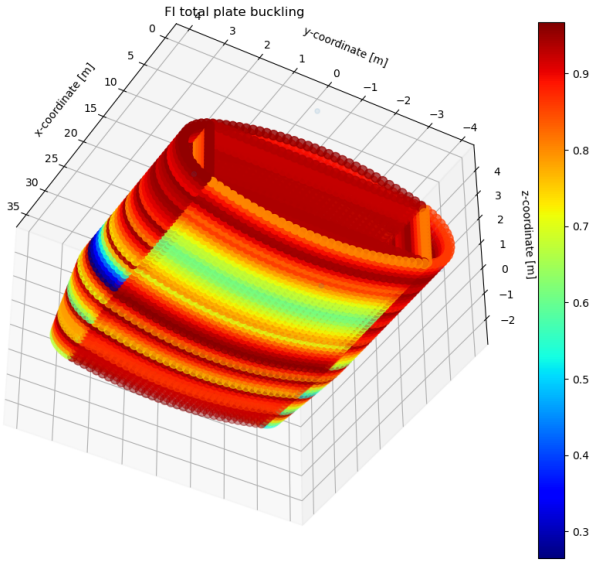

Figure 8.27: FI14 Plate buckling FI distribution

Figures 8.26 and 8.27 show the failure index distribution for plate buckling. The effect of the constant thickness skin panels is clearly visible, as the failure index varies significantly in a single panel. This is especially apparent in the panels of the tapered section. In the constant cabin section, the failure index does not vary as much for all panels. Therefore, constant thickness panels are likely a cost-effective solution, while not increasing the weight as much. For the tapered section skin panels, a different solution is potentially required. For each panel, one end has a critical FI, while the other end decreases to nearly half the value. Significant gains can be made for panels with a varying thickness. Plate buckling under combined loading is one of the key design drivers for the skin thickness in the structure. As the number of stringers was determined in the stringer trials (section 7.2.3), only the skin thickness was sized to counteract this failure mode.

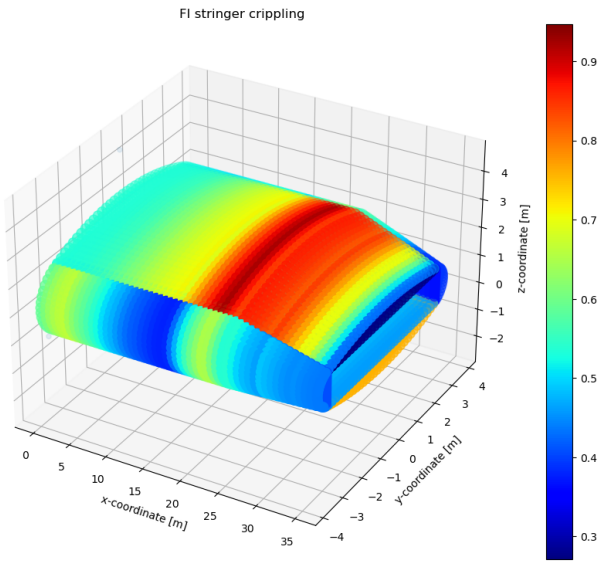

Figure 8.28: FI15 Stringer crippling FI distribution

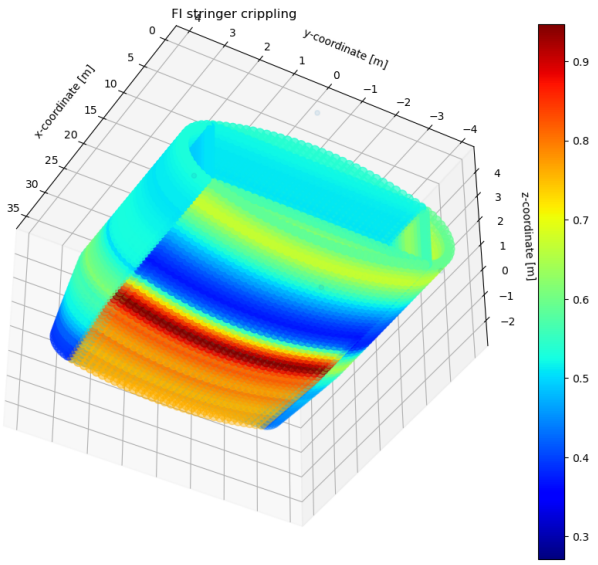

Figure 8.29: FI15 Stringer crippling FI distribution

Figures 8.28 and 8.29 show the failure index distribution for stringer crippling. The number of stringers is constant over the length of the cabin, while the skins vary in thickness. Still, the same argument can be made as for the panel buckling FI distribution: the distribution corresponds approximately to the running moment about z. This failure mode drives the stringer cross-section design significantly. Clearly, there are potential improvements. Only a limited region experiences crippling issues, on the crown and keel. The exact same stringer geometry is used throughout the whole structure. However, the stringer is sized for the critical panels. This discussion is continued in section 8.3.1.

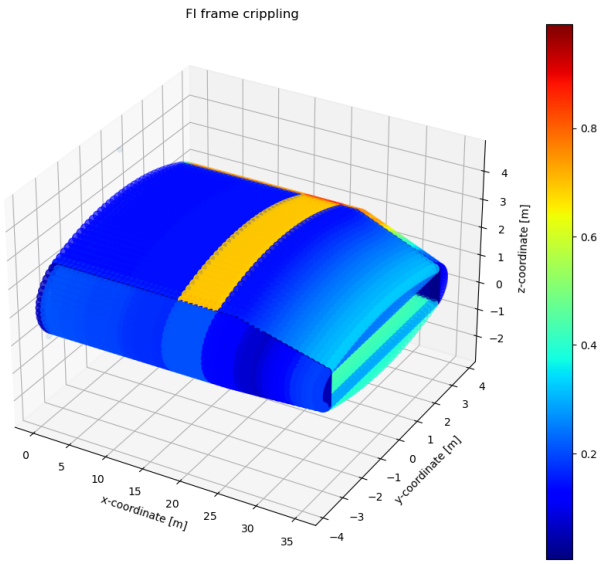

Figure 8.30: FI16 Frame crippling FI distribution

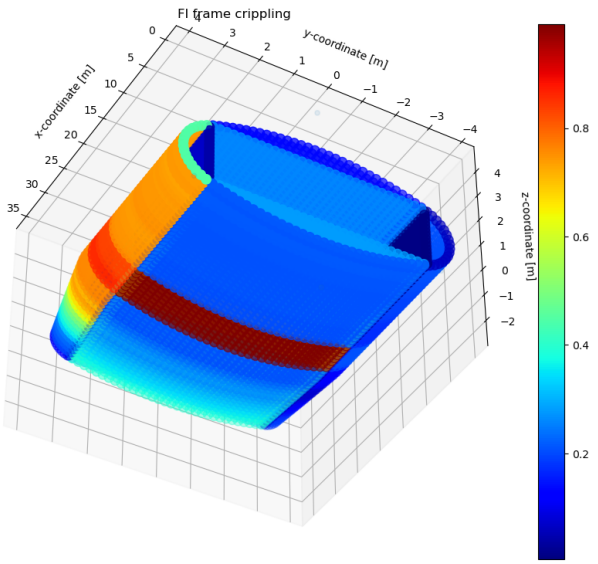

Figure 8.31: FI16 Frame crippling FI distribution

Figures 8.30 and 8.31 show the failure index distribution for frame crippling. Clearly, there are two regions which are of interest. Firstly, the pylon sections show critical crippling failure indices. The pylon introduces large bending loads, causing the crippling of the frame flanges. Secondly, the leading edge frames show a relatively high failure index. While not driving the design as in the frame sections, the failure index is still approximately 0.8. It is not clear why this occurs. Due to time constraints, and due to the fact that this failure mode is not locally driving the design, this has not been explored further. However, this behaviour is unexpected.

For the frame sizing, the height-thickness ratio was set equal for all frames, to control against frame crip-

pling centrally. Clearly, a large portion of the frames is over-designed against crippling. This failure mode drives the cross-section design of the frames significantly, leading to many frames which are over-designed. This discussion is continued in section 8.3.1.

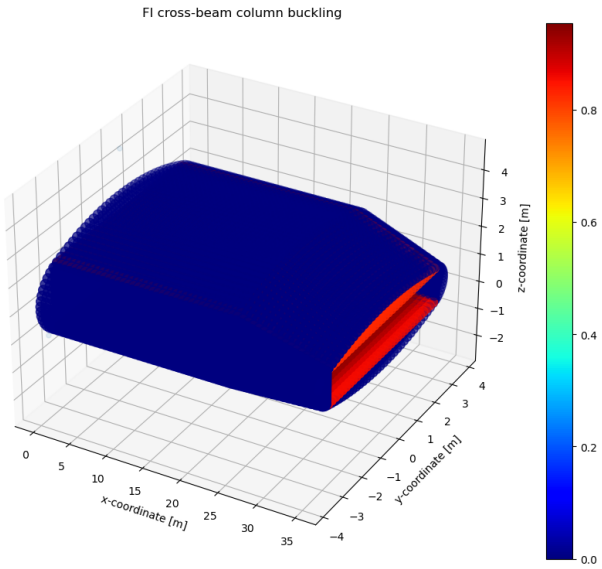

Figure 8.32: FI17 Column buckling distribution

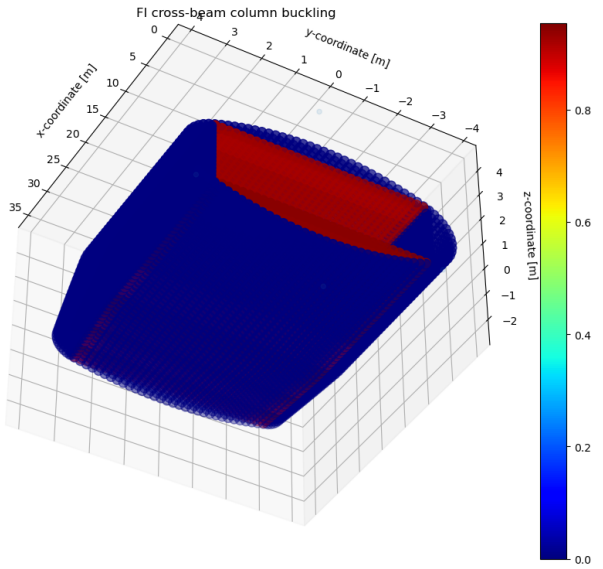

Figure 8.33: FI17 Column buckling distribution

Figures 8.32 and 8.33 show the failure index distribution for column buckling. The failure index is critical for the floor and ceiling, and are the primary drivers for the frame size in these components.

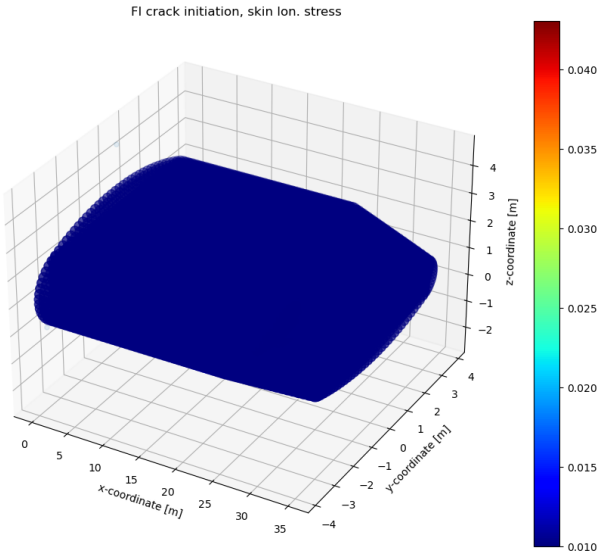

Figure 8.34: FI18 Skin longitudinal stress crack initiation FI distribution

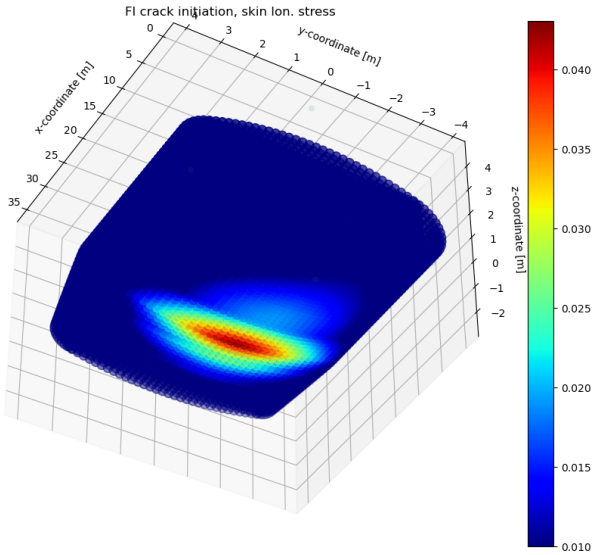

Figure 8.35: FI18 Skin longitudinal stress crack initiation FI distribution

Figures 8.30 and 8.31 show the failure index distribution for crack initiation of the skin under longitudinal stress. Firstly, it should be noted that the failure index distribution is very low. However, The location is of interest. The maximum FI region is located on the keel skin, at the location of maximum running moment about y. For reference on the running loads, see figures D.5, D.11, D.17. The same distribution was found for crack propagation of the skin under longitudinal stress. For brevity, this figure is omitted.

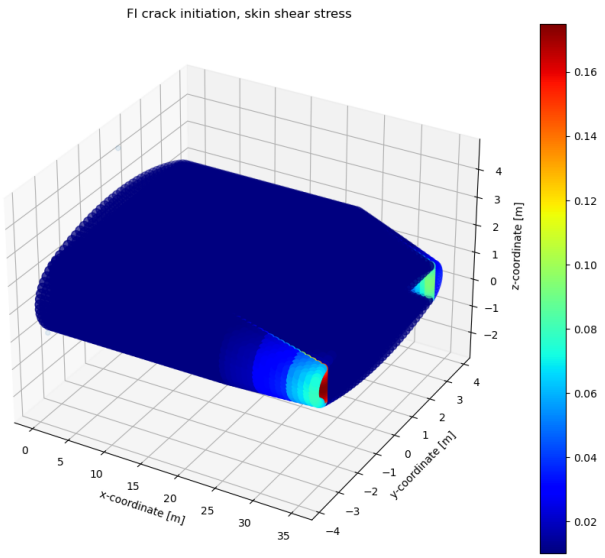

Figure 8.36: FI19 Skin shear stress crack initiation FI distribution. Peak at LE inboard-outboard transition.

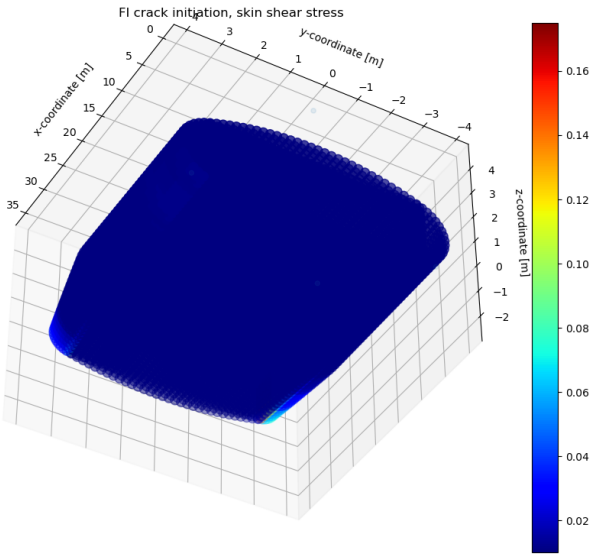

Figure 8.37: FI19 Skin shear stress crack initiation FI distribution

Figures 8.36 and 8.37 show the failure index distribution for crack initiation of the skin under shear stresses. The regions of interest are the walls, as they carry significant shear loads, but are very thin. Nonetheless, this failure mode appears to have no effect on the design.

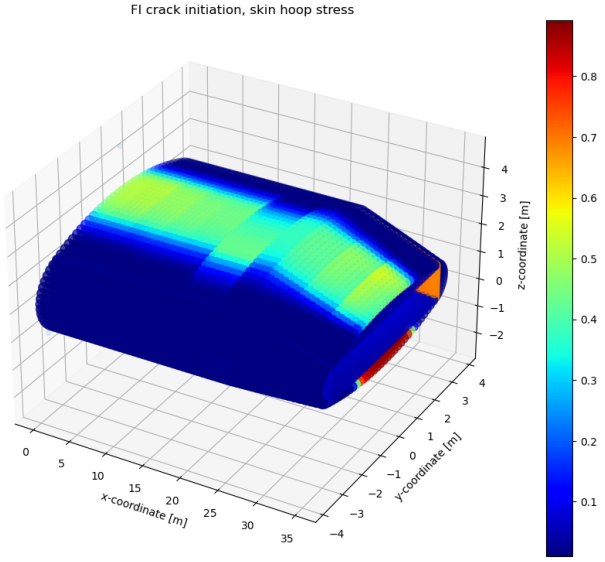

Figure 8.38: FI20 Skin hoop stress crack initiation FI distribution

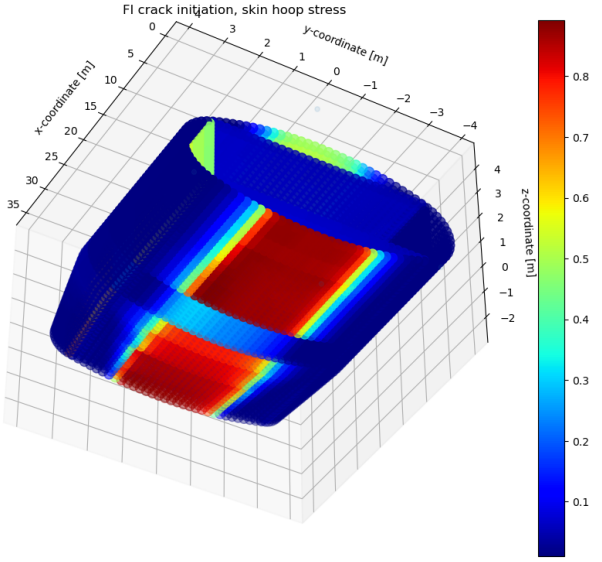

Figure 8.39: FI20 Skin hoop stress crack initiation FI distribution

Figures 8.38 and 8.39 show the failure index distribution for crack initiation of the skin under hoop stresses. Clearly, the failure contributes significantly to the design, as very high failure indices are found, mainly on the keel. The locations are where the largest tensile stresses occur in the skin due to pure axial stress and bending. Significant failure indices are found in the walls, as these are under significant tensile loads due to pressurisation. An almost identical distribution is found for the frame outer flange crack initiation distribution, but at lower magnitudes. Therefore, these figures are omitted.

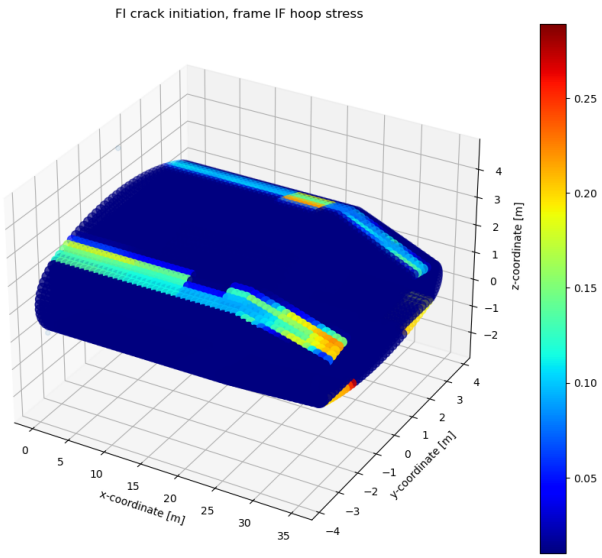

Figure 8.40: FI21 Frame inner flange hoop stress crack initiation FI distribution

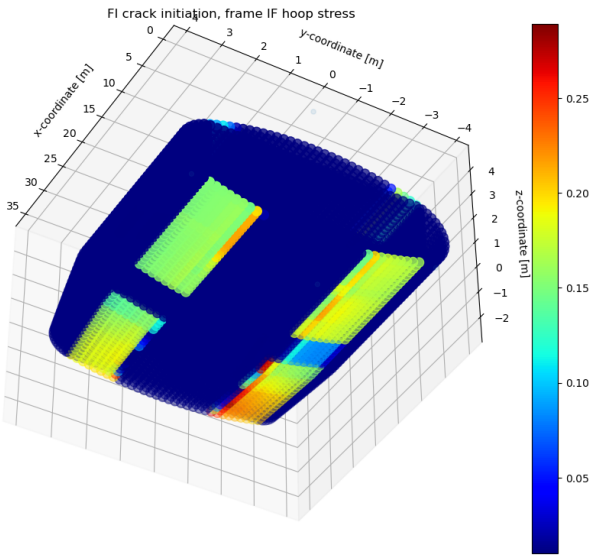

Figure 8.41: FI21 Frame inner flange hoop stress crack initiation FI distribution

Figures 8.40 and 8.41 show the failure index distribution for crack initiation of the frame inner flange (pointing towards the inside of the cabin). The regions of interest are where the bending induced tensile stresses are the highest: near the vertex joints.

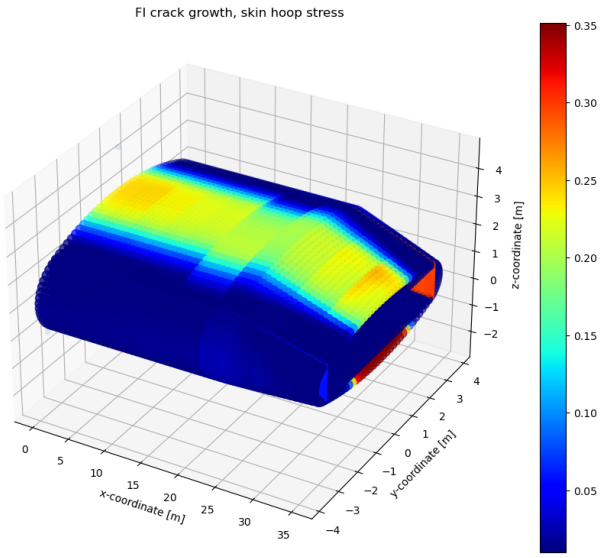

Figure 8.42: FI25 Skin hoop stress crack propagation FI distribution.

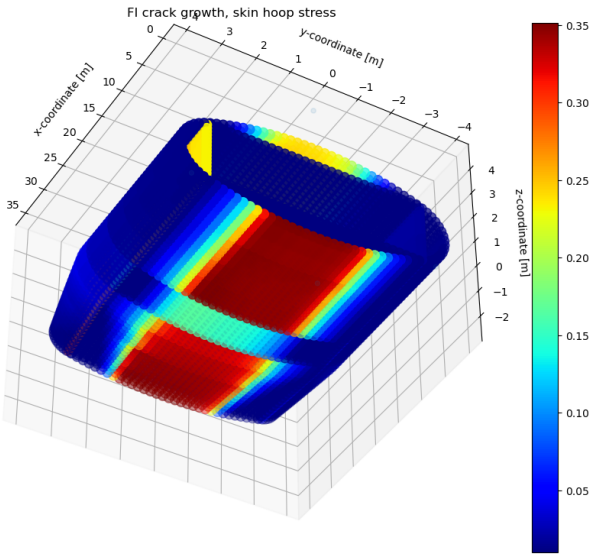

Figure 8.43: FI25 Skin hoop stress crack propagation FI distribution

Figures 8.42 and 8.43 show the failure index distribution for crack propagation in the skin. The obtained distribution is almost identical to the crack initiation distribution under hoop stress. However, the magnitude is significantly lower at a maximum of 0.36. Therefore, this failure mode is not driving the design.

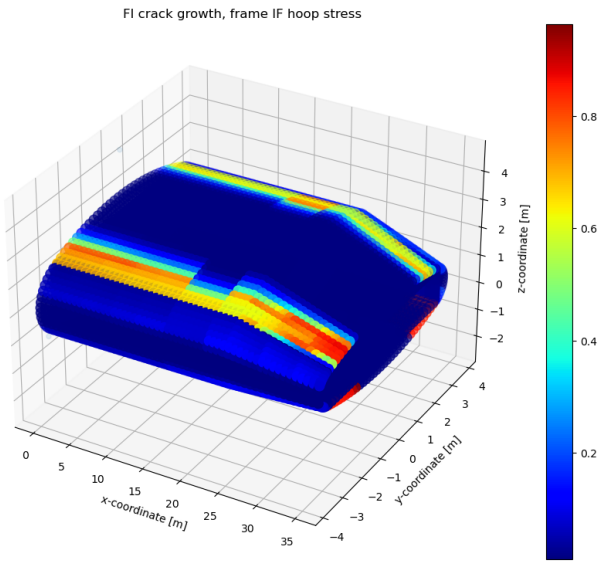

Figure 8.44: FI 26 Frame inner flange hoop stress crack propagation FI distribution

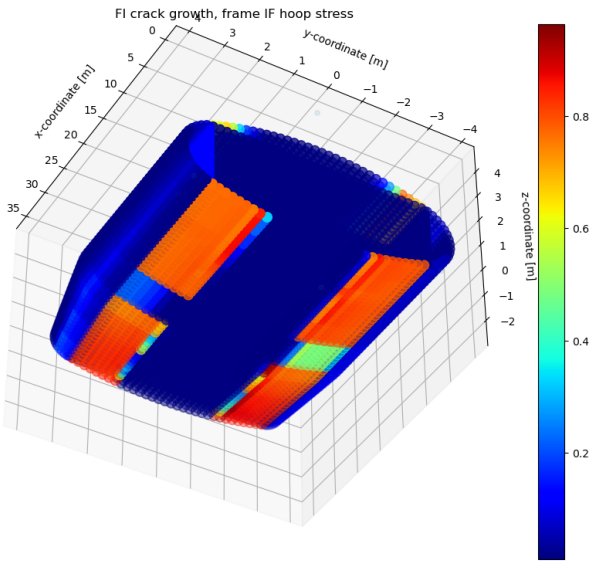

Figure 8.45: FI 26 Frame inner flange hoop stress crack propagation FI distribution

Figures 8.44 and 8.45 show the failure index distribution for crack propagation in the frame inner flanges (pointing towards the inside of the cabin). Clearly, the observed failure indices are very high, and are locally driving the frame design. The regions of high FIs correspond to the maximum bending induced tensile stresses in the frame inner flanges. This is specifically true for the keel frames.

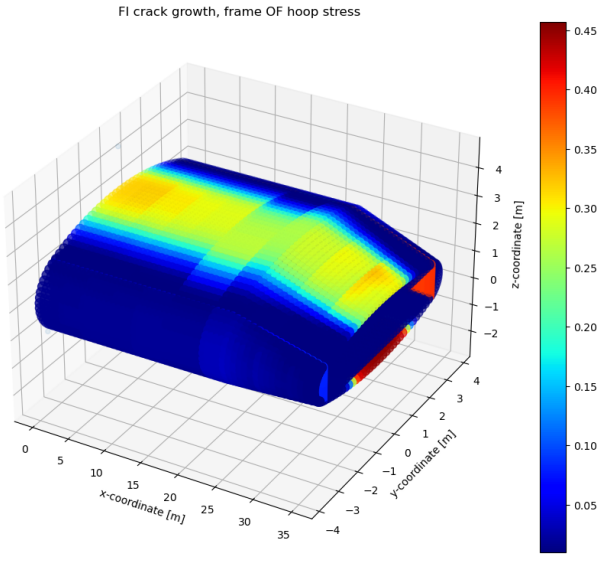

Figure 8.46: FI 27 Frame outer flange hoop stress crack propagation FI distribution

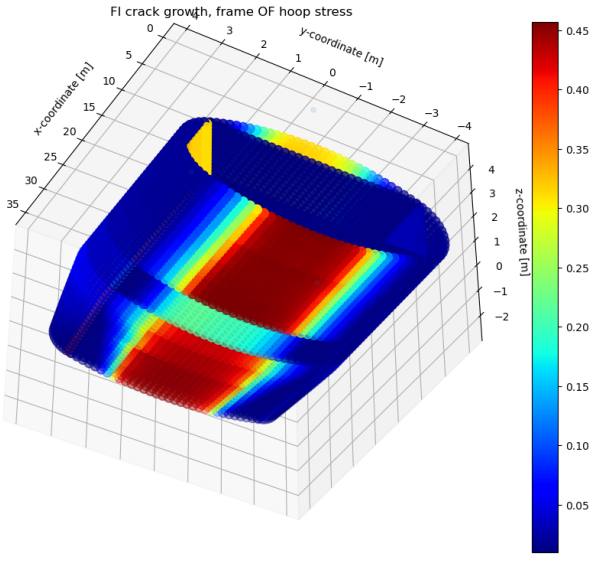

Figure 8.47: FI 27 Frame outer flange hoop stress crack propagation FI distribution

Figures 8.46 and 8.47 show the failure index distribution for crack propagation in the frame outer flanges (pointing outwards of the cabin). The distribution corresponds to the maximum tensile stresses in the inner flanges.

8.1.2. NLES concept results

The NLES concept wing-fuselage structure model weighs in at 22.6e3 kg, for the finest mesh (32 and 16 elements per horizontal and vertical component, respectively). This is a difference of 900 kg w.r.t. the original concept, which corresponds to a 4% modelled wing-fuselage weight increase. The obtained design, mass distribution and failure index distributions are discussed in the following paragraphs. The total structural mass is discussed in section 8.3.

Design

The obtained design is visualised below in terms of the skin thickness distribution (figures 8.48 and 8.49), as well as the frame height distribution (figures 8.50 and figure 8.51). The constant obtained design values are shown in table 8.3. The obtained results are very similar to the original concept.

Table 8.3: Constant parameters sizing results.

Parameter	Value	Unit
Crown/keel stringers	20	-
Floor/ceiling stringers	60	-
LE stringers	17	-
TE/wall stringers	12	-
Stringer web height	0.047	m
Stringer flange width	0.024	m
Stringer thickness	0.0021	m
Frame height-thickness ratio	35	-

The skin thickness distribution (figures 8.48 and 8.49) is very similar to the original concept. One exception is the leading edge. Contrary to what was expected, the leading edge is very thin. This can be explained by the presence of large frames on the leading edge (see figures 8.50, 8.51) which counteract the bending. Is is hypothesises that this allows for a thinner skin. This is not necessarily advantageous, as discussed in 8.3.1.

The frame height distribution follows a similar distribution as the original concept. The leading edge obviously has large frames. Due to pressurisation the LE arc is opened, leading to maximum moment at the centre of the LE arc. Clearly, this is where the frames are the largest. The floor and ceiling cross-beams are slightly larger. There are subtle differences in the crown and keel. Firstly, the regions where the frame is smallest have shifted forward to the transition with the LE. Secondly, the crown and keel frames are larger in the tapered region. However, the peak at the end of the trailing cabin, which is still observed on near the TE joint, has disappeared for the LE.

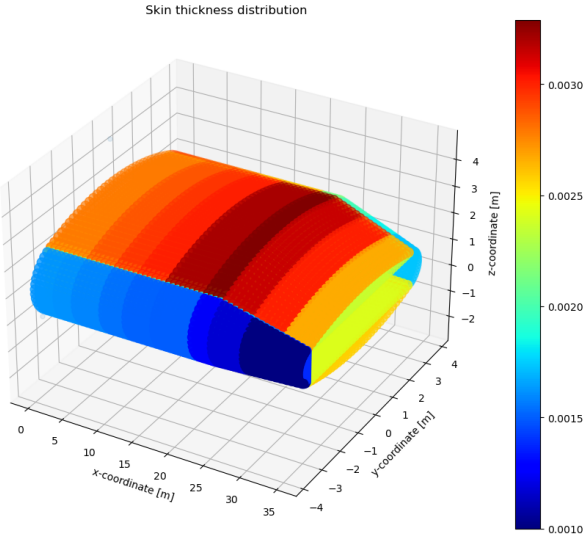

Figure 8.48: Skin thickness distribution. Aft top view.

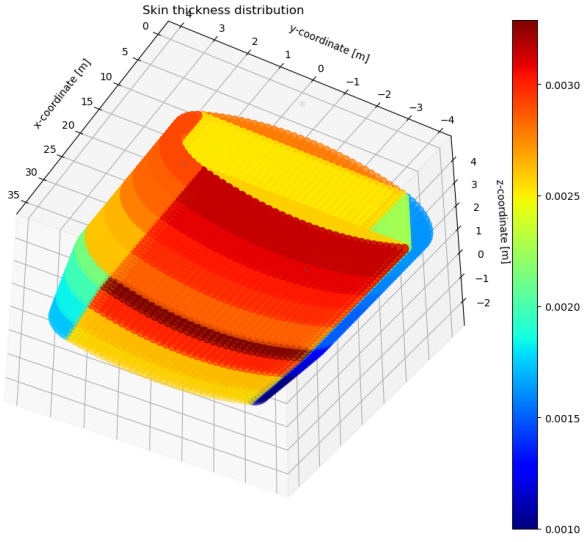

Figure 8.49: Skin thickness distribution. Front bottom view.

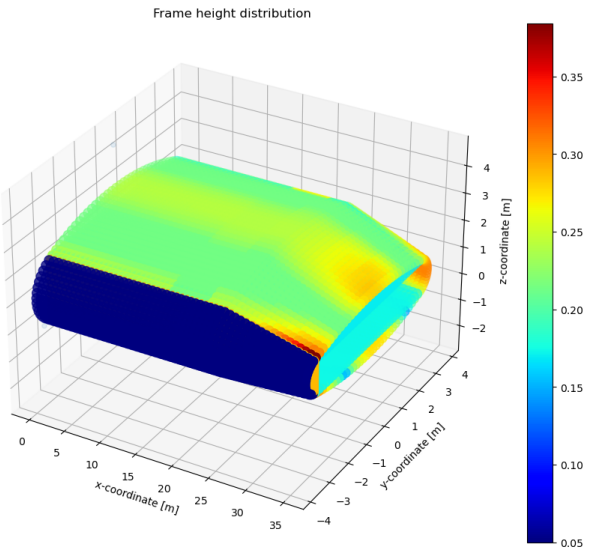

Figure 8.50: Frame height distribution. Aft top view.

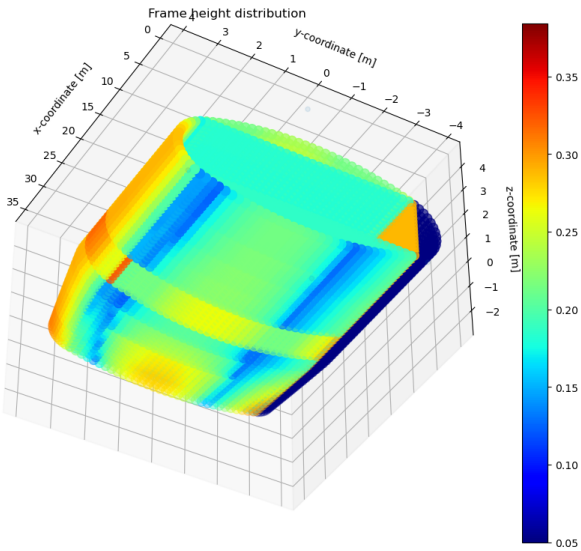

Figure 8.51: Frame height distribution. Front bottom view.

The obtained mass distribution can be found below in figures 8.52, 8.53 and 8.54. Compared to the original concept, the skin weight is reduced slightly (approx. 4%), while the frame weight is increased by a significant 13%. The stringer weight is increased by 2%, leading to an overall weight increase of 4%. Practically identical behaviour is shown for the skins and frames. However, one noteworthy difference is that the mass increase of the keel frames is even greater for the NLES concept in the tapered region. This is caused by bending loads in the crown and keel which are larger than experienced in the original concept.

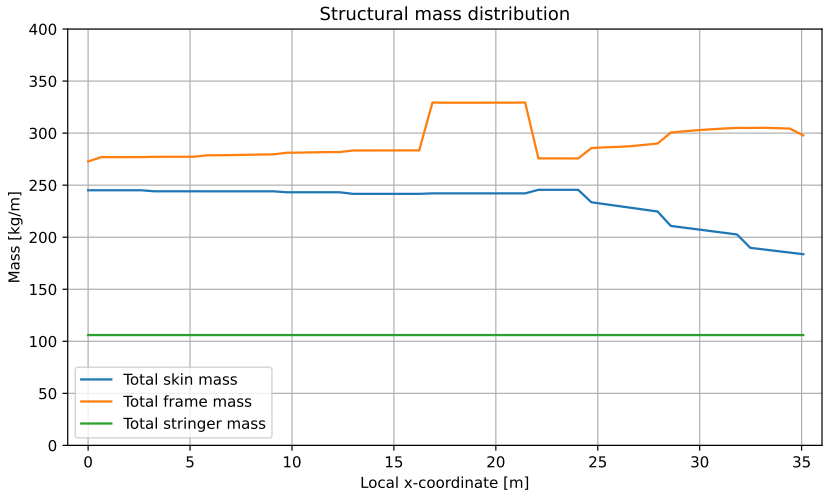

Figure 8.52: Mass distribution of the main structural mass groups.

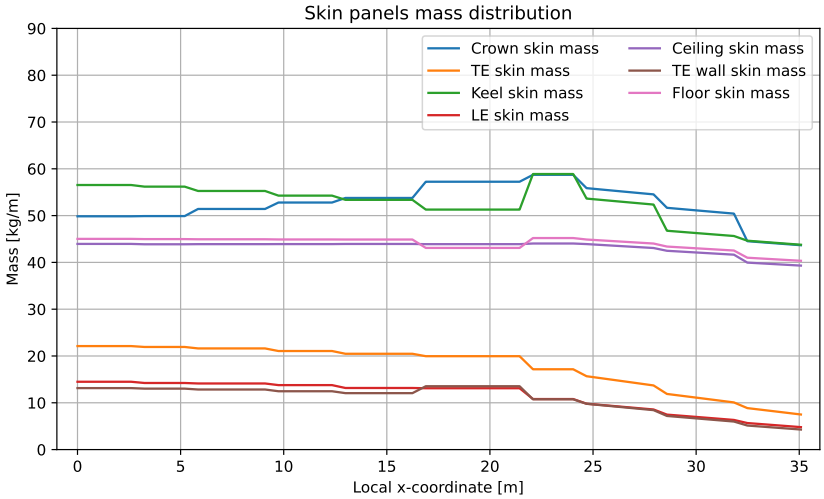

Figure 8.53: Mass distribution of the different skins.

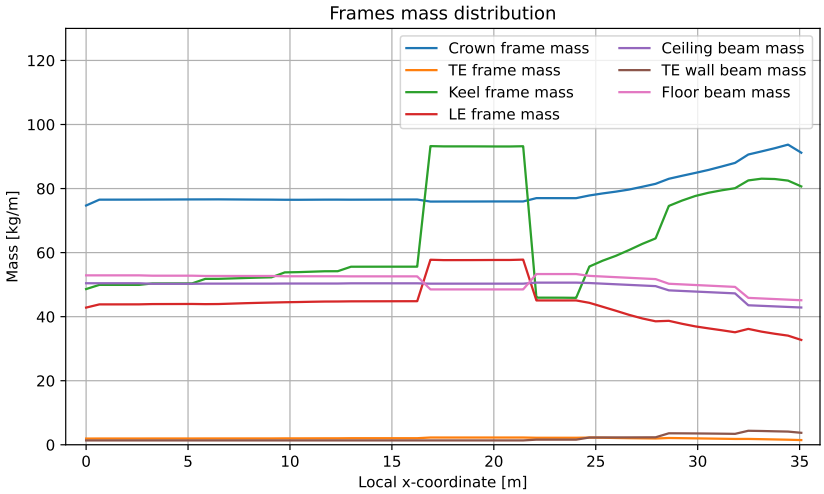

Figure 8.54: Mass distribution of the different frame/beam components.

Failure indices

The maximum failure indices are presented in table 8.4. The overall distribution is similar, with a notable increase in FI01, FI02 and FI19. From figures 8.59, 8.61 and 8.71, it can be seen that all these failure modes are critical exclusively at the end of the tapered section on the leading edge. Therefore, the significant rise in these FI is warranted.

Table 8.4: Maximum failure indices for the mean material solution. SMF = static material failure, CI = crack initiation, CP = crack propagation. Driving failure modes are shown in bold.

Code	Maximum FI	Value [-]
FI01	Skin axial SMF	0.72
FI02	Skin shear SMF	**0.92**
FI03	Stringers SMF	0.60
FI04	Frame inner flange SMF	0.79
FI05	Frame outer flange SMF	0.34
FI06	Biaxial global buckling	**0.94**
FI07	Shear global buckling	0.10
FI08	Combined global buckling	**0.94**
FI09	Biaxial panel buckling	**0.95**
FI10	Shear panel buckling	0.05
FI11	Combined panel buckling	**0.95**
FI12	Biaxial plate buckling	**0.95**
FI13	Shear plate buckling	**0.97**
FI14	Total plate buckling	**0.95**

Code	Maximum FI	Value [-]
FI15	Stringer crippling	**0.95**
FI16	Frame crippling	**0.97**
FI17	Crossbeam column buckling	**0.95**
FI18	Skin lon. axial CI	0.04
FI19	Skin shear CI	0.76
FI20	Skin hoop CI	**0.98**
FI21	Frame inner flange CI	0.36
FI22	Frame outer flange CI	0.62
FI23	Skin lon. axial CP	0.03
FI24	Skin shear CP	0.03
FI25	Skin hoop CP	0.37
FI26	Frame inner flange CP	**0.99**
FI27	Frame outer flange CP	0.48

Critical failure modes are indicated in figures 8.55 and 8.56. To stress the use of these figures, the following is repeated from previous section:

These figures should not be used directly to extract information on the most critical failure modes. Naturally, the shown failure modes correspond to the highest failure index at that location. However, as a high number of failure modes drive the design, for most locations in the structure there are many failure modes with a FI which is only a fraction lower than the critical one. The maximum failure mode at that location is simply the maximum one at the last state before the sizer stops, and is not necessarily the most important failure mode in that location.

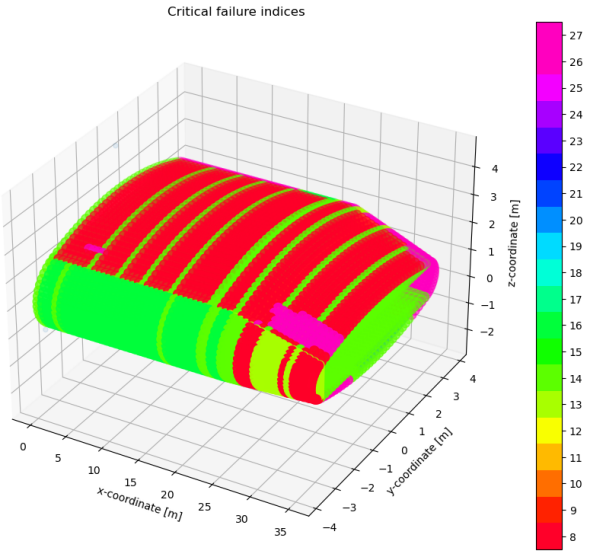

Figure 8.55: Critical failure modes.

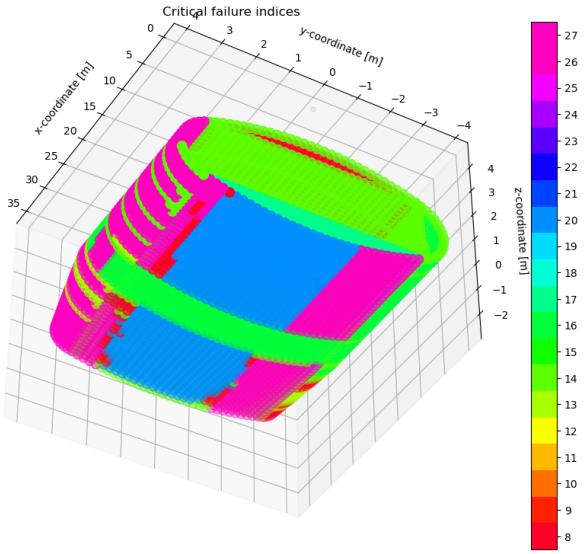

Figure 8.56: Critical failure modes.

The maximum failure index distribution is shown in figures 8.57 and 8.58. This distribution effectively shows the combined margin of safety of the structural components under all load cases, for the maximum load

cases. However, one should not interpret this as a token of the efficiency, or the level of optimisation, of the structure, as the maximum failure indices are shown.

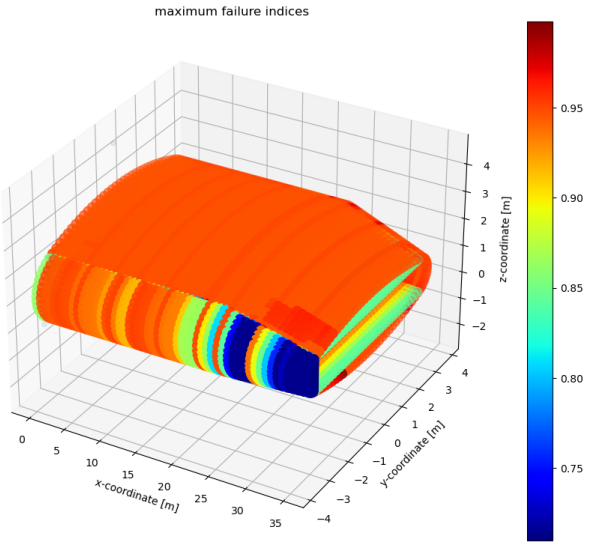

Figure 8.57: Maximum failure index distribution.

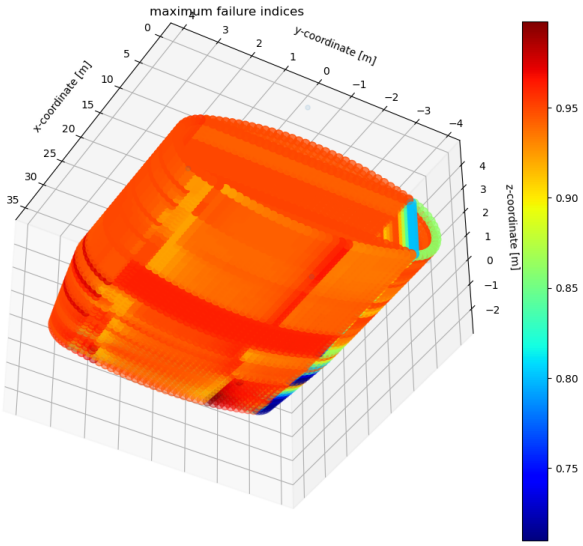

Figure 8.58: Maximum failure index distribution.

The individual failure indices are shown in the following pages. Overall, the distributions are analogous to that of the original concept. To minimise repetition, the key differences with the original concept failure index distributions are only discussed. Only the distributions which are significantly different are therefore shown. The omitted failure index distributions correspond to failure modes FI14, FI16, FI17, FI18, FI23 and FI24.

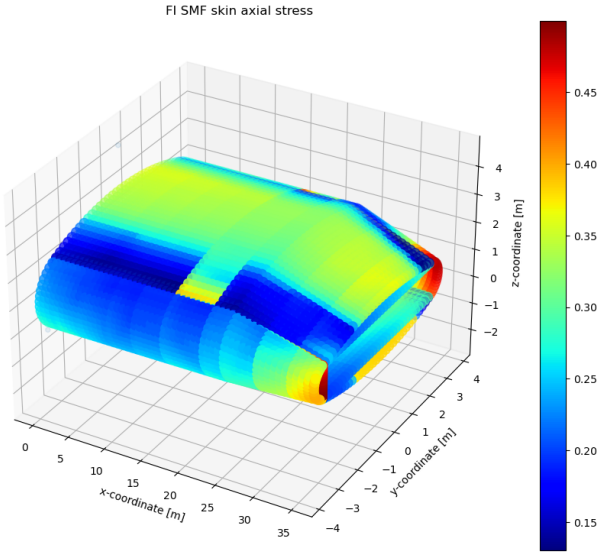

Figure 8.59: FI01 Skin principal axial stress static material failure.

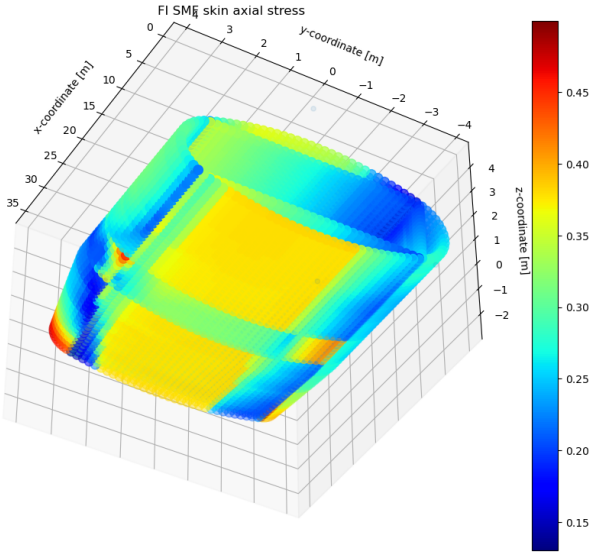

Figure 8.60: FI01 Skin principal axial stress static material failure.

For the principal axial stresses in the skins, as shown in figures 8.59 and 8.60, the overall distribution is very similar. However, the leading edge shows a significantly higher failure index (0.72 vs. 0.45), with a peak at the end of the tapered cabin.

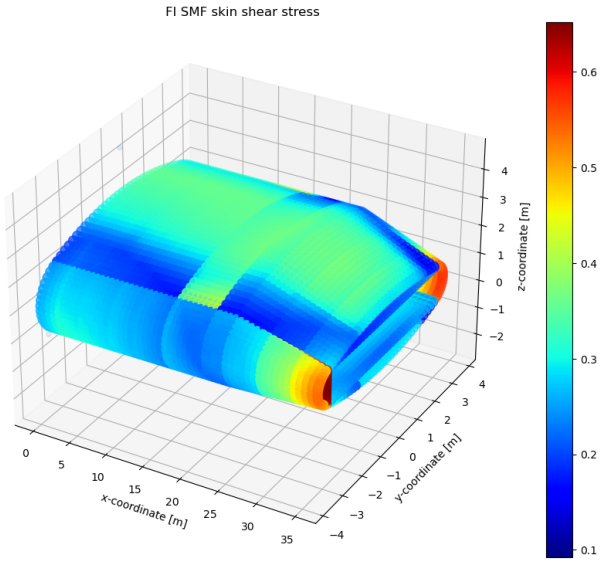

Figure 8.61: FI02 Skin principal shear stress static material failure.

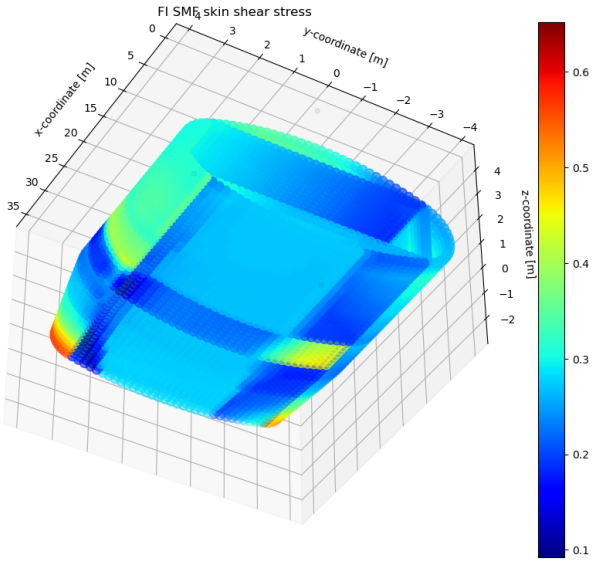

Figure 8.62: FI02 Skin principal shear stress static material failure.

For the principal shear stresses as shown in figures 8.61 and 8.62, a peak is observed in the LE at the end of the tapered cabin. For the original concept, the maximum value was in the walls. The magnitude of the maximum value is significantly higher compared to the original concept (0.92 vs. 0.53).

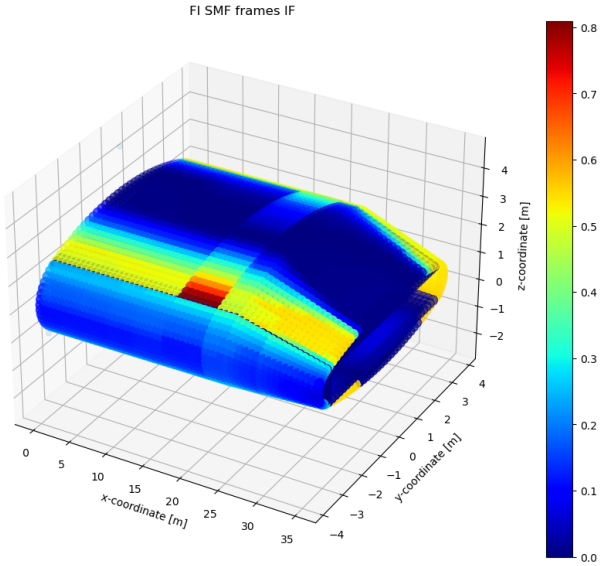

Figure 8.63: FI04 frame inner flange axial stress static material failure.

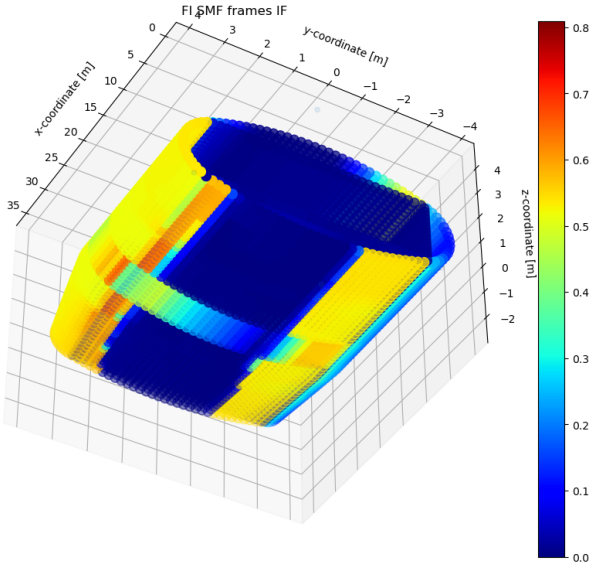

Figure 8.64: FI04 frame inner flange axial stress static material failure.

The frame inner flange static material failure FI distributions are shown in figures 8.63 and 8.64. Overall, the behaviour is quite similar to the original concept. However, the critical regions of the crown and keel have shifted further towards the leading edge. Additionally, the peak FI is larger for the ELG pylon frames (0.78 vs. 0.60).

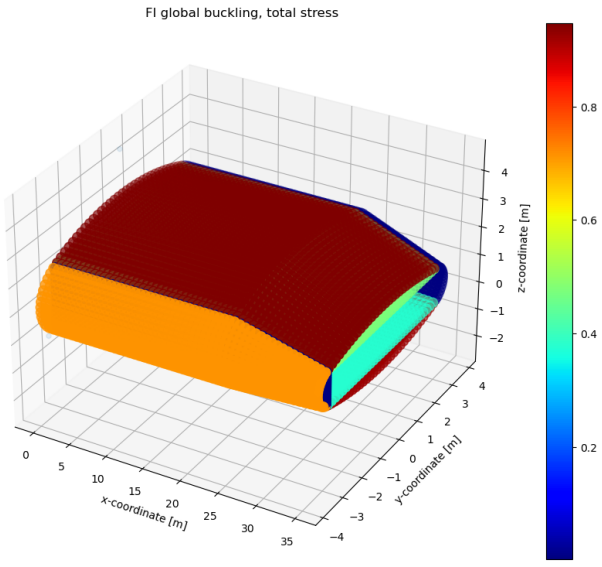

Figure 8.65: FI08 Global buckling FI distribution.

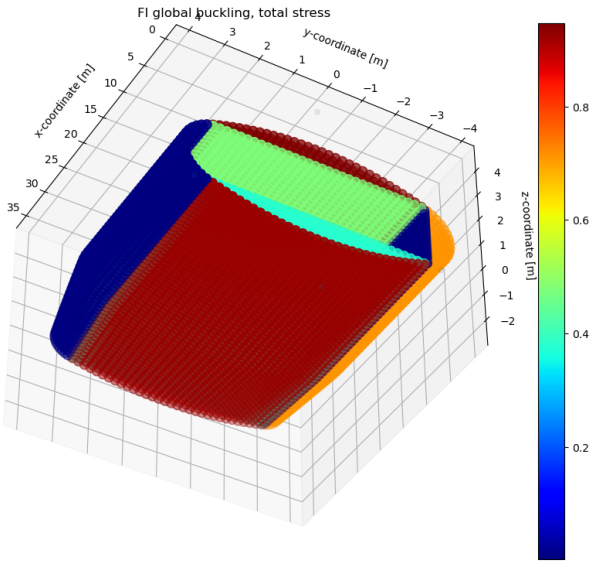

Figure 8.66: FI08 Global buckling FI distribution

The global buckling failure index distribution is shown in figures 8.65 and 8.66. The FI values are practically identical compared to the original concept, except the LE and TE. As the leading edge frames are so large, the failure index is very low. It is not clear why the TE failure index has risen considerably from 0.72 to 0.86.

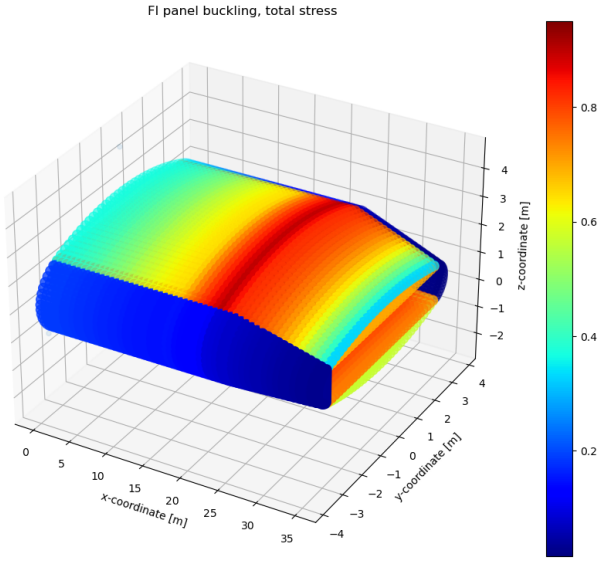

Figure 8.67: FI11 Panel buckling FI distribution.

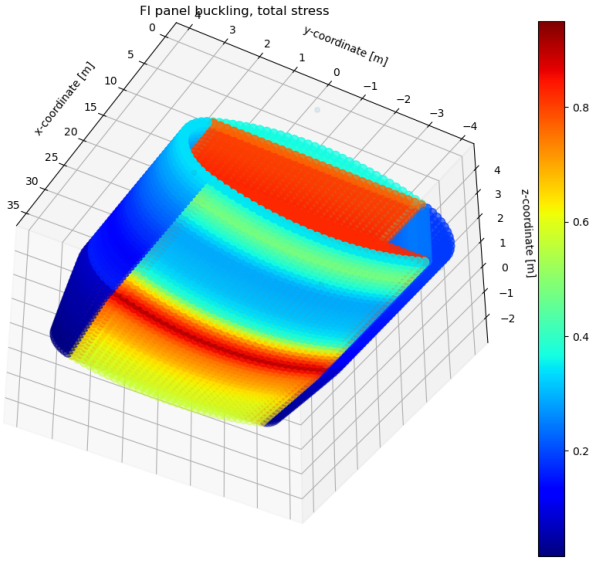

Figure 8.68: FI11 Panel buckling FI distribution.

Figures 8.67 and 8.68 show the FI distribution of panel buckling. The keel, crown, LE and TE distribution is practically identical to the original concept. However, the floor and ceiling FI has risen considerably from 0.62 to 0.78.

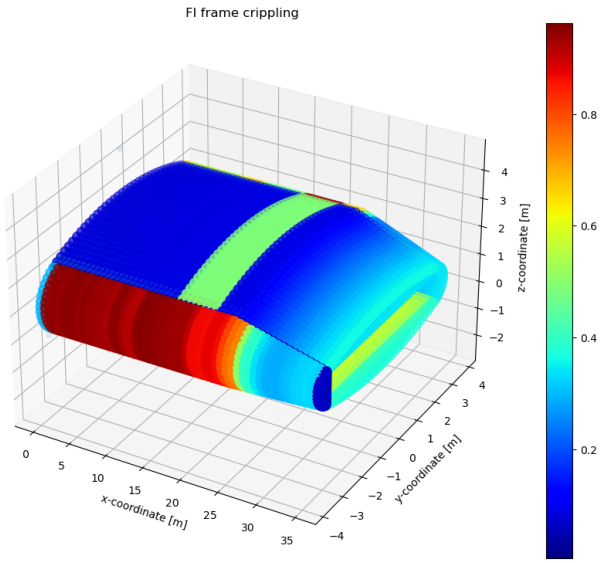

Figure 8.69: FI16 Frame crippling FI distribution

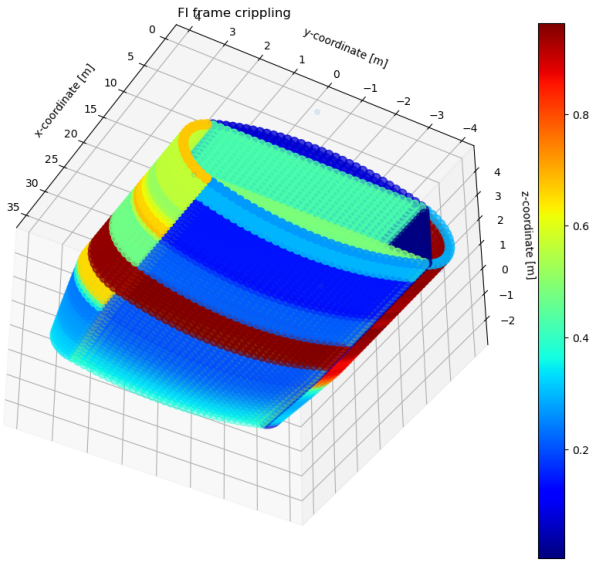

Figure 8.70: FI16 Frame crippling FI distribution

The frame crippling distribution can be found in figures 8.69 and 8.70. The most notable difference with the original concept is in the floor and ceiling. The FI in the floor and ceiling has increased, as the LE deformation induces significant bending in these components.

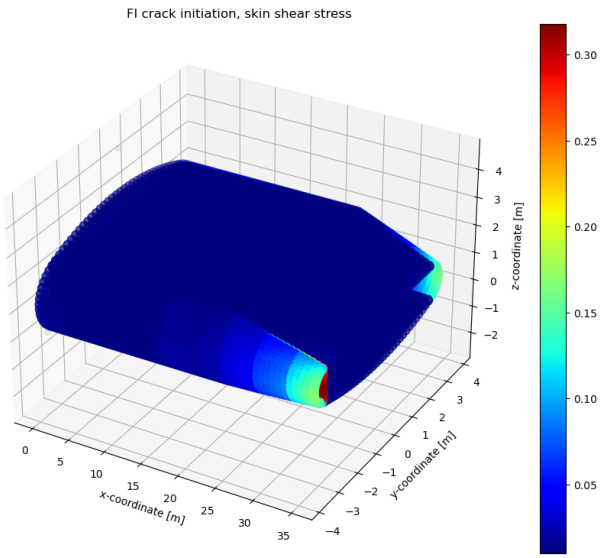

Figure 8.71: FI19 Skin shear stress crack initiation FI distribution.

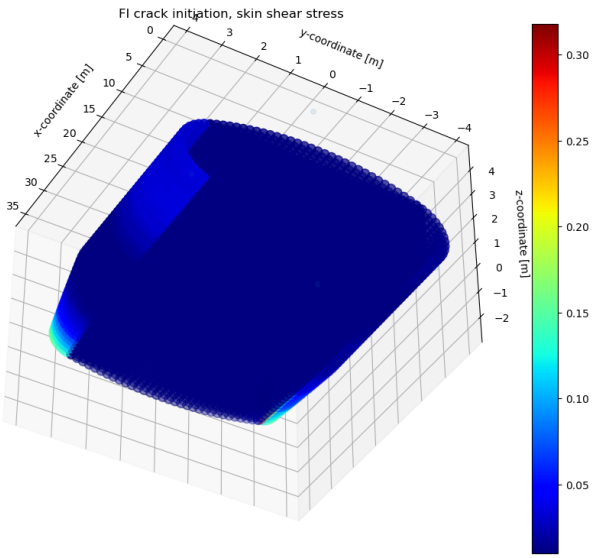

Figure 8.72: FI19 Skin shear stress crack initiation FI distribution

Figures 8.71 and 8.72 show the crack initiation FI distribution under shear stress. The maximum value has shifted from the walls in the original concept to the LE for the NLES concept. The maximum value has also increased significantly from 0.39 to 0.74.

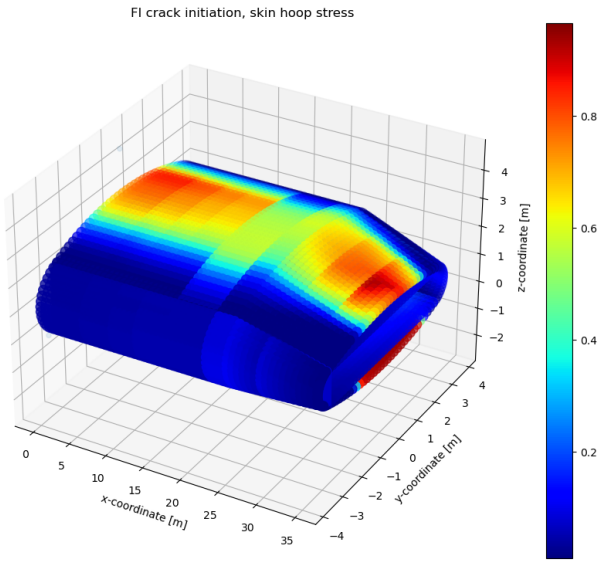

Figure 8.73: FI20 Skin hoop stress crack initiation FI distribution

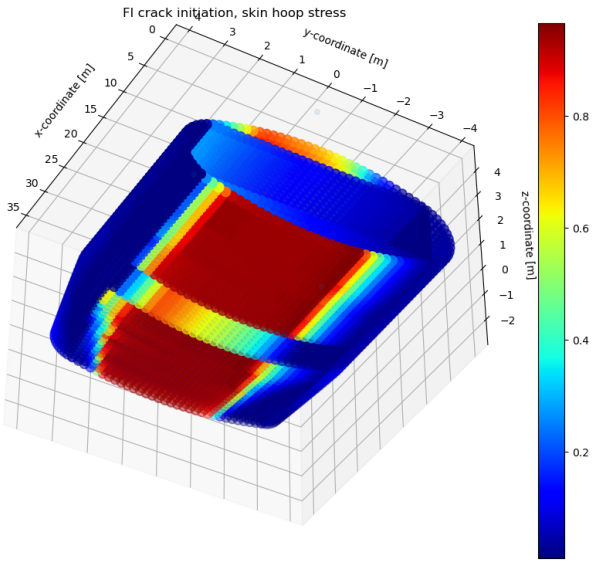

Figure 8.74: FI20 Skin hoop stress crack initiation FI distribution

The crack initiation FI distribution in the skin due to hoop stress is shown in figures 8.73 and 8.74. While overall distribution is similar, the affected regions are larger, especially on the keel. Secondly, the maximum FI has become very high, at a maximum of 0.98. This failure mode become the most important design driver for the keel frames.

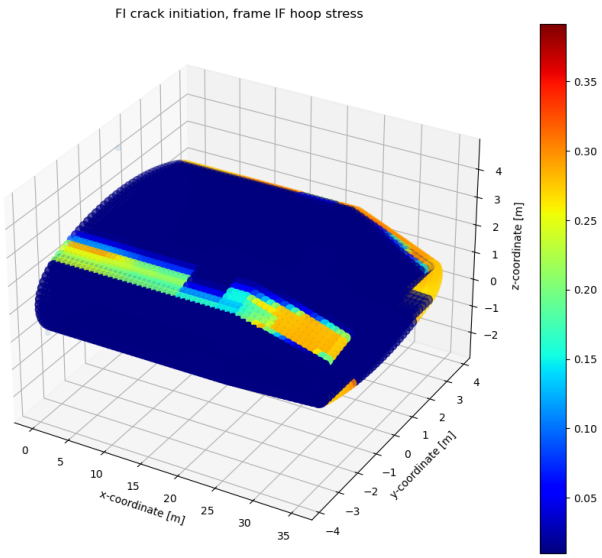

Figure 8.75: FI21 Frame inner flange hoop stress crack initiation FI distribution

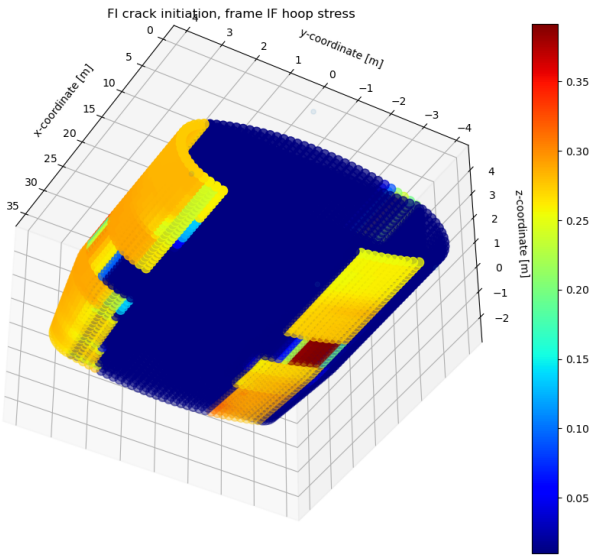

Figure 8.76: FI21 Frame inner flange hoop stress crack initiation FI distribution

Figures 8.75 and 8.76 show the crack initiation FI distribution of the frame inner flange. A clear difference is that the primary region of interest has shifted to the leading edge.

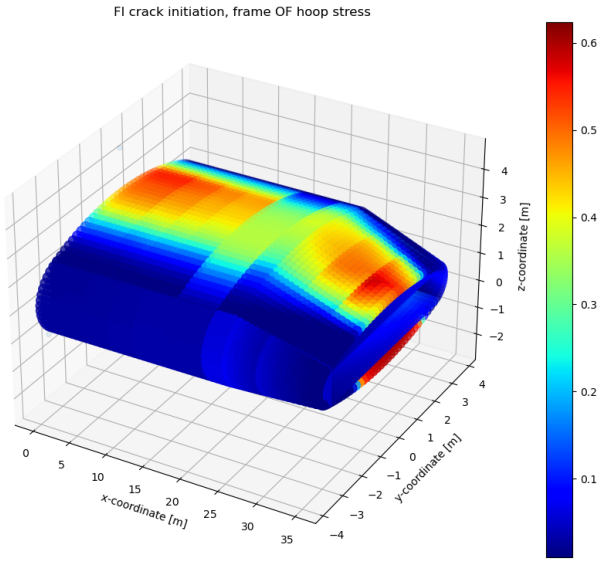

Figure 8.77: FI22 Frame outer flange hoop stress crack initiation FI distribution

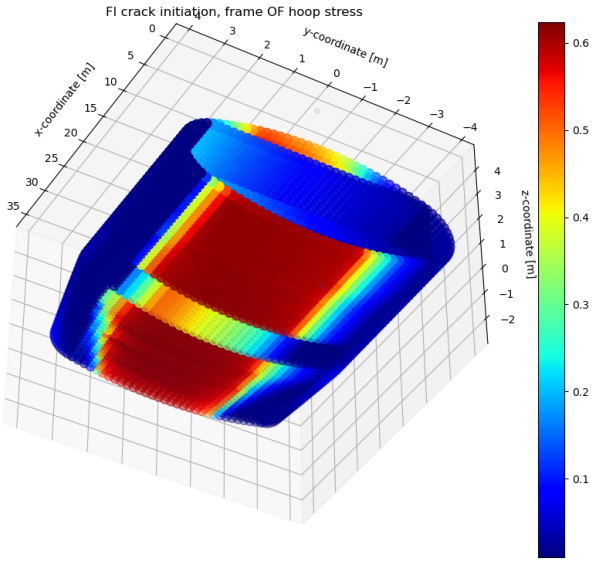

Figure 8.78: FI22 Frame outer flange hoop stress crack initiation FI distribution

Figures 8.77 and 8.78 show a behaviour which is analogous to the crack initiation in the skin under hoop stresses. The same explanation applies, but the maximum value is significantly lower.

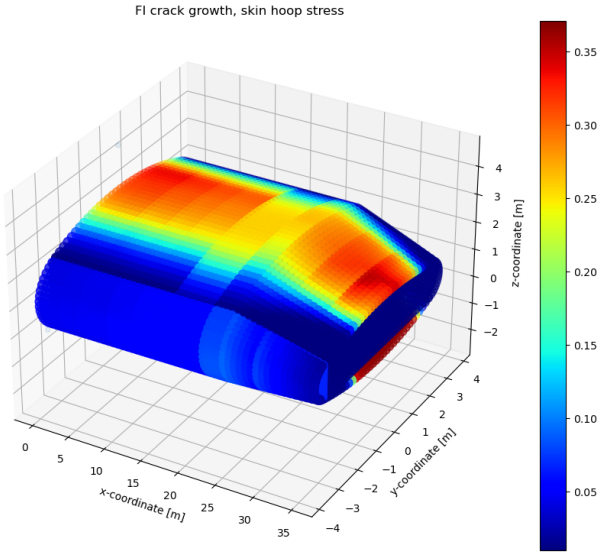

Figure 8.79: FI25 Skin hoop stress crack propagation FI distribution.

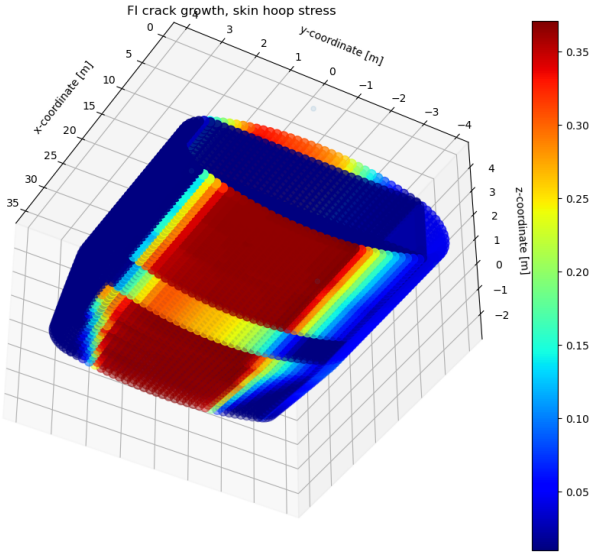

Figure 8.80: FI25 Skin hoop stress crack propagation FI distribution

Figures 8.79 and 8.80 show the same behaviour for crack propagation as crack initiation. In terms of magnitude, the distribution is similar to the original concept.

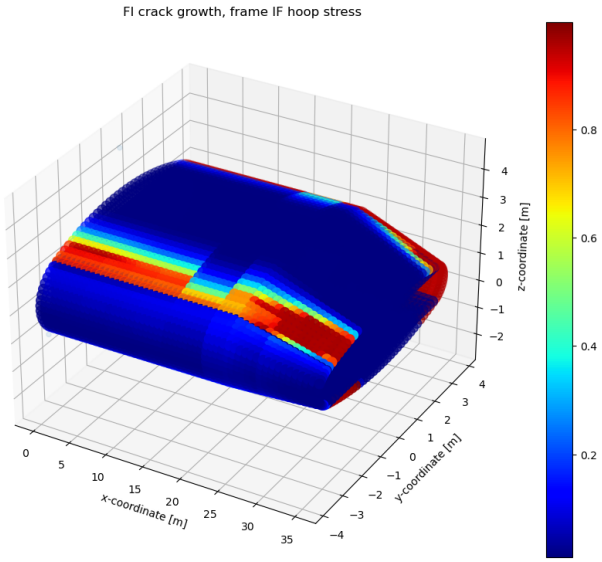

Figure 8.81: FI 26 Frame inner flange hoop stress crack propagation FI distribution

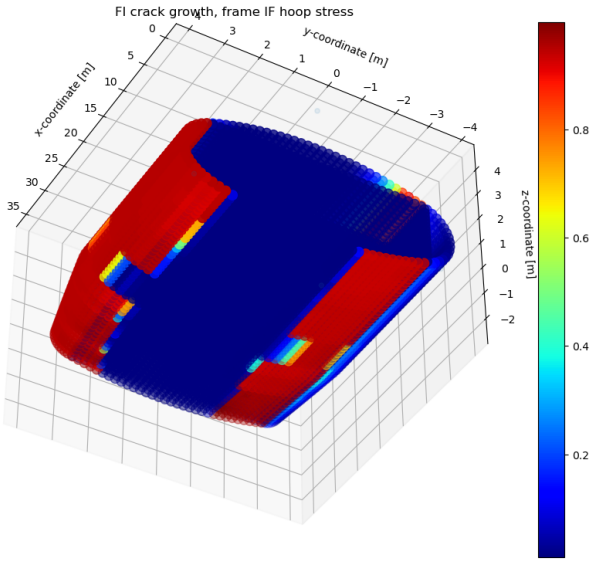

Figure 8.82: FI 26 Frame inner flange hoop stress crack propagation FI distribution

The crack propagation FI distribution for the inner flange of the frames is shown in figures 8.81 and 8.82. Compared to the original concept, the failure distribution has shifted towards the LE on the crown and keel. The affected regions on the keel and LE show an exceptionally high failure index at 0.99. This is the most driving failure mode of the keel and LE frames in the shown areas.

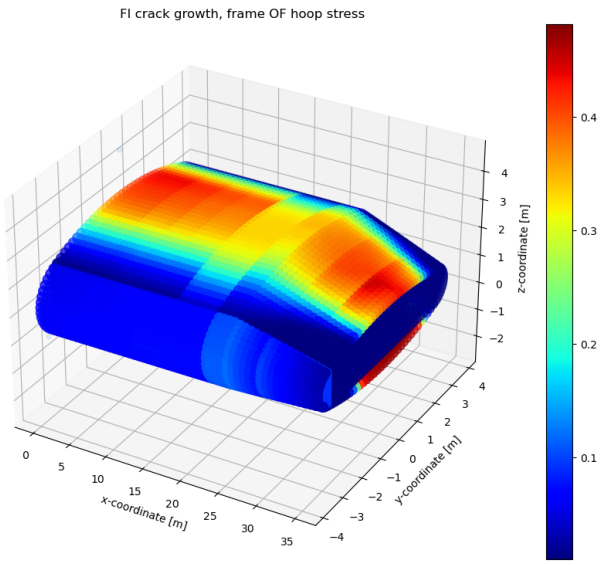

Figure 8.83: FI 27 Frame outer flange hoop stress crack propagation FI distribution

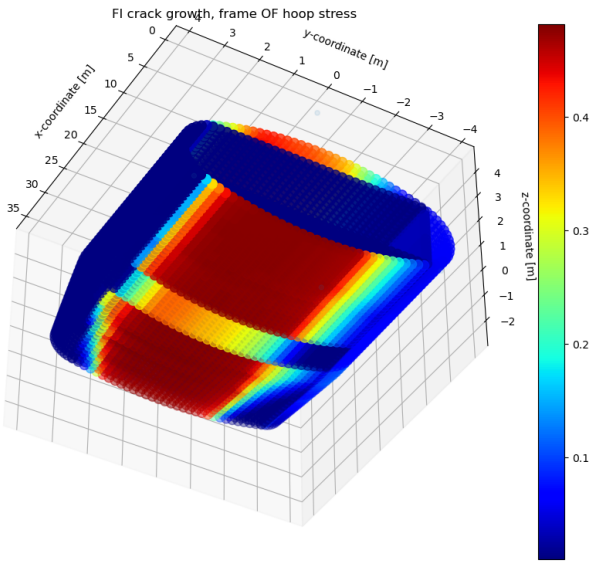

Figure 8.84: FI 27 Frame outer flange hoop stress crack propagation FI distribution

Figures 8.83 and 8.84 show a similar distribution as the other fatigue failure modes for the frame outer flange.

8.2. Mass results

The mass calculation as described in section 7.4 is performed with the obtained model mass of the wing fuselage. The base equation to calculate the total Flying-V structure weight is:

$$(W_{wing-fuselage} + W_{bulkhead}) * f_{MTR} f_{red} + W_{TE} + W_{OW} \tag{8.1}$$

Where f_{MTR} is the modelled-to-real weight factor (1.2) as discussed in section 7.4. f_{red} is the estimated reduction factor. The TE and outboard wing weight were determined as real weights, and not as modelled weights. Therefore, they are not subjected to the preceding factors.

A reduction factor can be based on the results from previous sections, and the sensitivity analyses shown in chapter 9. From the results, there is room for significant improvement. Primarily the stringer and frame mass can be reduced significantly, by discarding the constant height-thickness ratios, using multiple stringer geometries, and terminating stringers over the cabin length. Additionally, the sizing has been performed while prioritising runtime. Designing an improved sizing method, and applying thorough optimisation should lead to significant weight reductions. Secondly, the sensitivity analysis shows that the application of improved crippling stringer and frame sections may provide a significant weight reduction.

Due to time constraints, the calculation of a reduction factor was not performed. Instead, it is assumed that the modelled-to-real weight factor and reduction factor approximately cancel out. Therefore, the modelled weight is simply presented. Unfortunately, similar to previous research on the Flying V, the weight remains to be a large uncertainty. Further research should include an improved substantiation for these factors.

With the above approach, the estimated structural weight of the original concept equals 65.4e3 kg. Similarly, the NLES concept total structural weight is estimated to be 67.2e3. This is only a 2.8% increase compared to the original concept.

8.3. Discussion on results

A generalised discussion on the obtained results is presented below. Section 8.3.1 discusses the obtained designs for both concept and section 8.3.2 discusses the weight estimation results.

8.3.1. Structural designs

The obtained sizing results are discussed below. Firstly, the original and NLES concept are discussed generally in terms of design. Secondly, the different component groups (skins, frames, stringers) are discussed.

Original concept

The resulting design for the original concept is fairly straightforward. The obtained solution is remarkably symmetric, with the most noteworthy asymmetry being in the LE/TE thicknesses, which differ only by 0.2 mm. The structure shows a very gradual change in frame properties, as the cross-section loads drive this design. Therefore, the frames are suitable for a high commonality design, greatly reducing analysis efforts and costs.

NLES concept

The NLES concept is more similar to the original concept than expected, in terms of component design and weight. The leading edge frames are quite large, but have achieved the goal of removing the LE wall at a relatively small weight increase. With a frame height of approx 30 mm, the increase of cabin space is significant. However, the visibility of the windows may decrease due to the frame structure if a passenger is at an angle to the window.

Stringers

The number of stringers is constant per panel type (crown, TE, floor, etc.), and the stringer design is the same all over the structure. The floor and ceiling require a large amount of stringers (60 each), while the other components have relatively few. This is a clear improvement point. Applying at least two different stringers (one design for pressurised skins, one design for the floor/ceiling) should lead to a significant weight reduction. Currently, the stringers are over-designed for the majority of the structure, as they are only critical in a very limited region. Therefore, considering the termination of stringers along the cabin should also be considered in future research.

From the crippling FI distribution, it can be clearly seen that the there is only a small region on the crown where crippling is critical. The consequence is that the stringers for most components are too thick (as crippling is counteracted by increasing the thickness). For panel buckling, higher performance is obtained if the moment of inertia is maximised. This can be achieved by reducing the number of stringers for the same total stringer area (for the same geometric stringer ratios) or increasing the height-thickness ratio. While from these results it is unclear how much weight could be spared, it is clear that there is potential for significant gains.

Naturally, the cost aspect of manufacturing multiple stringers should be considered. However, if only a few different stringer types are used, this does not lead to a significant increase in costs.

Frames

While the frames were designed as individual frames (i.e. not constrained to the design of others), there is a large potential for the re-use of the same frames. This is apparent from figures 8.5 and 8.50. This is especially true for the untapered section. For the untapered section, a similar total frame mass would be obtained if a single frame design would be used for the untapered cabin, excluding the pylon frames. For the tapered cabin, the design varies more greatly. The size and shape for each frame is different in the tapered section, so reusing frames was not an option in the first place.

For each frame the optimal local size was determined along the length of the frames. However, the height-thickness ratio was kept equal for all frames, as it was controlled for the maximum frame crippling failure

index. Clearly, this has the potential to be improved significantly. As can be seen from 8.30 and 8.69, the frame crippling is only significant for the pylon frames. Therefore, the other frames are effectively too thick. This is associated with a significant weight penalty.

The frame height was limited with a lower bound of 50 mm. This was done to ensure that the structure would be able to cope with load cases which have not been included in this design. The primary examples are bird strike on the LE and fuel loads on the TE. Clearly, for the TE, LE and walls, the majority of the frames is limited by the lower bound. More detailed analysis of applied loads potentially leads to the removal of this bound, which in turn reduces the weight.

Lastly, the frame pitch should be considered. The frame pitch was kept constant at 0.65 m, as was recommended to van der Schaft [10] by Airbus. This value has not changed over the years, its inclusion in the design process was considered to be too complex. However, this value is solely based on a recommendation, which in turn was derived from frame pitches of conventional aircraft. Significant potential gains can be made in this respect. It should be noted that the frame pitch affects the prime assumption made in the cross-section stress analysis: a frame-to-frame wing-fuselage section can be simplified to a 2D cross-section. The spacing of the frames affects the validity of this statement. The applicability of the assumption has been verified to produce correct stresses in Appendix A. However, if the frame spacing is increased, the validity of the assumption is expected to reduce significantly, as the skins deform significantly different to the frames.

A note on the frames in the crack propagation analysis For the crack propagation analysis, a flange size of 50 mm was assumed. This was done as it was expected that the frames would be significantly larger than this. However, this is not the case in the LE, TE and walls, where the frame flanges are approximately half that size (ratio of 2 between web and flange size). Therefore, this assumption leads to an unconservative crack propagation analysis in these frames. As crack propagation in the flanges is not driving the local frame design, the impact on the final result should be limited.

Skins

From the three main structural categories, the skins are likely the closest to an optimised structure. The skin panels show high failure indices all over the cabin, with no apparent over-designed region.

The use of the constant thickness panels has shown to be justified in the constant cabin section. A relatively small decrease in maximum failure mode is observed over the skin panel. However, for the tapered section, significant weight improvements could be achieved by using variable thickness panels. Considering that the panels are curved and tapered, manufacturing is likely a significant challenge, in terms of difficulty and costs.

LE skin thickness for bird strike Bird strike has been identified as a potentially important failure mode, which could not be incorporated in the research. The leading edge skin may significantly increase in thickness to be able to withstand this load. Therefore, the uncertainty of the LE skin thickness is high.

Circular skin arc structure The fact that significant bending will be present in the cross-section reduces the need for a design which consists of multiple circular arcs for the outer skin geometry. For increased aerodynamic performance, it could be beneficial to abandon this requirement, as from a structural perspective, only small changes in performance are expected, as long as the the arcs are close to circular. This opens many possibilities for the cross-section geometry.

8.3.2. Structural mass

The preliminary structural mass estimations of the Flying-V for the original and NLES concept were obtained to be 65.4e3 kg and 67.2e3 kg, respectively. This is a 13.0e3 kg (24.7%) and 14.8e3 kg (28.2%) increase compared to Oosterom's[13] estimation (52.4e3 kg). This is a significant rise, and has large impact on the overall efficiency (and thus viability) of the aircraft. Breguet's range equation can be used to obtain a preliminary estimation on the impact of this increase:

$$W_F = \left(W_{OE} + W_p\right)\frac{1-k}{k}, \qquad k = exp\left(\frac{-Rc_j}{Ma\,(L/D)}\right) \tag{8.2}$$

The increase in fuel can be estimated with the increase on operating empty weight. The design fuel weight increases from 875e3 kg to 95.3e3 kg, an increase of 9%. Keeping all other weight groups constant, the MTOW is increased by the additional structure mass and fuel mass, totalling at 254.8e3 kg (an increase of 8.9%). Similarly, for the NLES concept, the fuel weight is increased by 10%, leading to a total MTOW of 255.9e3 kg, a 9.3% increase. The above is a simplification as all other systems would have to be redesigned for the adjusted mass. However, this is an indication of the reduction in performance w.r.t. Oosterom's results.

In order to improve the quality of the structural mass estimation, a number of topics are discussed below.

Inclusion of TE structure

While estimated with an empirical relation in section 7.4, the trailing edge structure was not modelled. The effects to the solution are discussed below.

The fuel tank / trailing edge structure should have been included fully in the whole model, in combination with a distributed fuel load. Currently, the trailing edge & fuel tank are being treated as the trailing edge normally would be in the conceptual design of a wing: it is not being regarded as a significant factor in the behaviour of the structure. For a conventional wing, the trailing edge is relatively small, and aerodynamic loads on trailing edges are relatively low. Therefore, not including it is a good first approximation, and empirical methods may be used to estimate the mass. However, in this case, the trailing edge is large, and large loads from the fuel are exerted on the trailing edge structure. The trailing edge structure will need to be considerably stiff and strong. This naturally causes a considerable contribution to the overall weight. Perhaps more important for this research, the trailing edge structure significantly affects the behaviour of the cross-section as a whole. It must be mentioned that implementing a distributed fuel load over the tank structure is not straightforward, as weight and pressure loads must be correctly applied to the structure for a variable level of fuel.

Accurate determination of weight factors

As discussed in section 8.2, two weight factors have been considered. One factor for the modelled-to-real mass, and one factor for the potential improvements in the analysis methods, structure choice and optimisation efforts. The factors were assumed to approximately cancel out, such that only the calculated mass is presented. Effectively, this cancels out many complex contributions to the mass, and may thus be considered to be unreliable. This is clearly an area where improvements can be made.

Inclusion of multiple materials

This research has limited itself to only two aluminium alloys, AL7075-T6 and AL2024-T3. As shown in the sizing method, AL2024-T3 was considered to be the preferred material for the driving failure modes, and was consequently applied to all structures. Clearly, besides this choice, no material application tailoring has been performed. Including more materials, and reassessing the material application should lead to a better use of different material properties. Therefore, a weight decrease is expected in reality.

Vertex joint structure

The presented research has shown that significant bending stresses typically originate near the vertex joints in the cabin, which connects the 4 structural components. These joints should not be taken for granted. A complex stress state, stress concentrations and limited space are ingredients for a very heavy joint. This is another potential advantage of the NLES concept, which has to connect 3 structures instead of 4. These joints should be analysed in much more detail, to assess fatigue failure and the manufacturing.

9
Sensitivity Analysis

The failure analysis and consequent sizing was performed based on the geometry and load inputs as described in chapters 3 and 4. Firstly, the effect of modelling refinement is assessed. Secondly, the impact of constant parameters are assessed. While some of the (geometric) parameters have been unchanged for years, their effect on the structural performance is unknown. While not being included in the design loop, it is deemed important to identify the sensitivity of the solution to these inputs. At the very least, this allows for more targeted further research.

9.1. Convergence analyses

Convergence analyses have been performed for the stress calculations and the sizing solution mass.

9.1.1. Mesh refinement for FEM stress

The sensitivity of the FEM solver to the number of elements in the cross-section was assessed. The generic design as described in Appendix F was used. The relative number of elements in the components were defined as: $m_{crown} = m_{keel} = m_{ceil} = m_{floor} = 2m_{LE} = 2m_{TE} = 2m_{walls} = 2m$. As the stresses are of primary interest in this research, the effect to the stresses were assessed. The pressurisation load case was used to test the stress field, as the peak stress near the joints are of high interest. The frame inner flange bending stresses show the highest peaks, and are therefore assessed. Figures 9.1, 9.2 show the stress solution of the first section under 57.5 kPa. Note the peak stresses near the joints are approximately equal, for a very different number of elements. Peak stress data is presented in table 9.1, from which it becomes clear that the peak bending stress is represented extraordinarily well for a low amount of elements.

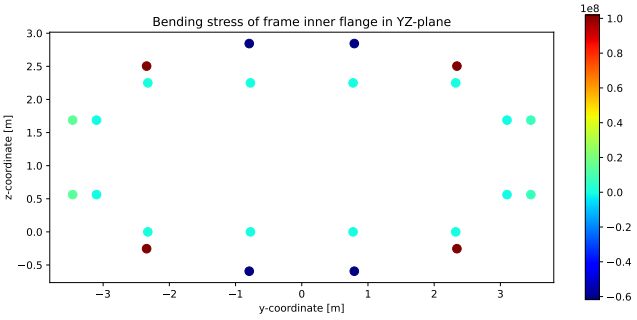

Figure 9.1: Frame inner flange stress field at $m = 2$.

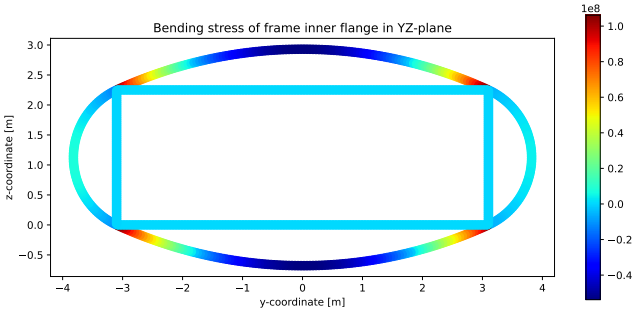

Figure 9.2: Frame inner flange stress field at $m = 64$.

Table 9.1: Peak crown frame bending stress for mesh refinement. FBS is frame bending stress. Pure axial stress presented for reference.

	Peak crown stress		
m [-]	Axial [MPa]	FBS + [MPa]	FBS - [MPa]
2	63.81	101.90	-61.77
4	63.82	105.06	-55.76
8	63.82	105.87	-54.31
16	63.82	106.07	-53.95
32	63.82	106.12	-53.86
64	63.82	106.14	-53.83

9.1.2. Mesh refinement for boom stress

Similarly to the previous paragraph, the sensitivity of the number of booms was assessed. The number of booms in the components were defined as: $m_{crown} = m_{keel} = m_{ceil} = m_{floor} = 2m_{LE} = 2m_{TE} = 2m_{walls} = 2m$. The selected load case was positive manoeuvring at design payload mass, zero cargo mass and maximum cruise fuel (LC01).

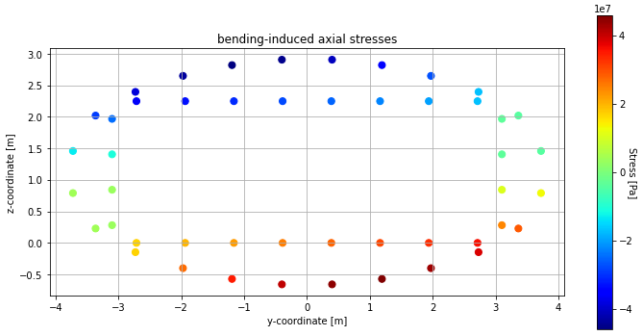

Figure 9.3: Bending induced axial stress field at $m = 4$.

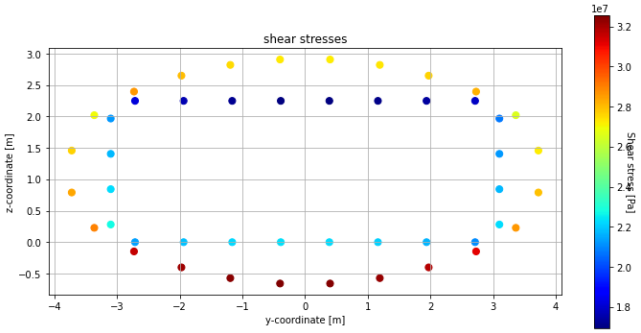

Figure 9.4: Shear stress field at $m = 4$.

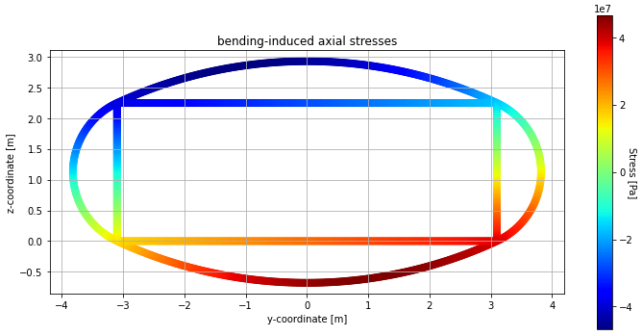

Figure 9.5: Bending induced axial stress field at $m = 128$.

Figure 9.6: Shear stress field at $m = 128$.

Table 9.2: Peak bending stresses in booms

m	Max [MPa]	Min [MPa]
2	1.617	-1.611
4	1.683	-1.678
8	1.708	-1.702
16	1.712	-1.706
32	1.714	-1.708
64	1.714	-1.708

Table 9.2 shows that peak stress values are adequately captured at a low number of booms. However, the offset is more significant than encountered for the FEM analysis.

9.1.3. Mesh refinement for solution mass

A convergence study was performed on the mass output as a function of the mesh refinement (i.e. number of elements per component). The results are presented in table 9.3 and figure 9.7. The mesh inputs corresponds to the number of elements in the vertical components (LE, TE, walls), and corresponds to half the number in the horizontal components (crown, keel, floor, ceiling).

Table 9.3: Concept mass solutions as a function of mesh input.

Mesh input [-]	Original solution mass [kg]	CLES solution mass [kg]
2	21248	23152
4	22025	23347
8	22342	22743
12	21680	22620
16	21665	22565

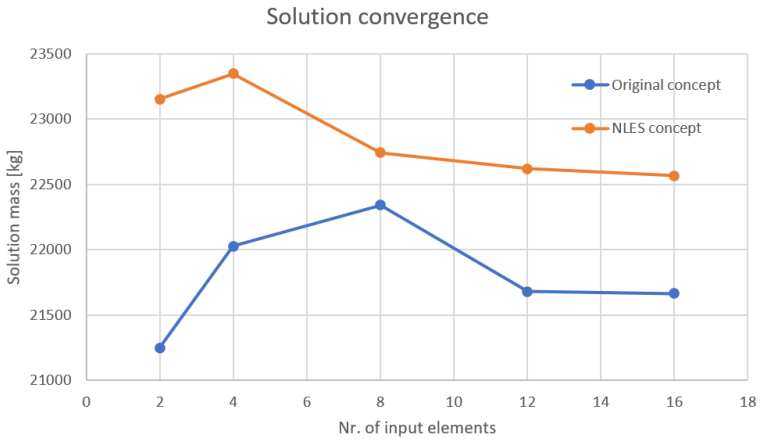

Figure 9.7: Solution mass a as a function of mesh input.

To obtain an indication if the same failure modes are critical during the refinement, the maximum failure indices were monitored. The failure index evolution during refinement is shown in tables 9.4 and 9.5 for the original concept and NLES concept, respectively. The original concept shows that all failure modes follow the same trend towards the final values attained at m=16. This is generally true as well for the NLES results, except for the value of FI1 and FI19, which show a significant change. As stated in 8.1.2, these failure modes are limited to a very small region at the end of the tapered cabin. Therefore, it is considered to be warranted.

Table 9.4: Original concept failure index evolution during mesh refinement.

	m_{input}				
FI code	2	4	8	12	16
1	0.49	0.49	0.50	0.50	0.50
2	0.56	0.56	0.57	0.57	0.57
3	0.49	0.49	0.50	0.50	0.50
4	0.68	0.61	0.61	0.65	0.65
5	0.36	0.35	0.33	0.34	0.34
6	0.64	0.86	0.89	0.92	0.95
7	0.06	0.03	0.07	0.06	0.07
8	0.64	0.86	0.89	0.92	0.95
9	0.98	0.99	0.97	0.97	0.97
10	0.07	0.06	0.06	0.06	0.06
11	0.98	0.99	0.97	0.97	0.97
12	0.98	0.99	0.96	0.96	0.96
13	0.97	0.99	0.97	0.97	0.97
14	0.98	0.99	0.97	0.97	0.97
15	0.94	0.93	0.95	0.94	0.94
16	0.95	0.99	0.99	0.98	0.98
17	0.96	0.97	0.97	0.96	0.96
18	0.04	0.05	0.04	0.04	0.04
19	0.16	0.20	0.17	0.17	0.17
20	0.99	0.85	0.88	0.92	0.92
21	0.41	0.34	0.23	0.25	0.27
22	0.59	0.53	0.57	0.58	0.59
23	0.03	0.03	0.03	0.03	0.03
24	0.03	0.03	0.03	0.03	0.03
25	0.37	0.31	0.35	0.36	0.36
26	0.98	0.85	0.88	0.91	0.95
27	0.45	0.39	0.45	0.47	0.47

Table 9.5: NLES concept failure index evolution during mesh refinement.

	m_{input}				
FI code	2	4	8	12	16
1	0.73	0.73	0.72	0.72	**0.50**
2	0.92	0.92	0.92	0.93	0.65
3	0.54	0.54	0.59	0.60	0.50
4	0.71	0.67	0.76	0.78	0.81
5	0.39	0.38	0.35	0.35	0.35
6	0.76	0.91	0.94	0.95	0.95
7	0.05	0.04	0.10	0.11	0.09
8	0.76	0.91	0.94	0.95	0.95
9	0.97	0.97	0.95	0.95	0.95
10	0.06	0.06	0.06	0.05	0.08
11	0.97	0.97	0.95	0.95	0.95
12	0.96	0.96	0.95	0.95	0.95
13	0.98	0.98	0.98	0.98	0.94
14	0.96	0.96	0.95	0.95	0.95
15	0.95	0.95	0.95	0.95	0.95
16	0.98	0.99	0.98	0.97	0.96
17	0.95	0.96	0.95	0.95	0.95
18	0.04	0.06	0.04	0.04	0.04
19	0.73	0.87	0.76	0.76	**0.32**
20	0.95	0.96	0.97	0.97	0.97
21	0.36	0.42	0.32	0.37	0.39
22	0.59	0.65	0.62	0.62	0.62
23	0.03	0.03	0.03	0.03	0.03
24	0.03	0.03	0.03	0.03	0.04
25	0.37	0.34	0.37	0.37	0.37
26	0.98	0.99	0.99	0.97	0.99
27	0.46	0.43	0.48	0.48	0.48

9.2. Sensitivity analyses

A number of sensitivity analyses have been performed, related to the mass output of the sizing solutions. As a significant amount of solutions needed to be produced, the mesh was kept relatively rough, at 8 elements for horizontal components, and 4 elements for vertical components. Multiple solutions needed to be produced as there is significant scatter in the sizing results, due to the fact that convergence is considered in a relaxed manner. This is discussed in more detail in section 7. The number of input stringers per component were not changed during the sensitivity analyses. Ideally, the number of stringers should be assessed as well to obtain a minimum mass result. However, this is associated with a too high runtime. The sensitivity results should therefore be interpreted as a preliminary estimate of the sensitivity of the parameters.

The parameters which were selected for sensitivity analysis were the ceiling width (section 9.2.1), outboard fuel mass (9.2.2), cabin pressurisation (section 9.2.4), crippling equation (section 9.2.3) and fatigue severity factor (section 9.2.5).

9.2.1. Sensitivity to reduced ceiling width

In previous research, the effect of angling the tension walls (i.e. the floor is not as wide as the ceiling) has been considered in the context of cabin shape and aerofoil shape. Angling the tension wall affects the geometry of the cross-section greatly, due to the coupling of parameters due to tangency requirements. In turn, angling the walls is expected to have a significant effect on the stress state in the cross-section. The sensitivity of this was assessed by changing the ceiling width (base 6.2 m), and extracting the crown stress values.

The results can be found in table 9.6. The inner flange bending stresses are also shown in figures 9.8 and 9.9. The peak stresses for the inner frame flange is shown in figures 9.10 and 9.11 as a function of ceiling width and crown radius, respectively.

Table 9.6: Crown peak stresses as a function of the ceiling width. S/r columns indicate stress value normalised by crown radius.

		axial stress		skin bending		frame bending	
ceiling width	radius	mean S	S/r	min S	S/r	max S	S/r
[m]	[m]	[MPa]	[MPa/m]	[MPa]	[MPa/m]	[MPa]	[MPa/m]
5.9	10	82.4	8.2	-35.6	-35.6	224.1	-112.4
6	8.92	74.9	8.4	-27.1	-27.1	170.9	-85.9
6.1	8.07	68.8	8.5	-21.2	-21.2	133.4	-67.4
6.2	7.41	63.8	8.6	-16.9	16.9	106.2	-53.9
6.3	6.87	59.6	8.7	-13.6	-13.6	86	-43.9
6.4	6.43	56.1	8.7	-11.2	-11.2	70.6	-36.3
6.5	6.07	53.2	8.7	-9.3	-9.3	58.7	-30.3

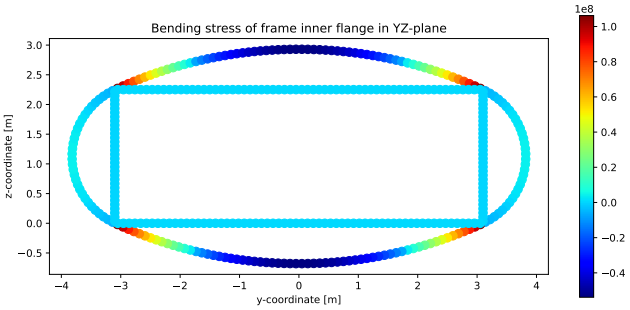

Figure 9.8: Frame inner flange bending stresses for $w_{floor} = w_{ceiling} = 6.2m$.

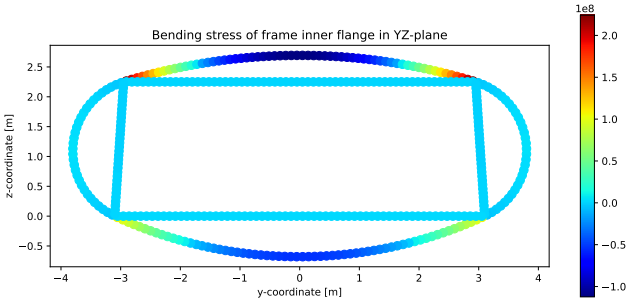

Figure 9.9: Frame inner flange bending stresses for $w_{floor} = 6.2m, w_{ceiling} = 5.9m$.

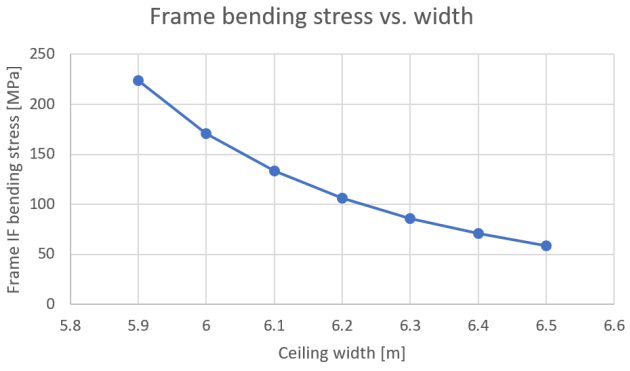

Figure 9.10: Frame inner flange bending stress as a function of ceiling width.

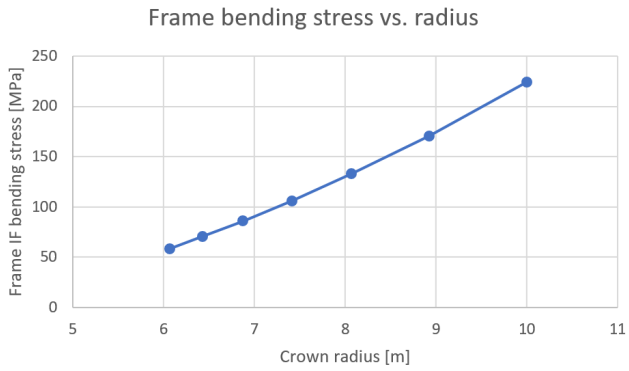

Figure 9.11: Frame inner flange bending stress as a function of crown arc.

From the results, it can be noted that the pure axial stress in the crown is quasi-linear with the crown radius, while the bending stresses behave very non-linearly. Clearly, angling the walls has a large effect on the peak stresses, and should thus not be treated lightly in design. The sensitivity of altering the ceiling width was assessed as well by generating a set of solutions. The results can be found in table 9.7 and figure 9.12. From the trend, the solution shows to be quite sensitive to the ceiling width, at a 350 kg increase for every 0.1 m that the ceiling is shortened. It should be noted that the decrease in ceiling width decreases the cabin area as well, as the floor width has been kept constant. The observed scatter is very high, and thus the substantiation for this conclusion is relatively poor.

Table 9.7: Solution mass sensitivity to ceiling width reduction.

Ceiling width reduction [m]	Solution mass [kg]
0	22025
0.05	21965
0.10	22394
0.15	22043
0.20	22870

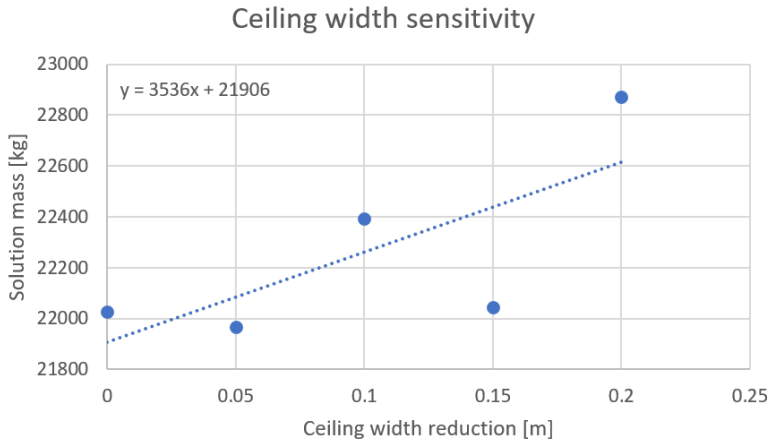

Figure 9.12: Ceiling width sensitivity.

9.2.2. Outboard fuel

The fuel allocation has been one of the most problematic issues in the development of the Flying-V. The main issues with the fuel allocation are the available volume, longitudinal balance and associated passenger safety. The effects of the fuel allocation in the outboard wing in particular was expected to be significant. The sensitivity of the solution to this outboard fuel is investigated in this section. In the original solution, the outboard wing contains a maximum of 14.3 cubic metres of fuel, corresponding to 26% of the total fuel. This is explained in more detail in section 4.2.2. As more outboard fuel was calculated to cause imbalance, the effect of reduced fuel is assessed.

The relevant running loads as a function of the outboard capacity are shown in figures **??** to **??** below, to indicate the effect of the outboard fuel. Ultimate load case 1 has been selected, which corresponds to pressurised ultimate positive manoeuvring with maximum design payload mass and zero cargo.

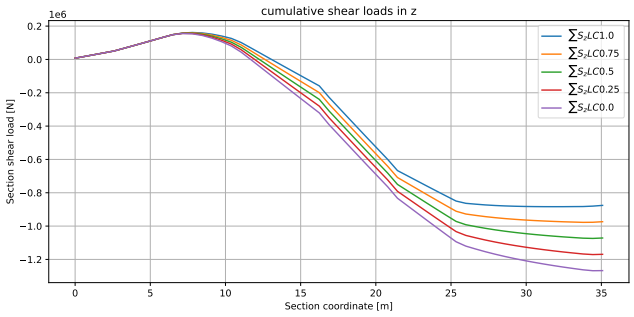

Figure 9.13: Cumulative shear in z as a function of the outboard tank capacity.

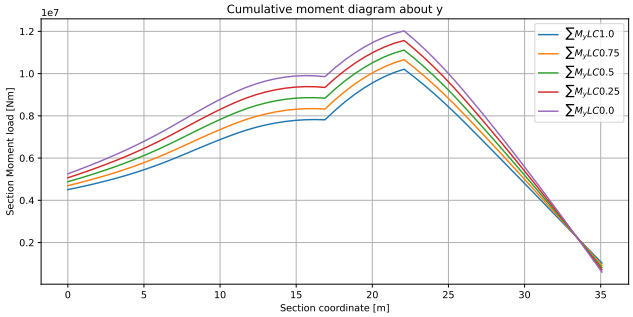

Figure 9.14: Cumulative moment about y as a function of the outboard tank capacity.

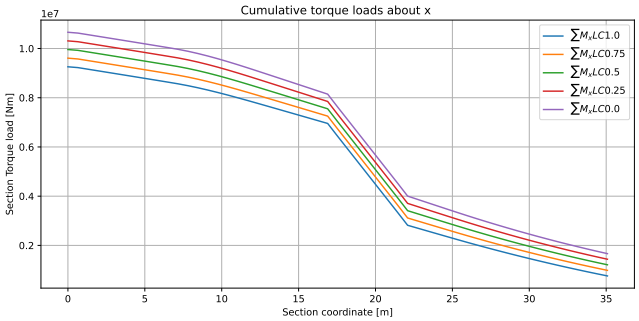

Figure 9.15: Cumulative torque about z as a function of the outboard tank capacity.

Table 9.8: Sensitivity of solution to outboard fuel tank mass. The fuel mass represents the fuel in a single outboard wing tank.

Max. outboard fuel mass [kg]	Fraction [-]	Solution mass [kg]
11400	0.26	22025
8550	0.21	22088
5700	0.13	22112
2850	0.065	22242
0	0	22370

The results of the sizing procedure are presented in table 9.8, and visualised in figure 9.16. Clearly, the sensitivity to fuel mass is low. Even when zero fuel is assigned to the outboard wing, the mass is increased by a mere 350 kg. This goes against the expectations from previous research, starting from Benad[7]. The insensitivity to the outboard fuel suggests that the cross-section stresses dominate the design. Ideally, this should be researched in more detail, as the fuel allocation is such an important topic for the Flying-V.

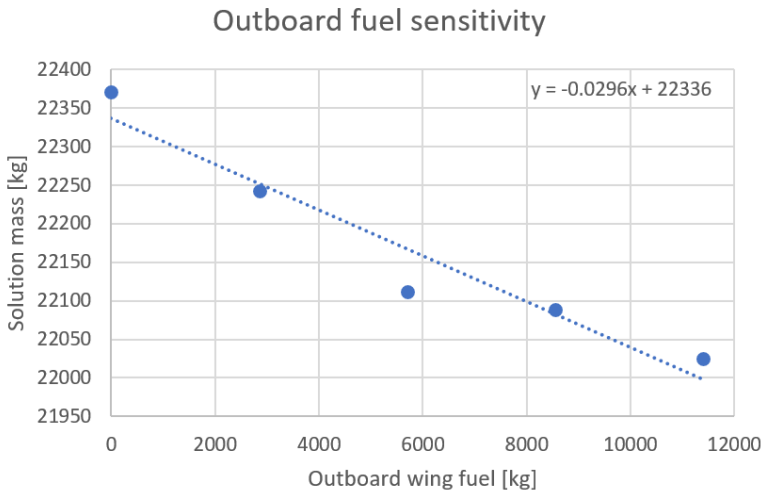

Figure 9.16: The sensitivity of the solution to outboard fuel mass.

9.2.3. Improved design against crippling

During the original sizing procedure, the stringers and frames consisted of regular z-sections and channel sections. While easy to manufacture and assemble, they do not have a high resistance to crippling, due to the one-edge-free flanges. Therefore, applying more crippling-resistant sections has been assessed. For both sections, the flanges may be supported by an additional angle at the end of the flange. Typically, the flange which is attached to the skin does not possess such an extra corner. The effect of adding extra corners is discussed in detail section 6.3.8. Overall, the corners should stabilise the flanges such that crippling occurs at a later stage.

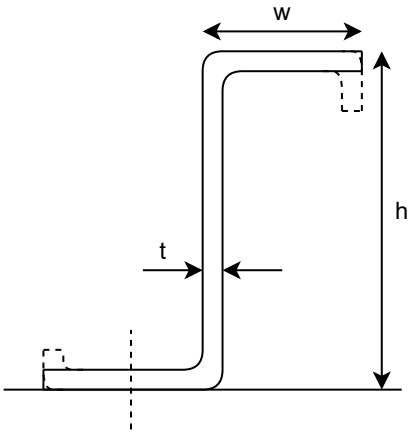

Figure 9.17

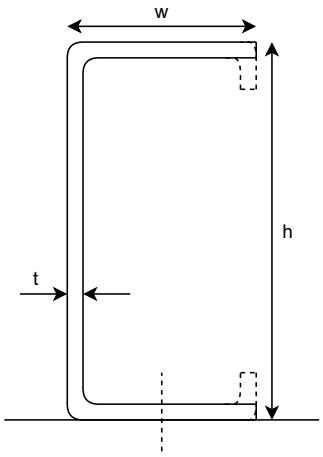

Figure 9.18

For both the stringers and frames, the effect of adding a single and double corners to the section was assessed. For simplicity, the corner geometries were not defined. It is simply considered that the last part of the flange curves, leading to an almost identical MOI, for the same total area. The results can be found in table 9.9. The results show an almost identical decrease of 8.3e2 kg. As the provided data is limited, this can only be regarded as a preliminary estimation.

Table 9.9: Results of improved sections against crippling.

Case (nr. of flanges & cuts)	Solution mass [kg]
Original (g=5)	22025
Single corner (g=8)	21188
Double corners (g=11)	21190

9.2.4. cruise altitude

The reasoning for different cruise altitudes was shown in section 4.3. The consideration is increasing the cruise altitude, causing the cabin pressure difference to rise from 57.5 kPa to 63.2 kPa. The pressure-induced stresses in the structure are linearly dependent on the pressure. However, this does not directly translate to increase in criticality of failure modes. Therefore, the sensitivity to increase pressure difference is best assessed by generating a full design solution. The results are shown in table 9.10 and figure 9.19. While significant scatter is presented, the trend shows an increase of 1.1e2 kg per kPa increase.

Table 9.10: Solution mass sensitivity to cabin pressurisation level.

Pressure difference [kPa]	Solution mass [kg]
57.5	22025
59.0	22181
60.4	22142
61.8	22657
63.2	22596

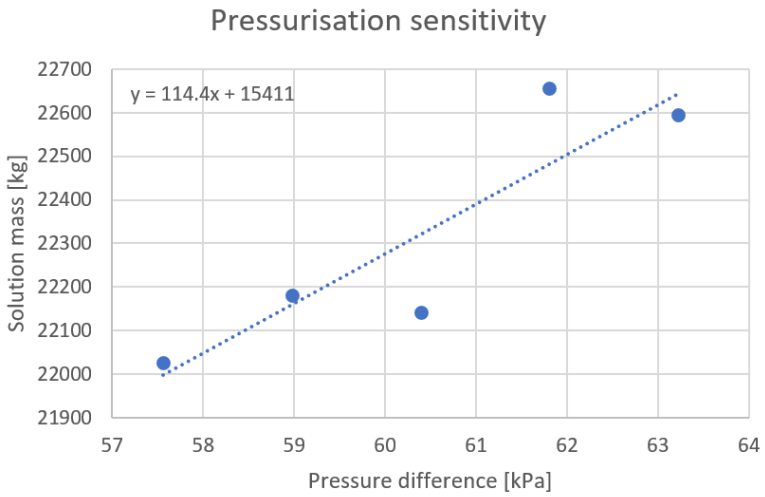

Figure 9.19: Solution mass sensitivity to pressurisation level.

9.2.5. Fatigue severity factor

The value for the fatigue severity factor, as discussed in section 6.2.4, has been a significant assumption in the fatigue analysis. The effect of the fatigue severity factor was assessed by finding a solution for a range of values, leading to the results of table 9.11 and figure 9.20. There is a lot of scatter, which leads to the low confidence in the result of 330 kg increase for a FSF increase from 4.5 to 5.5.

Table 9.11: Solution mass sensitivity to the fatigue severity factor.

Fatigue severity factor [-]	Solution mass [kg]
4.5	22025
4.75	22229
5.0	22168
5.25	22146
5.5	22479

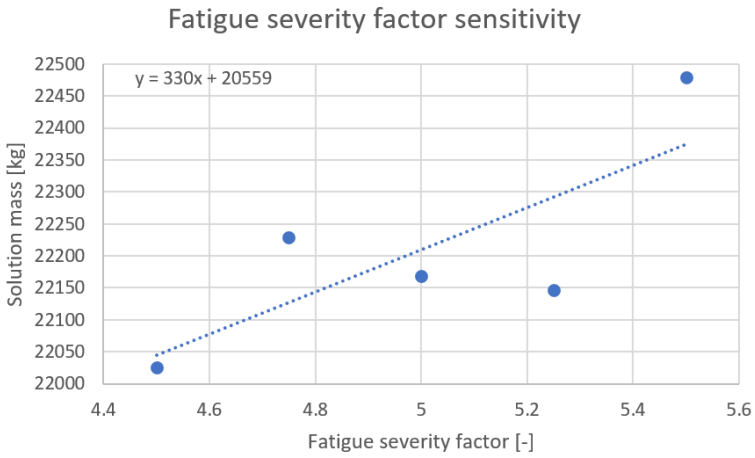

Figure 9.20: Caption

9.2.6. Discussion on sensitivity of inputs

The previous subsection has indicated the sensitivity of the solution to a small selection of different inputs. The scatter in the obtained solutions due to the sizing method dilutes the effectiveness of a sensitivity study. However, interesting conclusions can still be drawn from the above analyses.

Firstly, from section 9.2.1, it is remarkable to see the difference in bending stresses due to a small change in the geometry of the cabin. This raises large questions on the behaviour of the oval cabin structure. Clearly, the inclusion of bending fundamentally changes the required approach for the cross-section. It is highly recommended that a general study is performed on the (stress) response to the alteration of the properties of the different components. Potentially, straightforward rules of thumb could be derived, which could help greatly in the design of the wing-fuselage structure of the Flying-V.

Secondly, the mass solution insensitivity to the outboard fuel is quite staggering. For conventional wings, placing such a large mass at the end of a wing would lead to significant differences. In the case of the Flying-V, the difference between zero and 11.4 tonnes of fuel in the outboard wing leads to a difference of just 1.6%. This suggests that the longitudinal loads are even less important than what was obtained from the sizing results.

The crippling sensitivity analysis is simplistic, but presents a straightforward manner to potentially reduce the weight significantly.

Having observed the insensitivity to the running loads, the structure was expected to be sensitive to a larger pressure difference. However, for a 10% pressure increase, the structural mass only increases by 2.7%. This is manageable, and suggests the usefulness of the increased cruise altitude for emissions reduction purposes.

The characterisation of the sensitivity of the fatigue severity factor to the structural mass is limited due to large scatter. However, at the very minimum, it shows that the solution is not very sensitive to a significant increase in the FSF.

10
Conclusion and Recommendations

10.1. Conclusion

The Flying-V has shown to be a novel aircraft configuration with high potential. Aerodynamic and preliminary structural analyses have resulted in a fuel-efficient and light aircraft. However, the novel wing-fuselage structure is not well understood in terms of analysis and design. The goal of this research was therefore to create a structural sizing methodology for the wing-fuselage of the Flying V.

To set up the sizing methodology, three main tasks were performed. Firstly, an extensive identification of load cases under different weight distributions was performed. Secondly, the stresses were calculated in the longitudinal direction and cross-sectional plane of the wing-fuselage by using boom methods and an enriched 2D finite element model. A significantly improved understanding of the stress behaviour of the oval fuselage was generated. Thirdly, failure analyses were performed, focused on the improved representation of fatigue and buckling phenomena. A sizing methodology was set up by identifying the dominant load cases and variables for each failure mode. An iteration scheme was applied to update the design variables from the failure distributions throughout the structure. Different failure modes were effectively decoupled which allowed for a fast determination of structural designs.

The resulting sizing method was used to generate design solutions for the two conceptual cabin layouts, which led to similarly performing designs. For the original and NLES concept, the total structural mass was estimated at 65.4e3 kg and 67.2e3 kg, respectively.

The designs show a need for large frames to withstand the out-of plane and compressive loads, which are primarily induced by the pressurisation behaviour of the structure. This results in the frames being the largest weight group for both structures. A high degree of stiffening is required on the floor and ceiling, while the outer skins are only stiffened relatively lightly. The frame geometry remains nearly constant for the entirety of the constant cabin, leading to significant economical gains. Critical failure modes are a multitude of buckling modes, crack initiation in the skin and crack propagation in the frame flanges. The primary load case of interest was identified to be the pressurisation.

The NLES concept shows to be a viable alternative to the original oval cabin structure. At the cost of 1.8e3 kg extra mass, an unhindered continuous cabin geometry has been realised, which is expected to lead to increased passenger acceptance and useful space.

This research is part of the ongoing efforts to assess the viability of the Flying-V aircraft. The presented techniques and results aim to function as a stepping stone for more detailed research into the Flying-V structure, and other unconventional aircraft structures.

10.2. Recommendations

This research has shown an improved structural sizing method for the wing-fuselage of the Flying-V, leading to an updated design and weight. However, further research is clearly necessary. Firstly, the presented analysis and sizing methodology can be improved. The analyses can be improved in a few respects by:

- Including the trailing edge structure. Its large size and its unconventional function as a fuel tank lead it to be more important than the trailing edge for a conventional wing.
- Expanding the stability analysis. The effects of cut-outs, curved skin panels and bending-buckling should be added to obtain a more accurate assessment of the structural design against buckling.

- Using more sophisticated methods for the fatigue analyses. For the crack initiation analysis, an improvement can be primarily made in the determination of representative fatigue severity factors for different stress raisers. For the crack propagation, an improved structural representation should be implemented, beyond the consideration of independent plates. Both analyses will benefit from an improved inclusion of combined loading.

The sizing can be improved by:

- Using multiple stringer designs, and considering the termination of stringers.
- Including the frame pitch as a variable.
- Including a larger set of materials.

Secondly, the structures connected to the ELG pylon should be assessed in more detail. The pylon load application in this research is rather simplistic in that respect. Moreover, the construction of the pylon should be investigated in more detail, as the trailing edge pressure shell must be discontinued. Furthermore, the pylon itself should be designed in more detail. As the pylon is long, the contribution to the total weight is substantial.

Thirdly, a detailed analysis of the vertex joints should be performed. The joints have not been treated specifically in this research, but are expected to be prone to fatigue failure due to high loads, a complex stress state and deformations of the pressure arcs. To adequately counteract these problems, the resulting construction is likely very heavy.

Fourthly, the behaviour of the cross-section under out-of-plane loading should be characterised in general. In this research, the geometry from previous solutions was simply used as input. However, as became clear in the sensitivity analysis, the stresses in the cross-section are highly sensitive to seemingly minor changes in the cross-section design.

Another research recommendation is an improved fuel allocation study from a safety and certification perspective. The fuel is currently located next to the passengers in the trailing edge tanks. The likelihood of failing certification with this layout is appreciable, which would trigger a total redesign of the layout of the Flying-V systems.

Furthermore, the symmetry structure should be assessed. This research extended the wing-fuselage such that the symmetry structure could be disregarded. However, in terms of construction and failure, this region needs its own analysis. Similarly, the inboard-outboard wing transition structure should be assessed individually. Additionally, the aerodynamic continuity of the inboard-outboard wing should be assessed in more detail. Finally, an improved weight estimation method should be performed, by applying the above improvements, in combination with an accurate assessment of the model-to-reality structure factor.

Appendices

A
Stress analysis validation

The cross-section stress analysis is validated in this chapter. Specifically, the assumption that a frame-to-frame fuselage section can be analysed adequately in 2D with a number of corrections for 3D effects is validated. The aim of the validation is to show:

1. The predicted stress state of the skins in x-direction should be representative.
2. The stresses of the skin and frames along the arcs must be representative.

To validate, a FEM model was created in ABAQUS SE 2021. Only the cross-section loads were considered relevant in this analysis, and therefore were the only load that were applied. The pressurisation load case was selected in order to verify the structural behaviour. This is the case as the pressure loads in the YZ-plane are high, causing potentially high deformations and stresses in the cross-section. The pressurisation difference was set at a representative 60 kPa.

The original oval fuselage concept was selected to be validated, as it has the most components, and is therefore deemed the most complex to predict. As this validation was performed prior to sizing, the cross-section geometry was set up based on previous work presented by Oosterom [13]. It should be noted that this validation procedure was performed before the detailed set-up of the failure and sizing procedure. Therefore, the validated structures shown below deviate from the final used structures. However, the method is still considered to be validated.

A fuselage section is considered to contain all structural elements in between two frames, including two half-frames at each end. This includes the outer skin, longitudinal stiffeners, floor, ceiling and walls. For the purpose of the validation, the geometry was considered to be symmetrical about both y- and z-axes, such that the problem could be reduced to one-eighth of a section. The reduced problem is visualised in figure A.1.

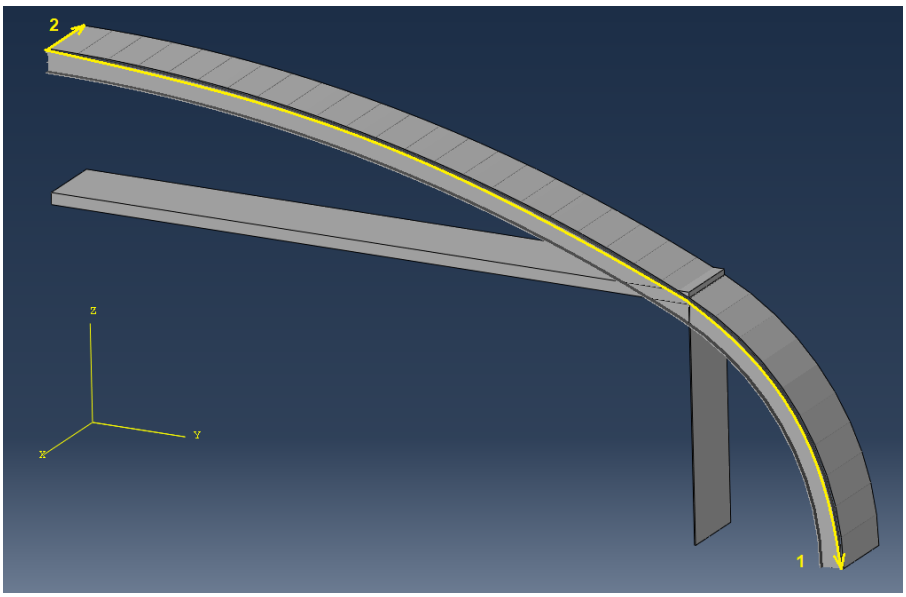

Figure A.1: One-eighth reduced model with global and local coordinate systems.

Skins According to Oosterom's weight data, the average skin thickness can be calculated to be approximately equal along the fuselage at 5 mm. The pressurisation causes much higher stresses in the crown and keel relative to the LE and TE skins for the same thickness. However, these skins will be facing other load cases which have been identified as potentially critical, i.e. bird strike and fuel containment (after ditching / emergency landing). Therefore, the thickness is kept constant for all skins.

Stringers The longitudinal stiffening is performed by stringers, which, according to Oosterom's analysis, vary greatly in total cross-sectional area over the fuselage axis. In an attempt to not over-stiffen the skins and delude the legitimacy of the validation, an average total stringer cross-sectional area was taken forward at 0.087 m^2. I-stringers were selected to be applicable for the purpose of this validation. The stringer dimensions were determined based on a number of simplified design rules:

1. symmetric about both axes
2. w = h/2 = 10t
3. constant stringer pitch

A stringer pitch was assumed at 150 mm. Maintaining a constant stringer pitch for all partaking stiffened panels, this led to stringers with dimensions $w = h/2 = 10t = 30mm$. With similar design rules ($w = h = 20t$), frames were designed. However, in this case Oosterom's results are deemed insufficient. For reference, from Oosterom's weight data, the frame dimensions would measure in at 72 by 72 mm. Oosterom did not consider the bending of the skin induced by pressurisation in his work, which is one of the main tasks which needs to be performed by the frames, in order to retain the aerodynamic shape. It is expected that the frames need to be considerably larger to accomplish this. As the structure was not yet sized, there was no clear route to pick a frame design, other than looking at the stress values for the frame. Oosterom's obtained frame area was therefore (arbitrarily) doubled, leading to a geometry of $w = h = 20t = 100mm$. While lacking strong substantiation, this was deemed acceptable for the purpose of the validation.

Floor / ceiling For the purpose of the validation, the floor and ceiling were considered to be identical structures. While not representative of the final design, the structure was simplified as a sandwich panel. The sandwich panel consists of two aluminium face sheets with a thickness of 2.5 mm, and a foam core material of 50 mm. The foam was assigned a negligible modulus of elasticity. As the goal of the validation was primarily to compare the skin panel behaviour, this was deemed acceptable[1].

Wall In this stage of the design, the walls are envisioned to experience mainly tension. Therefore, unstiffened continuous solid plates were used to represent the tension walls, with a thickness of 5 mm. It should be noted that further development of the tension walls will likely see cut-outs for the leading edge wall, which causes significantly different lateral behaviour (mainly due to Poisson's effect). Additionally, stiffening is likely required to prevent instability failure. As the goal of the validation was primarily to compare the skin panel behaviour, this was not deemed a priority. Therefore, this was not taken into account.

Boundary conditions A number of boundary conditions have been enforced on the reduced model to ensure equal behaviour:

1. the crown and ceiling symmetry nodes are constrained against translation in Y, rotation about X and rotation about Z.
2. The LE and wall symmetry nodes are constrained against translation in Z, rotation about y and rotation about X.
3. The frame is constrained against translation in X, rotation about Y and rotation about Z.
4. The centre of the frame-to-frame section is constrained against rotation about Y and rotation about Z.

It may be noted that this set of boundary conditions allows the section to contract and expand in X direction. Its relevance will become apparent in the stress analyses. The legitimacy of the above (symmetry) boundary conditions was evaluated by constructing a one-fourth model, which spans a full section with a quarter cross-section. The results were found to be identical.

[1] After the stress validation study, sandwich structures were excluded from the methodology.

Abaqus modelling constraints The crown, LE, ceiling and wall are jointly constructed as a single shell cross-section, each with different section assignments. The crown, LE and wall consist of skins measuring in at 5mm, where the mid-surface of the skin has the same coordinates as the nodes in the predictive model.

The frames are simplified as wire beams, with the aforementioned cross-section. The frames are attached to the underside of the skin panel, while considering the offset between the skin edge and mid-surface. Similarly, the stringers are modelled as wire beams and are attached to the inner skin surface. This causes frames and stringers to intersect. Implicitly, this assumes the stringers are free to intersect the frames. As this is a viable option in the fuselage construction, this is deemed acceptable in this stage.

Deformations

YZ-plane The nodal deformations of the Abaqus model and the 2D FEM model were compared to assess the validity of the Eigenvalue problem solution. The deformations of the Abaqus solution was requested along the skin arcs at the frame and in the section centre. This was compared to the corrected 2-dimensional prediction. For the translation in Y and Z (U1, U2), the differences between the frame nodes and section centre nodes are negligible. For clarity, only the frame node translations are shown, compared to the prediction in figures A.2 and A.3. The predicted y-deformation agrees in general with the results from Abaqus. However, there is a considerable mismatch anywhere other than the crown symmetry node and the vertex, where the two solutions are almost identical. The offset is especially pronounced at the leading edge symmetry node. The cause of this difference is not fully clear, but uncaptured 3D effects may be the cause **review**. While the deformation is not identical, the stresses in the structure are of primary interest. Therefore, the obtained stresses will determine whether this deformation solution is acceptable. Secondly, it should be noted that the deformation in y-direction are significantly smaller than the deformation in z-direction. The vertical deformation can be seen to agree very well with the prediction. The maximum deformation at the crown differs by 0.3%. However, larger offsets may be observed between the crown and vertex, up to 5%, which may be attributed to an uncaptured 3D effects **review.**.

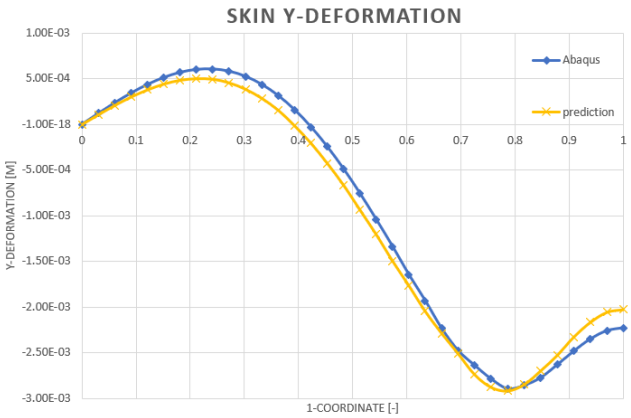

Figure A.2: Y-translation comparison.

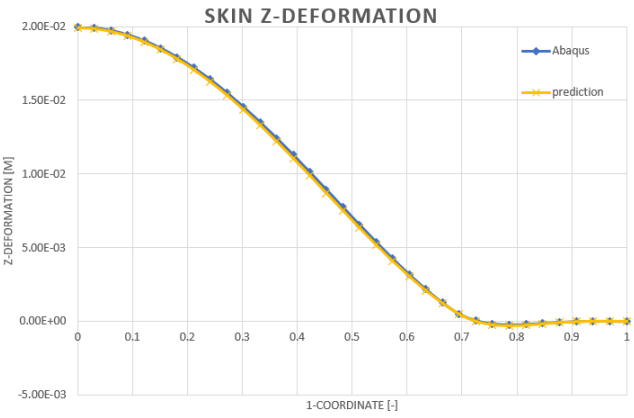

Figure A.3: Z-translation comparison.

While the translation of the Abaqus model frame nodes and skin centre nodes is practically identical, this is not the case for the rotation, as can be observed from figure A.4. Note that while the graph interpolates the shape, this is approximately equal to the observed deformation. While the frame nodes follow a smooth curve due to the high bending stiffness of the frame, the nodes in the section centre show a wavy behaviour near the vertex. This may be partly attributed to the increased flexibility of the section away from the frame, and the required continuity at the vertex. The stringers constrain the translation of the skin well, but this is not the case for the rotation. The skins rotate rather freely about the stringers, which allows the wavy behaviour. As the stringers are modelled as wires, the observed effect is more pronounced than would be expected in reality. The stringer flanges which are attached to the skin would resist this rotation more effectively. Depending on the attachment method, this effect could be increased or decreased. As the open I-section stringers possess a relatively low torsional stiffness compared to closed sections, this effect could be greatly reduced if closed section stiffeners were applied. Another option is to (locally) increase the

stringer pitch to counter this motion. It should also be noted that these stringers are the only stringers along the skins which actually show significant stresses, as visualised in figure A.20. This is another argument for a required local increase in stiffness. The specific reason for this behaviour is unknown, and warrants further research.

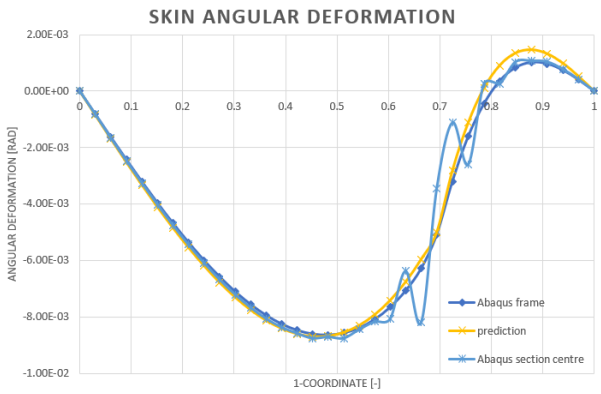

Figure A.4: Angular deformation comparison.

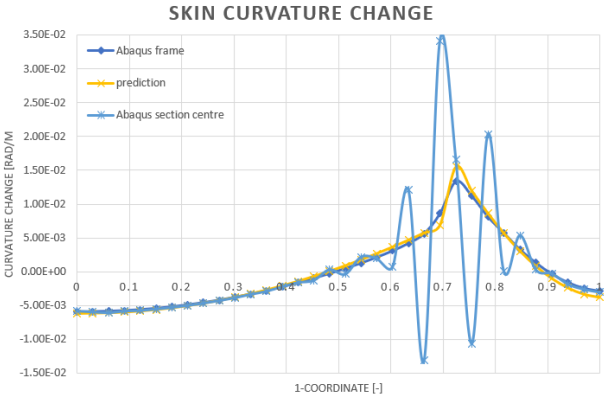

Figure A.5: Curvature change comparison.

While the rotations may be compared, it is also worthwhile to compare the change in curvature, as this is a directly related to the bending stress. The curvature change may be found in figure A.5. Indeed, the waviness near the vertex causes significant changes in curvature.

Lateral direction The deformation in lateral direction should be considered, as it has a significant effect on the overall behaviour. Due to the boundary conditions, the lateral motion is restricted such that all symmetry nodes lie on a single plane. In this validation, the whole problem is symmetric and therefore this causes all symmetry nodes to be planar with the YZ-plane. Therefore, the lateral translation is equal for all symmetry nodes. The Abaqus solution shows a translation of 6.61E-6 m for a half section. The prediction shows a translation of 6.45E-6 m, a difference of 2.4%. This difference is acceptable, as the lateral correction is very simplistic. However, plotting the lateral motion reveals some questionable behaviour in the Abaqus solution, shown in figure A.6. While the boundary values are all identical, in the skins near the vertex, large lateral motions are observed.Similar behaviour may be observed in the ceiling and wall, where repeating patterns may be observed. As this validation does not aim at obtaining the correct lateral motion for the section, the cause of this behaviour is not pursued in further detail. However, this phenomenon may be worthwhile to investigate in later studies.

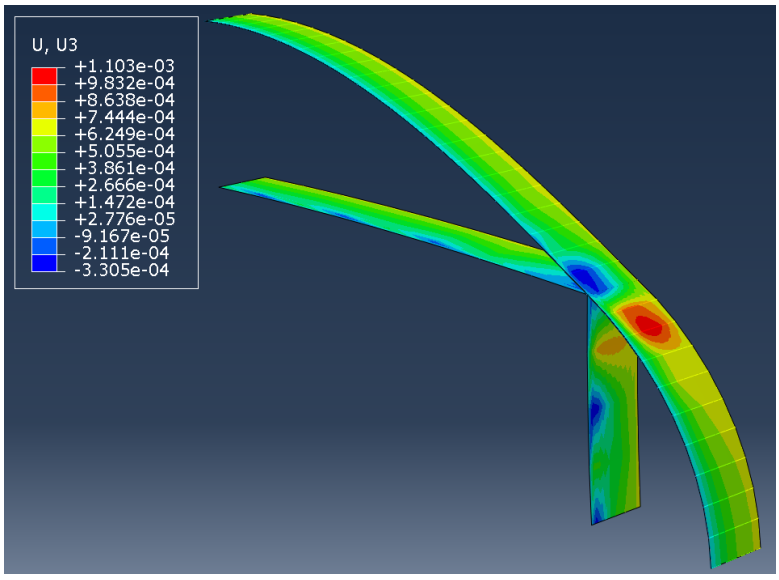

Figure A.6: Section motion in 2-direction. Wire frame and stringers follow identical motion as local skin

Skin stresses

1-direction The stress and deformation variation in the skin from the frame to section centre is the first point of interest. Without longitudinal stiffening, the deformation between the frames is observed to be considerable, causing structural and aerodynamic problems. This deformation can be greatly reduced by applying adequate stiffening. The stiffening may be provided by sandwich panels or stringers, each having their own beneficial and adverse properties. While determining the right stiffening solution is one of the aims of this piece of research, this is not to be answered during this analysis validation. Currently, stringers are being pursued as stiffening elements for the outer skins. Moreover, as the stringers cause increased local variation in the structure compared to a sandwich panel, it is deemed more sensible to use in this validation.

Under the assigned pressure load, the main stress of interest is in the local 1-direction (along the skin arcs). As the skin further expands away from the frames, bending-induced axial stress causes a variation in this stress, S_{11}. From figure A.7, the stress values can be seen to relatively constant from the frame to the section centre. However, near the vertex there are some visible differences. As the visualisation is rough, the variation in S_{11} is plot in a number of locations.

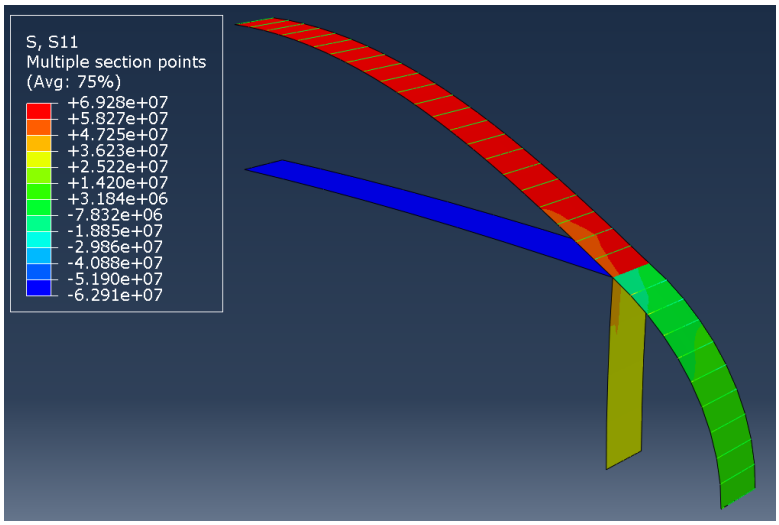

Figure A.7: S_{11} of the skin outer surface.

To illustrate two extremes in the variation, S_{11} is evaluated at the crown symmetry edge and near the vertex. This is visualised in figures A.8 and A.9. At the crown symmetry plane, the prediction is very good at the frame, and starts to deteriorate somewhat approaching the section centre. However, the prediction is off by a maximum of 1%. The stringers effectively limit the bubbling of the skin, and thus the stress variation is low. Near the vertex however, two distinct differences may be observed. Firstly, there is a large mismatch at the frame, of approx. -22%. Moving towards the centre of the section, the stress overtakes the prediction to a maximum difference of approx 9%. This difference may be attributed to the complex deformation of the structure near the vertex. While the prediction is not satisfactory, it will become apparent that the this poorly predicted region is relatively small.

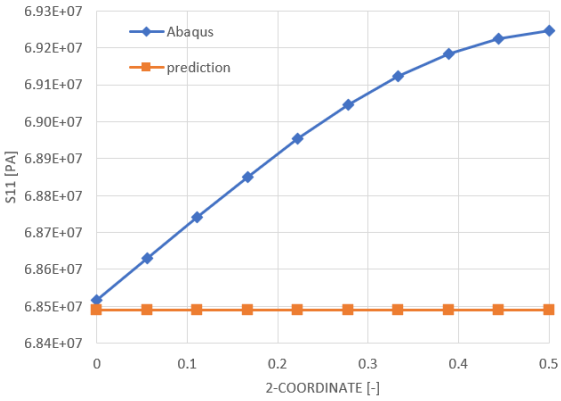

Figure A.8: Skin mid-plane S_{11} variation of the crown symmetry elements.

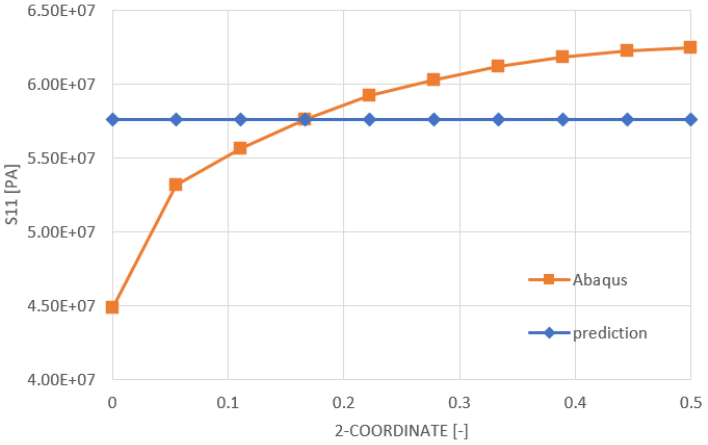

Figure A.9: Skin mid-plane S_{11} variation of the crown elements neighbouring the vertex.

Similarly, the LE symmetry elements are evaluated, as well as the elements neighbouring the vertex. Again, a similar behaviour may be observed: the stresses are quite constant away from the vertex, while the stresses vary greatly near it. The prediction of S_{11} of the crown symmetry elements is noticeably worse than that of the crown counterpart. Abaqus shows an average difference of 6% w.r.t. the prediction. While this is significant, it should be noted that the stresses are very low. Secondary effects which have not been adequately considered may cause this offset. As the stresses due to this load case are considerably low, this is regarded as acceptable. Near the vertex, the prediction is very poor. The following paragraph indicates the overall quality of the S_{11} prediction.

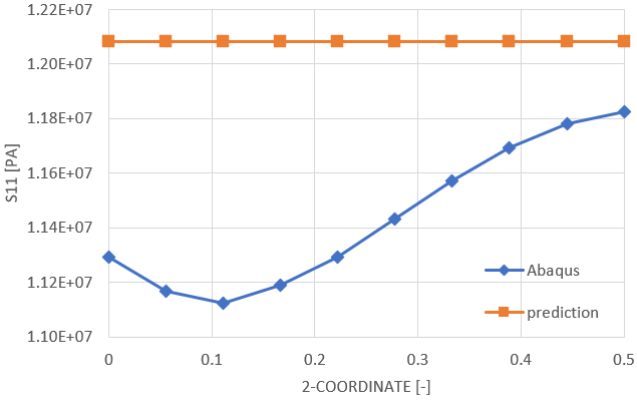

Figure A.10: Skin mid-plane S_{11} variation of the LE symmetry elements.

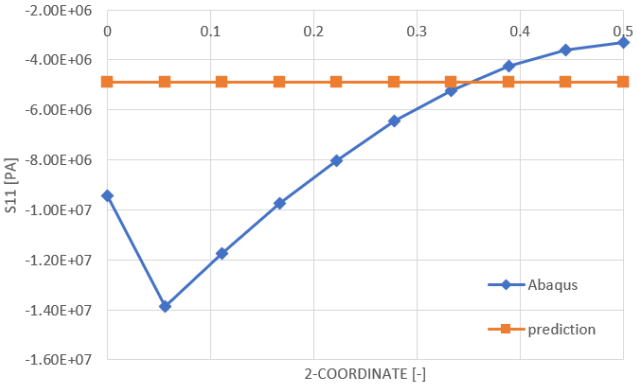

Figure A.11: Skin mid-plane S_{11} variation of the LE elements neighbouring the vertex.

In order to gain a better understanding of the applicability of the stress prediction in the skin along the arcs, the extreme S_{11} was evaluated at several lateral stations: at the frame, at the section centre, and at two equally spaced intermediate stations. The result is shown in figure A.12.

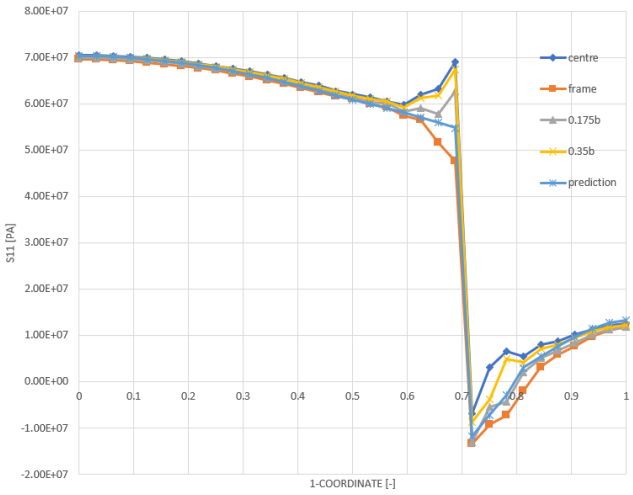

Figure A.12: Extreme S_{11} along the skins at multiple section stations.

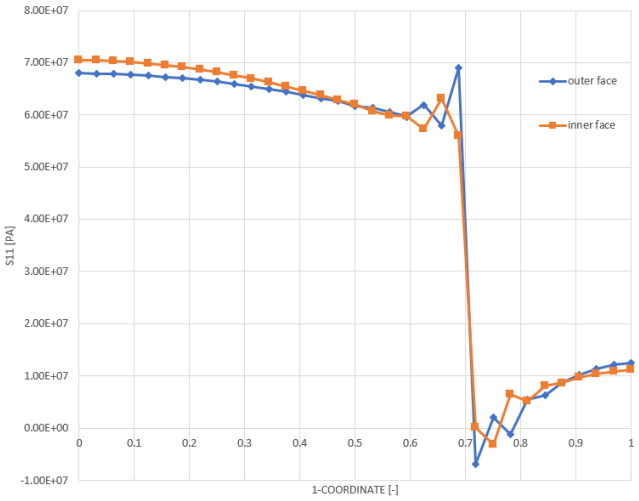

Figure A.13: S_{11} at the inner and outer surface of the skin at section centre.

The poorly predicted regions are near the vertex, for both the crown and the LE. The region near the vertex shows larger variation of the skin stresses along the section. It becomes clear that this is due to local changes in curvature, as seen in figure A.5. As the extreme stresses are portrayed in figure A.12, it appears that the inner or outer skin surface gradually increases or decreases stress when approaching the vertex. However, this is not the case, as is shown in figure A.13. The wavy behaviour causes significant local bending stresses, such that the extreme stress alternates between the inner and outer surface near the vertex. The skin centreline stresses are compared to assess the compared performance while mitigating this effect. This is shown in figure A.14. This improves the prediction significantly near the vertex, but there is still a significant variation along the section. Taking it one step further, the average section mid-plane S_{11} may be compared to the mid-plane predicted stress, leading to figure A.15. This shows the average predicted skin stresses in 1-direction agree very well with the Abaqus results. Notable offsets are found near the vertex, and the LE centreline. For the vertex, the prediction underestimates the stresses in the crown, while it overestimates the stresses in the LE. The mean over-prediction of the whole skin was calculated to almost cancel out at +0.005 MPa. Overall, the prediction is therefore not (un)conservative. However, it should be carried forward that the prediction is not accurate locally.

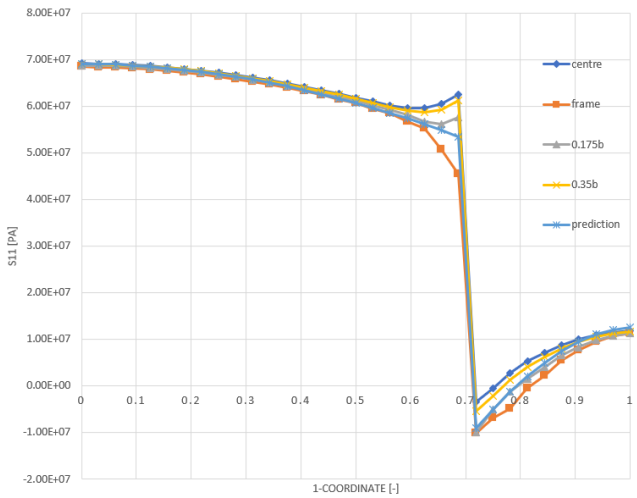

Figure A.14: Mid-plane skin S_{11} at multiple section stations.

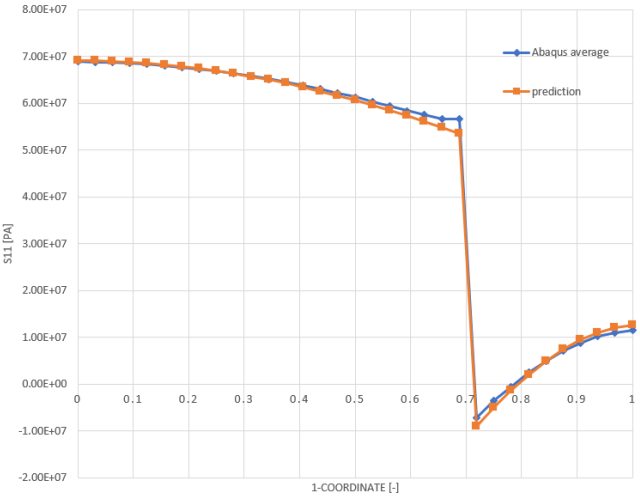

Figure A.15: Mid-plane skin S_{11}, section mean.

2-direction The importance of the lateral stress for the skins has been made apparent in section 5.3. The lateral stresses were compared to assess the validity of the corrections. The lateral stresses were requested in the Abaqus solution, and approximated with the solution as indicated in 5.2. The results are visualised in

figure A.16.

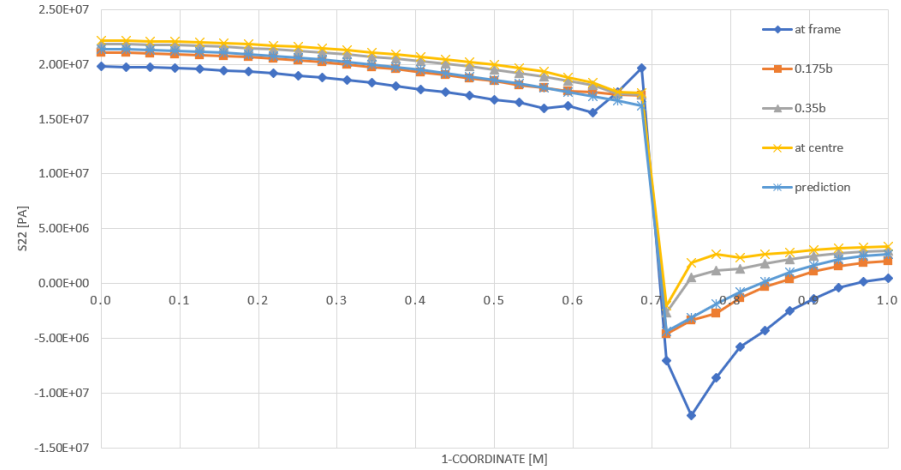

Figure A.16: Skin S_{22} at different section stations.

The prediction shows values of S_{22} which are consistent with the Abaqus solution. The difference in lateral stress for the different stations is likely caused by bending about the local 1-axis, induced by the pressure load. The mean, as shown in figure A.17, matches very well overall, as it is very similar to the stress plot in 1-direction as shown in figure A.15. Similar differences between the prediction and Abaqus solution can be observed in this case.

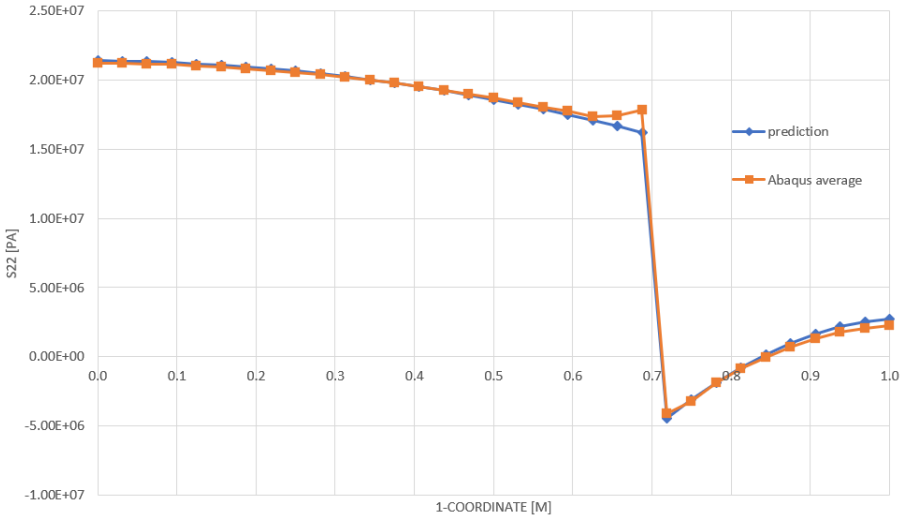

Figure A.17: Skin S_{22} prediction vs. mean Abaqus results.

Frame stresses

The frame stresses may be evaluated by considering the direct and bending contributions separately.

Direct The direct stresses are evaluated at the global neutral line to ensure bending is negated. The results may be found in figure A.18. For most of the crown, the prediction and Abaqus results match very well. However, when approaching the vertex, the Abaqus solution shows a decline in the axial stress before the vertex. When considering figure A.14, it may be concluded that the skin attracts more direct stress while approaching the vertex, while the opposite is true for the frame. As the area of the frame is much smaller than the area of the skin, the corresponding change in stress is higher. This can be seen to be true in general for the skin and frame S_{11} graphs. Overall, the direct stress prediction may be considered conservative.

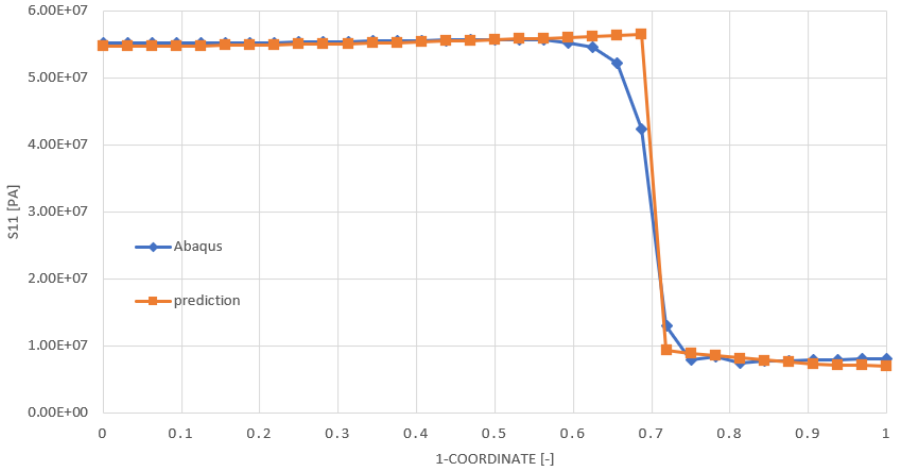

Figure A.18: Pure axial stress evaluated at global neutral line.

Bending The bending-induced axial stresses are evaluated at the top and bottom flange of the frame. As Abaqus evaluates the stresses at the mid-plane of these flanges, these are compared, instead of the stresses at the extreme surfaces. The prediction and Abaqus results are visualised in figure A.19. As the global neutral line is much closer to the top flange, the bending values of the top and bottom flange differ by approximately a factor of 8. However, the behaviour is identical. There are a number of aspects to be noted from the comparison. Firstly, the bending stresses for the crown match well, with a difference of 3.5% at the crown symmetry elements. However, when approaching the vertex, the similarity decreases. The prediction shows a sudden jump in bending at the vertex due to the transferred moment from the ceiling. The transition in the Abaqus results is more gradual. Why Abaqus show this more gradual decrease may be explained when looking at figure A.14. The skin stress at the frame shows comparable behaviour as the frame bending stress. Near the vertex, the skin takes up more bending, while the stress in/near the frame is reduces. The peak bending value at the vertex is off by approximately 14%. For the entirety of the LE, the prediction overestimates the bending stress. At the symmetry element, the Abaqus results are 25% lower than the prediction, which is significant. Overall, the mean overprediction is 1.5 Mpa. While there are some notable differences, the prediction results in more extreme bending stresses, which is conservative.

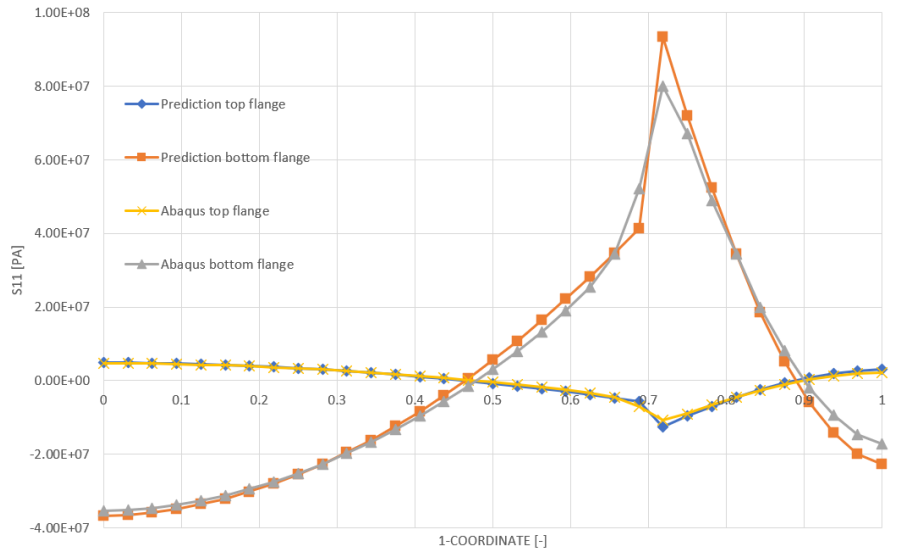

Figure A.19: Bending-induced S_{11} at the frame flange mid-planes.

Stringer stresses

Stringer stresses are only partly considered in the predictive model. Due to the lateral deformation, axial stresses are induced in the stringers, but bending is not considered. The direct stress can be calculated in a straightforward manner, based on the lateral deformation of the section. The predicted stress is 1.42 MPa, versus an Abaqus result of 1.47 MPa.

However, the 2D model does not allow for a bending calculation. Also, as the out-of-plane deformation of the skin couples the 1-direction and 2-direction stresses, this problem increases in complexity. This is a significant shortcoming of the applied approach. Predicted bending stresses with Abaqus are shown in figure A.20. Especially near the vertex joint, significant stresses are observed which are currently not included in the stress modelling approach.

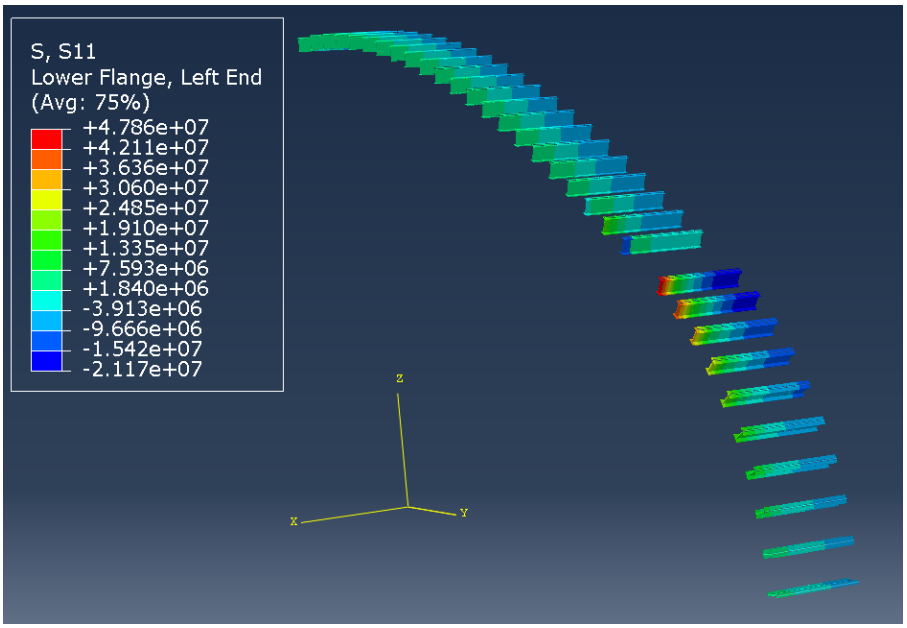

Figure A.20: Axial stresses in the stringers. Significant stress values obtained at LE near vertex.

Modelling correction

In the Abaqus model, the skins are connected to the ceiling and wall at their centre lines. The frame is attached to the inner skin faces. This is not equivalent to the predictive model, which models the members to be attached at their global neutral lines (this includes the frame for the skins). As the direct stresses in the support structure are high (primarily due to pressurisation), the force offset (from skin centreline to global skin-frame neutral line) creates a moment. This is visualised in figure A.21. The support structure force component which is parallel to the skin is multiplied by the aforementioned offset to obtain moments at the vertices, as a correction. These are added to the force vector, and the updated Eigenvalue problem may be solved once more.

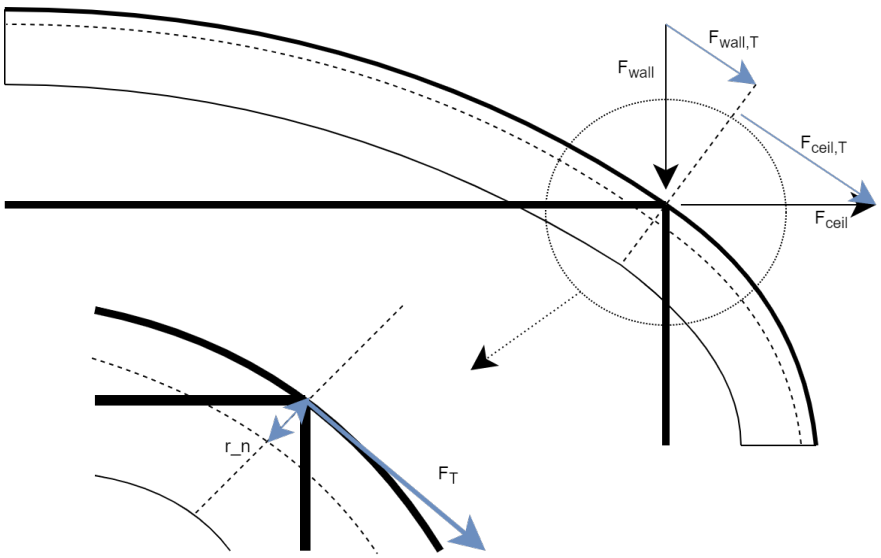

Figure A.21: Support structure offset induces a moment at the vertices.

While this appears to be a minor correction, the differences are significant, as can be seen in the frame bending stress prediction in figure A.22 below.

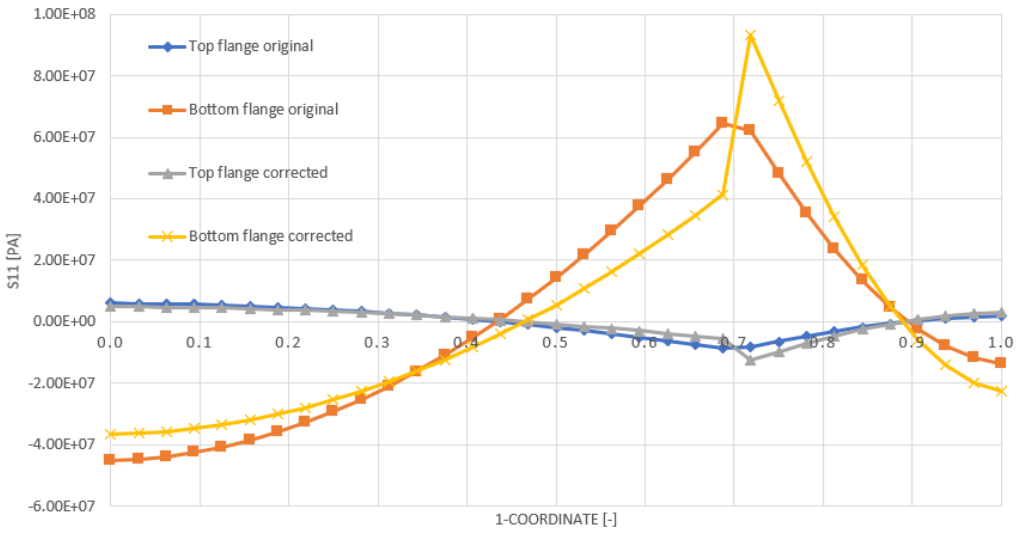

Figure A.22: Effect of correction on bending induced stresses in frame flanges.

B
Material data

All material-related data may be found in the sections below.

B.1. Material data

The material values used in this research are presented in table B.1.

Table B.1: Material property data, obtained from Handbuch Struktur Berechnung [19].

Property	AL2024-T3	AL7075-T6	Mean	Notes	HSB note
$\rho \left[\frac{kg}{m^3}\right]$	2800	2800	2800		12512-01 p.1,p.11.
$E\ [GPa]$	73.1	71.7	72.4		12512-01 p.1,p.11. mean C/T
$\nu\ [-]$	0.33	0.33	0.33		12512-01 p.1,p.11.
$S_{ut}\ [MPa]$	445	545	495 / 506	SMF/fatigue CI input	12512-01 p.1,p.11. mean 0.25/1.0-6.3 mm
$S_{uc}\ [MPa]$	445	545	495	Assumed $S_{uc} = S_{ut}$	Missing
$S_{us}\ [MPa]$	275	328	302		12512-01 p.1,p.11. mean 0.25/1.0-6.3 mm
$S_{yt}\ [MPa]$	310	484	397		12512-01 p.1,p.11. mean 0.25/1.0-6.3 mm
$S_{yc}\ [MPa]$	293	496	394		12512-01 p.1,p.11. mean 0.25/1.0-6.3 mm
$S_{ys}\ [MPa]$	198	286	242		12512-01, p.1,p.11. mean 0.25/1.0-6.3 mm
$S_f\ [MPa]$	162	159	160	Kt=1.0, Sm=0,	63111-01 pp.1-2, 63113-01 pp.1-2, AL7075-T6 clad
$m_F\ [-]$	2.70	3.02	2.91		63205-01 p.4
C_F $\left[\frac{mm}{cycle}\left(MPa\sqrt{mm}\right)^{1-m_F}\right]$	2.01e-8	1.28e-8	1.65e-8		63205-01 p.4
$K_F\ [MPa\sqrt{mm}]$	2256	2021	2139		63205-01 p.4

B.2. Material properties averaging method

For all relevant material properties, the weighted average value of the two alloys was calculated.

Young's modulus For the Young's modulus, the mean was taken. All related failure modes are linearly dependent on the stiffness. Effects caused by differences in adjacent stiffness were neglected. As the stiffness values of AL2024 and AL7075 are within 2%, this was deemed appropriate.

Static material strength Similarly, For the static strength properties, the mean was used, as the related failure indices are linearly related to the static strengths.

Crack initiation parameters For the crack initiation analysis, the ultimate tensile strength and fatigue strength have a very large effect on the SN-curves used to calculate the crack initiation life. For the fatigue strength (at 1e6 cycles), the values of AL7075 and AL2024 are identical. However, the ultimate tensile strengths are significantly different, by approx 20%. In the double logarithmic scale, the line connecting the ultimate tensile strength and the fatigue strength must be straight, at 1e2 and 1e6 cycles, respectively. Using Basquin's relation, the mean is determined in a straightforward manner, as shown below. For simplicity, as the fatigue strength of AL2024 and AL7075 is almost identical (162 and 159 MPa, respectively), the lower knee value was set at the average of 160.5 MPa.

$$N_{avg,445} = (N_{AL2024,445} + N_{AL7075,445})/2 = (1e2 + 1e6 * \frac{445^m}{160.5^m})/2 = 280 \tag{B.1}$$

where

$$m_{7075*} = \frac{log\left(\frac{1e2}{1e6}\right)}{\left(\frac{545}{207}\right)} \tag{B.2}$$

With the new value at 280cycles, m can be determined similarly as shown above. Then determining the strength at the upper knee for this relation:

$$S_{avg,up} = \left(\left(\frac{1e6}{1e2}\right)^{m_{avg}}\right)^{1/m_{avg}} = 506MPa \tag{B.3}$$

Crack propagation parameters The Forman constant was averaged, at 1.645e-8, as its effect on crack growth is linear. The Forman exponent has a significant effect on the crack growth rate. For AL2024-T3 and AL7075-T6, the Forman exponent is similar, at 2.70 and 3.02, respectively. A representative value was calculated in a straightforward manner:

$$m_F = \frac{log\left(\frac{1}{2}\left(dS^{m_{F,2024}} + dS^{m_{F,7075}}\right)\right)}{log(dS)} \tag{B.4}$$

where dS is the stress amplitude. The stress amplitude must be significantly below the static value, and was assumed at 150 MPa, leading to a Forman exponent of 2.918. The sensitivity is very low, as for 100 and 200 MPa, the exponent results in 2.914 and 2.921, respectively. Lastly, the Forman constant was averaged.

C
Buckling derivations

Plate biaxial buckling The stability of the stiffened panel is described by the von Karman equation:

$$D_{11}\frac{\partial^4 w}{\partial x^4} + 2\left(D_{12}+2D_{66}\right)\frac{\partial^4 w}{\partial x^2 \partial y^2} + D_{22}\frac{\partial^4 w}{\partial y^4} = N_x\frac{\partial^2 w}{\partial x^2} + 2N_{xy}\frac{\partial^2 w}{\partial x \partial y} + N_y\frac{\partial^2 w}{\partial y^2} - p_x\frac{\partial w}{\partial x} - p_y\frac{\partial w}{\partial y} + p_z \quad \text{(C.1)}$$

In this approach, only biaxial loads are considered. Therefore, the distributed loads p_x, p_y and p_z are zero. Secondly, the shear load N_{xy} is also considered zero. This terms that remain are:

$$D_{11}\frac{\partial^4 w}{\partial x^4} + 2\left(D_{12}+2D_{66}\right)\frac{\partial^4 w}{\partial x^2 \partial y^2} + D_{22}\frac{\partial^4 w}{\partial y^4} = N_x\frac{\partial^2 w}{\partial x^2} + N_y\frac{\partial^2 w}{\partial y^2} \quad \text{(C.2)}$$

The plate is simply-supported on all boundaries. Therefore, the moments and the displacements at the boundaries are zero:

$$\begin{aligned} w = M_x = -D_{11}\frac{\partial^2 w}{\partial x^2} - D_{12}\frac{\partial^2 w}{\partial y^2} = 0 for x = 0 \quad , \quad x = a \\ w = M_y = -D_{22}\frac{\partial^2 w}{\partial y^2} - D_{12}\frac{\partial^2 w}{\partial x^2} = 0 for y = 0 \quad , \quad y = b \end{aligned} \quad \text{(C.3)}$$

A trial function for displacement w which satisfies the simply-supported boundary conditions is:

$$w = \sum\sum A_{mn} sin\frac{m\pi x}{a} sin\frac{n\pi y}{b} \quad \text{(C.4)}$$

Substituting this into equation C.3 leads to:

$$A_{mn}\pi^2\left(D_{11}m^4 + 2\left(D_{12}+2D_{66}\right)m^2n^2\left(\frac{a}{b}\right)^2 + D_2n^4\left(\frac{a}{b}\right)^4\right) = -A_{mn}a^2\left(N_xm^2 + N_yn^2\left(\frac{a}{b}\right)^2\right) \quad \text{(C.5)}$$

As the plate buckles, the deflection is nonzero, and therefore the only legitimate values possess $A_{mn} \neq 0$,a nd thus cancel out. Rearranging:

$$N_0 = \frac{\pi^2\left(D_{11}m^4 + 2\left(D_{12}+2D_{66}\right)m^2n^2\left(\frac{a}{b}\right)^2 + D_2n^4\left(\frac{a}{b}\right)^4\right)}{a^2\left(m^2 + kn^2\left(\frac{a}{b}\right)^2\right)} \quad \text{(C.6)}$$

where k equals N_y/N_x, and $N_0 = -N_x$. This value is to be minimised by trialling pairs of m and n.

Plate shear buckling From the Von Karman equation (eq. C.1), the governing equation for the shear buckling of a plate may be determined to be:

$$D_{11}\frac{\partial^4 w}{\partial x^4} + 2\left(D_{12}+2D_{66}\right)\frac{\partial^4 w}{\partial x^2 \partial y^2} + D_{22}\frac{\partial^4 w}{\partial y^4} = 2N_{xy}\frac{\partial^2 w}{\partial x \partial y} \quad \text{(C.7)}$$

The displacement of the stiffened panel is assumed to be well-represented with the two-term relation shown in equation C.8. According to Kassapoglou [65], two terms are required as a minimum for this shear buckling problem.

$$w = w_1 \sin\frac{\pi x}{a}\sin\frac{\pi y}{b} + w_2 \sin\frac{2\pi x}{a}\sin\frac{2\pi y}{b} \tag{C.8}$$

Here w_1 and w_2 are unknown constants. This equation satisfies the boundary conditions, as the displacement is zero at all edges. The moments should also be zero at the edges:

$$\begin{aligned} M_x &= -D_{11}\frac{\partial^2 w}{\partial x^2} - D_{12}\frac{\partial^2 w}{\partial y^2} = 0 \qquad at \qquad x = 0, x = a \\ M_y &= -D_{12}\frac{\partial^2 w}{\partial x^2} - D_{22}\frac{\partial^2 w}{\partial y^2} = 0 \qquad at \qquad y = 0, y = b \end{aligned} \tag{C.9}$$

An energy minimisation approach is used to obtain an approximate solution. The total energy is represented below as strain energy and work term.

$$\begin{aligned} \Pi = \frac{1}{2}\iint \Bigg[& D_{11}\left(\frac{\partial^2 w}{\partial x^2}\right)^2 + 2D_{12}\frac{\partial^2 w}{\partial x^2}\frac{\partial^2 w}{\partial y^2} + D_{22}\left(\frac{\partial^2 w}{\partial y^2}\right)^2 + 4D_{66}\left(\frac{\partial^2 w}{\partial x \partial y}\right)^2 + 4D_{16}\frac{\partial^2 w}{\partial x^2}\frac{\partial^2 w}{\partial x \partial y} \\ & + 4D_{26}\frac{\partial^2 w}{\partial y^2}\frac{\partial^2 w}{\partial x \partial y}\Bigg] dxdy - \frac{1}{2}\iint N_x\left(\frac{\partial w}{\partial x}\right)^2 \mathrm{d}x\mathrm{d}y - \iint N_{xy}\frac{\partial w}{\partial x}\frac{\partial w}{\partial y} dxdy \end{aligned} \tag{C.10}$$

Substituting, the first term is equal to:

$$\begin{aligned} \left(\frac{\partial^2 w}{\partial x^2}\right)^2 = {} & w_1^2\frac{\pi^4}{4a^4}\left(1-\cos\frac{2\pi x}{a}\right)\left(1-\cos\frac{2\pi y}{b}\right) + w_2^2\frac{16\pi^4}{4a^4}\left(1-\cos\frac{4\pi x}{a}\right)\left(1-\cos\frac{4\pi y}{b}\right) \\ & + 2w_1 w_2\frac{4\pi^4}{a^4}\frac{1}{4}\left(\cos\frac{\pi x}{a} - \cos\frac{3\pi x}{a}\right)\left(\cos\frac{\pi y}{b} - \cos\frac{3\pi y}{b}\right) \end{aligned} \tag{C.11}$$

This can be done for the remaining terms as well. Integrating the terms yields:

$$\int_0^a\int_0^b \left(\frac{\partial^2 w}{\partial x^2}\right)^2 \mathrm{d}x\mathrm{d}y = w_1^2\frac{\pi^4}{4a^4}ab + w_2^2\frac{4\pi^4}{a^4}ab \tag{C.12}$$

$$\int_0^a\int_0^b \left(\frac{\partial^2 w}{\partial y^2}\right)^2 \mathrm{d}x\mathrm{d}y = w_1^2\frac{\pi^4}{4b^4}ab + w_2^2\frac{4\pi^4}{b^4}ab \tag{C.13}$$

$$\int_0^a\int_0^b \left(\frac{\partial^2 w}{\partial x^2}\frac{\partial^2 w}{\partial y^2}\right)\mathrm{d}x\mathrm{d}y = w_1^2\frac{\pi^4}{4a^2b^2}ab + w_2^2\frac{4\pi^4}{a^2b^2}ab \tag{C.14}$$

$$\int_0^a\int_0^b \left(\frac{\partial^2 w}{\partial x \partial y}\right)^2 \mathrm{d}x\mathrm{d}y = w_1^2\frac{\pi^4}{4a^2b^2}ab + w_2^2\frac{4\pi^4}{a^2b^2}ab \tag{C.15}$$

$$\int_0^a\int_0^b \left(\frac{\partial w}{\partial x}\right)^2 \mathrm{d}x\mathrm{d}y = w_1^2\frac{\pi^2}{4a^2}ab + w_2^2\frac{\pi^2}{a^2}ab \tag{C.16}$$

$$\int_0^a\int_0^b \left(\frac{\partial w}{\partial x}\frac{\partial w}{\partial y}\right)\mathrm{d}x\mathrm{d}y = \frac{w_1 w_2\pi^2}{2ab}\left(\frac{2a}{3\pi}+\frac{2a}{\pi}\right)\left(\frac{2b}{3\pi}-\frac{2b}{\pi}\right) + \frac{w_1 w_2\pi^2}{2ab}\left(\frac{2a}{3\pi}-\frac{2a}{\pi}\right)\left(\frac{2b}{3\pi}+\frac{2b}{\pi}\right) \tag{C.17}$$

Substituting this into the energy relation, and rearranging, yields:

$$\Pi = \frac{1}{2}\left(D_{11}\left[w_1^2\frac{\pi^4}{4a^3}b + w_2^2\frac{4\pi^4}{a^3}b\right] + 2\left(D_{12}+2D_{66}\right)\left[w_1^2\frac{\pi^4}{4ab} + w_2^2\frac{4\pi^4}{ab}\right] + D_{22}\left[w_1^2\frac{\pi^4}{4b^3}a + w_2^2\frac{4\pi^4}{b^3}a\right]\right) - \frac{N_o}{2}\left[w_1^2\frac{\pi^2}{4a}b + w_2^2\frac{\pi^2}{a}b\right] - kN_o w_1 w_2\left(-\frac{16}{9}\right)\left(-\frac{16}{9}\right) \tag{C.18}$$

Introducing the loading ratio k, which is defined as:

$$k = \frac{N_{xy}}{N_x} \tag{C.19}$$

and introducing $N_0 = N_{xcrit}$ where simultaneously under load $N_{xy} = kN_x$, buckling occurs due to the combined load case. The energy should be minimised w.r.t. the unknowns w_1 and W_2, and equated to zero.

$$\begin{aligned} \frac{1}{2}\left(D_{11}\frac{w_1\pi^4 b}{2a^3} + 2\left(D_{12}+2D_{66}\right)\frac{\pi^4 w_1}{2ab} + D_{22}\frac{w_1\pi^4 a}{2b^3}\right) - N_o\frac{w_1\pi^2 b}{4a} + \frac{32}{9}kN_o w_2 = 0 \\ \frac{1}{2}\left(D_{11}\frac{8w_2\pi^4 b}{a^3} + 2\left(D_{12}+2D_{66}\right)\frac{8\pi^4 w_2}{ab} + D_{22}\frac{8w_2\pi^4 a}{b^3}\right) - N_o\frac{w_2\pi^2 b}{a} + \frac{32}{9}kN_o w_1 = 0 \end{aligned} \tag{C.20}$$

Introducing K_1 to improve readability:

$$K_1 = \frac{1}{4}\left[D_{11}\frac{\pi^4 b}{a^3} + 2\left(D_{12}+2D_{66}\right)\frac{\pi^4}{ab} + D_{22}\frac{\pi^4 a}{b^3}\right] \tag{C.21}$$

Now equation C.20 can be considered as the following Eigenvalue problem:

$$\begin{bmatrix} K_1 & 0 \\ 0 & 16K_1 \end{bmatrix}\begin{Bmatrix} w_1 \\ w_2 \end{Bmatrix} = N_o\begin{bmatrix} \frac{\pi^2 b}{4a} & -\frac{32}{9}k \\ -\frac{32}{9}k & \frac{\pi^2 b}{a} \end{bmatrix}\begin{Bmatrix} w_1 \\ w_2 \end{Bmatrix} \tag{C.22}$$

Which is of the form:

$$Ax = \alpha Bx \tag{C.23}$$

This common Eigenvalue problem is solved by:

$$B^{-1}Ax = \alpha B^{-1}Bx = \alpha Ix \tag{C.24}$$

where I represents the identity matrix. The inverse of B is easily computed:

$$B^{-1} = \frac{1}{\frac{\pi^4 b^2}{4a^2} - \left(\frac{32}{9}k\right)^2}\begin{bmatrix} \frac{\pi^2 b}{a} & \frac{32}{9}k \\ \frac{32}{9}k & \frac{\pi^2 b}{4a} \end{bmatrix} \tag{C.25}$$

Then:

$$\begin{bmatrix} \frac{\pi^2 b}{a} & 16\frac{32}{9}k \\ \frac{32}{9}k & \frac{\pi^2 b}{4a}16 \end{bmatrix}\begin{Bmatrix} w_1 \\ w_2 \end{Bmatrix} = N_o\left(\frac{\pi^4 b^2}{4a^2} - \left(\frac{32}{9}k\right)^2\right)\frac{1}{K_1}\begin{Bmatrix} w_1 \\ w_2 \end{Bmatrix} \tag{C.26}$$

defining α as:

$$\alpha = N_o\left(\frac{\pi^4 b^2}{4a^2} - \left(\frac{32}{9}k\right)^2\right)\frac{1}{K_1} \tag{C.27}$$

To obtain an nontrivial solution:

$$det\left[B^{-1}A-\alpha I\right]=0 \tag{C.28}$$

which yields:

$$\left(\frac{\pi^2 b}{a}-\alpha\right)\left(\frac{4\pi^2 b}{a}-\alpha\right)-\frac{512(32)}{81}k^2=0 \tag{C.29}$$

solving for the eigenvalue and rearranging for N_0:

$$N_o=\frac{\pi^2}{a^2}\frac{\left(D_{11}+2\left(D_{12}+2D_{66}\right)\frac{a^2}{b^2}+D_{22}\frac{a^4}{b^4}\right)}{2-\frac{8192}{81}\frac{a^2}{b^2\pi^4}k^2}\left[5\pm\sqrt{9+\frac{65536}{81}\frac{a^2}{\pi^4 b^2}k^2}\right] \tag{C.30}$$

This method assumed combined loading as the input, but in this case the load is purely shear. The load ratio k is then effectively infinite, which leads to a simplification:

$$N_o=\pm\frac{\pi^2}{a^2}\frac{\left(D_{11}+2\left(D_{12}+2D_{66}\right)\frac{a^2}{b^2}+D_{22}\frac{a^4}{b^4}\right)}{\frac{32}{9}\frac{a}{b\pi^2}k} \tag{C.31}$$

Then, as $N_{xy}=N_o k$, the critical shear load is obtained, and the factor k disappears from the relation:

$$N_{xycrit}=\pm\frac{9\pi^4 b}{32a^3}\left(D_{11}+2\left(D_{12}+2D_{66}\right)\frac{a^2}{b^2}+D_{22}\frac{a^4}{b^4}\right) \tag{C.32}$$

Note that the $\pm$ sign makes sense, as for shear in either direction, buckling may occur. As stated by Kassapogou [**?**], this solution is typically 27-30% higher than the exact solution. As a higher buckling load is unconservative, this load is therefore divided by 1.3.

$$N_{xycrit}=\pm\frac{9\pi^4 b}{1.3*32a^3}\left(D_{11}+2\left(D_{12}+2D_{66}\right)\frac{a^2}{b^2}+D_{22}\frac{a^4}{b^4}\right) \tag{C.33}$$

The obtained solution may be directly applied to obtain an estimate of the critical buckling load under pure shear. Notably, this approach does not require the evaluation of a number of m,n terms to obtain the minimum buckling load. This trait lends itself very well to the design problem at hand.

D
Load cases and load distributions

A comprehensive overview of the different load cases, distributed resultant loads and running loads are shown below.

- Pressurised positive manoeuvring, evaluated at:
  LC01: Design payload mass, zero cargo, maximum cruise fuel mass.
  LC02: Design payload mass, zero cargo, minimum cruise fuel mass.
  LC03: Maximum payload mass, maximum cargo, maximum associated fuel mass.
  LC04: Design payload mass, maximum cargo, minimum associated fuel mass.
  LC05: Zero payload mass, zero cargo mass, maximum cruise fuel mass.
  LC06: Zero payload mass, zero cargo , minimum cruise fuel mass.
- Unpressurised positive manoeuvring, evaluated at identical weights as above **(LC07-LC12)**.
- Pressurised negative manoeuvring, evaluated at identical weights as above **(LC13-LC18)**.
- Unpressurised negative manoeuvring, evaluated at identical weights as above **(LC19-LC24)**.
- Unpressurised landing cases:
  LC25: 3-point landing landing at MTOW, 6 fps descent velocity. MTOW consisting of design payload mass and maximum fuel.
  LC26: 2-point landing landing at MTOW, 6 fps descent velocity. MTOW consisting of design payload mass and maximum fuel.
  LC27: 3-point landing landing at MLW, 10 fps descent velocity. MLW consisting of design payload mass and associated fuel.
  LC28: 2-point landing landing at MLW, 10 fps descent velocity. MLW consisting of design payload mass and associated fuel.
  LC29: 3-point landing landing at MTOW, 6 fps descent velocity. MTOW consisting of design payload mass, maximum cargo mass and associated fuel mass.
  LC30: 2-point landing landing at MTOW, 6 fps descent velocity. MTOW consisting of design payload mass, maximum cargo mass and associated fuel mass.
  LC31: 3-point landing landing at MLW, 10 fps descent velocity. MLW consisting of design payload mass, maximum cargo mass and associated fuel mass.
  LC32: 2-point landing landing at MLW, 10 fps descent velocity. MLW consisting of design payload mass, maximum cargo mass and associated fuel mass.
- Unpressurised ground braking:
  LC33: Braking at maximum braking coefficient at MRW. MRW consisting of design payload mass, zero cargo and maximum ramp fuel.
  LC34: Braking at maximum braking coefficient at MRW. MRW consisting of design payload mass, maximum cargo and associated ramp weight fuel.
  LC35: Braking at 1.2*maximum braking coefficient at MLW. MLW consisting of design payload mass, zero cargo and maximum landing fuel.
  LC36: Braking at 1.2*maximum braking coefficient at MRW. MRW consisting of design payload mass, maximum cargo and associated ramp weight fuel.
- Take-off
  LC37: Take-off at MTOW. Maximum thrust. MTOW consisting of design payload mass, zero cargo and maximum fuel.
  LC38: Take-off at MTOW. Maximum thrust. MTOW consisting of design payload mass, zero cargo and maximum fuel.

LC39: Take-off at MTOW. Maximum thrust. MTOW consisting of design payload mass, maximum cargo and maximum associated fuel.
LC40: Take-off at MTOW. Maximum thrust. MTOW consisting of design payload mass, maximum cargo and minimum associated fuel.
LC41: Take-off at low mass. Maximum thrust. Mass consisting of zero payload mass, zero cargo mass and maximum fuel mass.
LC42: Take-off at low mass. Maximum thrust. Mass consisting of zero payload mass, zero cargo mass and minimum fuel mass.

- Overpressure:
  LC01: Over-pressure load. Pressurisation of cruise level, multiplied by a factor 1.33 and safety factor, excluding other loads, as per CS 25.365d.

Table D.1: Load case set. For ultimate load cases: SF_p=1.33, SF=1.5.

Code	**Payload**	**Cargo**	**Fuel**	**delta p [kPa]**	n_z **[-]**	**Note**
LC01	DPLM	0	Max Cruise	57.5*SF_p	2.5*SF	Manoeuvres
LC02	DPLM	0	Min Cruise	57.5*SF_p	2.5*SF	
LC03	DPLM	Max	Max Cruise	57.5*SF_p	2.5*SF	
LC04	DPLM	Max	Min Cruise	57.5*SF_p	2.5*SF	
LC05	0	0	Max Cruise	57.5*SF_p	2.5*SF	
LC06	0	0	Min Cruise	57.5*SF_p	2.5*SF	
LC07	DPLM	0	Max Cruise	0	2.5*SF	
LC08	DPLM	0	Min Cruise	0	2.5*SF	
LC09	DPLM	Max	Max Cruise	0	2.5*SF	
LC10	DPLM	Max	Min Cruise	0	2.5*SF	
LC11	0	0	Max Cruise	0	2.5*SF	
LC12	0	0	Min Cruise	0	2.5*SF	
LC13	DPLM	0	Max Cruise	57.5*SF_p	-1.0*SF	
LC14	DPLM	0	Min Cruise	57.5*SF_p	-1.0*SF	
LC15	DPLM	Max	Max Cruise	57.5*SF_p	-1.0*SF	
LC16	DPLM	Max	Min Cruise	57.5*SF_p	-1.0*SF	
LC17	0	0	Max Cruise	57.5*SF_p	-1.0*SF	
LC18	0	0	Min Cruise	57.5*SF_p	-1.0*SF	
LC19	DPLM	0	Max Cruise	0	-1.0*SF	
LC20	DPLM	0	Min Cruise	0	-1.0*SF	
LC21	DPLM	Max	Max Cruise	0	-1.0*SF	
LC22	DPLM	Max	Min Cruise	0	-1.0*SF	
LC23	0	0	Max Cruise	0	-1.0*SF	
LC24	0	0	Min Cruise	0	-1.0*SF	
LC25	DPLM	0	Max TO	0	$(1+\delta n_{6fps})$*SF	3-point landing
LC26	DPLM	0	Max TO	0	$(1+\delta n_{6fps})$*SF	2-point landing
LC27	DPLM	0	Max Land	0	$(1+\delta n_{10fps})$*SF	3-point landing
LC28	DPLM	0	Max Land	0	$(1+\delta n_{10fps})$*SF	2-point landing
LC29	DPLM	Max	Max TO	0	$(1+\delta n_{6fps})$*SF	3-point landing
LC30	DPLM	Max	Max TO	0	$(1+\delta n_{6fps})$*SF	2-point landing
LC31	DPLM	Max	Max Land	0	$(1+\delta n_{10fps})$*SF	3-point landing
LC32	DPLM	Max	Max Land	0	$(1+\delta n_{10fps})$*SF	2-point landing
LC33	DPLM	0	Max Ramp	0	1.0*SF	Braking
LC34	DPLM	Max	Max Ramp	0	1.0*SF	
LC35	DPLM	0	Max Land	0	1.2*SF	
LC36	DPLM	Max	Max Land	0	1.2*SF	
LC37	DPLM	0	Max Take-off	0	1.0	TO Thrust
LC38	DPLM	0	Min Take-off	0	1.0	TO Thrust
LC39	DPLM	Max	Max Take-off	0	1.0	TO Thrust
LC40	DPLM	Max	Min Take-off	0	1.0	TO Thrust
LC41	0	0	Max Take-off	0	1.0	TO Thrust
LC42	0	0	Min Take-off	0	1.0	TO Thrust
LC61	N/A	N/A	N/A	57.5*1.33*SF_p	0	Overpressure

Table D.2: Criticality identification of load cases. Classification: 'x': critical, 'or': two similar cases which are critical, 'any': loads are similar enough to pick any.

	Running loads						Cross-section load		Selected
Load case	Sx	Sy	Sz	Mx	My	Mz	Sy	Sz	-
LC01	any	or	or	or			or		
LC02			or					x	**x**
LC03		or	x	or	x	x	or	x	**x**
LC04									
LC05									
LC06									
LC07	or								
LC08									
LC09	or								**x**
LC10									
LC11									
LC12									
LC13	any		or	or			or		
LC14			or						
LC15			x	or	x		or		**x**
LC16									
LC17									
LC18									
LC19	or								
LC20									
LC21	or								**x**
LC22									
LC23									
LC24									
LC25			or						
LC26	x	x	or	or	x		or		**x**
LC27									
LC28				or		x	or	x	**x**
LC29									
LC30	x								**x**
LC31	or								
LC32	or					x			**x**
LC33							or	or	
LC34	x	x	x	x	x	x	or	or	**x**
LC35								or	
LC36									
LC37									
LC38									
LC39	x	x	x			or	or		**x**
LC40									
LC41						or	or		
LC42									

D.1. Cumulative load distributions

The figures below show the running loads for the ultimate load cases LC01-LC42. They are shown to give an impression of the load distribution throughout the wing-fuselage structure. These were used to identify the most severe load cases per category.

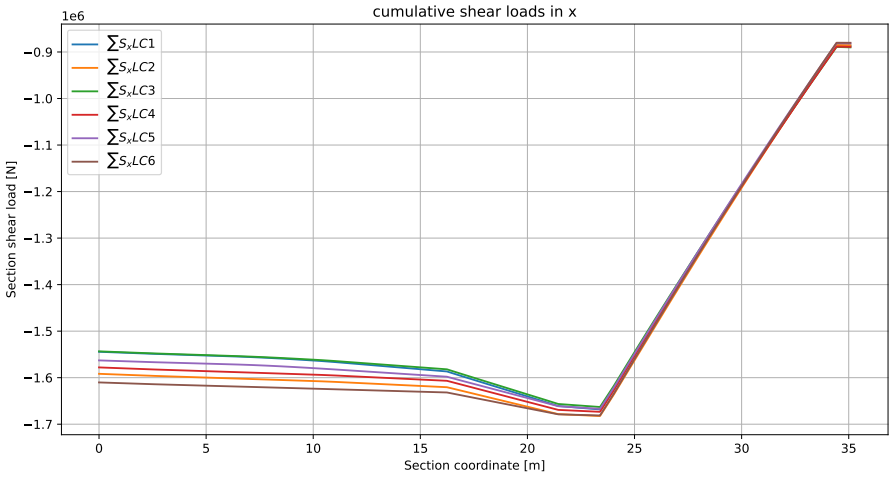

Figure D.1: Cumulative Sx for pressurised positive manoeuvring (LC01-LC06).

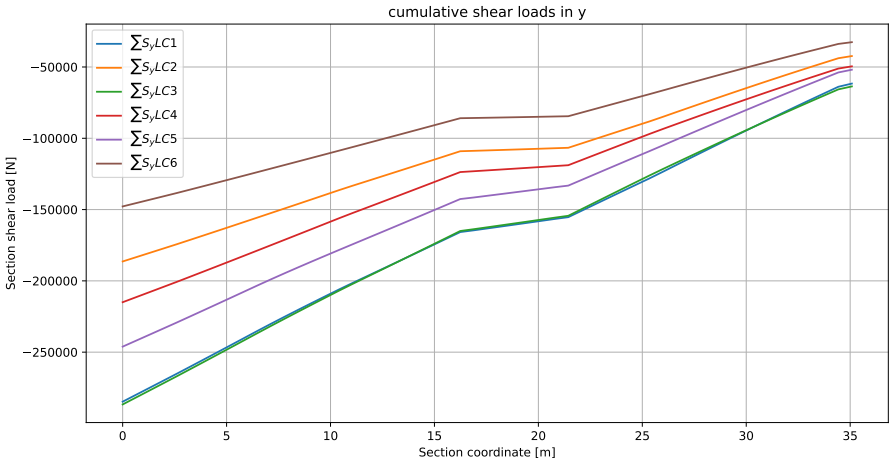

Figure D.2: Cumulative Sy for pressurised positive manoeuvring (LC01-LC06).

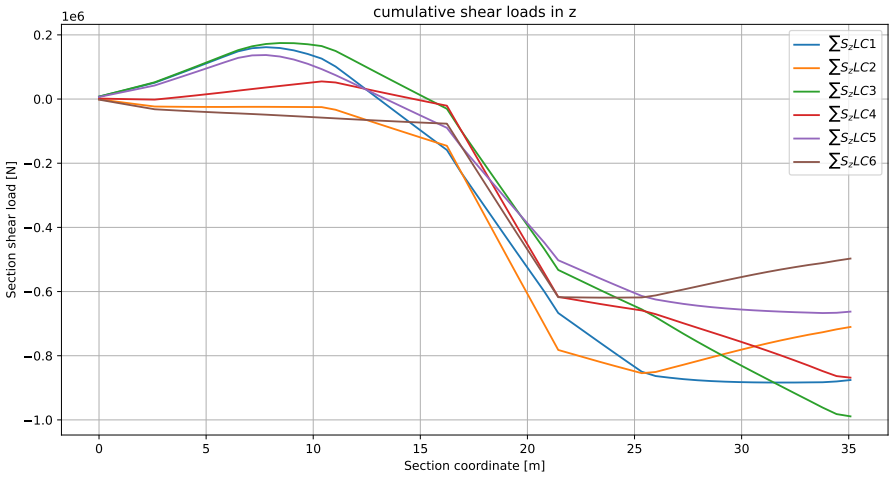

Figure D.3: Cumulative Sz for pressurised positive manoeuvring (LC01-LC06).

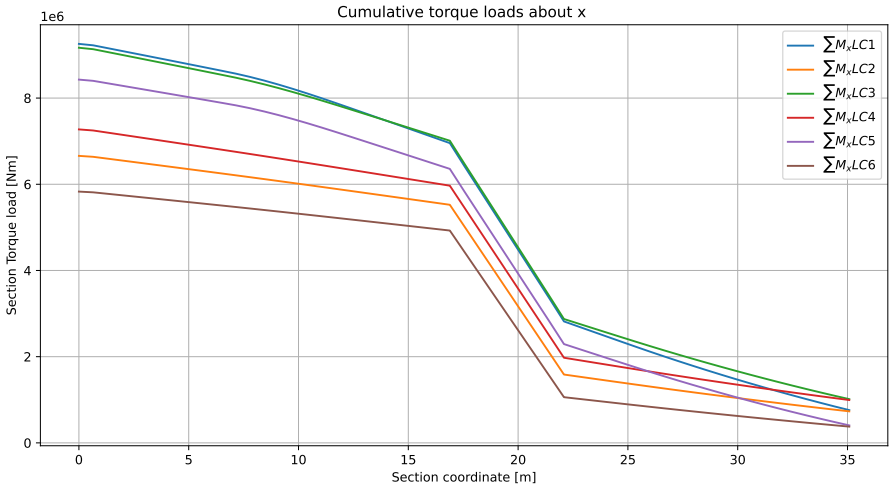

Figure D.4: Cumulative Mx for pressurised positive manoeuvring (LC01-LC06).

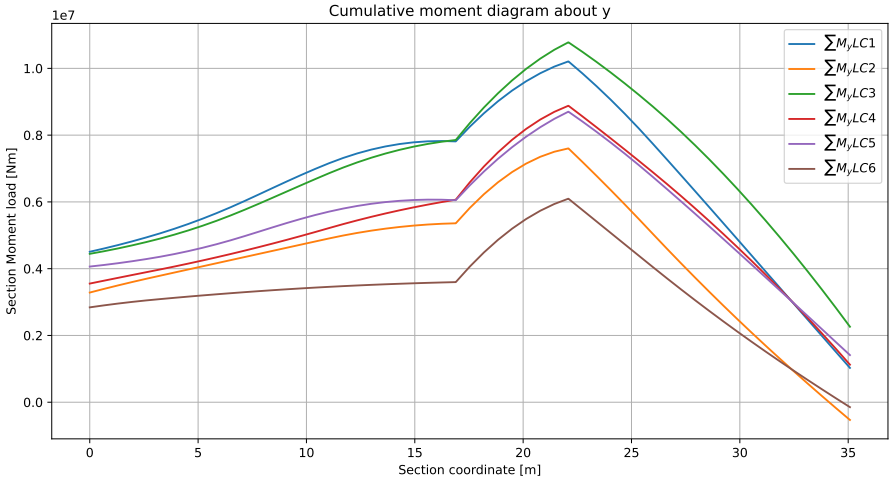

Figure D.5: Cumulative My for pressurised positive manoeuvring (LC01-LC06).

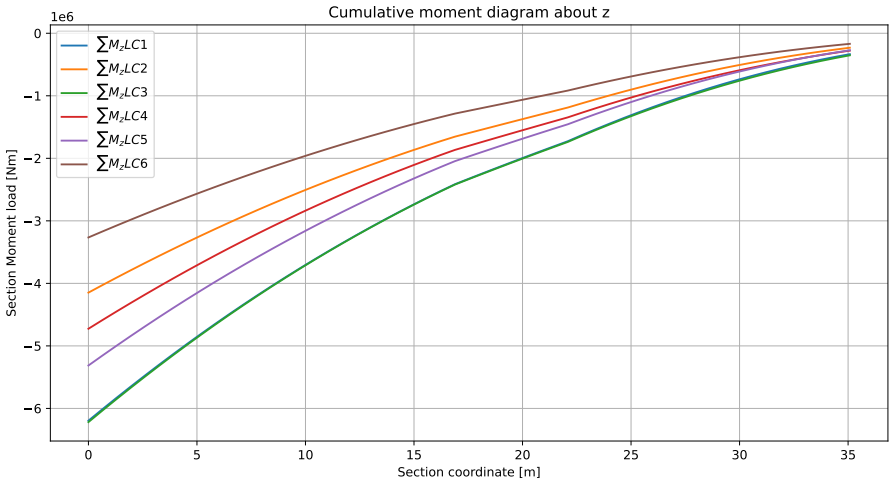

Figure D.6: Cumulative Mz for pressurised positive manoeuvring (LC01-LC06).

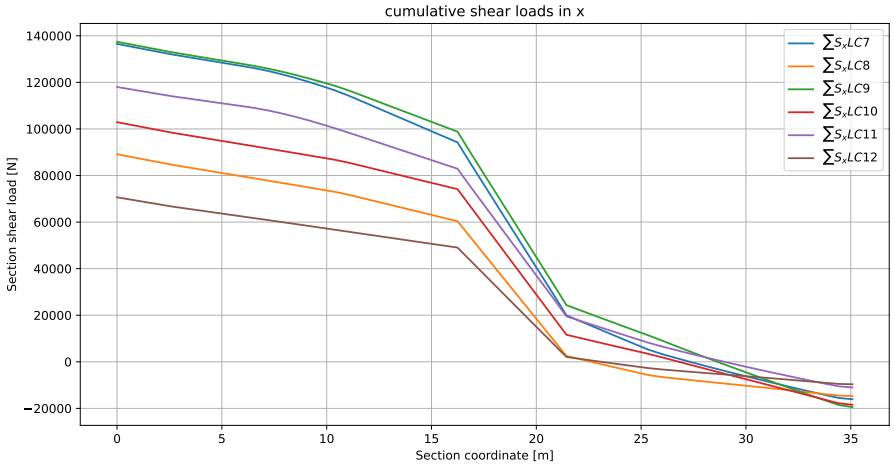

Figure D.7: Cumulative Sx for unpressurised positive manoeuvring (LC07-LC12).

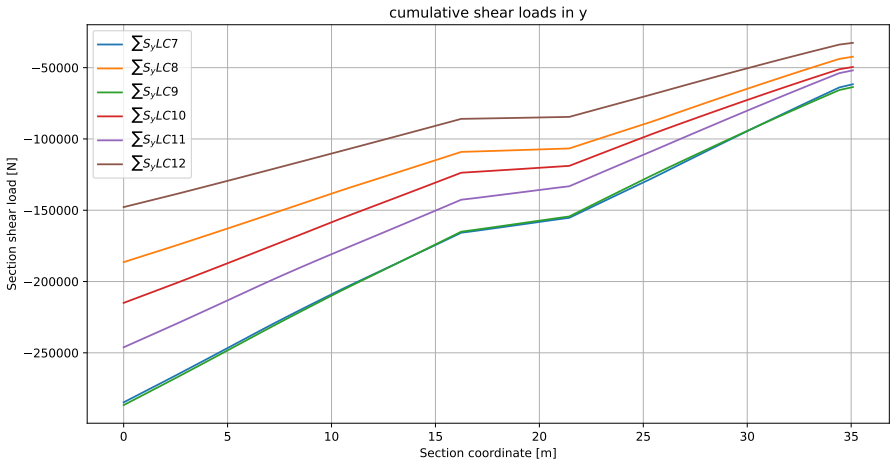

Figure D.8: Cumulative Sy for unpressurised positive manoeuvring (LC07-LC12).

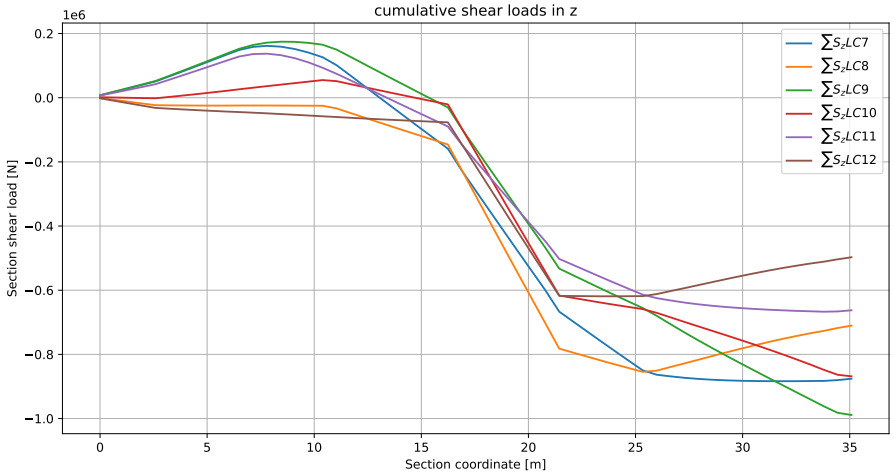

Figure D.9: Cumulative Sz for unpressurised positive manoeuvring (LC07-LC12).

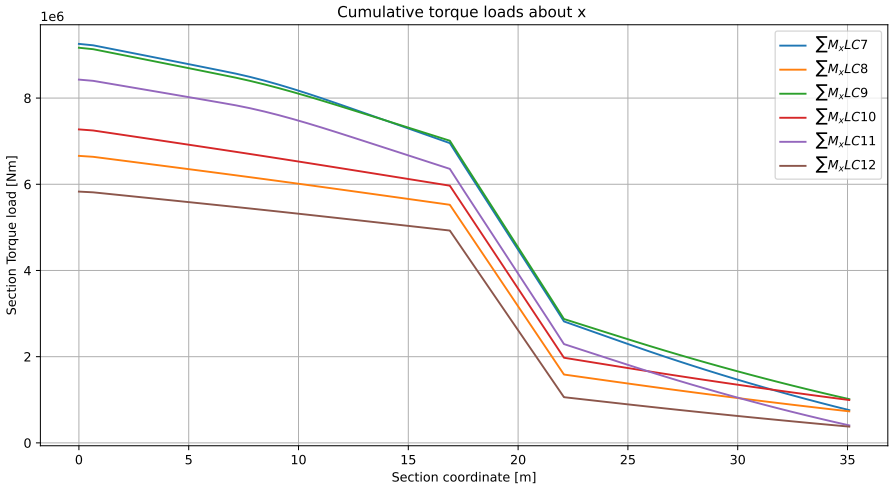

Figure D.10: Cumulative Mx for unpressurised positive manoeuvring (LC07-LC12).

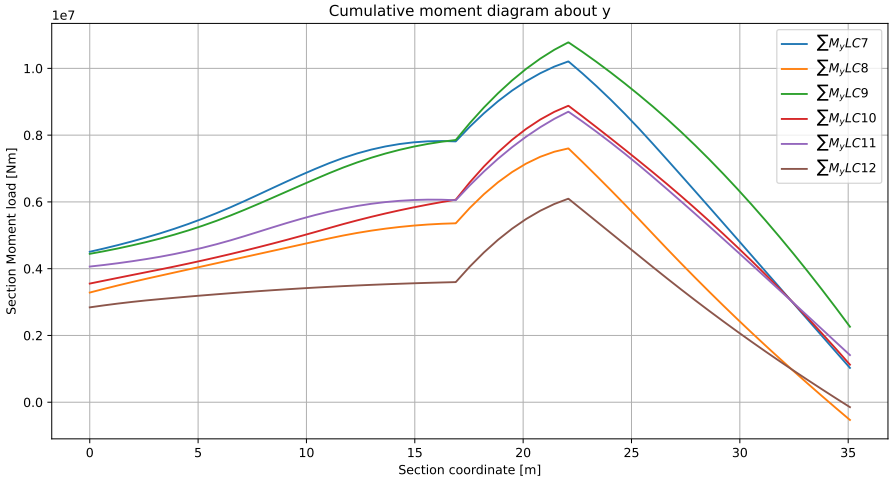

Figure D.11: Cumulative My for unpressurised positive manoeuvring (LC07-LC12).

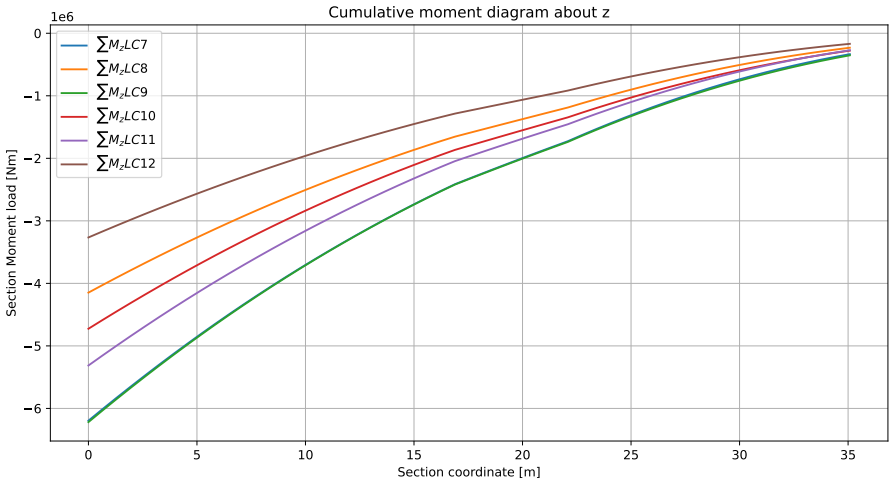

Figure D.12: Cumulative Mz for unpressurised positive manoeuvring (LC07-LC12).

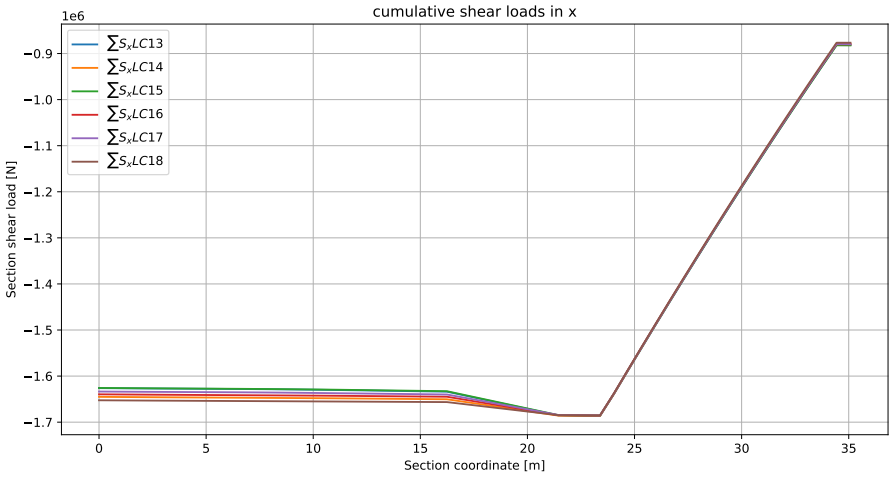

Figure D.13: Cumulative Sx for pressurised negative manoeuvring (LC12-LC18).

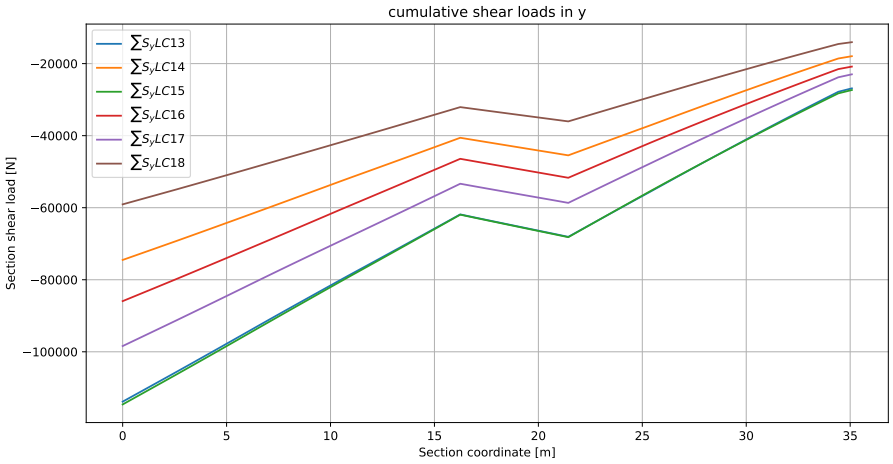

Figure D.14: Cumulative Sy for pressurised negative manoeuvring (LC12-LC18).

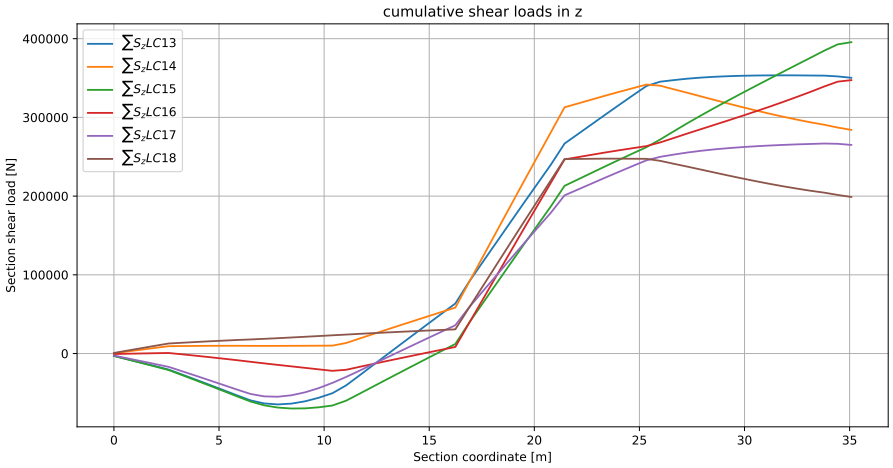

Figure D.15: Cumulative Sz for pressurised negative manoeuvring (LC12-LC18).

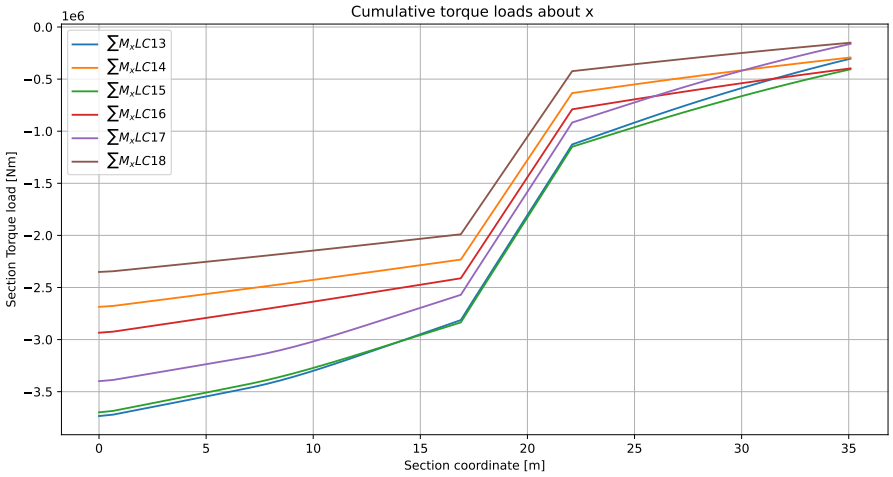

Figure D.16: Cumulative Mx for pressurised negative manoeuvring (LC12-LC18).

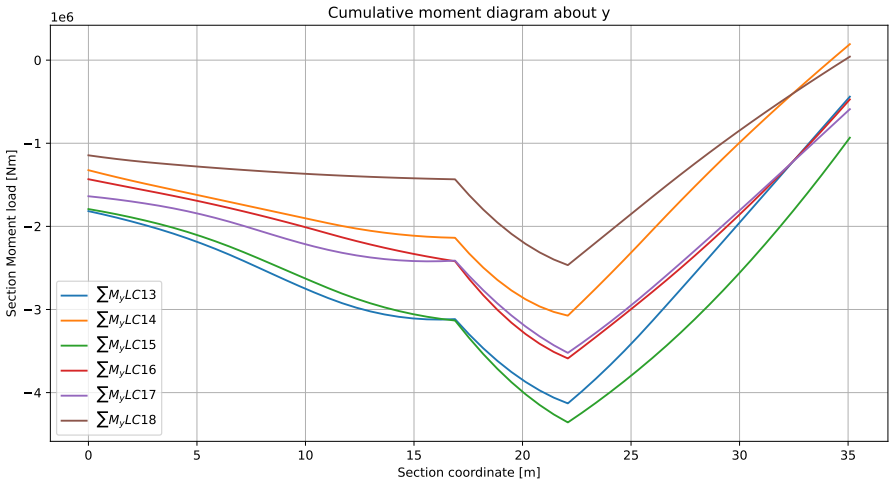

Figure D.17: Cumulative My for pressurised negative manoeuvring (LC12-LC18).

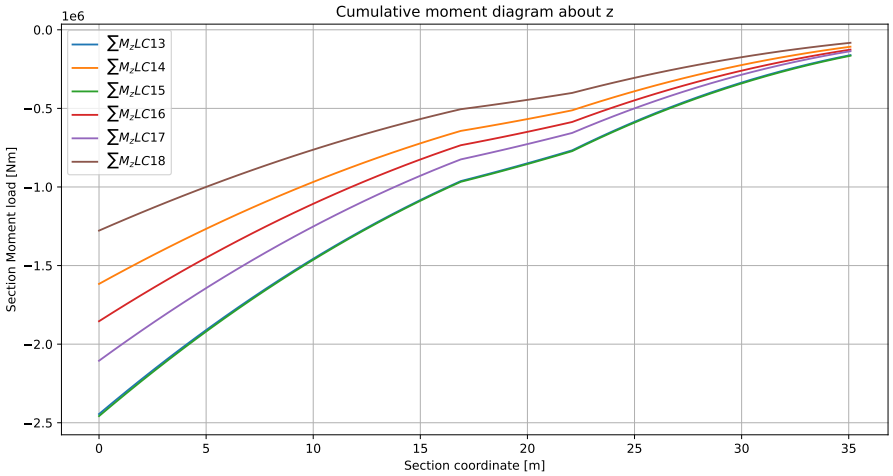

Figure D.18: Cumulative Mz for unpressurised negative manoeuvring (LC12-LC18).

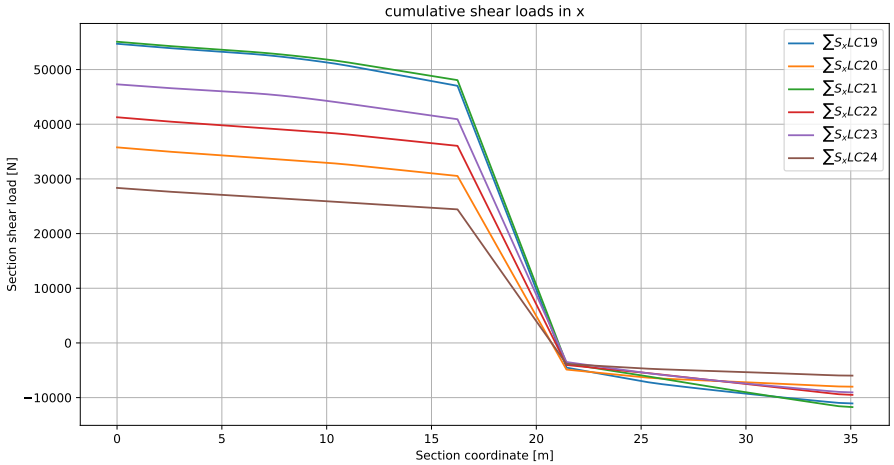

Figure D.19: Cumulative Sx for unpressurised negative manoeuvring (LC19-LC24).

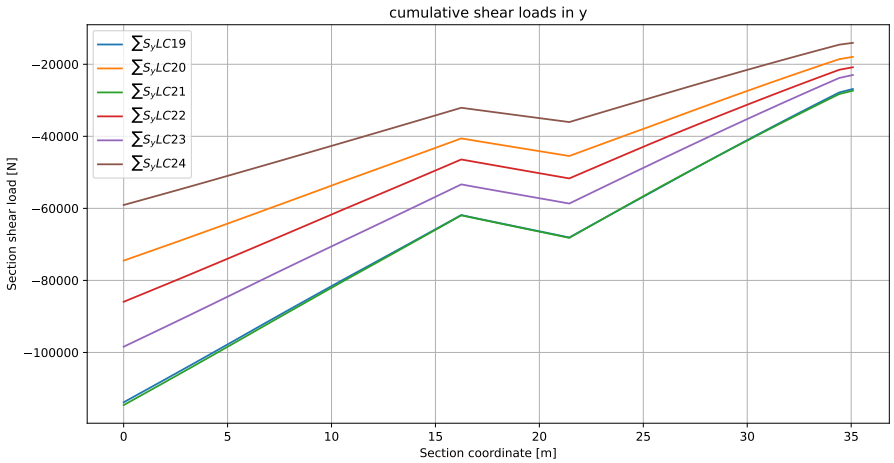

Figure D.20: Cumulative Sy for unpressurised negative manoeuvring (LC19-LC24).

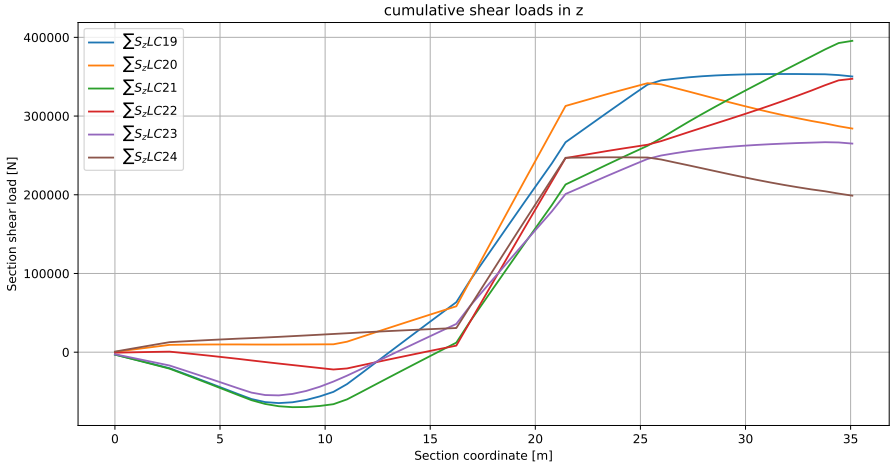

Figure D.21: Cumulative Sz for unpressurised negative manoeuvring (LC19-LC24).

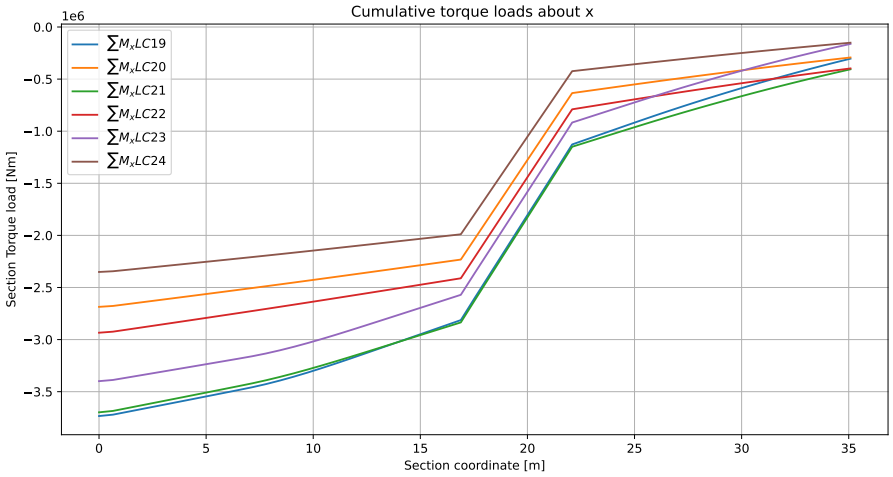

Figure D.22: Cumulative Mx for unpressurised negative manoeuvring (LC19-LC24).

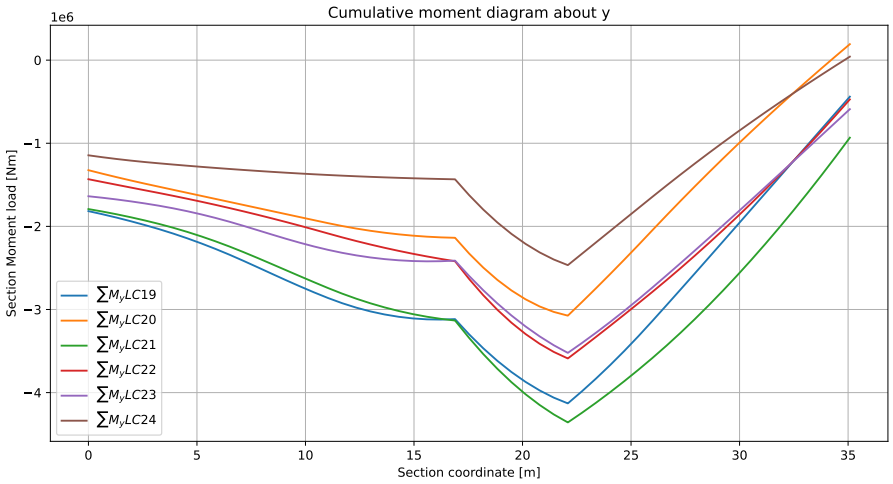

Figure D.23: Cumulative My for unpressurised negative manoeuvring (LC19-LC24).

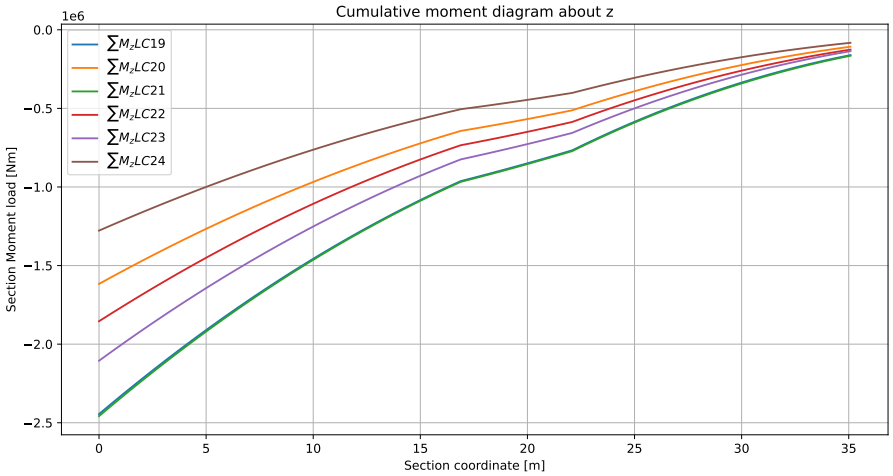

Figure D.24: Cumulative Mz for unpressurised negative manoeuvring (LC19-LC24).

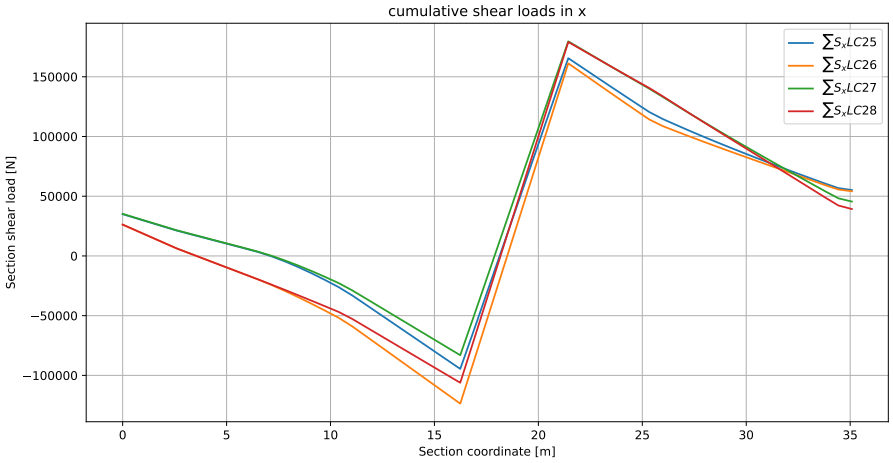

Figure D.25: Cumulative Sx for unpressurised 2-point landing g (LC25-LC28).

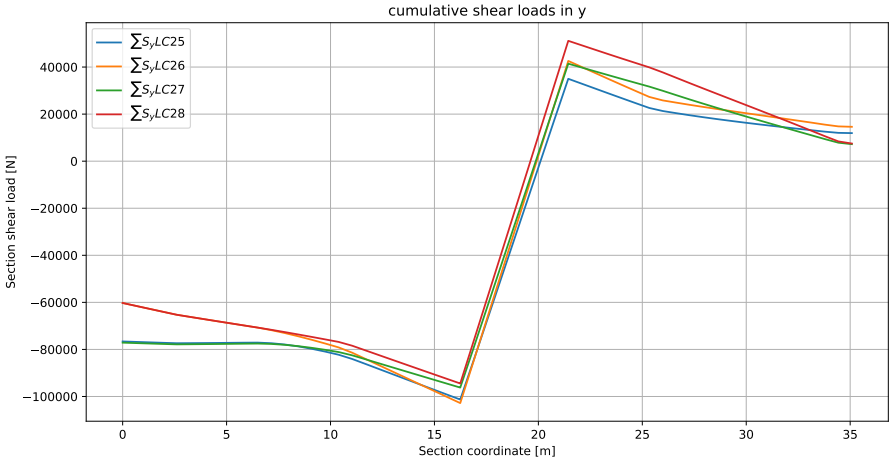

Figure D.26: Cumulative Sy for unpressurised 2-point landing (LC25-LC28).

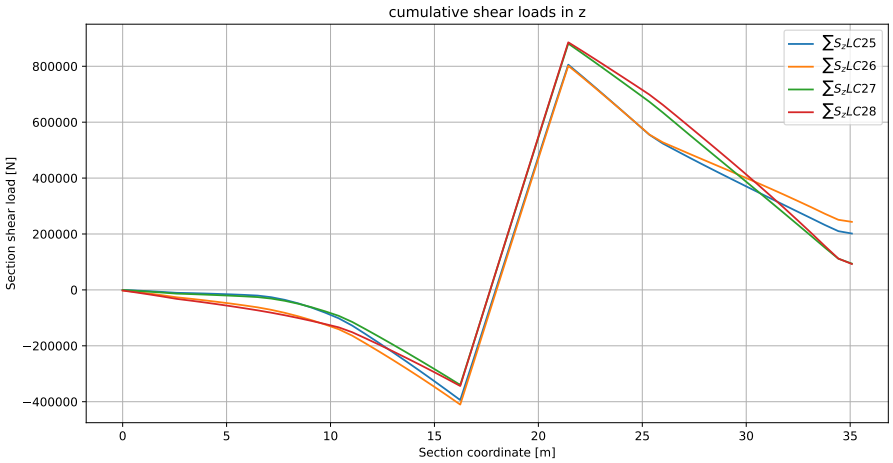

Figure D.27: Cumulative Sz for unpressurised 2-point landing (LC25-LC28).

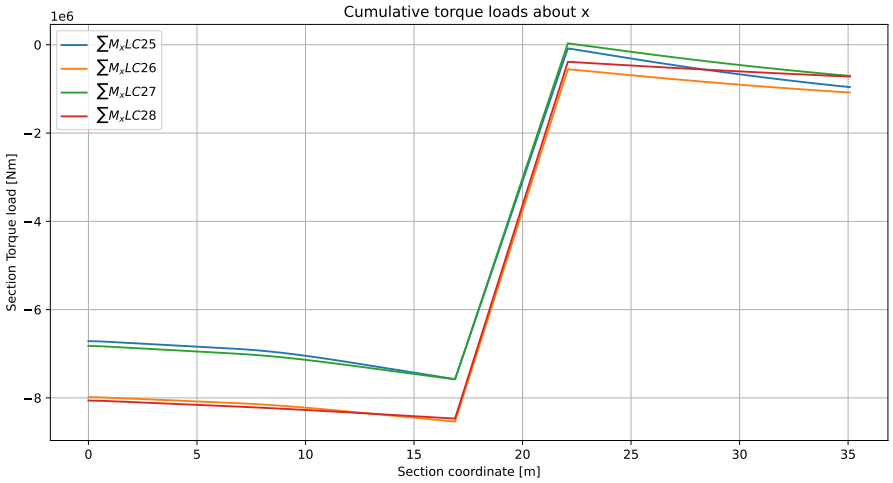

Figure D.28: Cumulative Mx for unpressurised 2-point landing (LC25-LC28).

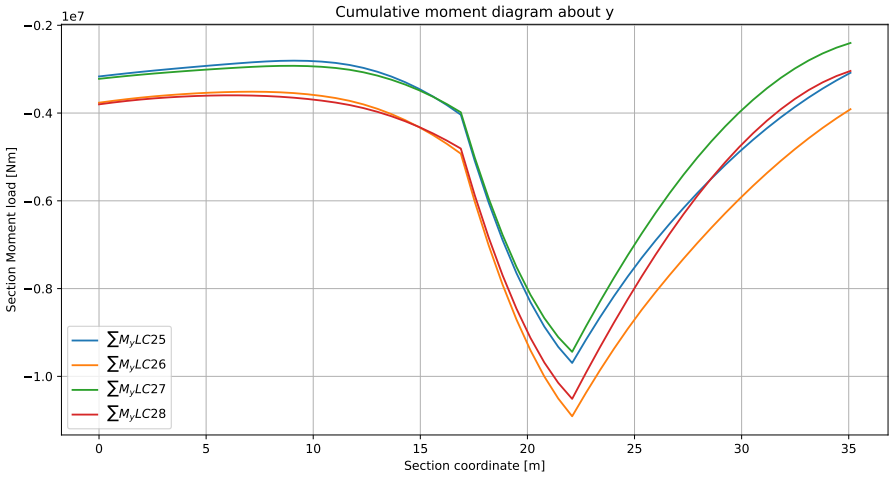

Figure D.29: Cumulative My for unpressurised 2-point landing (LC25-LC28).

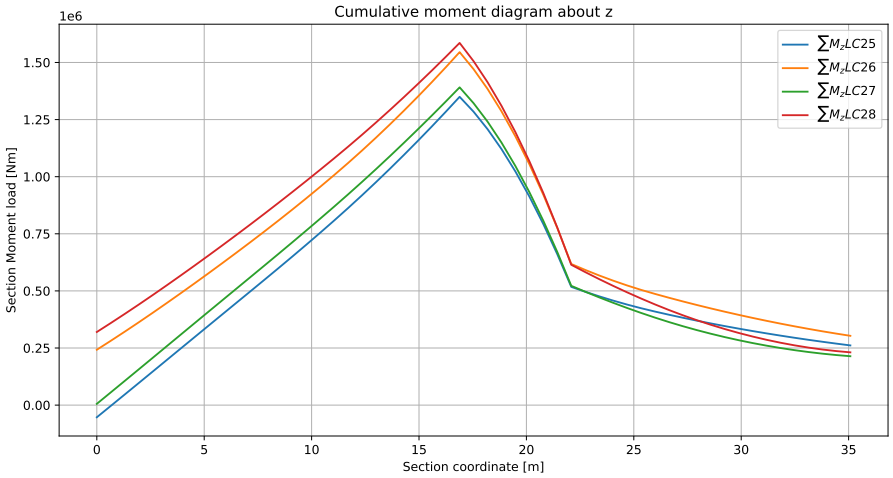

Figure D.30: Cumulative Mz for unpressurised 2-point landing (LC25-LC28).

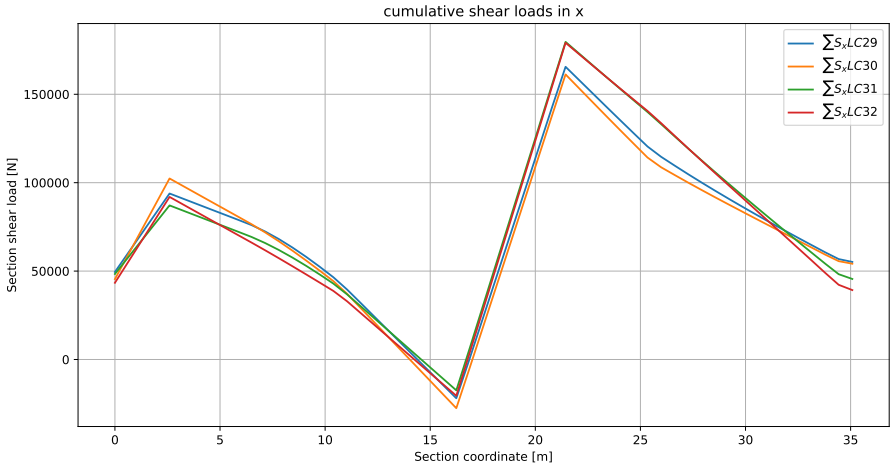

Figure D.31: Cumulative Sx for unpressurised 3-point landing (LC29-LC32).

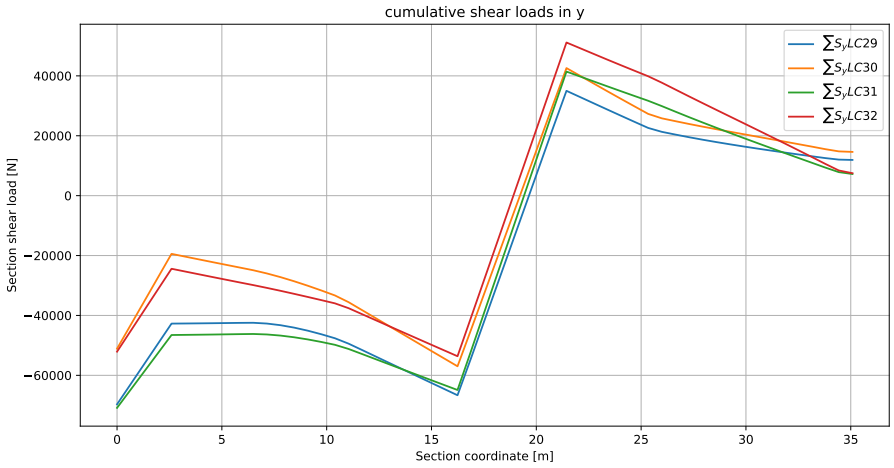

Figure D.32: Cumulative Sy for unpressurised 3-point landing (LC29-LC32).

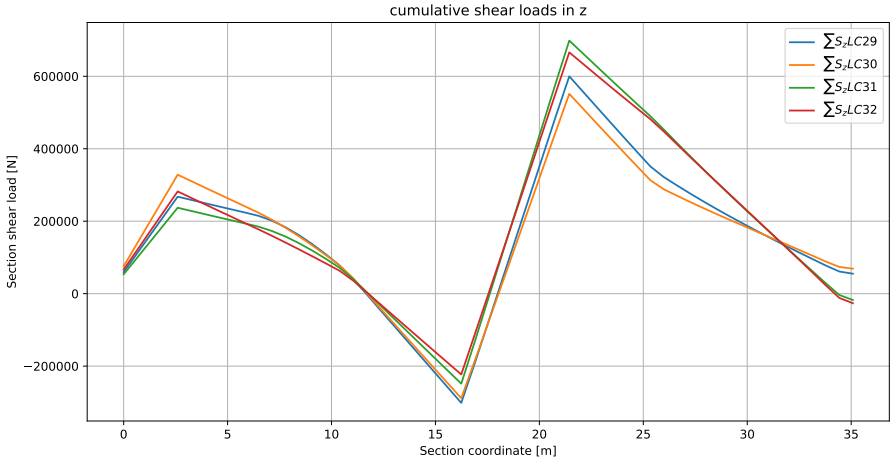

Figure D.33: Cumulative Sz for unpressurised 3-point landing (LC29-LC32).

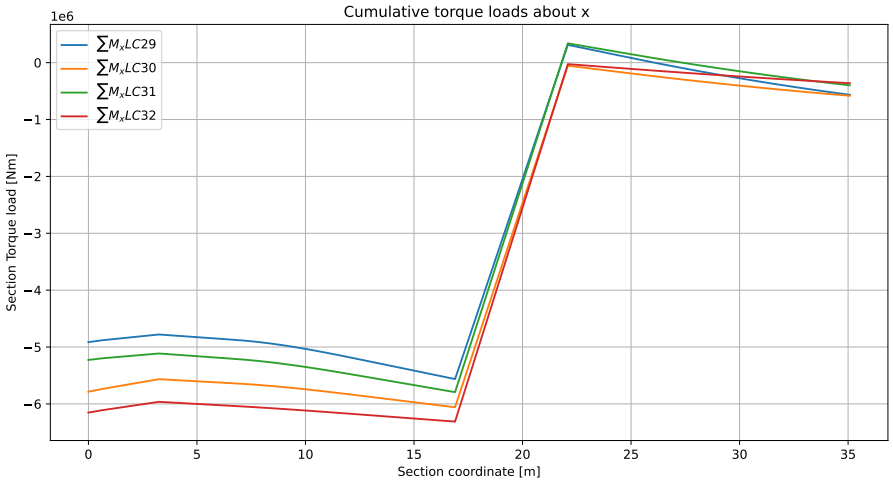

Figure D.34: Cumulative Mx for unpressurised 3-point landing (LC29-LC32).

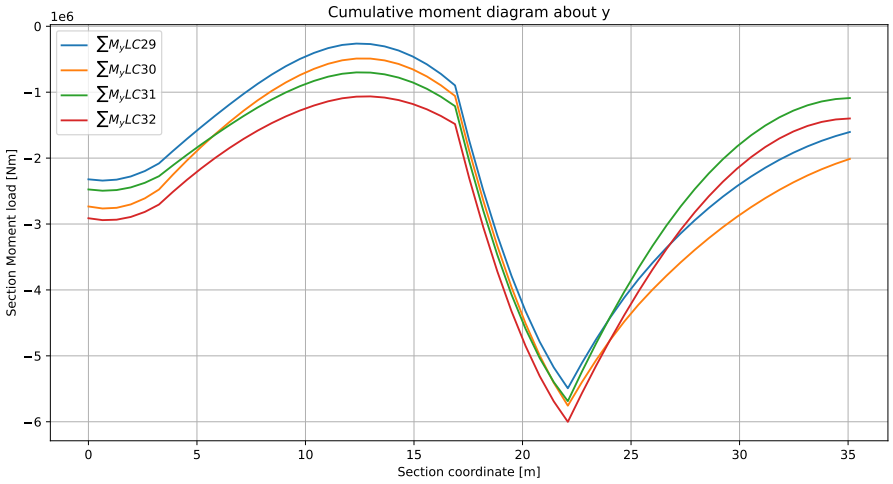

Figure D.35: Cumulative My for unpressurised 3-point landing (LC29-LC32).

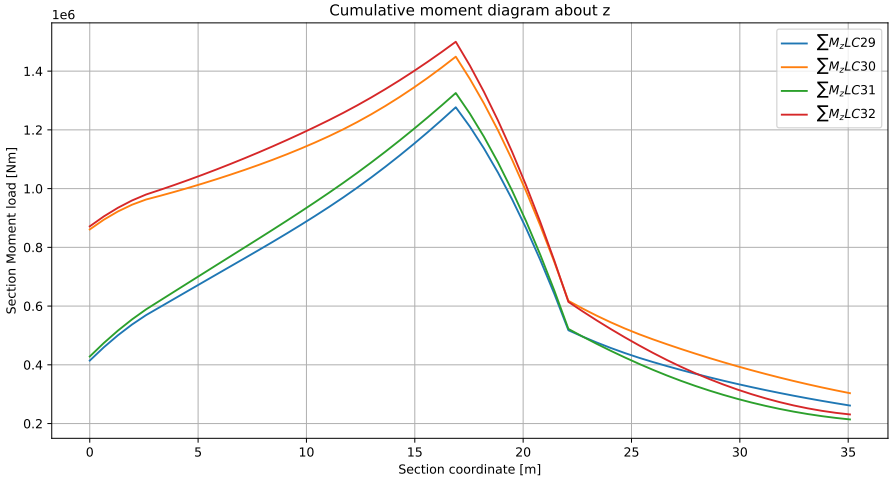

Figure D.36: Cumulative Mz for unpressurised 3-point landing (LC29-LC32).

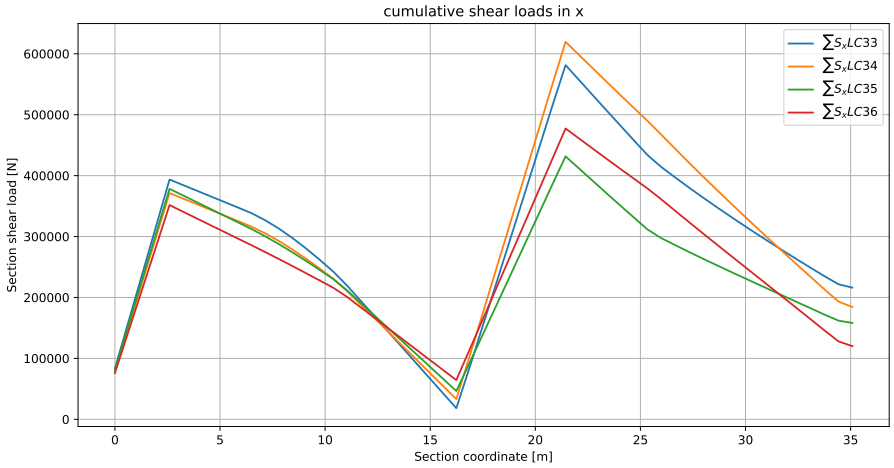

Figure D.37: Cumulative Sx for unpressurised maximum braking (LC33-LC36).

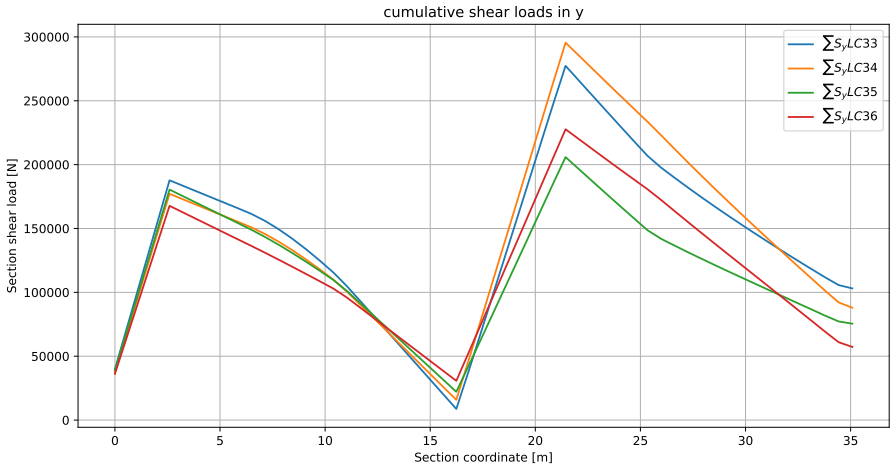

Figure D.38: Cumulative Sy for unpressurised maximum braking (LC33-LC36).

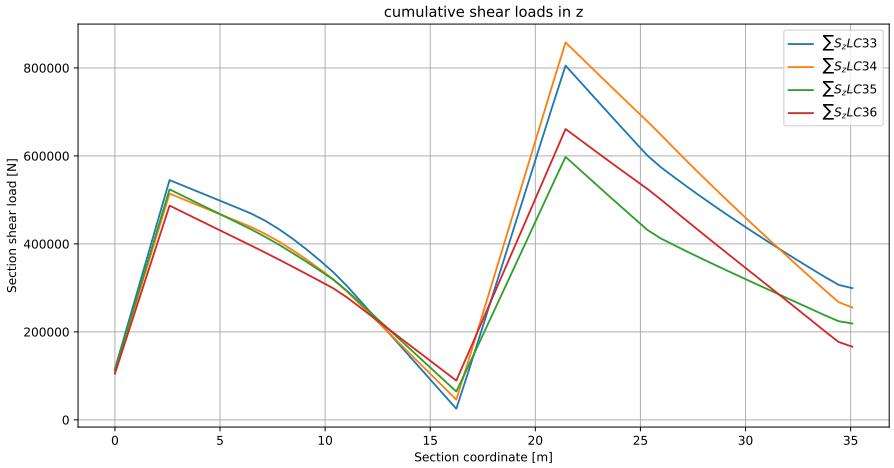

Figure D.39: Cumulative Sz for unpressurised maximum braking (LC33-LC36).

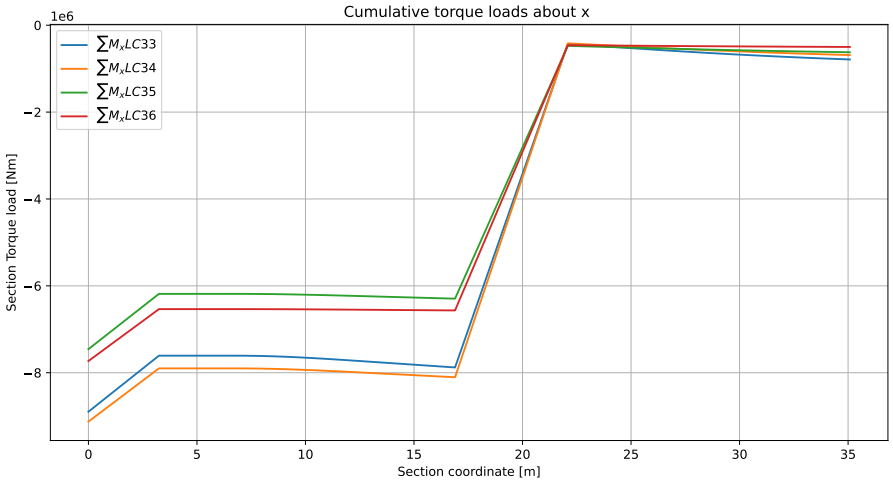

Figure D.40: Cumulative Mx for unpressurised maximum braking (LC33-LC36).

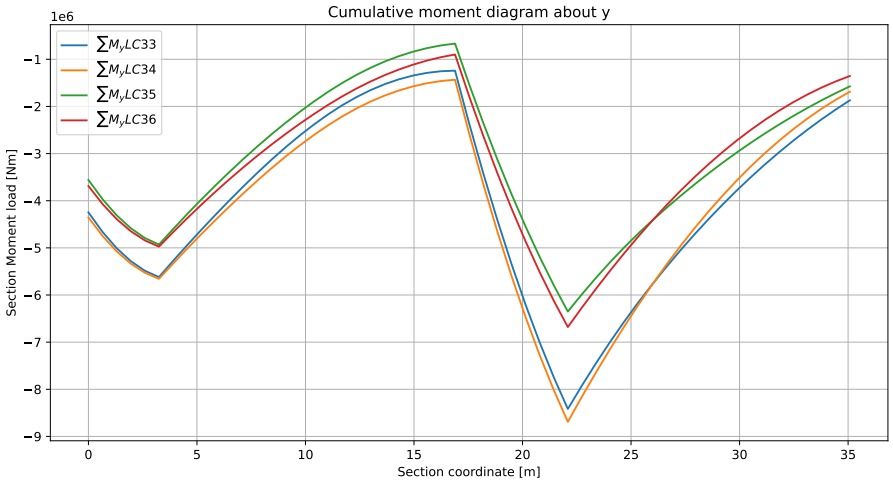

Figure D.41: Cumulative My for unpressurised maximum braking (LC33-LC36).

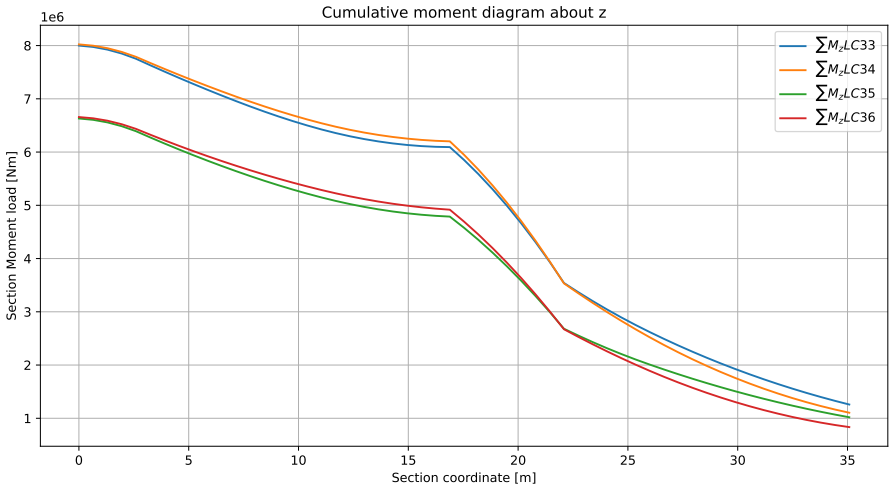

Figure D.42: Cumulative Mz for unpressurised maximum braking (LC33-LC36).

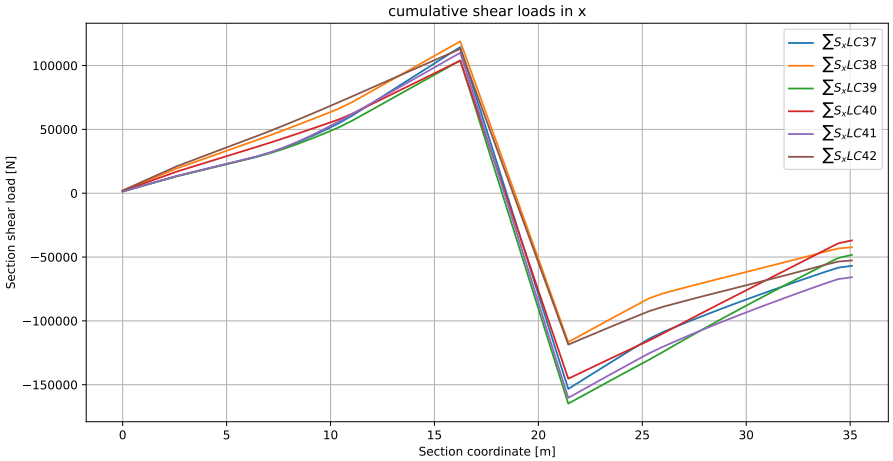

Figure D.43: Cumulative Sx for unpressurised take-off (LC37-LC42).

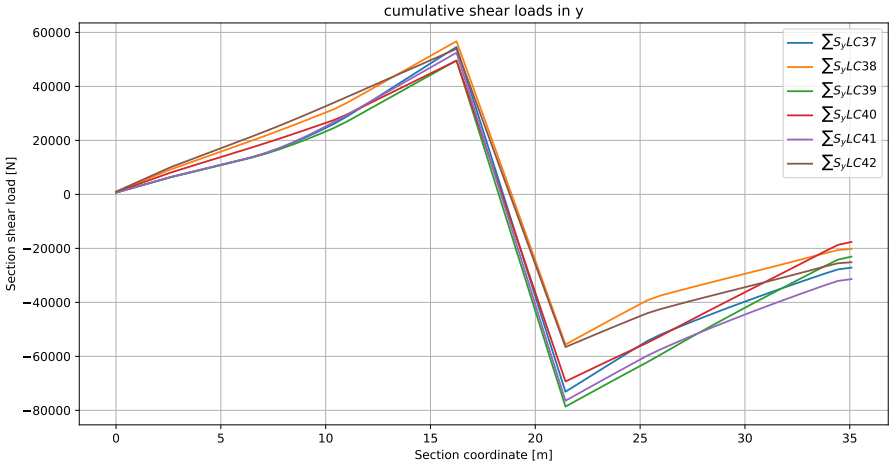

Figure D.44: Cumulative Sy for unpressurised take-off (LC37-LC42).

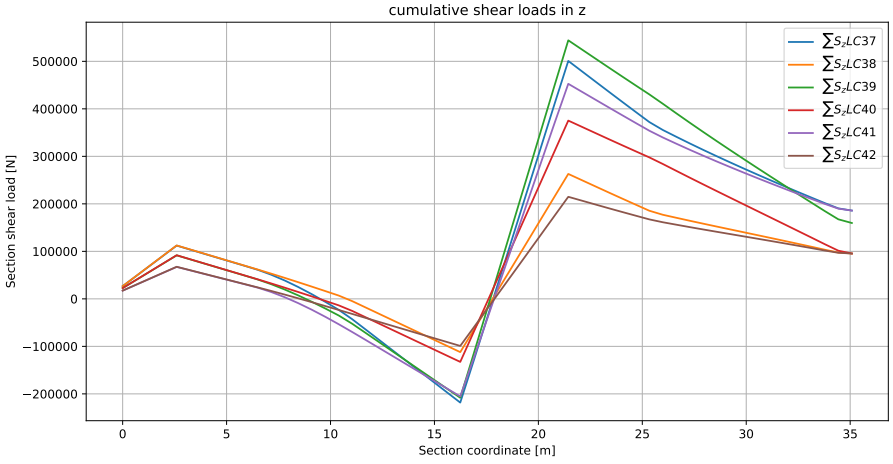

Figure D.45: Cumulative Sz for unpressurised take-off (LC37-LC42).

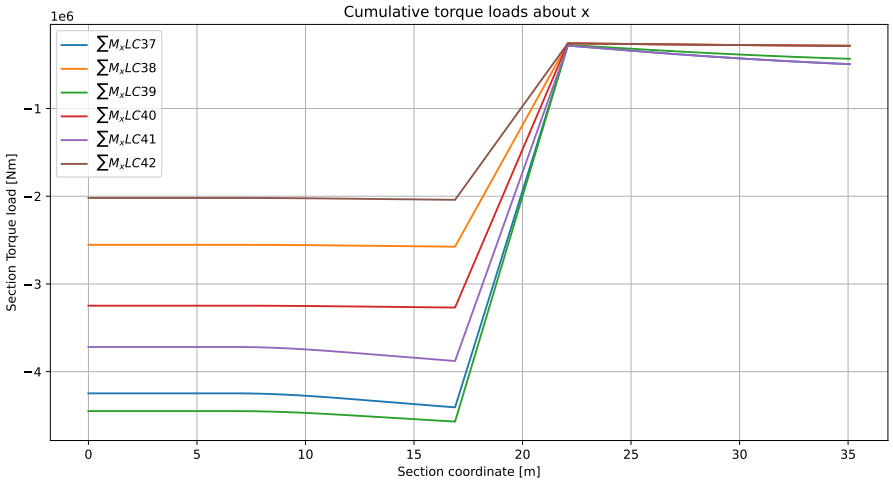

Figure D.46: Cumulative Mx for unpressurised take-off (LC37-LC42).

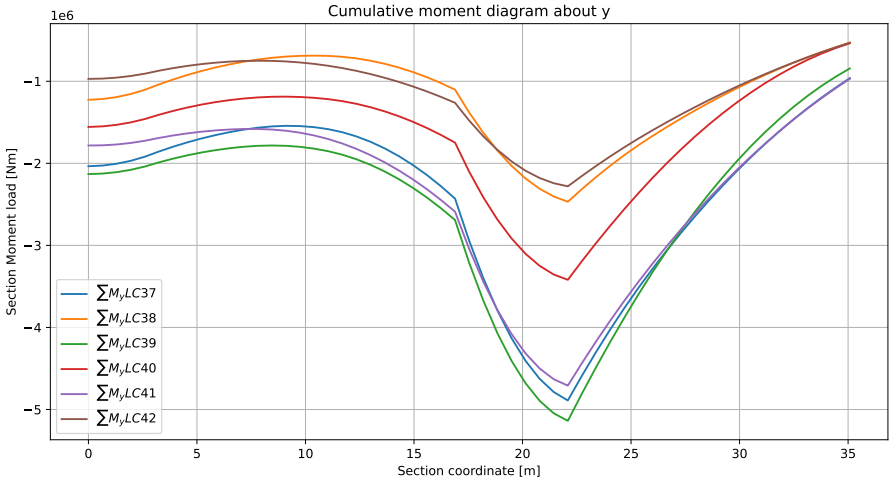

Figure D.47: Cumulative My for unpressurised take-off (LC37-LC42).

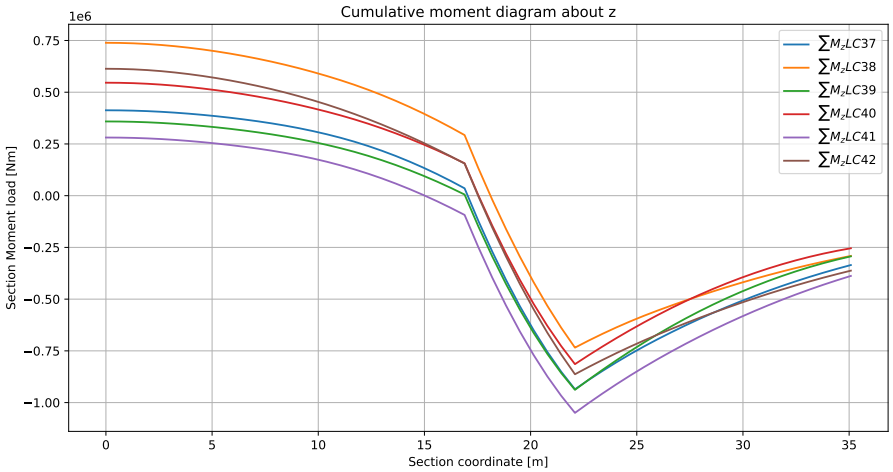

Figure D.48: Cumulative Mz for unpressurised take-off (LC37-LC42).

D.2. Local resultant shear loads

The local resultant shear loads are shown below, for the ultimate load cases. These resultant shear loads were used to identify the most severe load cases for the cross-section loads.

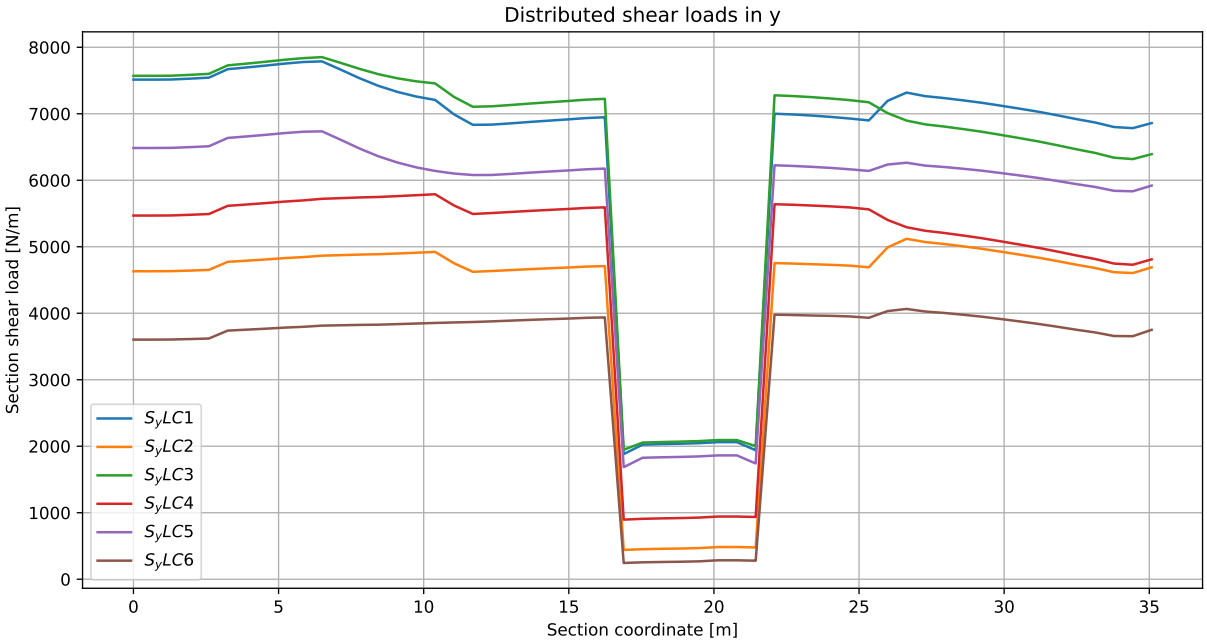

Figure D.49: Resultant Sy distribution for pressurised positive manoeuvring (LC01-LC06).

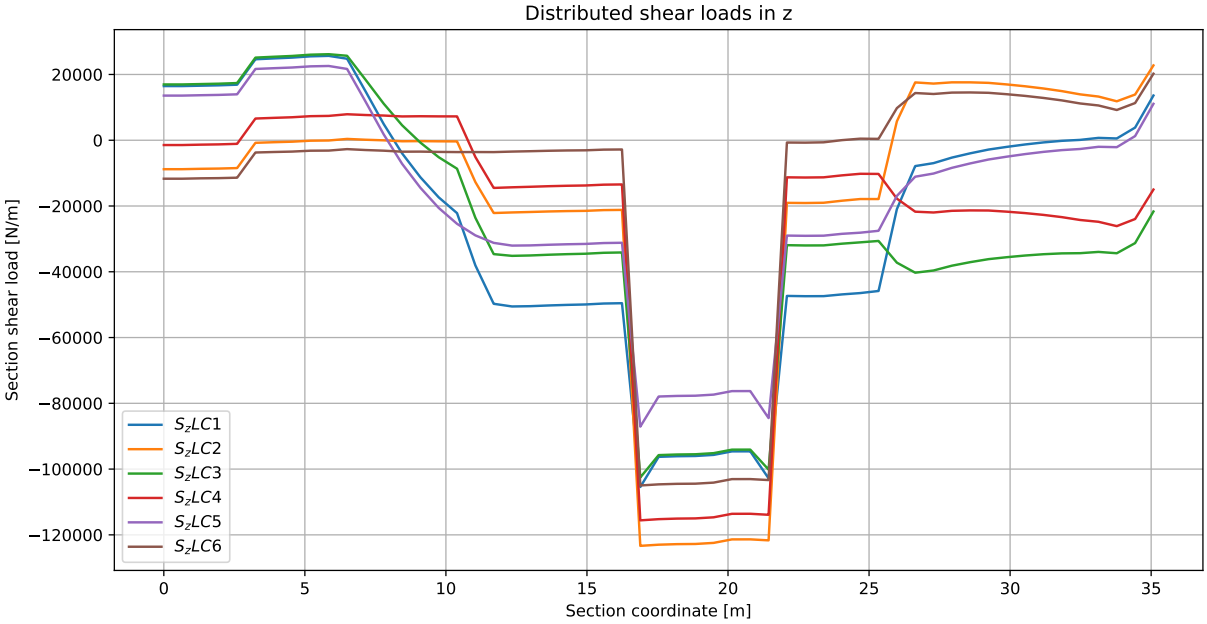

Figure D.50: Resultant Sz distribution for pressurised positive manoeuvring (LC01-LC06).

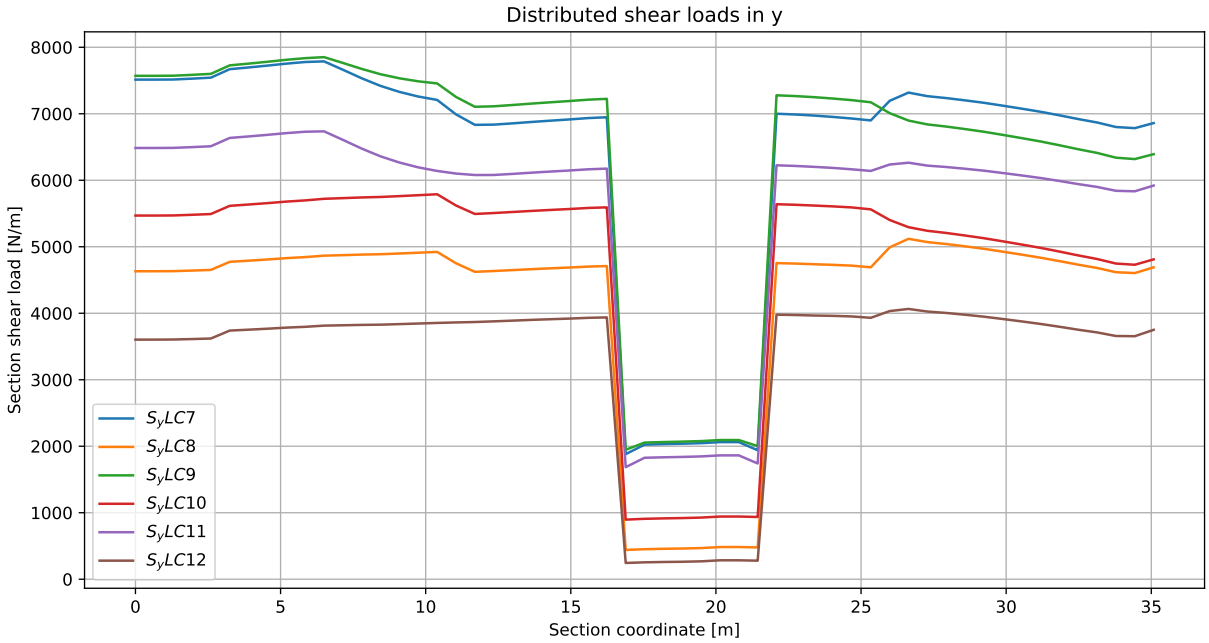

Figure D.51: Resultant Sy distribution for unpressurised positive manoeuvring (LC07-LC12).

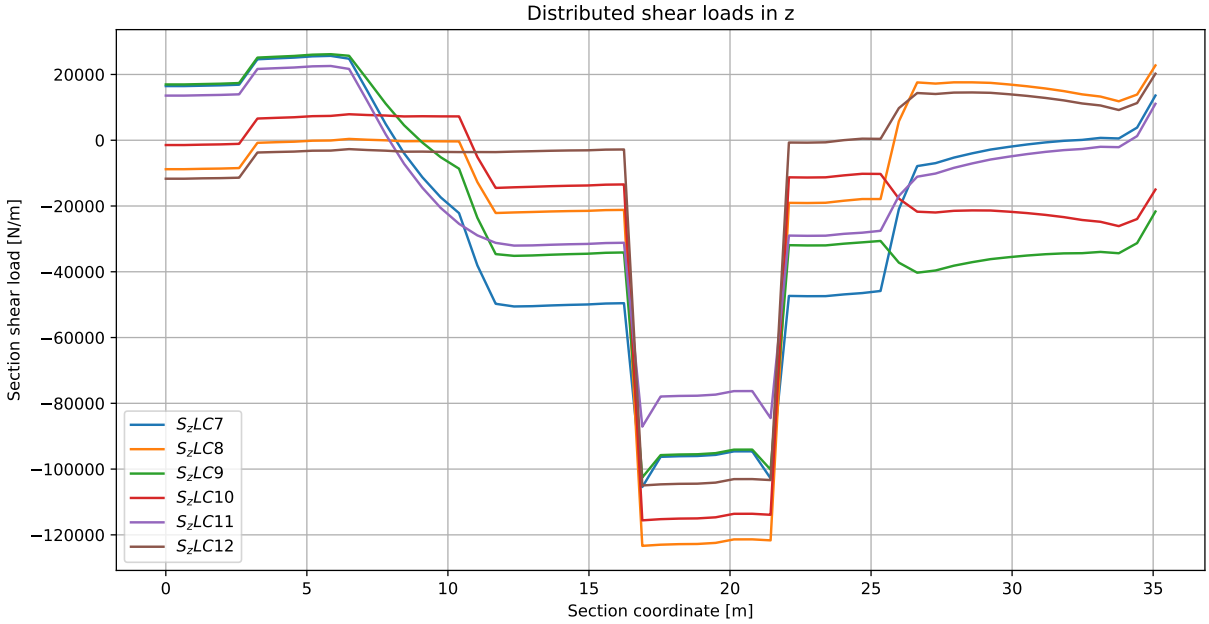

Figure D.52: Resultant Sz distribution for unpressurised positive manoeuvring (LC07-LC12).

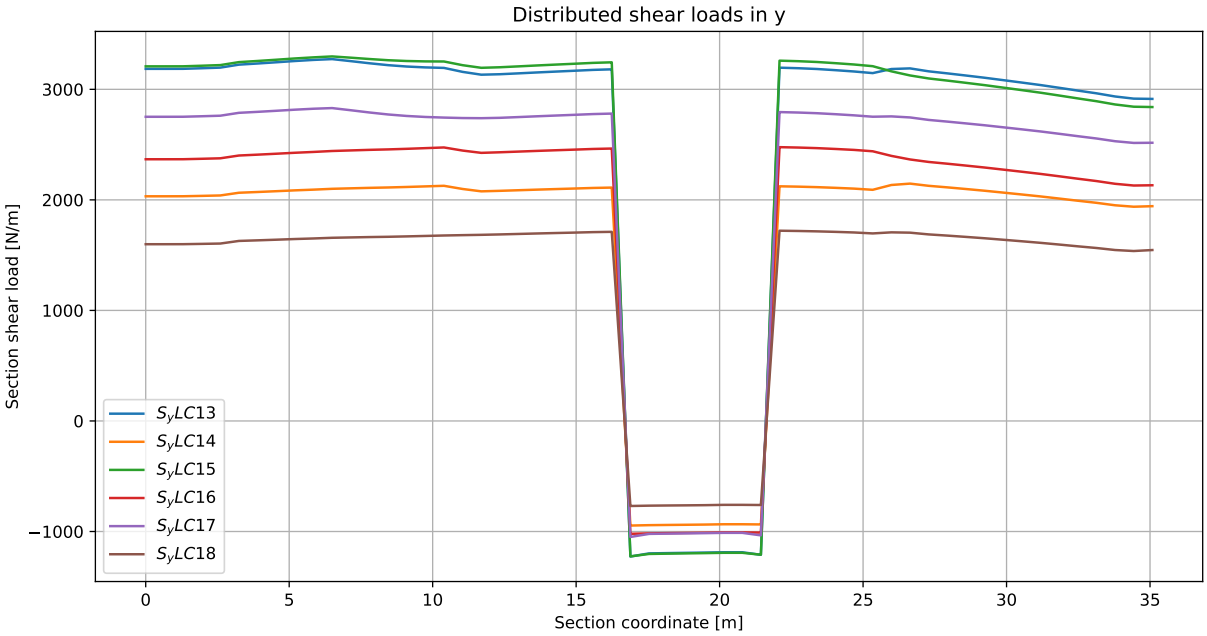

Figure D.53: Resultant Sy distribution for pressurised negative manoeuvring (LC12-LC18).

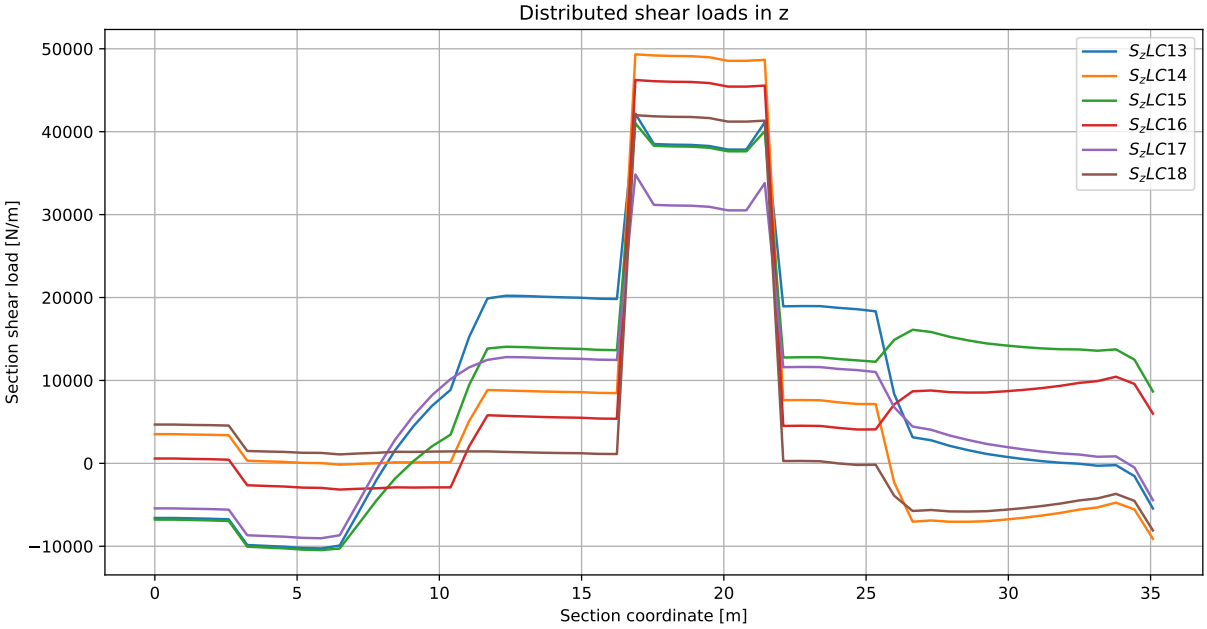

Figure D.54: Resultant Sz distribution for pressurised negative manoeuvring (LC12-LC18).

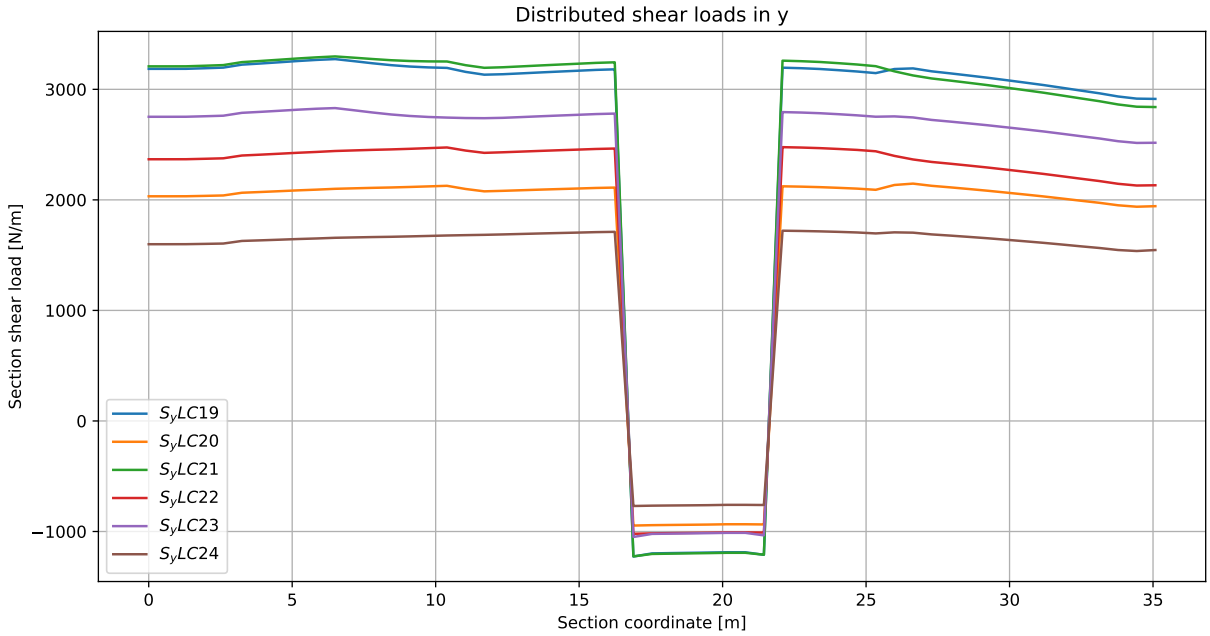

Figure D.55: Resultant Sy distribution for unpressurised negative manoeuvring (LC19-LC24).

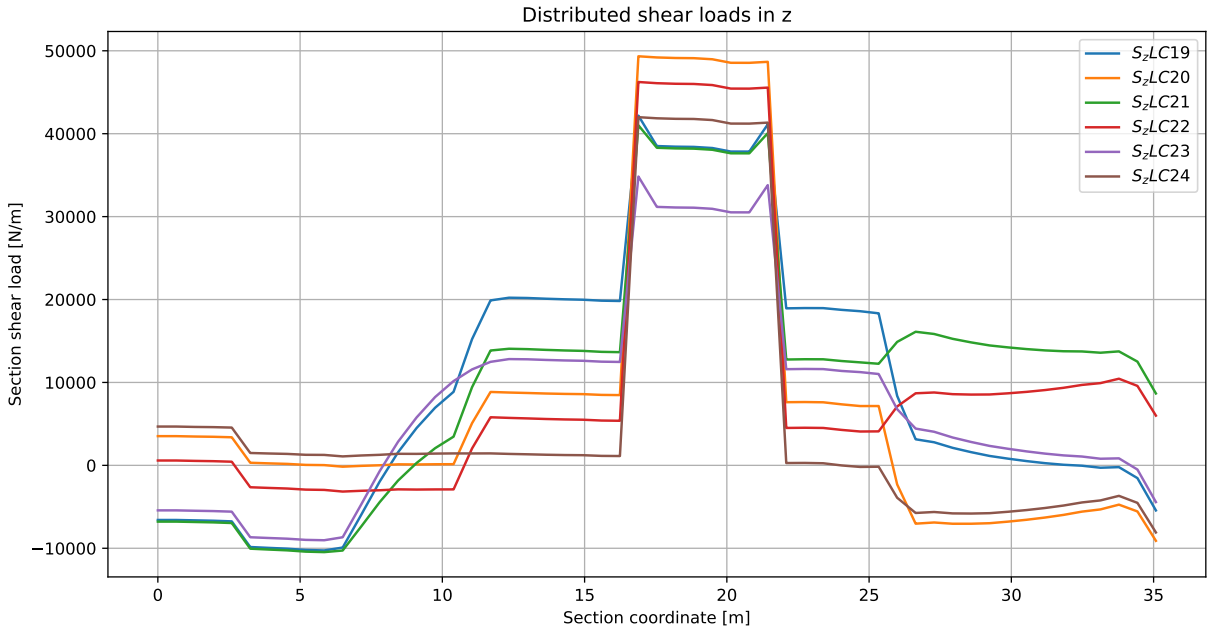

Figure D.56: Resultant Sz distribution for unpressurised negative manoeuvring (LC19-LC24).

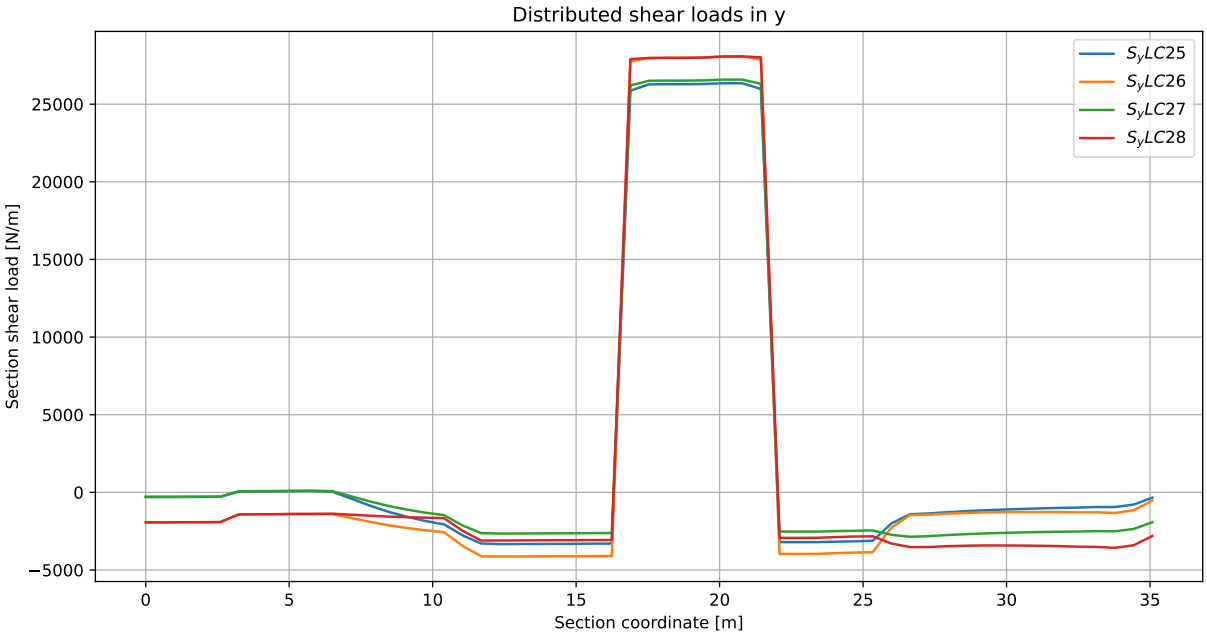

Figure D.57: Resultant Sy distribution for unpressurised 2-point landing (LC25-LC28).

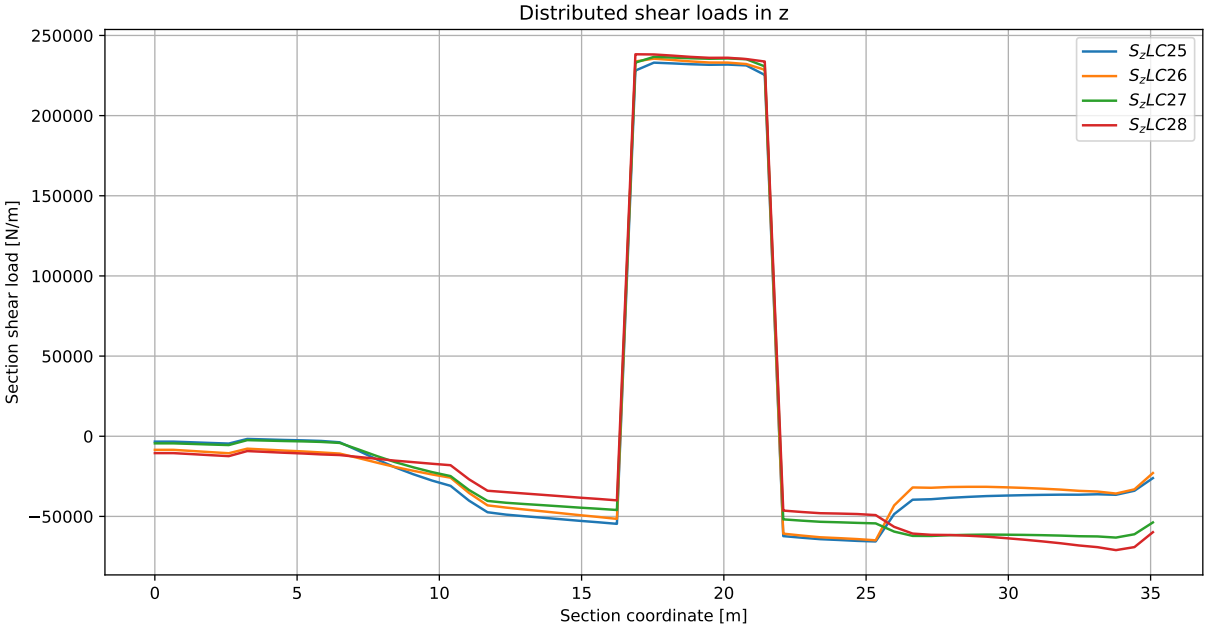

Figure D.58: Resultant Sz distribution for unpressurised 2-point landing (LC25-LC28).

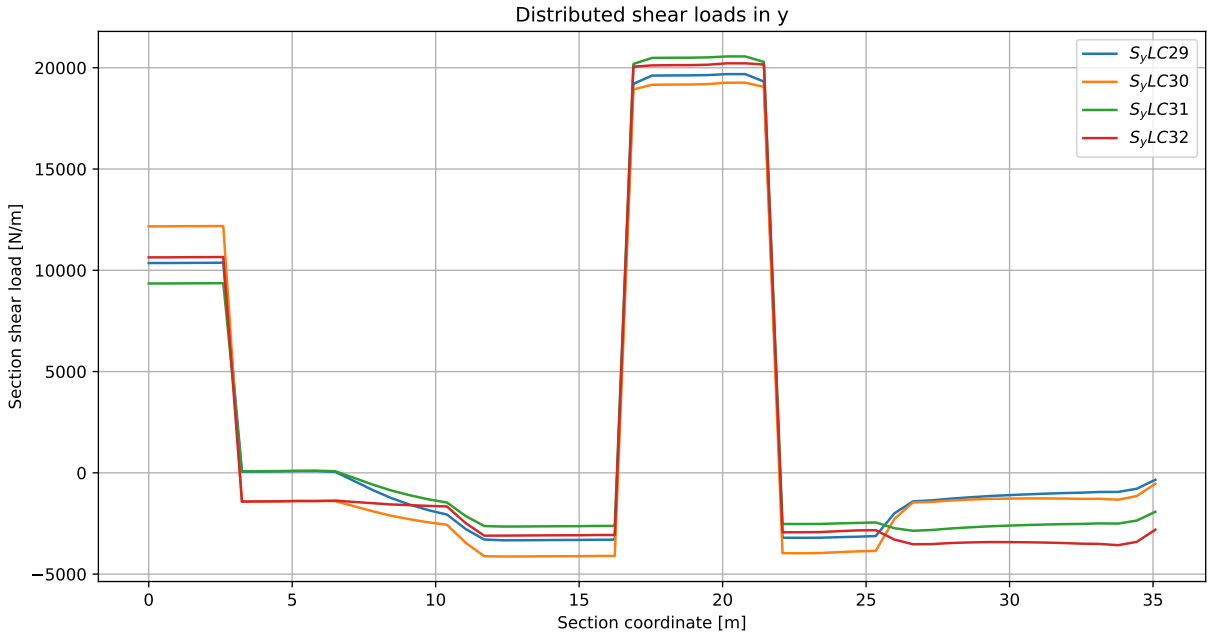

Figure D.59: Resultant Sy distribution for unpressurised 3-point landing (LC29-LC32).

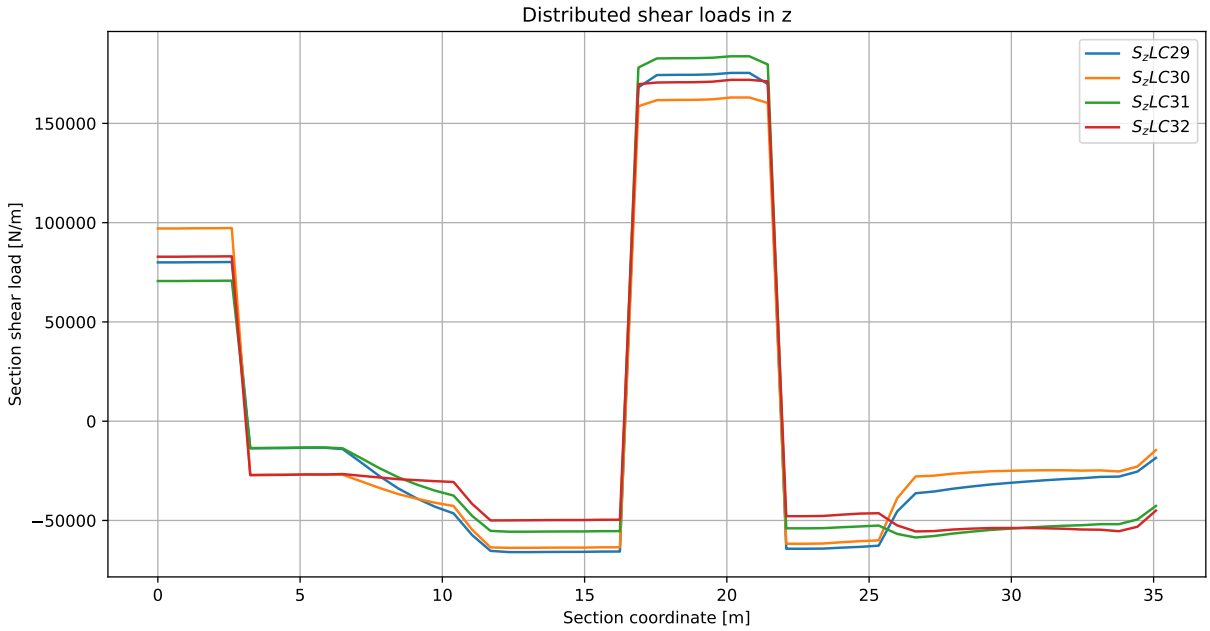

Figure D.60: Resultant Sz distribution for unpressurised 3-point landing (LC29-LC32).

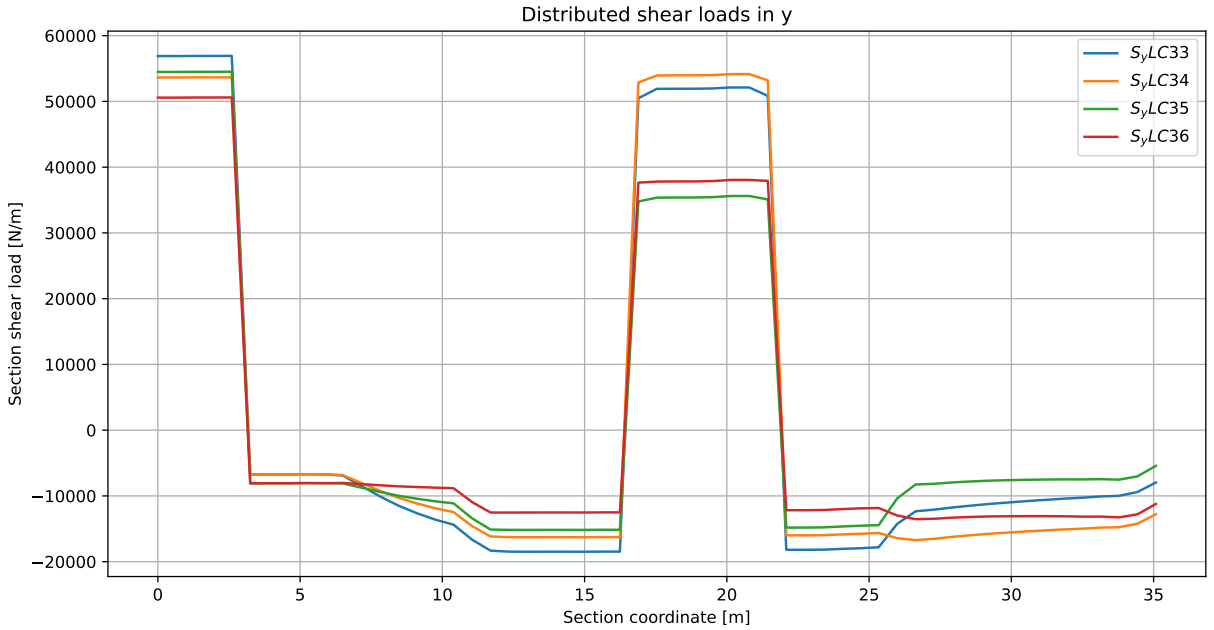

Figure D.61: Resultant Sy distribution for unpressurised maximum braking (LC33-LC36).

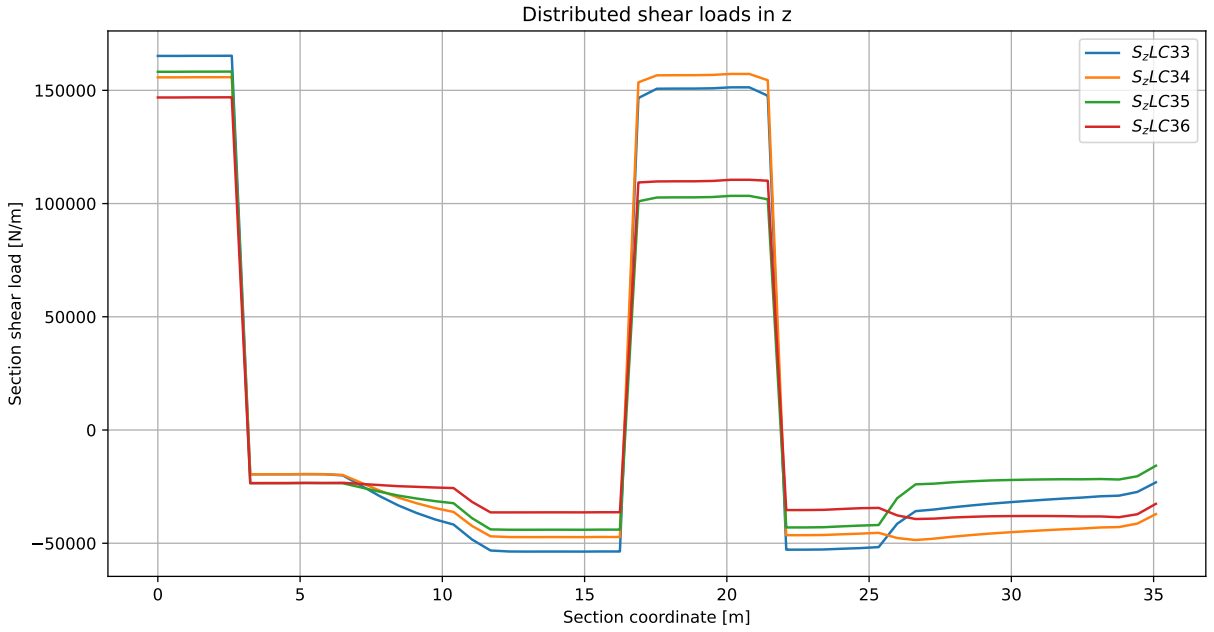

Figure D.62: Resultant Sz distribution for unpressurised maximum braking (LC33-LC36).

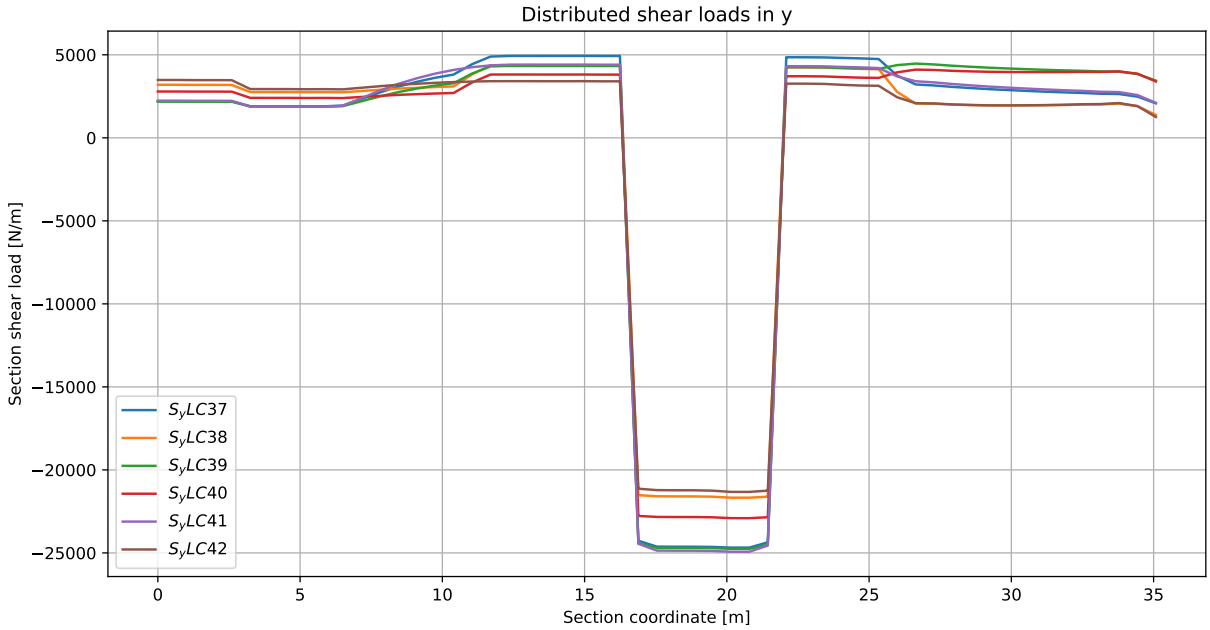

Figure D.63: Resultant Sy distribution for unpressurised take-off (LC37-LC42).

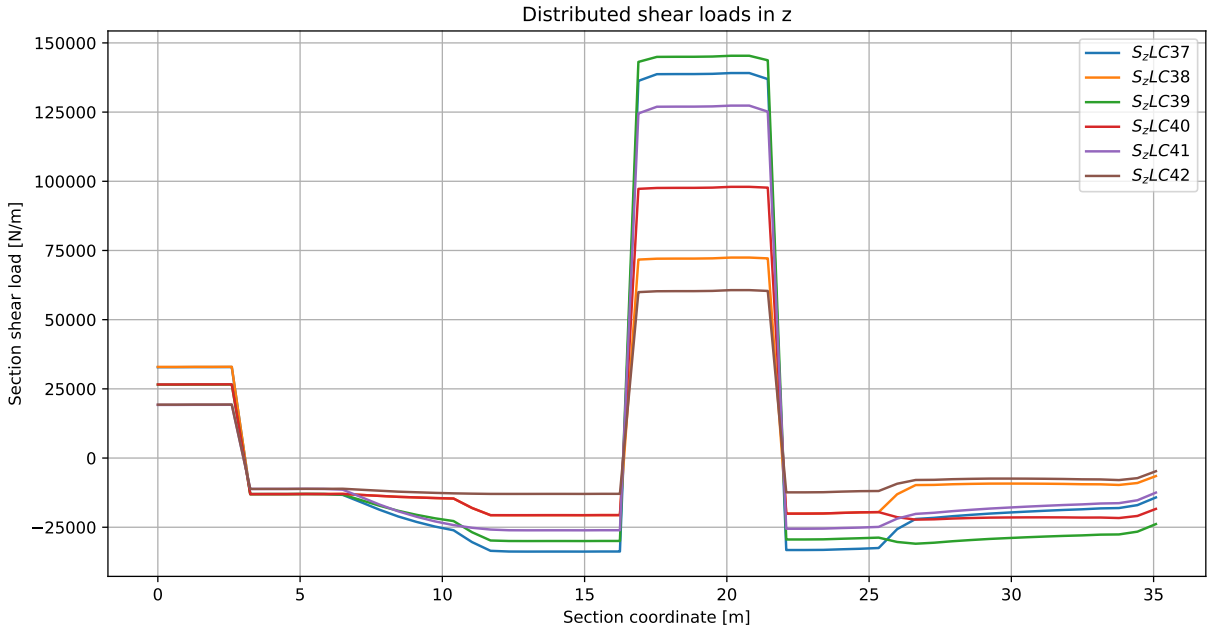

Figure D.64: Resultant Sz distribution for unpressurised take-off (LC37-LC42).

E
Additional results

E.1. Stress distribution in generic structure

As an example, the stress distributions for a number of load cases are shown in the following subsections. The generic example structure from section 5.3.3 has been used here as well, in order to determined the stress fields. Note that the structural properties are constant for every section. Therefore, these stress fields should not be interpreted to be indicative of the final stress state of a sized structure. Within this context, these plots were regarded to be useful for the next chapters.

Note that the aspect ratio is incorrect, which has been done to obtain a better overview of the stress distribution.

E.1.1. LC01

As an example, the stress distributions for the pressurised positive manoeuvring limit load (LC01) are shown below.

Longitudinal stresses longitudinal stresses for the skins and stringers for limit LC01.

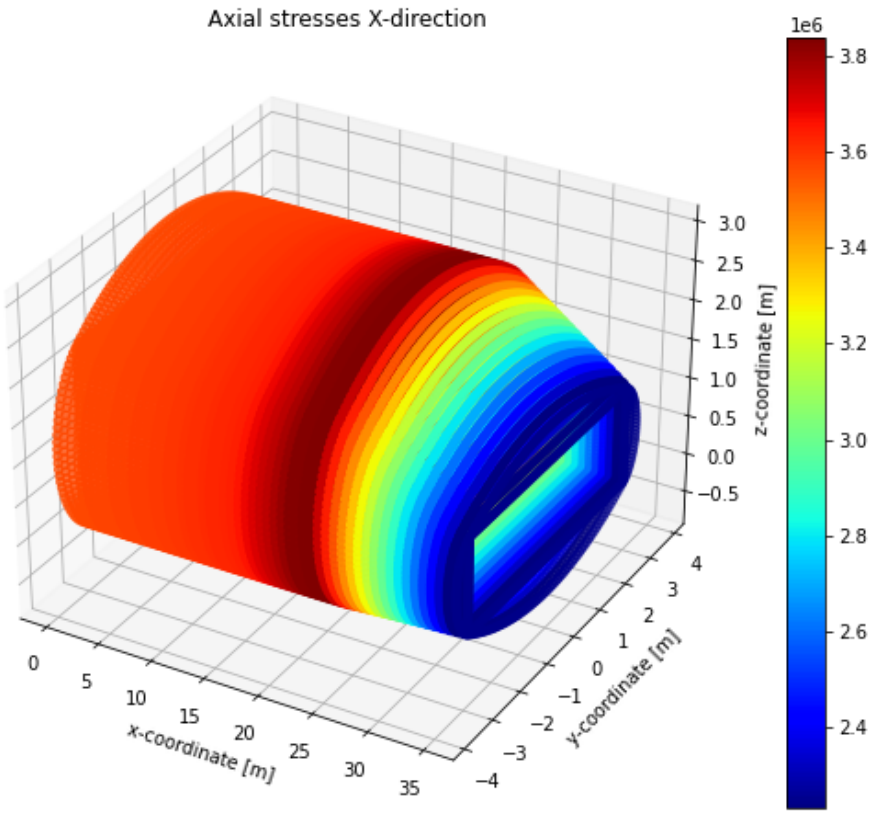

Figure E.1: Longitudinal axial stresses in skins and stringers, excludes bending. Aft top view.

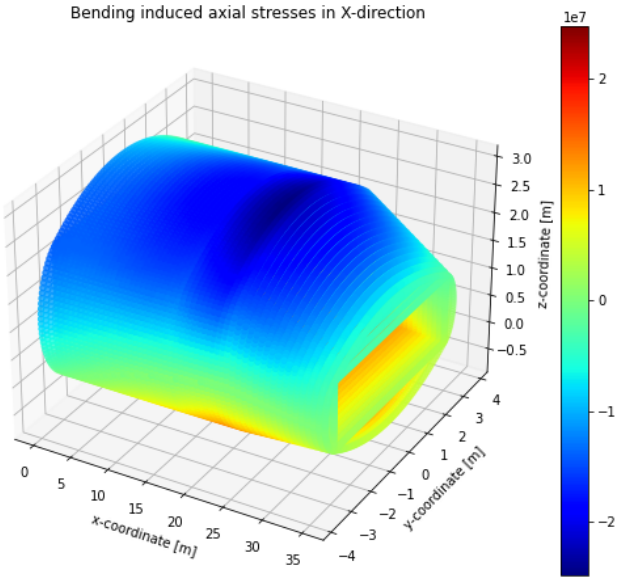

Figure E.2: Longitudinal bending stresses in skins and stringers. Aft top view.

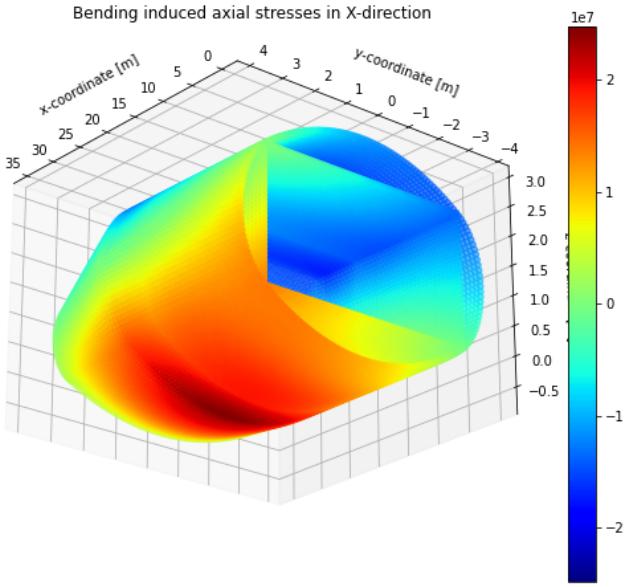

Figure E.3: Longitudinal bending stresses in skins and stringers. Front bottom view.

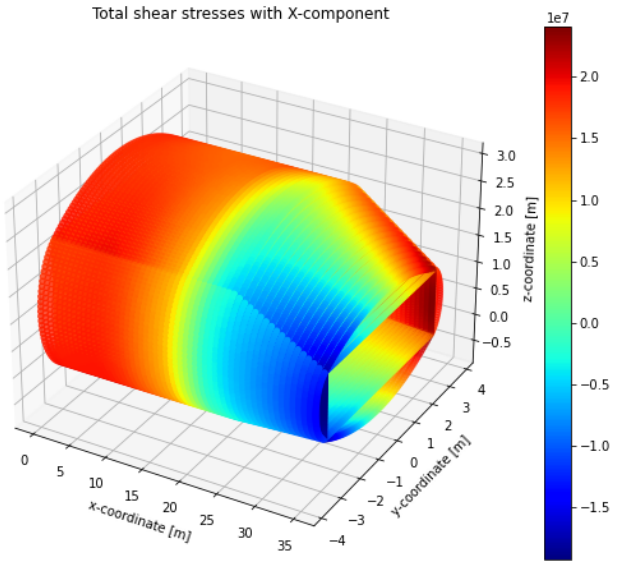

Figure E.4: Example shear stresses in the skins. Aft top view.

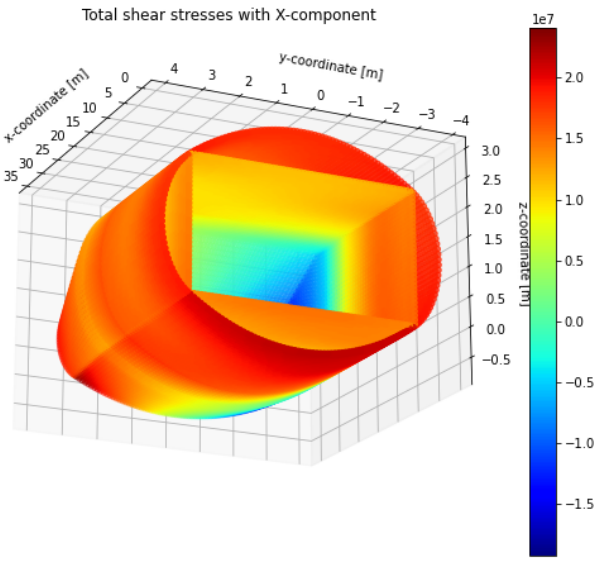

Figure E.5: Example shear stresses in the skins. Front bottom view.

CS stresses Stresses in the cross-sectional direction for the skins and frames for limit LC01. Clearly, the significant loads on the engine/MLG pylon section structure shows that reinforcement is needed in this area.

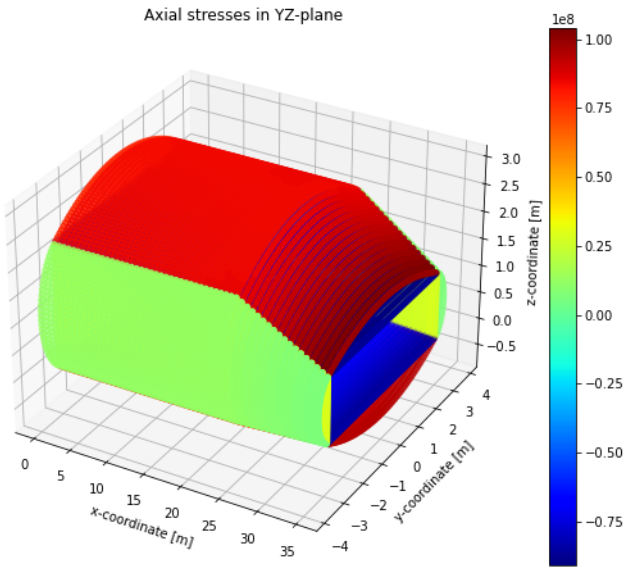

Figure E.6: Pure cross-section axial stresses in the skins of the panels. Aft top view.

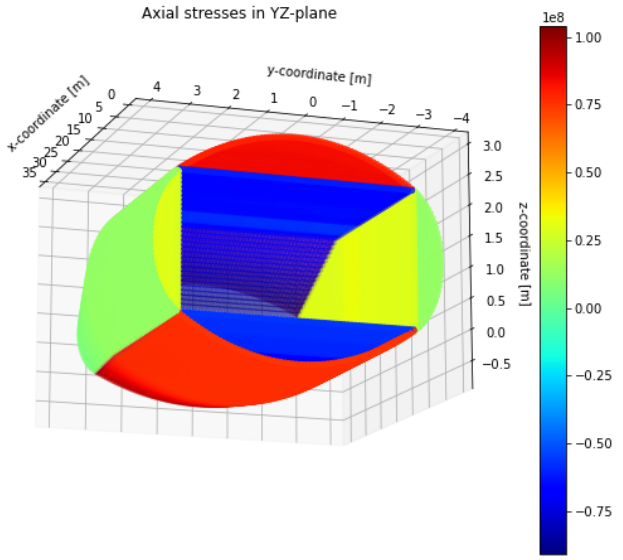

Figure E.7: Pure cross-section axial stresses in the skins of the panels. Front bottom view.

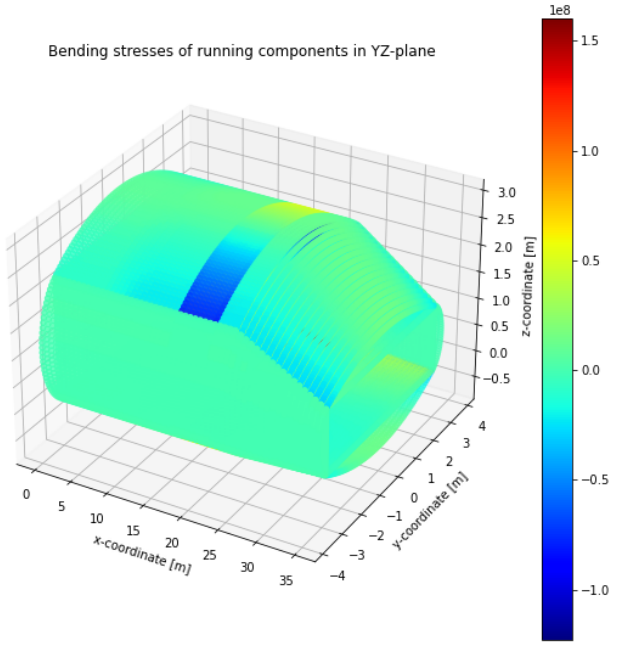

Figure E.8: Maximum absolute bending induced axial stresses in the skin. Aft top view.

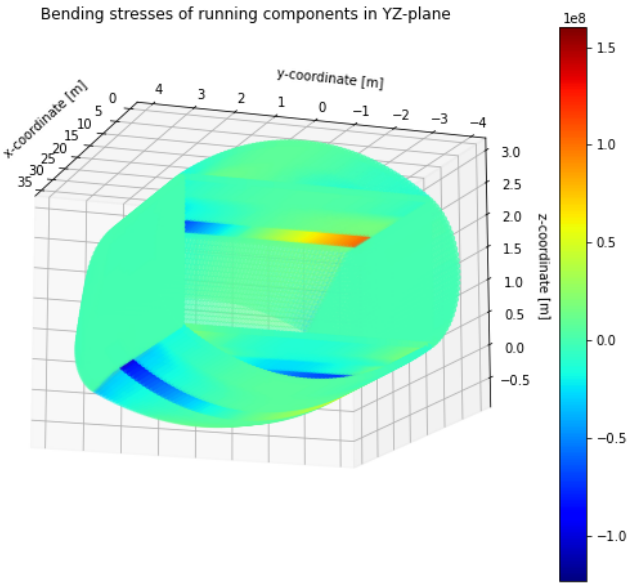

Figure E.9: Maximum absolute bending induced axial stresses in the skin. Front bottom view.

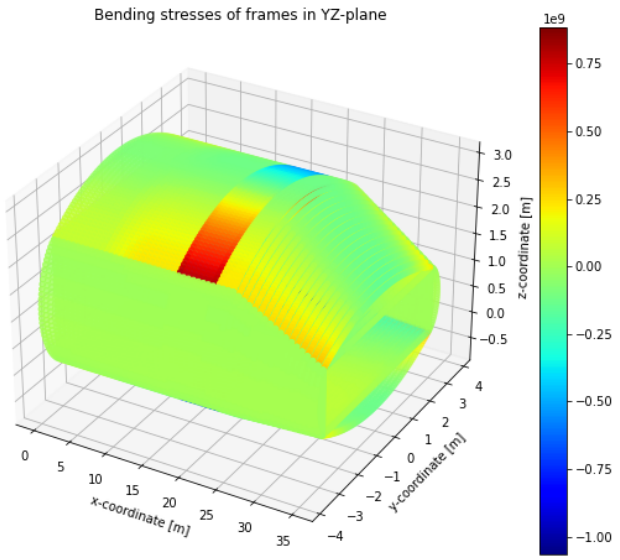

Figure E.10: Maximum absolute bending induced axial stresses in the frames. Aft top view.

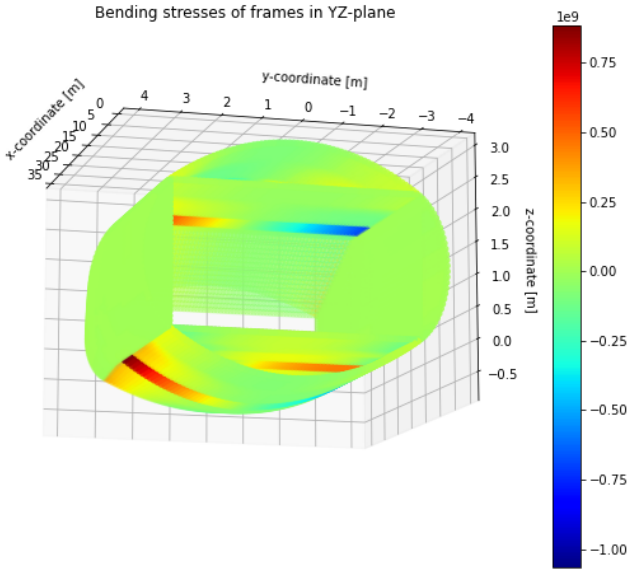

Figure E.11: Maximum absolute bending induced axial stresses in the frames. Front bottom view.

E.1.2. Pure pressurisation

As an example, the stress distributions for pure pressurisation (60kPa) are shown below. These stress fields are not representative for the final stress distributions of the sized structure, but are helpful for the interpretation of the following chapters.

longitudinal stresses The longitudinal stresses are practically identical to the pure axial stress plot shown in the previous subsection, as LC01 is also pressurised.

CS stresses The pure cross-section axial stresses in the skins are practically identical to the stress plots shown in the previous subsection, as LC01 is also pressurised.

The bending, on the other hand, shows a different response under pure pressurisation compared to LC01:

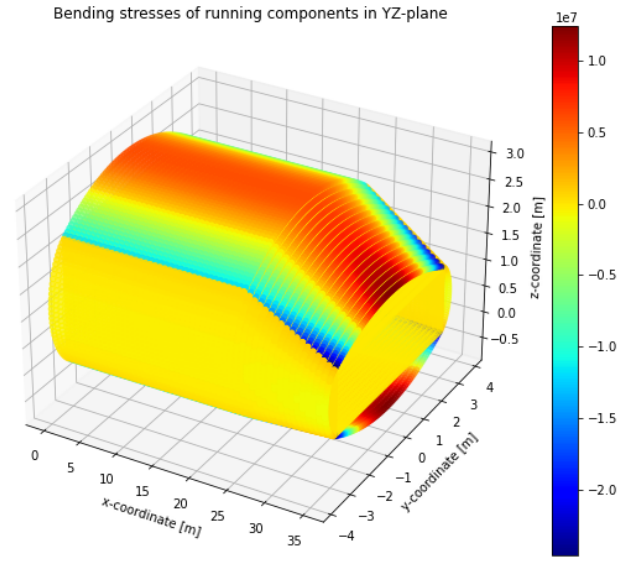

Figure E.12: Maximum absolute bending induced axial stresses in the skins. Aft top view.

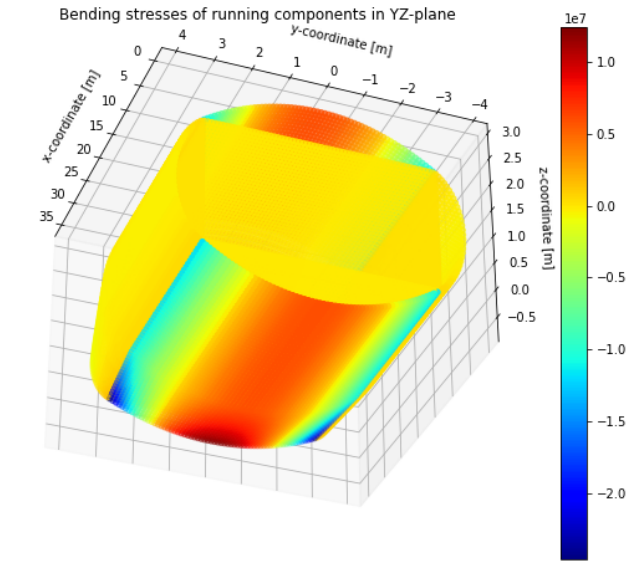

Figure E.13: Maximum absolute bending induced axial stresses in the skins. Front bottom view.

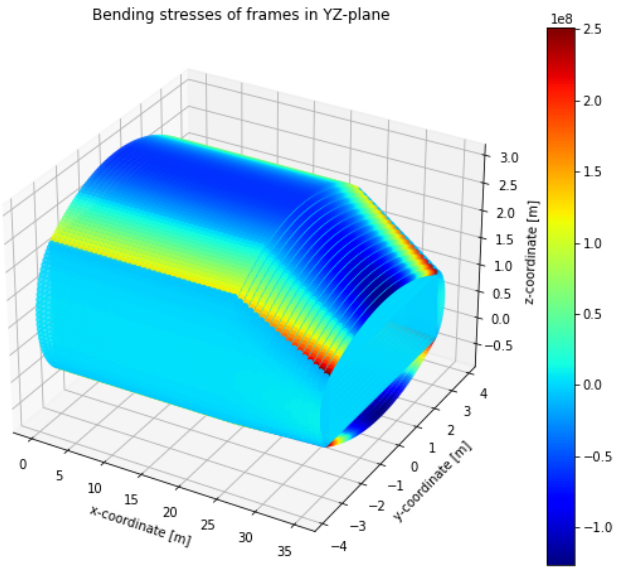

Figure E.14: Maximum absolute bending induced axial stresses in the frames. Aft top view.

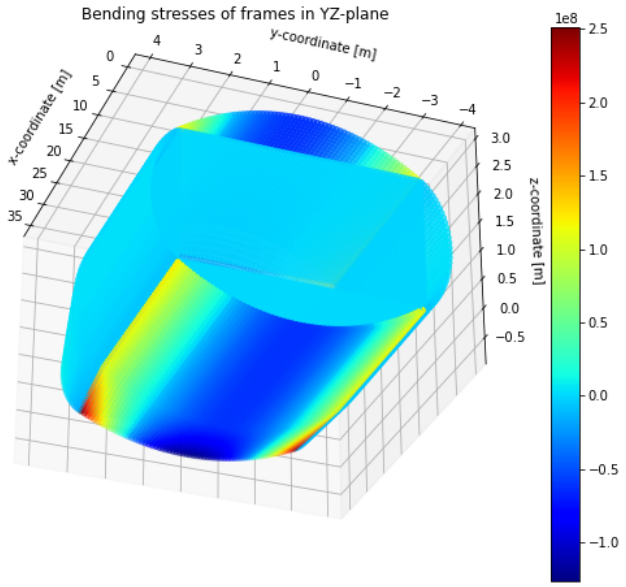

Figure E.15: Maximum absolute bending induced axial stresses in the frames. Front bottom view.

E.2. Results for mean material values

Below, the results for mean materials are shown after the stringer trials as described in section 7.2.3. The results for the original oval fuselage concept and the no LE spar (NLES) concept are presented, respectively.

E.2.1. Original concept critical failure modes

Below the critical failure modes for the mean material solution is shown. From the initial stringer trials in section 7.2.3, 18 crown/keel stringers, 54 floor/ceiling stringers and 12 LE/TE/walls stringers were applied. The solution was generated for $2m_{input} = 16 = m_{crown} = m_{keel} = m_{ceiling} = m_{floor} = 2m_{LE} = 2m_{TE} = 2m_{walls}$, which resulted in a mass of 23035 kg.

The maximum failure indices are presented in table E.1. The maximum failure mode distribution may be found in figures E.16 and E.17. The failure modes which drove the design for the mean materials are discussed shortly below. A detailed analysis was determined to be unnecessary, as it is apparent that buckling and crack propagation are critical in all structures. Therefore, the selected material for all components is AL2024-T3.

- Clearly, static material failure is not critical anywhere in the structure.
- Crack propagation (CP) is more critical than crack initiation (CI) in all regions. The fatigue failure modes are most critical in the crown and keel. The frame inner flange is critical near the vertex joints, while the frame outer flange is critical in the centre of the crown/keel.
- Stability failure modes are most critical in the LE, TE, floor, ceiling and walls. For the trailing edge, global buckling is mostly critical. For the floors and ceiling, column buckling of the cross-beams is critical. However, it should be noted from the individual failure index plots, that multiple stability-related failure modes have very high failure indices.

Table E.1: Maximum failure indices for the mean material solution. SMF = static material failure, CI = crack initiation, CP = crack propagation. Driving failure modes are shown in bold.

FI code	**Maximum component FI**	**Value** [-]
FI01	Skin axial SMF	0.41
FI02	Skin shear SMF	0.50
FI03	Stringers SMF	0.41
FI04	Frame inner flange SMF	0.58
FI05	Frame outer flange SMF	0.29
FI06	Biaxial global buckling	**0.94**
FI07	Shear global buckling	0.14
FI08	Combined global buckling	**0.95**
FI09	Biaxial panel buckling	**0.95**
FI10	Shear panel buckling	0.05
FI11	Combined panel buckling	**0.95**
FI12	Biaxial plate buckling	**0.95**
FI13	Shear plate buckling	**0.97**
FI14	Total plate buckling	**0.95**

FI code	**Maximum component FI**	**Value** [-]
FI15	Stringer crippling	**0.95**
FI16	Frame crippling	**0.96**
FI17	Crossbeam column buckling	**0.95**
FI18	Skin lon. axial CI	0.04
FI19	Skin shear CI	0.17
FI20	Skin hoop CI	0.78
FI21	Frame inner flange CI	0.09
FI22	Frame outer flange CI	0.49
FI23	Skin lon. axial CP	0.06
FI24	Skin shear CP	0.07
FI25	Skin hoop CP	0.75
FI26	Frame inner flange CP	**0.99**
FI27	Frame outer flange CP	0.94

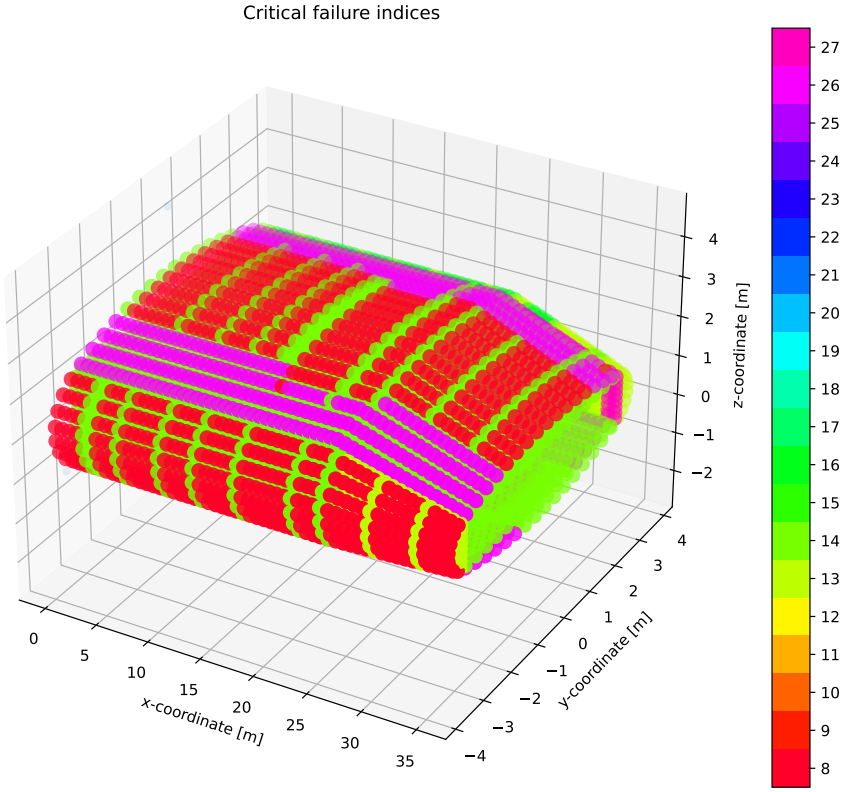

Figure E.16: Critical failure modes. 1-5: SMF, 6-17 stability modes, 18-22: CI, 23-27: CP. Aft top view.

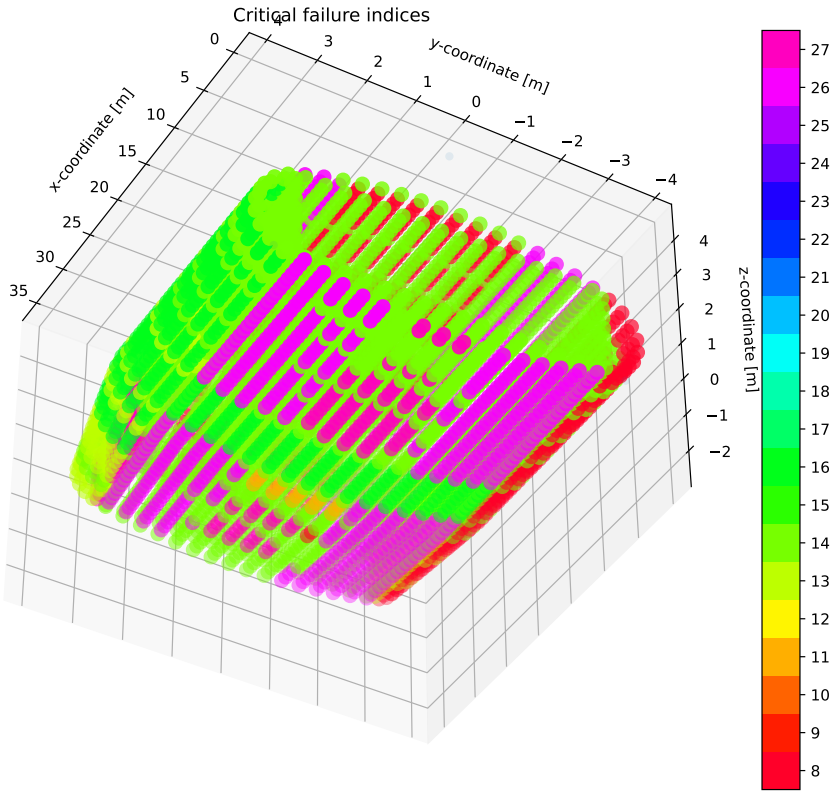

Figure E.17: Critical failure modes. 1-5: SMF, 6-17 stability modes, 18-22: CI, 23-27: CP. Front bottom view.

E.2.2. NLES concept critical failure modes

The maximum failure indices for the NLES concept are shown in table E.2. From the initial stringer trials in section 7.2.3, 20 crown/keel stringers, 60 floor/ceiling stringers, 14 LE stringers and 12 TE/walls stringers were applied. The solution was generated for $2m_{input} = 16 = m_{crown} = m_{keel} = m_{ceiling} = m_{floor} = 2m_{LE} = 2m_{TE} = 2m_{walls}$, which resulted in a mass of 25025 kg. The maximum failure index distributions are shown in figures E.18 and E.19.

The maximum failure modes are very similar to the maximum failure modes of the original concept, with two exceptions: FI02 Skin shear static material failure and FI19 Skin shear crack initiation, which have increased significantly. This is linked with the fact that the leading edge has to transfer much higher shear loads, due to pure shear and torque. Similarly to the original concept, the driving shown failure modes in all structures are crack propagation and multiple stability modes. Therefore, AL2024-T3 was applied to all structures.

Table E.2: Maximum failure indices for the NLES concept mean material solution. SMF = static material failure, CI = crack initiation, CP = crack propagation. Driving failure modes are shown in bold.

FI code	**Maximum component FI**	**Value** [-]
FI01	Skin axial SMF	0.42
FI02	Skin shear SMF	0.57
FI03	Stringers SMF	0.42
FI04	Frame inner flange SMF	0.73
FI05	Frame outer flange SMF	0.31
FI06	Biaxial global buckling	**0.93**
FI07	Shear global buckling	0.12
FI08	Combined global buckling	**0.93**
FI09	Biaxial panel buckling	**0.95**
FI10	Shear panel buckling	0.08
FI11	Combined panel buckling	**0.95**
FI12	Biaxial plate buckling	**0.95**
FI13	Shear plate buckling	**0.97**
FI14	Total plate buckling	**0.95**

FI code	**Maximum component FI**	**Value** [-]
FI15	Stringer crippling	**0.95**
FI16	Frame crippling	**0.95**
FI17	Crossbeam column buckling	**0.95**
FI18	Skin lon. axial CI	0.05
FI19	Skin shear CI	0.27
FI20	Skin hoop CI	0.89
FI21	Frame inner flange CI	0.09
FI22	Frame outer flange CI	0.52
FI23	Skin lon. axial CP	0.07
FI24	Skin shear CP	0.10
FI25	Skin hoop CP	0.81
FI26	Frame inner flange CP	**0.99**
FI27	Frame outer flange CP	**0.95**

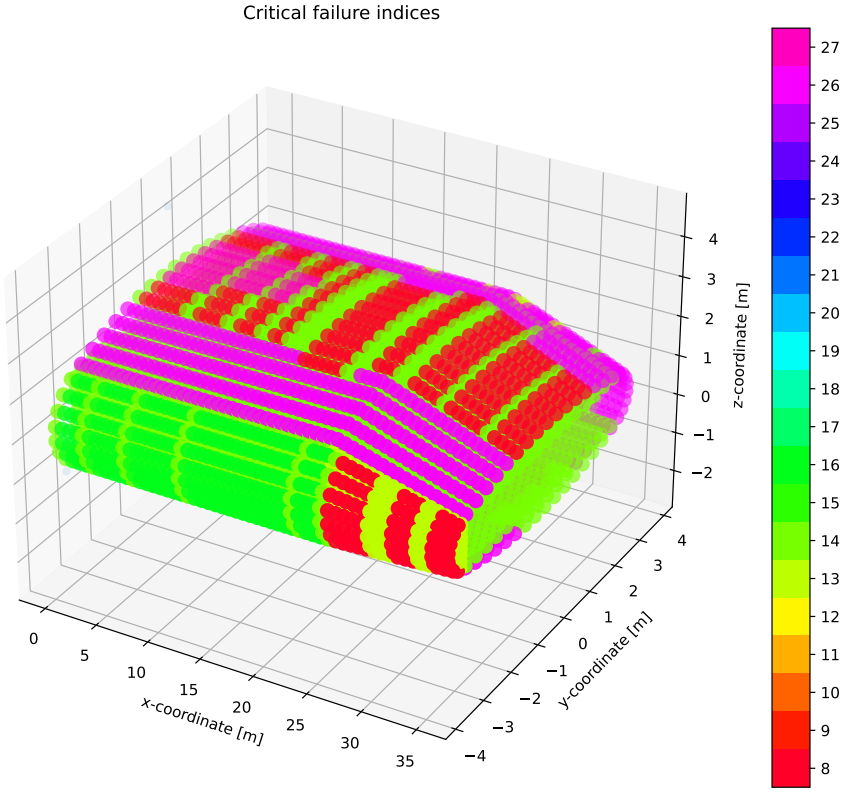

Figure E.18: NLES concept critical failure modes for mean material solution. 1-5: SMF, 6-17 stability modes, 18-22: CI, 23-27: CP. Aft top view.

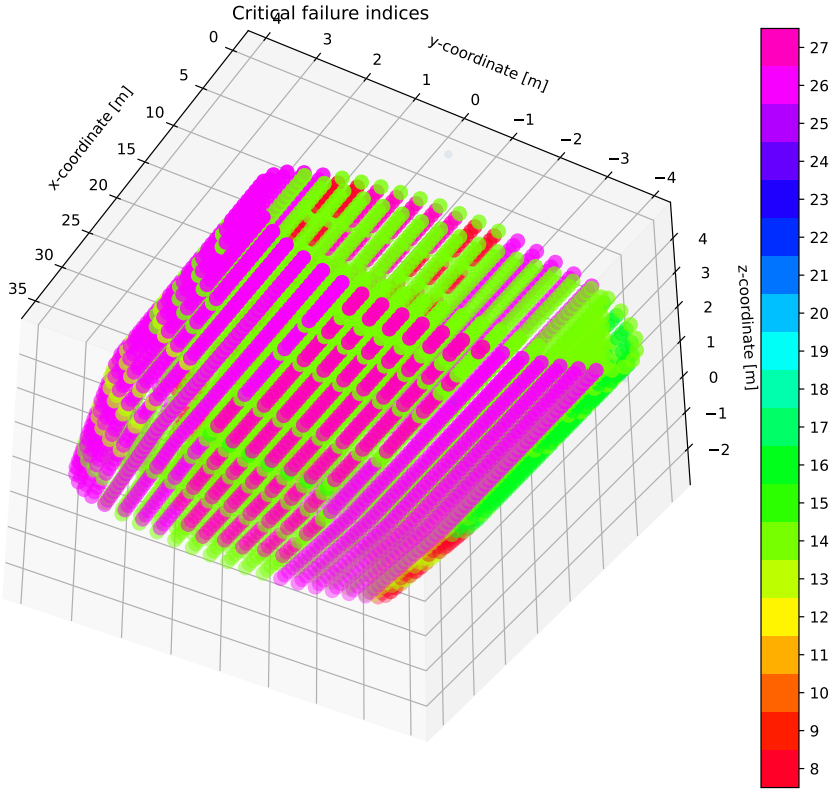

Figure E.19: NLES concept critical failure modes for mean material solution. 1-5: SMF, 6-17 stability modes, 18-22: CI, 23-27: CP. Front bottom view.

F

Generic structure

A generic structure was determined, which was used for the identification of the behaviour of stresses in the cross-section. The structure consists of a single frame-to-frame wing-fuselage section, with constant component geometry along the length of all components.

Oosterom's[13] sizing results were the best estimation of representative properties so far. Therefore, these results are used as a basis. From Oosterom's weight data, the approximate geometry of the components could be calculated. for the skin thickness, it was unclear what the thicknesses were of the individual skins, as all skin weights were bundled. While the crown and keel skin experience much higher stresses, the LE and TE arcs must withstand bird strike and withstand fuel loads, respectively. Therefore, for the purpose of this comparison, all skin thickness remain equal, calculated to be 5 mm.

Similarly, from the frame weight data, the frame geometry could be approximated. As Oosterom did not consider bending, the frames are expected to be very undersized. Therefore, the frame area was (arbitrarily) approximately doubled. The following geometric ratios for the frame were applied: $h_f = 2w_f = 20t_f$. This resulted in $h_f = 2w_f = 20t_f = 100mm$. While lacking proper substantiation, this was deemed acceptable to obtain a better understanding of the structural behaviour.

G
Additional concepts

The two concepts described below were not included in the analysis due to time constraints, and a high likelihood of performing poorly. For future reference, they are presented below.

Concept 2: removing the tension wall and ceiling A second proposed concept is to remove the ceiling in addition to the LE tension structure. Most of the above-mentioned reasoning may not be applied to the ceiling. Bending will be higher for this concept, and thus requires significant reinforcement. However, it may turn out that a LE and ceiling with a very high MOI is more favourable then the original concept. The original ceiling material may be used more effectively on the ceiling. Additionally, the increased available vertical space may lead to a reduced overall size of the cabin, which contributes to reducing the structural weight.

Concept 3: horizontal supports While it contradicts the earlier claim about the likely necessity of the trailing edge vertical structure, it may also be removed to assess the structural performance. The effective cabin space is increased, but the passengers would be positioned in close proximity to the fuel tank in the trailing edge fairing. While this concept is not deemed viable for this reason, the performance may still be evaluated. As the goal is to obtain a better understanding of the oval fuselage performance, this knowledge could be useful for other concepts, which do not possess trailing edge fuel tanks. This may be useful in the case of hydrogen propulsion, as the tanks will likely not be located in the trailing edge, as shown by van Woensel[70].

H

Flying-V dimensions

The figure below indicates the current conceptual layout of the Flying-V interior and exterior. The figure was obtained directly from Vos.

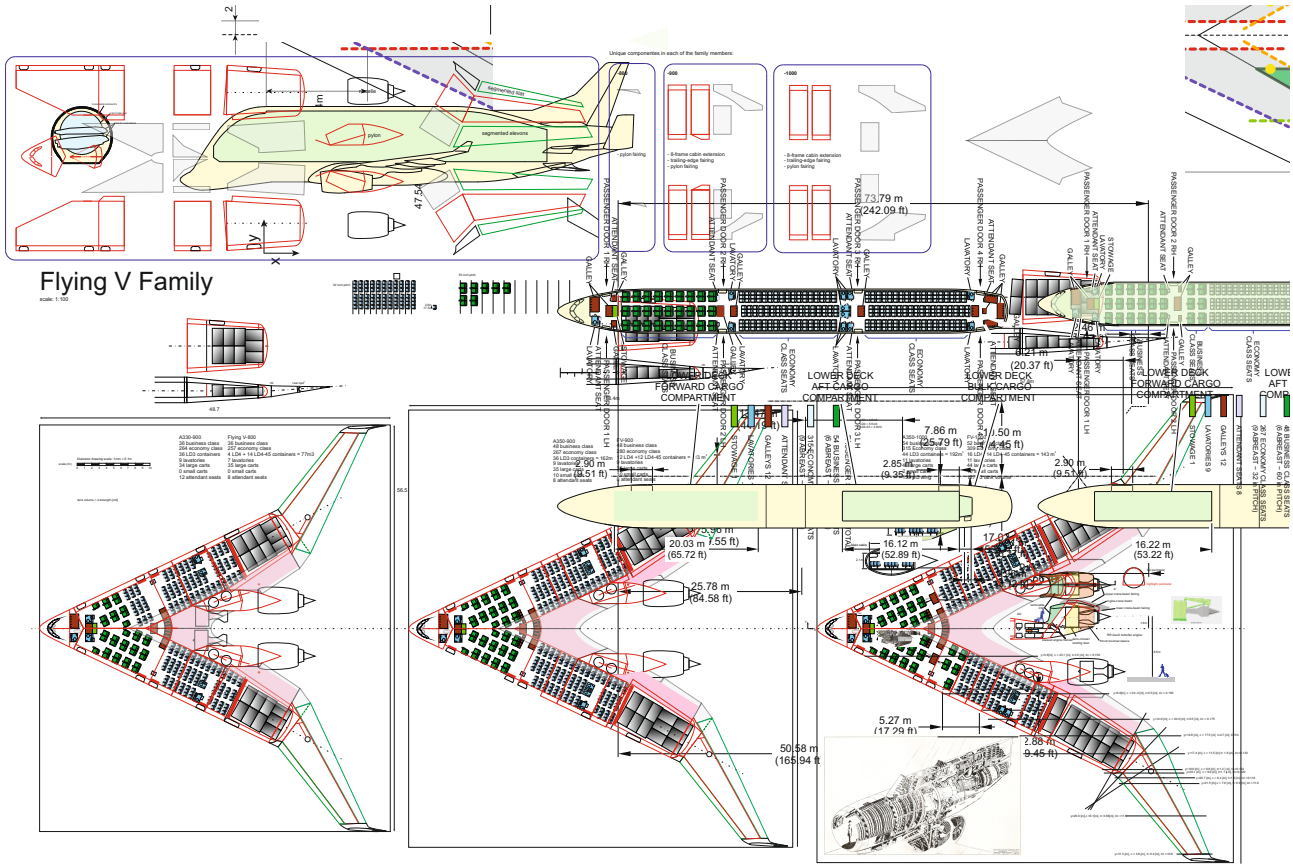

Figure H.1: Flying-V family.

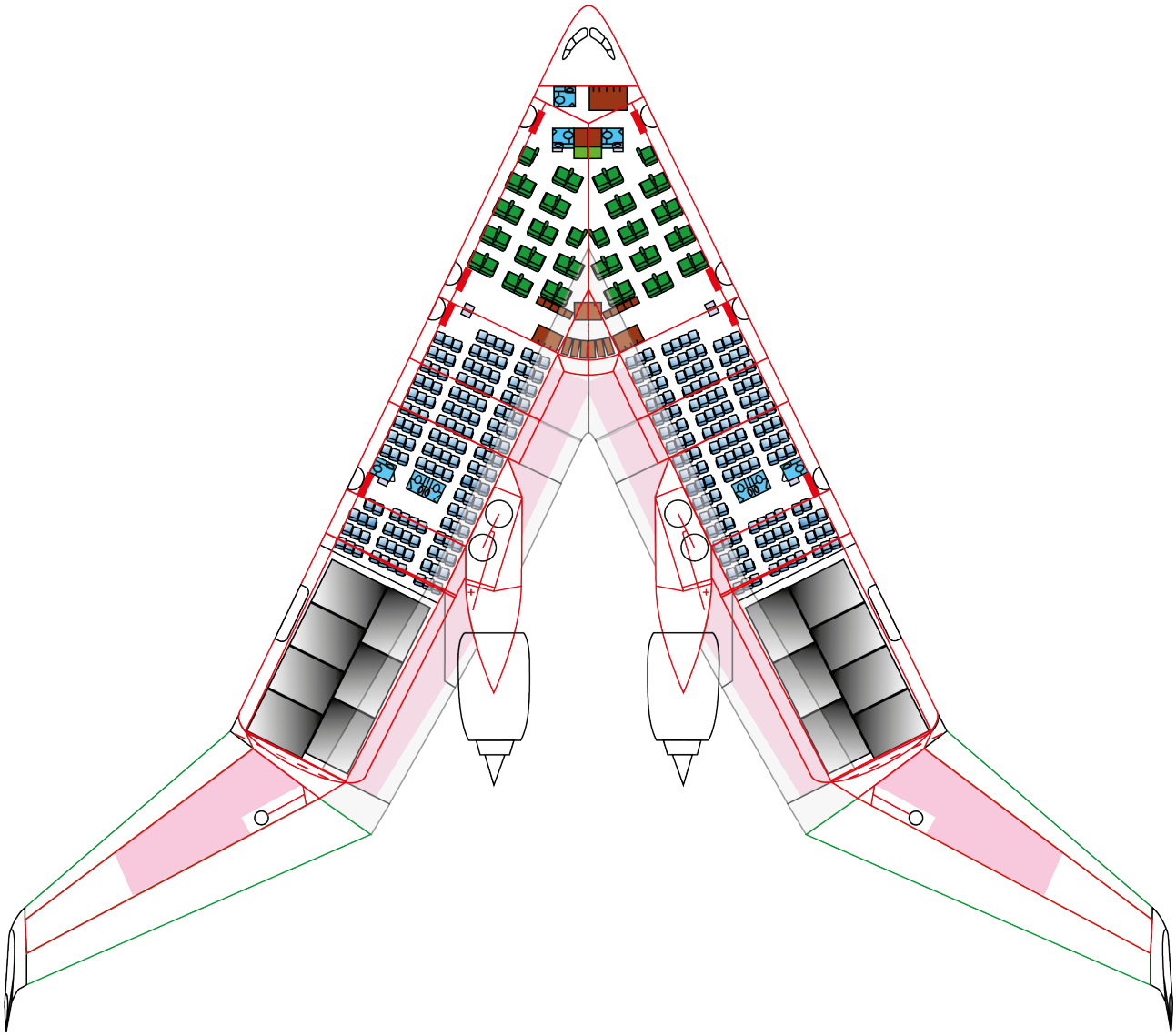

Figure H.2: Current interior concept, as obtained directly from Roelof Vos.

I

CS 25

The following list has been fully obtained from *Certification Specification and Acceptable Means of Compliance for Large Aeroplanes* by the *European Aviation Safety Agency* [41]. This compiled list serves to centrally contain all relevant regulations which were to be considered during this piece of research.

- CS 25.301a: Strength requirements are specified in terms of limit loads (the maximum loads to be expected in service) and ultimate loads (limit loads multiplied by prescribed factors of safety). Unless otherwise specified, prescribed loads are limit loads.
- CS 25.301b: Unless otherwise provided the specified air, ground and water loads must be placed in equilibrium with inertia forces, considering each item of mass in the aeroplane. These loads must be distributed to conservatively approximate or closely represent actual conditions.
- CS 25.303: Unless otherwise specified, a factor of safety of 1.5 must be applied to the prescribed limit load which are considered external loads on the structure.
- CS 25.305a: The structure must be able to support limit loads without detrimental permanent deformation. At any load up to limit loads, the deformation may not interfere with safe operation.
- CS 25.305b: Static tests conducted to ultimate load must include the ultimate deflections and ultimate deformation induced by the loading (...)
- CS 25.321d: The significant forces acting on the aeroplane must be placed in equilibrium in a rational or conservative manner. The linear inertia forces must be considered in equilibrium with the thrust and all aerodynamic loads, while the angular inertia forces must be considered in equilibrium with thrust and all aerodynamic moments, ...
- CS 25.331d: Maximum pitch control displacement at V_A. The aeroplane is assumed to be flying in steady level flight and the cockpit control is suddenly moved to obtain extreme nose up pitching acceleration. (...)
- CS 25.333 The strength requirements must be met at each combination of airspeed and load factor on and within the boundaries of the representative manoeuvring envelope ...
- CS 25.333b: Design dive speed V_D must be selected such that V_C/M_C is not greater than $0.8V_D/M_D$, ...
- CS 25.337a: Except where limited by maximum lift coefficients, the aeroplane is assumed to be subjected to symmetrical manoeuvres resulting in the limit manoeuvring load factors prescribed in this paragraph. ...
- CS 25.337b: The positive limit manoeuvring load factor n for any speed up to V_D may not be less than $2.1 + \left(\frac{24000}{W+10000}\right)$ except that n may not be less than 2.5 and need not be greater than 3.8 - where W is MTOW (lbs).
- CS 25.337c: The negative limit manoeuvring load factor: May not be less than -1.0 at speeds up to V_C; and must vary linearly with speed from V_C to zero at V_D.
- CS 25.341a: Discrete Gust Design Criteria. The aeroplane is assumed to be subjected to symmetrical vertical and lateral gusts in level flight. Limit gust loads must be determined in accordance with the following provisions: Loads on each part of the structure must be determined by dynamic analysis. [...]
- CS 25.343a: The disposable load combinations must include each fuel and oil load in the range from zero fuel and oil to the selected maximum fuel and oil load.
- CS 25.343b1: The structure must be designed for a condition of zero fuel and pol in the wing at limit loads corresponding to: A manoeuvring load factor of +2.25; and the gust and turbulence conditions of CS 25.341, but assuming 85% of the gust velocities and turbulence intensities prescribed.
- CS 25.343b2: Fatigue evaluation of the structure must account of any increase in operating stresses

resulting from the design condition of CS 25.343b1.

- CS 25.345: If wing-flaps are to be used during take-off, approach or landing, at the design flap speeds established for these stages under CS 335e and with the wing-flaps in the corresponding conditions, the aeroplane is assumed to be subjected to symmetrical manoeuvres and gusts. The resulting limit loads must correspond to the conditions determined as follows: Manoeuvring to a positive limit load factor of 2.0; and positive and negative gusts of 7.62 m/sec EAS acting normal to the flight path in level flight.
- CS 25.349a:(Rolling conditions) Manoeuvring. The following conditions, speeds, aileron deflections and cockpit roll control motions (except as the deflections and the motions may be limited by pilot effort) must be considered in combination with an aeroplane load factor of zero and of two-thirds of the positive manoeuvring factor used in design. ... In determining the required or resulting aileron deflections, the torsional flexibility of the wing must be considered in accordance with CS 25.301 (b): (1) Conditions corresponding to steady rolling velocities must be investigated In addition, conditions corresponding to maximum angular acceleration must be investigated for aeroplanes with engines or other weight concentrations outboard of the fuselage, and for aeroplanes equipped with electronic flight controls, where the motion of the control surfaces does not bear a direct relationship to the motion of the cockpit control devices. For the angular acceleration conditions, zero rolling velocity may be assumed in the absence of a rational time history investigation of the manoeuvre. (2) At VA, a sudden deflection of the aileron to the stop is assumed. (3) At VC, the aileron deflection must be that required to produce a rate of roll not less than that obtained in sub-paragraph (a) (2) of this paragraph. (4) At VD, the aileron deflection must be that required to produce a rate of roll not less than one-third of that in sub-paragraph (a) (2) of this paragraph. ...
- CS 25.349b:(Rolling conditions) Unsymmetrical gusts. The aeroplane is assumed to be subjected to unsymmetrical vertical gusts in level flight. The resulting limit loads must be determined from either the wing maximum airload derived directly from CS 25.341(a), or the wing maximum airload derived indirectly from the vertical load factor calculated from CS 25.341(a). It must be assumed that 100 percent of the wing airload acts on one side of the aeroplane and 80 percent of the wing airload acts on the other side.
- CS 25.351: (yaw manoeuvre conditions) The aeroplane must be designed for loads resulting from the yaw manoeuvre conditions specified in sub-paragraphs (a) through (d) of this paragraph at speeds from VMC to VD. Unbalanced aerodynamic moments about the centre of gravity must be reacted in a rational or conservative manner considering the aeroplane inertia forces. In computing the tail loads the yawing velocity may be assumed to be zero. (a) With the aeroplane in unaccelerated flight at zero yaw, it is assumed that the cockpit rudder control is suddenly displaced to achieve the resulting rudder deflection, as limited by: (1) the control system or control surface stops; or (2) a limit pilot force of 1335 N (300 lbf) from VMC to VA and 890 N (200 lbf) from VC/MC to VD/MD, with a linear variation between VA and VC/MC. (b) With the cockpit rudder control deflected so as always to maintain the maximum rudder deflection available within the limitations specified in sub-paragraph (a) of this paragraph, it is assumed that the aeroplane yaws to the overswing sideslip angle. (c) With the aeroplane yawed to the static equilibrium sideslip angle, it is assumed that the cockpit rudder control is held so as to achieve the maximum rudder deflection available within the limitations specified in sub-paragraph (a) of this paragraph. (d) With the aeroplane yawed to the static equilibrium sideslip angle of sub-paragraph (c) of this paragraph, it is assumed that the cockpit rudder control is suddenly returned to neutral.
- CS 25.361a1: Each engine mount, pylon and adjacent supporting airframe structures must be designed for the effects of: a limit engine torque corresponding to take-off power/thrust [...] acting simultaneously with 75% of the limit loads from flight condition A of CS25.333b; a limit engine torque corresponding to the maximum continuous power/thrust and [...] acting simultaneously with the loads from flight condition A of CS25.333b.
- CS 25.361a2: The limit engine torque to be considered under CS 25.361a1 must be obtained by: for turbine engines, the limit engine torque must be eual to the maximum accelerating torque for the case considered.
- CS 25.361a3 The engine mounts, pylons and adjacent supporting airframe structure must be designed to withstand 1 g level flight loads acting simultaneously with the limit engine torque loads imposed by

each of the following conditions to be considered separately: Sudden maximum engine deceleration due to malfunction or abnormal condition; and the macimum acceleration of the engine.

- CS 25.363a Each engine and APU mount and its supporting structure must be designed for a limit load factor in a lateral direction, for the side load on the engine and APU mount, at least equal to the maximum load factor obtined in the yawing conditions but no less than: 1.33; or one-third of the limi load factor for flight condition A as prescribed in CS 25.333b
- CS 25.363b: The side load prescribed in CS 25 636a may be assumed to be independent of other flight conditions.
- CS 25.365a The aeroplane structure must be strong enough to withstand the flight loads combined with pressure differential loads from zero up to the maximum relief valve setting.
- CS 25.365b: The external pressure distribution in flight, and stress concentrations and fatigue effects must be accounted for.
- CS 25.365c: If landings may be made with the compartment pressurised, landing loads must be combined with pressure differential loads from zero up to the maximum allowed during landing.
- CS 25.365d: The aeroplane structure must be strong enough to withstand the pressure differential loads corresponding to the maximum relief valve setting multiplied by a factor of 1·33, omitting other loads.
- CS 25.365e: Any structure, component or part, inside or outside a pressurised compartment, the failure of which could interfere with continued safe flight and landing, must be designed to withstand the effects of a sudden release of pressure through an opening in any compartment at any operating altitude resulting from each of the following conditions: (1) The penetration of the compartment by a portion of an engine following an engine disintegration. (2) Any opening in any pressurised compartment up to the size H_o in square feet; however, small compartments may be combined with an adjacent pressurised compartment and both considered as a single compartment for openings that cannot reasonably be expected to be confined to the small compartment. The size H_o must be computed by the following formula: $H_o = Pa_s$, where H_o is the maximum opening in square feet, need not exceed 20 feet, P is $\frac{A_s}{6240} + 0.024$ and A_s is the maximum cross sectional area of the pressurised shell normal to the longitudinal axis, in square feet.
- CS 25.365g: Bulkheads, floors, and partitions in pressurised compartments for occupants must be designed to withstand conditions specified in sub-paragraph (e) of this paragraph. In addition, reasonable design precautions must be taken to minimise the probability of parts becoming detached and injuring occupants while in their seats.

- CS 25.471a: Limit ground loads are obtained under this subpart are considered to be external forces applied to the aeroplane structure; and in each specified ground load condition, the external loads must be placed in equilibrium with the linear and angular inertia loads in a rational or conservative manner.
- CS 25.473a The aeroplane is assumed to contact the ground: in the altitudes defined in CS 25.479 and CS 25.481; with a limit descent velocity of 3.05 m/s at the design landing weight (the maximum weight for landing conditions at maximum descent velocity); and With a limit descent velocity of 1·83 m/sec (6 fps) at the design take-off weight (the maximum weight for landing conditions at a reduced descent velocity).
- CS 25.473b: Aeroplane lift, not exceeding aeroplane weight, may be assumed, unless the presence of systems or procedures significantly affects the lift.
- CS 25.473e: The coefficient of friction between the tyres and ground may be established by considering the effects of skidding velocity and tyre pressure. However, this coefficient of friction need not be more than 0.8.
- CS 25.479: In the level attitude, the aeroplane is assumed to contact the ground at forward velocity components, ranging from VL1 to 1·25 VL2 parallel to the ground under the conditions prescribed in CS 25.473 with: (1) VL1 equal to VS0(TAS) at the appropriate landing weight and in standard sea-level conditions; and (2) VL2, equal to VS0(TAS) at the appropriate landing weight and altitudes in a hot day temperature of 22.8ºC (41ºF) above standard. (3) The effects of increased contact speed must be investigated if approval of downwind landings exceeding 19 km/h (10 knots) is requested. (b) For the

level landing attitude for aeroplanes with tail wheels, the conditions specified in this paragraph must be investigated with the aeroplane horizontal reference line horizontal in accordance with Figure 2 of Appendix A of CS –25. (c) For the level landing attitude for aeroplanes with nose wheels, shown in Figure 2 of Appendix A of CS –25, the conditions specified in this paragraph must be investigated assuming the following attitudes: (1) An attitude in which the main wheels are assumed to contact the ground with the nose wheel just clear of the ground; and (2) If reasonably attainable at the specified descent and forward velocities an attitude in which the nose and main wheels are assumed to contact the ground simultaneously. (d) In addition to the loading conditions prescribed in sub-paragraph (a) of this paragraph, but with maximum vertical ground reactions calculated from paragraph (a), the following apply: (1) The landing gear and directly affected structure must be designed for the maximum vertical ground reaction combined with an aft acting drag component of not less than 25 % of this maximum vertical ground reaction. (2) The most severe combination of loads that are likely to arise during a lateral drift landing must be taken into account. In absence of a more rational analysis of this condition, the following must be investigated: (i) A vertical load equal to 75 % of the maximum ground reaction of CS 25.473(a)(2) must be considered in combination with a drag and side load of 40 % and 25 %, respectively, of that vertical load. (ii) The shock absorber and tyre deflections must be assumed to be 75 % of the deflection corresponding to the maximum ground reaction of CS 25.473(a)(2). This load case need not be considered in combination with flat tyres. (3) The combination of vertical and drag components is considered to be acting at the wheel axle centreline.

- CS 25.481: (a) In the tail-down attitude, the aeroplane is assumed to contact the ground at forward velocity components, ranging from VL1 to VL2, parallel to the ground under the conditions prescribed in CS 25.473 with: (1) VL1 equal to VS0 (TAS) at the appropriate landing weight and in standard sea-level conditions; and (2) VL2 equal to VS0 (TAS) at the appropriate landing weight and altitudes in a hot-day temperature of 22.8°C (41°F) above standard. The combination of vertical and drag components is considered to be acting at the main wheel axle centreline. For the tail-down landing condition for aeroplanes with tail wheels, the main and tail wheels are assumed to contact the ground simultaneously, in accordance with Figure 3 of Appendix A. Ground reaction conditions on the tail wheel are assumed to act (1) Vertically; and (2) Up and aft through the axle at 45° to the ground line. (c) For the tail-down landing condition for aeroplanes with nose wheels, the aeroplane is assumed to be at an attitude corresponding to either the stalling angle or the maximum angle allowing clearance with the ground by each part of the aeroplane other than the main wheels, in accordance with Figure 3 of Appendix A, whichever is less.
- CS 25.485: In addition to CS 25.479(d)(2) the following conditions must be considered: (a) For the side load condition, the aeroplane is assumed to be in the level attitude with only the main wheels contacting the ground, in accordance with Figure 5 of Appendix A. (b) Side loads of 0·8 of the vertical reaction (on one side) acting inward and 0·6 of the vertical reaction (on the other side) acting outward must be combined with one-half of the maximum vertical ground reactions obtained in the level landing conditions. These loads are assumed to be applied at the ground contact point and to be resisted by the inertia of the aeroplane. The drag loads may be assumed to be zero.
- CS 25.493: ... (b) For an aeroplane with a nose wheel, the limit vertical load factor is 1·2 at the design landing weight, and 1·0 at the design ramp weight. A drag reaction equal to the vertical reaction, multiplied by a coefficient of friction of 0·8, must be combined with the vertical reaction and applied at the ground contact point of each wheel with brakes. The following two attitudes, in accordance with Figure 6 of Appendix A, must be considered: (1) The level attitude with the wheels contacting the ground and the loads distributed between the main and nose gear. Zero pitching acceleration is assumed. (2) The level attitude with only the main gear contacting the ground and with the pitching moment resisted by angular acceleration. (c) ... (d) An aeroplane equipped with a nose gear must be designed to withstand the loads arising from the dynamic pitching motion of the aeroplane due to sudden application of maximum braking force. The aeroplane is considered to be at design takeoff weight with the nose and main gears in contact with the ground, and with a steady state vertical load factor of 1·0. The steady state nose gear reaction must be combined with the maximum incremental nose gear vertical reaction caused by sudden application of maximum braking force as described in sub-paragraphs (b) and (c) of this paragraph. (e) In the absence of a more rational analysis, the nose gear vertical reaction

prescribed in sub-paragraph (d) of this paragraph must be calculated in accordance with the following formula: $V_N = \frac{W_T}{A+B}\left(B + \frac{f v AE}{A+B+vE}\right)$, where: VN = Nose gear vertical reaction WT = Design take-off weight A = Horizontal distance between the c.g. of the aeroplane and the nose wheel. B = Horizontal distance between the c.g. of the aeroplane and the line joining the centres of the main wheels. E = Vertical height of the c.g. of the aeroplane above the ground in the 1·0 g static condition. ? = Coefficient of friction of 0·8. f = Dynamic response factor; 2·0 is to be used unless a lower factor is substantiated. In the absence of other information, the dynamic response factor f may be defined by the equation: $f = 1 + exp\left(\frac{-\pi\xi}{\sqrt{1-\xi^2}}\right)$ Where: ξ is the critical damping ratio of the rigid body pitching mode about the main landing gear effective ground contact point.

- CS 25.561a: The aeroplane, although it may be damaged in emergency landing conditions on land or water, must be designed as prescribed in this paragraph t protect each occupant under those conditions.
- CS 25.561b: The structure must be designed to give each occupant every reasonable chance of escaping serious injury in a minor crash landing when: Proper use is made of seats, belts, and all other safety design provisions; and The wheels are retracted (where applicable); and The occupant experiences the following ultimate inertia forces acting separately relative to the surrounding structure: (i) Upward, 3·0g; (ii) Forward, 9·0g; (iii) Sideward, 3·0g on the airframe and 4·0g on the seats and their attachments; (iv) Downward, 6·0g; (v) Rearward, 1·5g (See AMC 25.561 (b) (3).)
- CS 25.571a: General. An evaluation of the strength, detail design, and fabrication must show that catastrophic failure due to fatigue, manufacturing defects, environmental deterioration, or accidental damage, will be avoided throughout the operational life of the aeroplane. ...
- CS 25.571b: Fatigue and damage tolerance evaluation. The evaluation must include a determination of the probable locations and modes of damage due to fatigue, environmental deterioration (e.g. corrosion), or accidental damage. ... The residual strength evaluation must show that the remaining structure is able to withstand loads (considered as static ultimate loads) corresponding to the following conditions: (1) The limit symmetrical manoeuvring conditions specified in CS 25.331 at all speeds up to VC and in CS 25.345. (2) The limit gust conditions specified in CS 25.341 at the specified speeds up to VC and in CS 25.345. (3) The limit rolling conditions specified in CS 25.349 and the limit unsymmetrical conditions specified in CS 25.367 and CS 25.427(a) through (c), at speeds up to VC. (4) The limit yaw manoeuvring conditions specified in CS 25.351 at the specified speeds up to VC. (5) For pressurised cabins, the following conditions: (i) The normal operating differential pressure combined with the expected external aerodynamic pressures applied simultaneously with the flight loading conditions specified in sub-paragraphs (b)(1) to (b)(4) of this paragraph if they have a significant effect. (ii) The maximum value of normal operating differential pressure (including the expected external aerodynamic pressures during 1 g level flight) multiplied by a factor of 1·15 omitting other loads.
- CS 25.571e: Discrete source damage tolerance evaluation. The aeroplane must be capable of successfully completing a flight during which likely structural damage occurs as a result of bird impact as specified in CS25.631. The damaged structure must be able to withstand the static loads (considered as ultimate loads) which are reasonably expected to occur at the time of the occurrence and during the completion of the flight. Dynamic effects on these static loads do not need to be considered.
- CS 25.613b: Material design values must be chosen to minimise the probability of structural failures due to material variability. Except as provided in sub-paragraphs (e) and (f) of this paragraph, compliance must be shown by selecting material design values which assure material strength with the following probability: (1) Where applied loads are eventually distributed through a single member within an assembly, the failure of which would result in loss of structural integrity of the component, 99 % probability with 95 % confidence. (2) For redundant structure, in which the failure of individual elements would result in applied loads being safely distributed to other load carrying members, 90 % probability with 95 % confidence.

Bibliography

[1] T.H.G Megson. *Aircraft Structures*. Elsevier Ltd., 2013. ISBN 978-0-08-096905-3.

[2] J.B. de Jonge, D. Schütz, H. Lowak, and J. Schijve. A standardized load sequence for flight simulation tests on transport aircraft wing structures. Technical report, Nationaal Lucht- en Ruimtevaartlaboratorium, 1973.

[3] Edwin Wallet. Flying V Composite.

[4] Airbus. Airbus reveals new zero-emission concept aircraft, 2020. URL https://www.airbus.com/newsroom/press-releases/en/2020/09/airbus-reveals-new-zeroemission-concept-aircraft.html.

[5] A. L. Bolsunovsky, N. P. Buzoverya, B. I. Gurevich, V. E. Denisov, A. I. Dunaevsky, L. M. Shkadov, O. V. Sonin, A. J. Udzhuhu, and J. P. Zhurihin. Flying wing - Problems and decisions. *Aircraft Design*, 4(4):193–219, 2001. ISSN 13698869. doi: 10.1016/S1369-8869(01)00005-2.

[6] M. A. Page, E. J. Smetak, and S. L. Yang. Single-aisle airliner disruption with a single-deck blended-wing-body. *31st Congress of the International Council of the Aeronautical Sciences, ICAS 2018*, 2018.

[7] J. Benad. the Flying V - a New Aircraft Configuration for Commercial Passenger Transport. In *Deutscher Luft- und Raumfahrtkongress*, number November, 2015. URL http://www.dglr.de/publikationen/2015/370094.pdf.

[8] R K Schmidt. *A Semi-Analytical Weight Estimation Method for Oval Fuselages in Novel Aircraft Configurations (MSc thesis)*. 2013.

[9] Francesco Faggiano, Roelof Vos, Max Baan, and Reinier Van Dijk. Aerodynamic design of a flying V aircraft. *17th AIAA Aviation Technology, Integration, and Operations Conference, 2017*, 2017. doi: 10.2514/6.2017-3589.

[10] L A Van Der Schaft. *Development, Model Generation and Analysis of a Flying V Structure Concept (MSc thesis)*. 2017. URL http://resolver.tudelft.nl/uuid:d9c9c02f-d67a-4e3c-93a7-eb20ed67cd03.

[11] M. B. P. Claeys. *Flying V and Reference Aircraft Structural Analysis and Mass Comparison (MSc thesis)*. 2018. URL http://resolver.tudelft.nl/uuid:ee7f2ecb-cdb6-46de-8b57-d55b89f8c7e6.

[12] M Hillen. *Parametrisation of the Flying V Outer Mould Line (MSc thesis)*. 2020.

[13] W. J. Oosterom. Flying-V Family Design, 2021. URL http://resolver.tudelft.nl/uuid:9e8f9a41-8830-405d-8676-c46bf6b07891.

[14] Yaïr Brouwer. Aerodynamic surface data, 2021. URL https://zenodo.org/record/5726773.

[15] Ted L. Lomax. *Structural Loads Analysis for Commercial Transport Aircraft*. American Institute of Aeronautics and Astronautics, Washington DC, 1 1996. ISBN 978-1-56347-114-8. doi: 10.2514/4.862465. URL https://arc.aiaa.org/doi/book/10.2514/4.862465.

[16] Michael C Niu. *Airframe Stress Analysis and Sizing (2nd Ed 1999)*. Conmilit Press Ltd., 1999. ISBN 978-9627128120. URL http://cataleg.upc.edu/record=b1240761~S1*cat.

[17] Jaap Schijve. *Fatigue of Structures and Materials*. Springer, Delft, 2009. ISBN 9781402068072.

[18] J.C. Newman Jr. An Improved Method of Collocation for the Stress Analysis of Cracked Plated with Various Shaped Boundaries. Technical report, National Aeronautics and Space Administration, 1971.

[19] AIRBUS and IASB. Handbuch struktur berechnung Version 0.7.0. Technical report, Airbus, IASB, 2007.

[20] Elmer Franklin Bruhn. *Analysis and Design of Flight Vehicle Structures*. 1973. ISBN 0961523409.

[21] Michael Chun-Yung Niu. *Airframe Structural Design: Practical Design Information and Data on Aircraft Structures*. Conmilit Press Ltd., 1988. ISBN 962-7 128-04-X. URL http://scholar.google.com/scholar?hl=en&btnG=Search&q=intitle:Airframe+Structural+Design#5.

[22] R. Martinéz-Val. Flying Wings. A New Paradigm for Civil Aviation? *Acta Polytechnica*, 47(1), 2007. ISSN 1210-2709. doi: 10.14311/914.

[23] Matthew Marino and Roberto Sabatini. Benefits of the Blended Wing Body Aircraft Compared to Current Airliners. In *International Symposium on Sustainable Aviation (ISSA 2015)*, number June, 2015.

[24] R. Vos, F. J.J.M.M. Geuskens, and M. F.M. Hoogreef. A new structural design concept for blended wing body cabins. In *53rd AIAA/ASME/ASCE/AHS/ASC Structures, Structural Dynamics and Materials Conference*, number April, 2012. ISBN 9781600869372.

[25] International Air Transport Association (IATA). Aircraft Technology Roadmap to 2050. Technical report, International Air Transport Association, Geneva, 2019. URL https://www.iata.org/contentassets/8d19e716636a47c184e7221c77563c93/technology20roadmap20to20205020no20foreword.pdf.

[26] Ivan Jakovljević, Radomir Mijailović, and Petar Mirosavljević. Carbon dioxide emission during the life cycle of turbofan aircraft. *Energy*, 148(February):866–875, 2018. ISSN 03605442. doi: 10.1016/j.energy.2018.02.022.

[27] Joyce E. Penner, David H. Lister, David J. Griggs, David J. Dokken, and Mack McFarland. IPCC special report. Technical report, Intergovernmental Panel on Climate Change, 1999.

[28] V. E. Denisov, A. L. Bolsunovsky, Buzoverya N. P., and Gurevich B. I. Recent Investigations of the Very Large Passenger Blended-Wing-Body Aircraft, 1998. URL http://www.icas.org/ICAS_ARCHIVE/ICAS1998/PAPERS/4102.PDF.

[29] R. H. Liebeck. Design of the Blended Wing Body Subsonic Transport. *Journal of Aircraft*, 41(1):10–25, 2004. ISSN 15333868. doi: 10.2514/1.9084.

[30] Andy Ko, L.T. Leifsson, J.A. Schetz, and R.T. Haftka. MDO of a Blended-Wing-Body Transport Aircraft with Distributed Propulsion. In *AIAA's 3rd Annual Aviation Technology, Integration, and Operations (ATIO) Technical Forum*, number November, 2003. ISBN 978-1-62410-104-5.

[31] Berta Rubio Pascual. *Engine-airframe integration for the flying v (MSc thesis)*. 2018. URL https://repository.tudelft.nl/islandora/object/uuid%3A75be27a7-6fd4-4112-a600-45df2999758f.

[32] M. N. Roelofs. *Semi-analytical composite oval fuselage mass estimation (MSc thesis)*. 2016. ISBN 9781624104473. doi: 10.2514/6.2017-0466.

[33] C. Soutis. Fibre reinforced composites in aircraft construction. *Progress in Aerospace Sciences*, 41(2):143–151, 2005. ISSN 03760421. doi: 10.1016/j.paerosci.2005.02.004.

[34] M.F.M. Hoogreef. *The Oval Fuselage (MSc thesis)*. Number August. 2012.

[35] Francesco Faggiano. *Aerodynamic design Optimization of a flying V Aircraft (MSc thesis)*. 2016. ISBN 9781624105081. doi: 10.2514/6.2017-3589.

[36] G Bourget. The effect of landing gear implementation on Flying V aerodynamics , stability and controllability, 2020.

[37] EASA. TYPE-CERTIFICATE DATA SHEET for Trent XWB series engines. Technical report, 2021. URL https://www.easa.europa.eu/sites/default/files/dfu/EASAE111TCDSissue14_TrentXWB.pdf.

[38] Jan Roskam. *Airplane Design Part 5: Component Weight*. Roskam Aviation and Engineering Corporation, 1985.

[39] Egbert Torenbeek. *Synthesis of Subsonic Airplane Design*. Martinus Bijhoff Publishers, 1982. ISBN 9024727243.

[40] Airbus. Airbus-AC-A350-900-1000-Characteristics, Airport and Maintenance Planning. Technical report, Airbus, 2005.

[41] European Aviation Safety Agency. Certification Specifications and Acceptable Means of Compliance for Large Aeroplanes. Technical Report Amendment 25, European Aviation Safety Angency, 2020.

[42] Nicolas Turrel and Didier Auriche. Widespread Fatigue Damage: A300B Compliance with ageing aircraft regulation. *Fast 51*, pages 17–23, 2013.

[43] FAA. ESTABLISHING AND IMPLEMENTING LIMIT OF VALIDITY TO PREVENT WIDESPREAD FATIGUE DAMAGE. Technical report, Federal Aviation Administration, 2011.

[44] Isabelle Remaury-Lando, Delphine Meunier, and Hugo Alberto Quijano Fiallos. Supporting ageing fleets: scheduling the unscheduled. *Airbus technical magazine - Flight Airworthiness Support Technology*, (61):32–37, 2018. URL https://www.airbus.com/content/dam/corporate-topics/publications/fast/airbus-fast61-april2018.pdf.

[45] Legal Information Institute. 14 CFR 129.115 - Limit of validity. URL https://www.law.cornell.edu/cfr/text/14/129.115.

[46] Airbus. Airbus-AC-A300-Characteristics, Airport and Maintenance Planning. Technical report, Airbus, 2002.

[47] Airbus. Airbus-AC-A300-600-Characteristics, Airport and Maintenance Planning. Technical report, Airbus, 2002.

[48] Airbus. Airplane characteristics for airport planning A310. Technical report, Airbus, 2002.

[49] Airbus. Aircraft Characteristics Airport and Maintenance Planning a320. Technical report, Airbus, 2005.

[50] Airbus. Airbus-AC-A330 Characteristics, Airport and Maintenance Planning. Technical report, Airbus, 2005.

[51] Airbus. Airbus-AC-A340-200-300-Characteristics, Airport and Maintenance Planning. Technical report, Airbus, 2005.

[52] Airbus. Airbus-AC-A340-500-600-Characteristics, Airport and Maintenance Planning. Technical report, Airbus, 2005.

[53] Airbus. Airbus A380 fatigue test reaches 15,000 flight cycles, 2006. URL https://www.airbus.com/newsroom/press-releases/en/2006/07/airbus-a380-fatigue-test-reaches-15-000-flight-cycles.html.

[54] Airbus. Airbus-AC-A380-Characteristics, Airport and Maintenance Planning. Technical report, Airbus, 2005.

[55] Boeing. Boeing-B737 Airplane Characteristics for Airport Planning. Technical report, Boeing, 2013.

[56] Boeing. Boeing-B747-8 Airplane Characteristics for Airport Planning. Technical report, Boeing, 2012.

[57] Boeing. Boeing-B757 StartupBoeing. Technical report, Boeing, 2007. URL http://www.boeing.com/resources/

boeingdotcom/company/about_bca/startup/pdf/historical/757_passenger.pdf.

[58] Boeing. Boeing-B767 Airplane Characteristics for Airport Planning. Technical report, Boeing, 2005.

[59] Boeing. Boeing-B777-200/300 Airplane Characteristics for Airport Planning. Technical report, Boeing, 1998.

[60] Boeing. Boeing-B777-200LR/-300ER/-Freighter Airplane Characteristics for Airport Planning. Technical report, Boeing, 2015.

[61] G.R. Irwin. Analysis of stresses and strains near the end of a crack traversing a plate. *Journal of Applied Mechanics, Transactions ASME*, 24:361–364, 1957.

[62] C.E. Feddersen. Discussion on cracks. *ASTM STP*, 410:77–79, 1966.

[63] R.G. Forman, V.E. Kearney, and R.M. Engle. Numerical analysis of crack propagation in cyclic-loaded structures. *Journal of Basic Engineering*, D89:459–464, 1967.

[64] George Gerard and Herbert Becker. naca-tn-3783 handbook of structural stability part III buckling of curved plates and shells, 1957.

[65] Christos Kassapoglou. *Design and analysis of composite structures: with applications to aerospace structures*. John Wiley & Sons, Ltd, 2010. ISBN 9780470972632. doi: 10.4050/jahs.35.46.

[66] J.M. Whitney. *Structural analysis of laminated anisotropic plates*. Technomic Publishing, 1987. ISBN 9781351413268.

[67] George Gerard and Herbert Becker. Handbook of Structural Stability - Part 1: Buckling of Flat Plates. Technical report, NACA, 1957. URL http://naca.central.cranfield.ac.uk/reports/1957/naca-tn-3781.pdf.

[68] N Eswara Prasad, Amol Gokhale, and R.J.H. Wanhill. *Aluminium-Lithium Alloys: Processing, Properties, and Applications*. Elsevier Science, 2013. ISBN 9780124016798.

[69] Egbert Torenbeek. Development and Application of a Comprehensive, Design-sensitive Weight prediction Method for Wing Structures of Transport Category Aircraft, 1992.

[70] C.W.C van Woensel. *Integration of a Liquid Hydrogen Fuel Tank into the Concept of the Flying-V (MSc thesis)*. 2021.